Summer 2010

A study of the growth and structure of chromium and iron oxide films on Pd(001) using X-ray photoelectron diffraction and low energy electron diffraction

Tina Dhekial-Phukan

Department: Physics

A STUDY OF THE GROWTH AND STRUCTURE OF CHROMIUM AND IRON OXIDE FILMS ON Pd(001) USING X-RAY PHOTOELECTRON DIFFRACTION AND LOW ENERGY ELECTRON DIFFRACTION

by

TINA DHEKIAL PHUKAN

A DISSERTATION

Presented to the Faculty of the Graduate School of the

MISSOURI UNIVERSITY OF SCIENCE AND TECHNOLOGY

In Partial Fulfillment of the Requirements for the Degree

DOCTOR OF PHILOSOPHY

in

PHYSICS

2010

Approved by

George D. Waddill, Advisor
Oran A. Pringle
Julia E. Medvedeva
Alexey Yamilov
F. Scott Miller

ABSTRACT

In this study, attempts were made to grow well-ordered chromium- and iron-oxide films on a Pd(001) surface, and two sample preparation techniques, the multilayer and the sequential growth techniques, were used to grow these transition metal oxide films. The study is a part of a larger project that aims to look into the interaction between metal substrates and the overlayers grown on them. Previous studies of oxide films on Ag(001) resulted in the growth of 4-fold and 3-fold symmetry oxide structures from the multilayer and sequential growth techniques respectively. The present investigation's goal was to study how the growth of the oxide films on Pd(001) will be impacted by the growth technique.

For the Cr_xO_y films grown on Pd(001), the multilayer growth technique resulted in a p(1x1) LEED pattern for both the low and high coverage oxide films. Attempts were made to match XPD results with model calculations from a CrO(001) structure, a reconstructed Cr_3O_4(001), as well as from a mixed CrO-Cr_3O_4 phase with weighted compositions from each individual phase. The best fit between experiment and theory was obtained for a mixed phase of CrO(001) with $a_0^{CrO} = a_0^{Pd} = 2.75$ Å, and Cr_3O_4(001) with $a_0^{Cr_3O_4} = 2.86$ Å (here $a_0^{Cr_3O_4}$ and a_0^{CrO} represent the in-plane lattice parameters). The sequential growth technique did not lead to the growth of well-ordered films, and as such XPD scans could not be performed on the sequentially grown films.

For the Fe_xO_y films grown on Pd(001), both the sample preparation techniques resulted in a c(8x2) LEED pattern. This pattern is consistent with the structure of FeO(001) with a reconstructed surface. However, from the XPD scans, there were structural differences observed between the low and high coverage systems. Comparison of the XPD results with MSCD calculations showed that the thin films adopted the in-plane lattice parameters of the Pd substrate ($a_0^{FeO} = a_0^{Pd} = 2.75$ Å). MSCD calculations for the thicker films showed that the oxide structure for the high coverage systems is also a reconstructed FeO(001) but with more bulk-like FeO in-plane lattice parameters. The best agreement for the high coverage XPD curves is obtained for a FeO(001) structure with $a_0^{FeO} = 3.05$ Å, and with a first interlayer separation ~16% less than the bulk value.

ACKNOWLEDGMENTS

I would like to thank my research advisor Dr. G. D. Waddill for his invaluable guidance and support throughout my studies and research, and I appreciate his immense patience in helping me during the process of my dissertation writing. Working with him has not only been a pleasure, but also a great learning experience. I am also grateful to my other PhD committee members, Dr. O. A. Pringle, Dr. J. E. Medvedeva, Dr. A. Yamilov, and Dr. F. S. Miller for their time in reviewing my graduate work, and for their help.

Special thanks go to R. Summers, C. McWhorter, P. Crabtree, E. Kindle, and B. Swift for their kind help and support.

I'm deeply indebted to my parents, my husband, Manash, and my sister, Niha, for all their love, support and encouragement, for always believing in me, and for having stood by me every step of the way.

Finally, I extend my heartfelt gratitude to all my friends and colleagues in the MST Physics department, who have made my graduate-student life experience richer with their friendship, camaraderie, and help. And last, but not least of all, I am deeply grateful to Ola and Allison for their caring friendship and support, and for the wonderful memories that we have built up over the years here in Rolla.

TABLE OF CONTENTS

LIST OF ILLUSTRATIONS

LIST OF TABLES

NOMENCLATURE

Symbol	Description
XPS	X-ray Photoelectron Spectroscopy
XPD	X-ray Photoelectron Diffraction
LEED	Low Energy Electron Diffraction
UHV	Ultra-High Vacuum
FM	Frank-van der Merwe
SK	Stranski-Krastanov
VW	Volmer-Weber
EDC	Energy Distribution Curve
DOS	Density of States
TM	Transition Metal
TMO	Transition Metal Oxide
MSCD	Multiple-Scattering Calculation of Diffraction
SSC	Single-Scattering Cluster

1. INTRODUCTION

1.1. SURFACES AND SURFACE PHYSICS

A surface or interface, in general, may be defined as a part of a system where there is an abrupt change in the system properties with distance. In case of crystalline solids in vacuum, this surface is effectively confined to the outermost few atomic layers that differ significantly from the bulk. Surface properties can sometimes differ significantly from bulk properties. For example, it was found [1] that the (100) surface of Fe_3O_4 (magnetite) undergoes a metal-insulator transition above room temperature, which is well above the Verwey temperature of 123 K for the metal-insulator transition for the bulk. Typical properties showing an abrupt change at an interface are density, crystal structure, crystal orientation, chemical composition, charge, and ferromagnetic ordering.

The study of solid surface phenomenon is of great importance in physics, and the interactions with the immediate surroundings (vapor, liquid, solid) resulting from the existence of such an interface finds applications in many technologies like heterogeneous catalysis, microelectronics, electrochemistry, corrosion, and optoelectronic and magnetic devices. Epitaxial growth of thin films is a subject of considerable importance in the study of surfaces and interfaces, and there are numerous methods for growing films epitaxially. Multilayer films can be produced by sputtering, ultra-high vacuum methods (UHV) such as *molecular beam epitaxy* (MBE) and *metal-organic chemical vapor deposition* (MOVCD) methods, *pulsed laser deposition* (PLD), and other wet-chemistry methods. There are various experimental techniques available for characterization of surfaces. Due to the fact that many of these techniques are sensitive to only a few of the surface properties, the classification can be done mainly on the basis of the surface characteristics to which they are most sensitive. Firstly, there are methods which are sensitive to atomic geometry at surfaces. These include techniques like Low Energy Electron Diffraction (LEED), Electron Microscopy, Atomic Scattering and Diffraction, X-ray Photoelectron Diffraction (XPD), Surface-Sensitive Extended X-ray Absorption Fine Structure (SEXAFS), among others. Then, there are methods sensitive to chemical composition at surfaces like Auger Electron Spectroscopy (AES), Ion-Scattering Spectroscopy (ISS), Thermal Desorption Spectroscopy (TDS), and X-ray Photoelectron

Spectroscopy (XPS). Some methods, like Infrared Spectroscopies (IR) and Raman Spectroscopy, and Electron Tunneling Spectroscopy, are sensitive to vibrational structure of surfaces. Techniques like, work function measurements, are sensitive to electron distribution at surfaces. The list is not exhaustive and there are many other methods.

1.1.1. Surface Energy and Film Growth Modes. The concept of surface energy is an important factor in understanding the morphology and composition of surfaces and interfaces. It quantifies the disruption of intermolecular bonds that occurs when a surface is created. The surface has to be considered differently from the bulk in that surfaces are intrinsically less energetically favorable than the bulk of a material - for instance, the pressure in the bulk of an isotropic solid is equal in all directions, while the pressure on the surface plane is highly anisotropic. The surface energy can be viewed in relation to the work that would be required to bring two ideal surfaces in vacuum together.

The surface free energy is one of the basic quantities in surface physics. It is of great importance in understanding a wide range of surface phenomenon like crystal growth phenomenon, the equilibrium shape of mesoscopic crystals, faceting, roughening, surface segregation, sintering, catalytic behavior, adsorption, and the formation of grain boundaries.

Near equilibrium, growth of epitaxial overlayers on a substrate can occur through three different growth mechanisms when interdiffusion does not occur - the layer-by-layer deposition, called the Frank-van der Merwe (FM) growth, the Volmer-Weber (VM) mode which corresponds to the formation of three-dimensional crystals from the vapor phase, and the Stranski-Krastanov (SK) mode which corresponds to the nucleation of 3D crystals after a layer-by-layer deposition of few monolayers on the substrate. Bauer was the first to investigate the growth modes of overlayer films in terms of surface free energies [2].

Figure 1.1 schematically illustrates the three growth modes. As shown in Figure 1.1(a), when the deposited atoms are more strongly bound to each other than they are to the substrate, the three-dimensional island or Volmer-Weber (VM) growth mode results. The FM or pseudomorphic growth mode (Figure 1.1(c)) arises out of a stronger interaction of the atoms of the deposited material with the substrate than among the

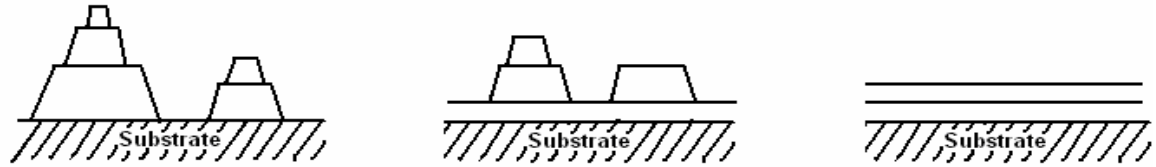

(a) **(b)** **(c)**

Figure 1.1. Schematic representation of three growth modes: (a) island, or Volmer-Weber growth; (b) layer-plus-island, or Stranski-Krastanov growth; (c) layer-by-layer, or Frank-van der Merwe growth.

deposited atoms themselves. For an intermediate case, the layer-plus-island or Stranski-Krastanov mode (Figure 1.1(b)), growth occurs through the initial formation of layers followed by the growth of islands later on. After the growth of a few monolayers, the adsorbate-substrate interaction weakens, the interfacial energy increases as the layer thickness increases and strain develops in the layer to fit the substrate. The interfacial stress is relieved in the overlayer by the initiation of the growth of 3D overlayer structures. In terms of the spreading coefficient $S_{A/B}$, where,

$$S_{A/B} = \gamma_A + \gamma_{AB} - \gamma_B \tag{1.1}$$

and γ_B, γ_A, γ_{AB}, are the surface free energies of the substrate, film, and substrate-film interface, respectively, when $S_{A/B} > 0$, VW growth mode occurs, and for $S_{A/B} \leq 0$, SK or FM growth modes take place. This macroscopic theory of wetting phenomenon cannot be applied for the study of overlayers in the monolayer range. Such a theory, that predicts the growth mode from information about the spreading coefficient $S_{A/B}$, assumes experimental equilibrium being reached between the condensed phases and their vapors which is not realized in practice. A more accurate understanding of these growth mechanisms can be obtained from a microscopic theory of wetting phenomenon as described by Gautier and Stoeffler [3].

Another concept is the surface chemical potential which can be very useful, from the point of view of its dependence on the overlayer thickness, in understanding these growth modes. Chemical potential is a thermodynamic quantity that expresses the

incremental energy content of a system per unit particulate mass. Higher chemical potential indicates higher chemical reactivity and a spontaneous reaction. In bulk phases, the contribution of the surface energy to total energy content is inconsequential and the surface chemical potential hardly comes into play. However, at the nanoscale level, the surface energy forms a major part of the total energy and has to be included in the calculation of chemical potential. This 'surface chemical potential' can be regarded as the surface or interfacial energy per unit particulate mass. Thus higher surface chemical potential means higher surface energy. The surface chemical potential is defined by:

$$\mu_i^{\sigma} = \left(\frac{\partial G^{\sigma}}{\partial n_i^{\sigma}} \right)_{T,p,n} \tag{1.2}$$

Here, G^{σ} is the surface excess Gibbs energy, and T, p, represent the temperature and pressure, respectively. The subscript n denotes the fact that the numbers of molecules of all the different chemical components (n_1, n_2…) except the one number n_i are kept constant. For different deposit and substrate materials, the difference in the chemical potentials of the substrate and deposit crystals arises from the difference in the nature and strength of the chemical bonds in each system, as well as from the difference in the lattice structure and parameters.

Thermodynamically, the different growth modes arise from the dependence of the chemical potential of the overlayer on its thickness which constitutes the main difference of the epitaxial growth from the usual crystal growth and which gives rise to the appearance of the three well-known mechanisms of epitaxial growth [4]. Figure 1.2 schematically illustrates the dependence of the nucleation and growth of overlayers on a substrate on the chemical potential. Considering complete condensation of the vapor atoms arriving at the substrate before re-evaporation, the atoms will randomly diffuse on the surface to form 2D nuclei after a period of thermal accommodation. The 2D nuclei grow further by the adatoms diffusing and attaching to the edges of the nuclei on the substrate surface and on the exposed surface as well. The chemical potential of the deposit will vary from monolayer to monolayer due to the interaction with the substrate.

Figure 1.2. Schematic representation of (a) nucleation of 2D islands of the second monolayer; (b) surface transport from the edges of the lower islands to the edges of the upper islands; (c) surface transport transformation of the layer configuration into a crystal of two-monolayer height which leads to nucleation of islands of the third monolayer.

Thus, the chemical potential $\mu(n)$ is a function of the overlayer thickness, where n represents the number of overlayers. When $\mu(1) > \mu(2)$, so that $d\mu/dn < 0$, the adatom population on top of the first monolayer islands is supersaturated with respect to the bulk deposit crystal, and this favors the nucleation on top of the first monolayer islands (Figure 1.2(a)). The first layer adatom concentration, n_{s1}^{e}, in equilibrium with the island edges is such that $n_{s1}^{e} > n_{s2}^{e}$, where n_{s2}^{e} is the equilibrium adatom concentration for the second layer. This will cause the surface transport to occur from the edges of the lower island to the edges of the upper island (Figure 1.2(b)). Thus the upper islands will grow at the expense of the lower islands and after some time catch up with the lower islands to produce islands with double height (Figure 1.2(c)). For high enough temperatures to facilitate the surface transport, island or VW growth mode will be observed. But if the temperature is low, the edge-to-edge surface transport will be hindered and the first monolayer island will grow laterally to coalesce and cover the substrate completely before any growth on top of them takes place giving rise to a metastable *layerlike* growth, and such films, being metastable, will break up to form 3D island upon heating. When $\mu(1) < \mu(2)$, that is, $d\mu/dn > 0$ (Figure 1.2(b)), the islands of the second monolayer will have a higher chemical potential than that of the lower islands and the surface transport of atoms will occur from the edges of the upper islands to the edges of the lower islands. The upper islands will decay, and the FM growth mode will be observed irrespective of the temperature. For the SK growth mode to occur, a transition will have to occur from $d\mu/dn > 0$ to $d\mu/dn < 0$. Once a certain thickness is reached, the corresponding chemical potential becomes higher than the equilibrium chemical potential μ_{∞}, and 3D islands will form and grow at high temperatures. Surface transport takes place from the edges of the more elastically strained islands to the edges of the islands with less or no strain at all, resulting in the SK growth mode. At low temperatures, formation of successive monolayers occurs, and again if such low temperature films are annealed, the material in excess of the first stable monolayers (for which $d\mu/dn > 0$) will break up to form 3D islands.

While the knowledge of the surface free energies and interfacial energies enables the determination of film growth mode, these energies are rather difficult to determine experimentally. In spite of considerable experimental efforts, for many metals the

recommended values of surface energy have uncertainties of unknown magnitude. In addition, misfit strain energies must be taken into account with increase in film thickness. Surface energy values have been compiled by few authors like Boer et al. [5] and these provide one of the most consistent choices of surface energies in existence. In addition, numerous theoretical models [6-10] exist to form essential guides to surface energy values and for explaining the trends exhibited experimentally. As such, determination of film growth mode kinematically has to be a selective and careful process.

1.1.2. Relaxation and Reconstruction of Surfaces. The analysis of surface structures involves the study of important structural changes. Surface relaxations [11] can occur, in which surface atoms seek new equilibrium positions that change the interlayer distance between the first and second layers of atoms or ions leading to contraction or expansion. This kind of change does not affect the coordination number or the rotational symmetry of the surface atoms. Then, there is reconstruction of clean surfaces and surfaces with adsorbates. The surface atoms seek new equilibrium positions that change not only the bond angles but also the rotational symmetry and coordination number. Since the surface atoms are surrounded by atoms only on one side and there is vacuum on the other side, they may change their coordination number by slight relocation and simultaneous changes of electronic structure. Finally, there are relaxation or reconstruction processes induced by changes of surface composition. The surface may be entirely clean or it may have foreign atoms deposited on it or incorporated in it. For polyatomic solids the surface composition may be very different from that in the bulk. With variation in surface composition, new oxidation states may be stabilized in the surface layer.

Since the surface atoms have lost some nearest neighbors compared to the bulk, the bond lengths, for clean surfaces, between the atoms in the first and second layer are somewhat contracted compared to the bond lengths in the bulk. The lower the coordination number, the larger is the bond contraction. In most cases atoms adsorbed on the surface can remove this bond contraction and restore the bulk bond length between the surface and the second layer, or induce further contraction on the other hand. For surfaces in the clean state that undergo reconstruction, either the surface atoms relocate substantially from their ideal bulk positions to form superlattices or undergo sufficient

bond length and bond angle modifications. On unreconstructed surfaces, the lattice constant parallel to the surface generally does not change, and only the first interlayer atomic separation decreases, and is generally small though discernible. The bond length contractions are more for less closely packed surfaces – bcc(100), fcc(110), bcc(111), fcc(311) – than they are for more closely packed surfaces – fcc (111), hcp(0001), bcc(110), and fcc(100). Phenomenologically, the origin of these contractions can be considered to be electrostatic forces drawing the surface atoms towards the substrate, and this effect should be stronger the less closely packed the surface is. Also, with less closely packed surfaces, the fewer the neighbors, the smaller the two-body repulsion energy, thereby allowing greater atomic orbital overlap and more favorable bonding at shorter bond lengths. Also, the tendency of the cleaved surfaces to eliminate the dipole moment normal to the surface by transferring and distributing the bonding electrons from the broken bonds to the remaining unbroken bonds will reduce the bond length. When adsorbates are deposited on surfaces, the shortened bond lengths for the surfaces are systematically lengthened again by the presence of adsorbates. This behavior has been experimentally observed by both LEED and ion scattering experiments. For example, for adsorption of oxygen on the Fe(100) surface, the underlying metal bond lengths expand to beyond their bulk value and the FeO bulk oxide geometry is approached, exhibiting the first stage of the oxidation process at a surface. A variety of reconstruction geometries can occur on surfaces, and these reconstructions are usually destroyed in favor of the unreconstructed geometry in the presence of adsorbates due to the strong substrate-overlayer bonding in the chemisorption process. But, this effect is not always strong enough though as has been observed for the case of a full film of xenon on Ir(100) which does not seem to destroy the reconstruction [11].

1.1.3. Growth of Metal-Oxide/ Metal Interfaces. Major scientific efforts have been expended in trying to understand the growth morphology and resulting physical and chemical properties of ultra-thin metal oxide films. Due to the insulating nature of many metal-oxides, the only way to characterize their physical properties is to study an ultra-thin metal oxide film grown on a conducting substrate since characterizing bulk samples with either electron or ion spectroscopies results in severe sample charging. Another way to avoid charging would be to dope the film to increase carrier density – this technique,

however, would be applicable only for metal oxides that can be doped. For the former, the excess charge would be removed through the substrate after tunneling through the insulating oxide film. In the latter case, conductivity through the film is employed. A number of factors critically influence the overlayer growth mode of these oxides – choice of the substrate, degree of substrate misorientation, degree of adsorbate-substrate interaction, growth temperature, oxygen pressure, the diffusion rates of metal or oxygen species across the interface, oxide film preparation technique, impurity diffusion, and kinematically-limited growth.

Substrate-overlayer interactions during the growth of a heteroepitaxial system can be significant, and depending on the type of interaction, it can lead to three kinds of growth modes: (a) Frank-van der Merwe (FM) growth mode is realized when adsorbate-substrate interactions dominate, (b) Volmer-Weber (VW) growth occurs when adsorbate-adsorbate interactions dominate, and (c) Stranski-Krastanov (SK) growth mode is realized when the first few monolayers grow layer-by-layer, and then to relieve interfacial stress, subsequent 3D overlayer structures are formed. The three growth modes have been discussed in greater detail in Section 1.1.1.

The three growth modes described above are assumed for an ideal substrate for that is perfectly oriented and free from defects. In reality, the overlayer growth mode depends critically on the degree of substrate misorientation. There are vicinal substrates, in which the substrate normal deviates slightly from a major crystallographic axis. On these substrates, growth of an overlayer starts with nucleation of the adsorbed atoms at the step edges, followed by a step-flow growth propagating out from the step edges. Presence of defect sites at the substrate surface can also affect the growth mode of the overlayer. These defects can act as nucleation sites for the adsorbate atoms during the initial stages of growth resulting in a VW growth mode, in contrast to a situation where FM or SK growth would normally proceed on a defect-free substrate.

The choice of the substrate for growth of the metal-oxide overlayer depends on the kind of requisites desired for that particular film growth. For growth of a uniform overlayer with low defect density, it is necessary to choose a well-oriented substrate with similar parallel symmetry and lattice parameter to minimize interfacial stress effects. At other times, substrates with defects and mismatched lattice may be desired for creating

unique overlayer structures with novel electronic, magnetic, and chemical properties, increasing the chemical reactivity of the metal-oxides, or for observing unique surface chemistry.

The growth morphologies of heteroepitaxial systems can be critically affected by the growth temperature. At low to moderate temperatures, the diffusion rate of ions and electrons during metal-oxide growth are quite low, as typically ionic materials have strong internal electrostatic forces. For temperatures well above room temperature, diffusion rates increase, leading to the growth of high-quality, defect-free metal-oxide overlayers. However, at excessively high temperatures, impurity segregation can adversely affect the crystalline quality of the overlayer, in addition to formation of a non-abrupt interface due to intermixing of the overlayers atoms with the substrate. In addition, at constant temperature, oxygen pressure variation can significantly influence the phase composition, microstructural evolution of the metal-oxide overlayer, surface termination, and diffusion rates.

Epitaxial metal-oxide/metal interfaces can be grown by primarily two techniques – oxidation of the surface region of a single-crystal metal substrate, and preparation of metal-oxide overlayers onto a substrate. The former technique is limited in scope as most metal oxides do not grow epitaxially on the native metals due to the comparatively large mismatch between lattice parameters of the metal crystal and the corresponding oxide. The latter technique is the more versatile of the two and involves growing the metal-oxide by evaporation of the metal onto a substrate. Oxidation can be performed either during the metal evaporation in an oxygen atmosphere, or by oxidizing the metal after it is deposited by evaporation. This deposition technique is preferred for situations when interfacial stresses need to be reduced by choosing a metal substrate with similar surface symmetry and surface lattice constants as that of the epitaxial metal-oxide overlayer to be grown. In the present study, the deposition technique of first evaporating the metal onto a substrate followed by oxidation is employed, and there are two ways in which this is achieved. Multilayer deposition involves depositing multiple layers of the metal film (Fe or Cr) on a Pd substrate followed by oxidation at specific oxygen pressure and elevated substrate temperature. Sequential deposition involves depositing metal films of

submonolayer thickness followed by oxidation, and repetition of the cycle of submonolayer deposition and oxidation until desired thickness is achieved.

Reconstructions are particularly frequent on semiconductor surfaces. The concept of 'autocompensation' was originally developed for surfaces of compound semiconductors. However, autocompensation has proved very successful in predicting the reconstructions of metal oxide surfaces also. The most stable surfaces are predicted to be those for which the excess charge from cation-derived dangling bonds compensates anion-derived dangling bonds [12]. The net result is that the cation- (anion-) derived dangling bonds are completely empty (full) on stable surfaces. Thus, autocompensation model allows for not only ionic solids, but also those metal oxides that are partially covalent in character. Fulfilling the autocompensation criterion is equivalent to conditions for creating non-polar surfaces of ionic or partially ionic crystals as described by Tasker [13]. As shown in Figure 1.3, the ionic crystal can be represented by replacing each plane of ions parallel to the surface with a plane of uniform charge density ρ. Three distinct types of stacking sequences for ionic crystals can then be described : (a) A type 1 stacking sequence where the net charge density in each plane is zero, since each plane consists of anions and cations in their correct stoichiometric ratio, resulting in a non-polar

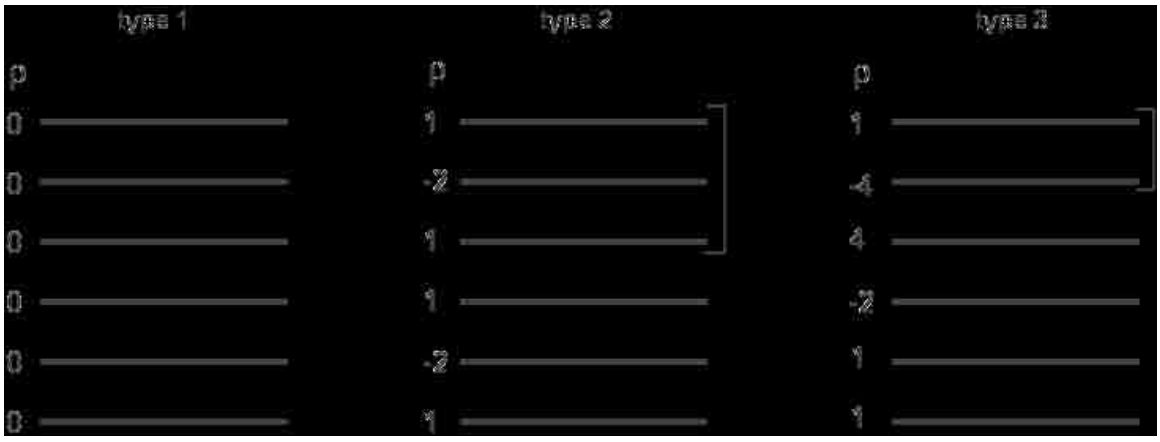

(a) **(b)** **(c)**

Figure 1.3. Tasker's representation of the three distinct types of stacking sequences for an ionic crystal. Each plane of ions parallel to the surface is replaced with a plane of uniform charge density ρ.

surface, as shown in Figure 1.3(a); (2) a type 2 stacking sequence where there is a net charge density in each plane, but the repeat unit of the crystal has no net dipole moment normal to the surface resulting in a non-polar surface (Figure 1.3(b)); (c) a type 3 stacking sequence where there is a net charge density in each plane and a net dipole moment for the repeat unit resulting in a polar surface (Figure 1.3(c)). A polar surface is unstable, and the instability is overcome by charge neutralization which can occur through (1) a surface reconstruction, (2) a change in the charge state of the surface ions, or (3) charge transport to the surface regions if the oxide is conducting. For metal-oxides that are either insulators or semiconductors, charge redistribution is difficult without a large-scale mass transport. Therefore, the predominant surface terminations for metal-oxides during growth are non-polar. For natural crystals that grow preferentially along polar directions, most are stabilized by impurity adsorption at the surface.

1.2. TRANSITION METAL OXIDES

Transition metal oxides (TMOs) constitute a class of inorganic solids exhibiting a very wide variety of structures, properties, and phenomena. There are TMOs with metallic properties (e.g., RuO_2, ReO_3, $LaNiO_3$), with insulating behavior ($BaTiO_3$, TiO_2), semiconductors (FeO), and superconductors (e.g., $YBa_2Cu_3O_7$); oxides with ferromagnetic (e.g., CrO_2), ferrimagnetic (e.g., Fe_3O_4) and antiferromagnetic (e.g., NiO) properties. There are oxides exhibiting metal to non-metal transitions with changes in temperature, pressure, or composition (e.g., V_2O_3). Interesting electronic properties are accompanied with diverse magnetic properties. One of the reasons for these unusual physical and chemical properties of transition metals (TM) and TMOs is due to the unique nature of outer *d* electrons, the metal-oxygen bonding in TMOs varying anywhere from nearly ionic to metallic. The extraordinarily varied chemical and physical properties of TMOs are a feature of the progressive filling of shells of localized *d* orbitals across each transition series. Oxides of d-block transition elements have narrow electronic bands because of the small overlap between the metal *d* and oxygen *p* orbitals, resulting in important electron correlation effects. While bulk oxide properties are important, it is the surface properties of these oxides that are increasingly becoming more important for

scientific and technological applications. In the study of the growth of epitaxial metal-oxide/metal interfaces, the interaction between the substrate and over- layer can often result in new structures that are not thermodynamically stable in their bulk forms. However, due to their varied features, establishing theoretical models for transition metal oxides is often difficult and challenging. But the extraordinary range of structures and properties of the transition metal oxides make them extremely versatile for a wide range of applications such as catalysis, corrosion passivation, magnetism and solid state electronics, making them worthy of special attention.

One of the straight forward ways of producing a TMO film is oxidation of a transition metal surface. Several studies on synthesis of TMOs by direct oxidation of a TM surface have been reported [14-17]. However, this method does not often lead to growth of films with good crystalline quality, and the stoichiometry cannot be controlled. Deposition of an oxide film on a appropriate substrate by methods such as molecular beam Epitaxy (MBE), atomic layer deposition (ALD), laser ablation deposition (LAD), and chemical vapor deposition (CVD) have proved very successful in recent years, aided by the rapid development of ultra-high vacuum technology. Close lattice match between the substrate (e.g.: MgO, Al_2O_3, Cu, Ag) can result in high crystallographic order in the oxide thin film.

In this study, TMO films on a single crystal surface of Pd (001) were grown, and the films were characterized using x-ray photoelectron spectroscopy (XPS), x-ray photoelectron diffraction (XPD), and low energy electron diffraction (LEED). In XPS, approximately monoenergetic x-rays impinge on the sample, resulting in the interaction of the photons with atoms in the sample and production of core-level photoelectrons. The fact that the core energy levels probed by XPS are atom specific makes elemental analysis of the sample possible. Features such as binding energy shifts arising from difference in the local electron distribution can give information regarding the possible oxidation states of the given sample. Like XPS, XPD is an elemental specific structural analysis technique, in which intensity modulations of the emitted photoelectron signal due to structural variations in the sample are measured. In LEED, electrons of well-defined energy and direction of propagation diffract off a crystal surface through elastic

backscattering. LEED has been used as a complementary technique to XPS and XPD for determination of surface order and lattice structure of overlayers.

1.3. DISSERTATION OUTLINE

In this dissertation, investigation on the structures of ultra-thin surfaces of Cr_xO_y and Fe_xO_y grown on Pd(001) surface are presented. The films were characterized using X-ray photoelectron spectroscopy (XPS), x-ray photoelectron diffraction (XPD), and low energy electron diffraction (LEED). Two sample preparation techniques, multilayer growth and sequential growth, were used to grow these transition metal oxide films. In the multilayer growth technique, multilayer Fe (or Cr) metal films were deposited followed by oxidation of the deposited metal. In the sequential growth technique, submonolayer thickness Fe (or Cr) metal films were deposited followed by oxidation, and the process was repeated until the desired thickness was achieved. Both kinds of growth were done at specific substrate temperatures and oxygen partial pressures. Previous studies of iron-oxide and chromium-oxide films on noble substrates like Ag showed strong dependence of the overlayer structure on the deposition technique. Relatively weak interaction between the Ag substrate and the oxide film layer resulted in the growth of various structures depending on the growth technique, such that it was possible to obtain oxide structures with both four-fold and three-fold symmetries on a substrate with four-fold symmetry. The aim of the present study was to see if interaction between a more reactive substrate like Pd and the overlayers grown on it impacted the variety of oxide structures that could be realized.

Both sample preparation techniques result in a c(8x2) LEED pattern for Fe_xO_y on Pd(001). The symmetry of the LEED patterns remains four-fold irrespective of the growth technique or the film coverage. The structure was identified to be reconstructed FeO(001) surface. From XPD results and model calculations, the high coverage phase (for both sequential and multilayer growth) is proposed to have bulk-FeO like in-plane lattice parameters, whereas the low coverage phase exhibited the effect of dominance of the substrate on the oxide structure by forcing the film to adopt the in-plane lattice parameters of the Pd(001) substrate. Attempts were also made in the model calculations

to incorporate possible inter-layer relaxation effects for both the low and high coverage films.

For the multilayer growth of Cr_xO_y films, a p(1x1) LEED pattern was observed at all coverages. Two possible structural determinations have been made – a CrO(001) surface, and a reconstructed Cr_3O_4(001) surface. It is unlikely that it will be possible to make a distinction with any amount of reasonable accuracy whether the multilayer Cr_xO_y surface is a CrO(001) or the reconstructed Cr_3O_4(001). It is also possible that the oxide structure is a mixed CrO-Cr_3O_4 phase. The fact that stable bulk CrO is not found in nature, gives rise to the possibility that there may be ways of mediating the stability of a CrO structure on the nanoscale level on a substrate. Attempts were also made in the model calculations to incorporate possible inter-layer relaxation effects for both kinds of structure. For the sequentially grown films Cr_xO_y, no stable structure was obtained. At the elevated substrate temperature at which the multilayer oxide films were grown, it was possible to obtain a c(4x2) LEED pattern for the sequentially grown films, but, this phase was unstable, and even after several growth attempts at different substrate temperatures, the phases were not stable and ordered enough to justify further characterization.

2. SAMPLE PREPARATION AND ANALYTICAL TECHNIQUES

2.1. X-RAY PHOTOELECTRON SPECTROSCOPY (XPS)

X-ray photoelectron spectroscopy (XPS) is a widely used technique for studying properties of atoms, molecules, solids, and surfaces. The first experiments of this type were carried out by Robinson and Rawlinson in 1914. Steinhardt and co-workers first observed that core photoelectron peak intensities could be used for quantitative analysis and that core electron binding energies exhibited chemically-induced shifts [18-19].

In photoelectron spectroscopy, the photoelectrons are the information carriers [20]. The fundamental experiment involves exposing the specimen to be studied to a flux of nearly monoenergetic radiation with mean energy *hν*, and then observing the resultant emission of photoelectrons – the photoelectric effect. Detection is possible if the energy absorbed is sufficient for the electron to be ejected from the sample, and in the case of solids, this energy must include the work function of the material.

$$h\nu = E_b^V(k) + E_{kin} + \phi \tag{2.1}$$

$E_b^V(k)$ is the binding energy of the *k*th level as referred to the vacuum level, E_{kin} is the photoelectron kinetic energy, and ϕ is the work-function of the material. Though both Auger electrons and secondary electrons are also emitted from the specimen, it is generally possible to distinguish these electrons from true photoelectrons. A schematic of the process of photoelectron emission is shown in Figure 2.1.

Auger electrons are produced when an electron from a core level of the atom is ejected by an incident electron or photon, and an electron from a higher energy level fills the core hole left behind, with the subsequent emission of an electron from an outer level for energy compensation [2]. Figure 2.2 is a schematic illustrating the process of Auger electron emission, for which the energy equation can be given by:

$$E_k = E_A - E_B - E_C \tag{2.2}$$

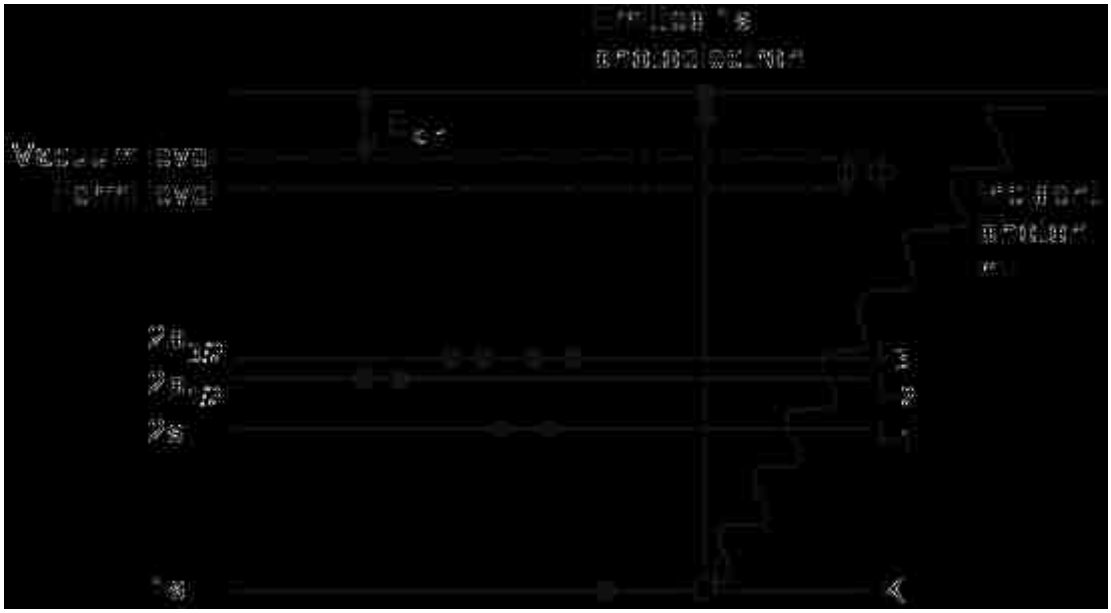

Figure 2.1. Schematic of core-level photoemission process. An incident photon of energy *hv* is annihilated and its energy absorbed by an electron which is then ejected as the photoelectron.

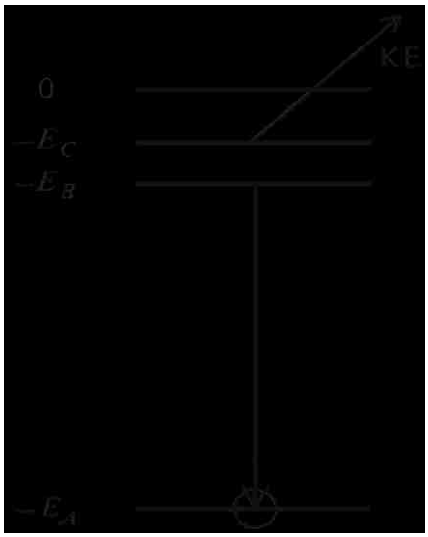

Figure 2.2. Energy level diagram showing the filling of a core level hole in level A, giving rise to Auger electron emission.

Here E_k is the Auger electron kinetic energy, and E_A, E_B, and E_C are the different energy levels involved in the emission process. The emitted electron is characteristic of some combination of atomic energy levels of the emitter. This is true even if either, or both, of the levels B and C are valence band levels as at least one core level (E_A), characteristic of the atomic species alone, is involved. Auger transitions will be discussed again in a later section.

One of the ways to distinguish between core-level photoelectrons and Auger electrons is to observe the x-ray photoelectron spectrum using different photon energies. Core-level photoelectrons have kinetic energies that depend on the incident photon energy. This kinetic energy will change whenever different photon wavelengths are used for spectroscopy, and the photoelectron peaks will be observed at the different kinetic energies whenever the energy of excitation source is changed. Auger electrons, on the other hand, are independent of the photon energy, as their kinetic energy depends only on the energy difference of the levels involved in the Auger transition. The Auger peaks will always be observed at the same kinetic energies for a particular Auger transition, irrespective of the incident photon energy used.

Figure 2.3 gives an illustration of some of the main features observed in fixed-angle XPS spectrum data obtained from a Pd (001) specimen exposed to soft x-rays of energy 1253.6 eV. A broad-scan spectrum of 1000 eV width is displayed. The photoelectron peaks are considerably narrower and simpler in structure than the Auger peaks; the Mo peaks are due to a thin Mo foil surrounding the Pd sample, put in to hold the sample in place, while the C1s peak is due to an outermost thin surface layer of contaminants containing carbon. Each photoelectron peak exhibits an approximately constant background on its low-kinetic-energy side that is due to inelastic scattering. This background is due to electrons, arising via the primary photoemission process, that are scattered inelastically while escaping the specimen and appear in an “inelastic tail” or energy loss spectrum. The characteristic stair-case shape of the inelastic background is due to the fact that at high kinetic energies (low binding energies), there are fewer of the primary electrons undergoing inelastic scattering, but as more and more energy levels lying deeper in the atom are probed, additional electrons are produced, so that with each new emission as the XPS spectrum proceeds towards the higher binding energy side,

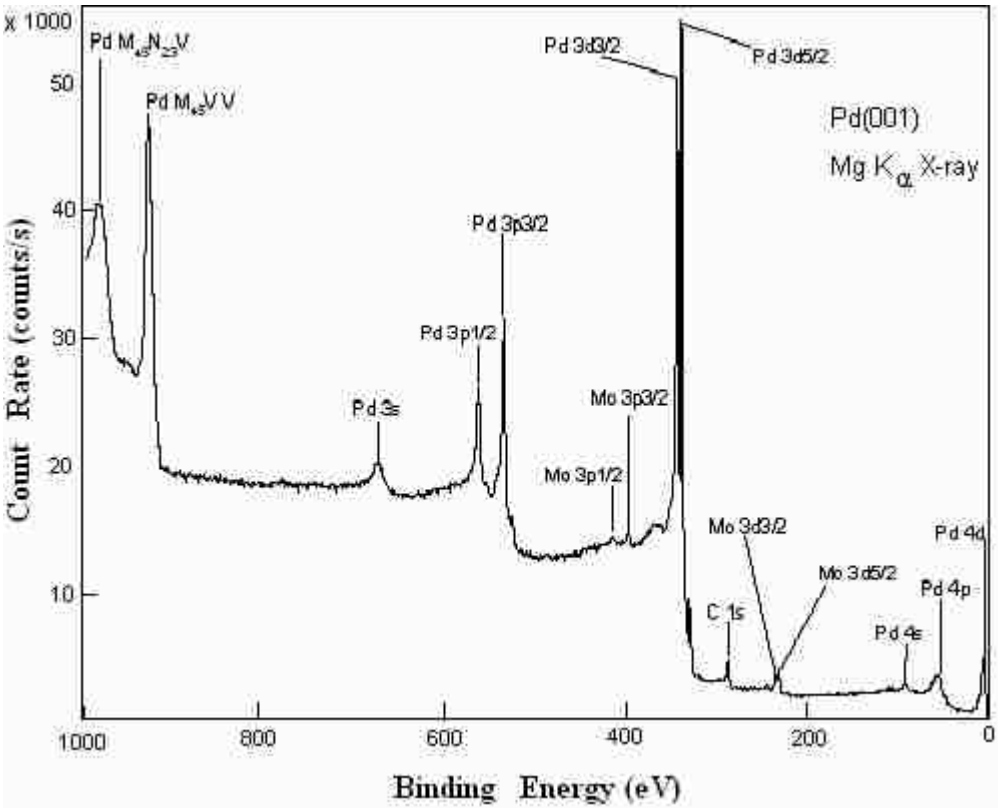

Figure 2.3. XPS spectrum of Pd(001).

more and more electrons with lesser kinetic energy are available for inelastic scattering [2]. In general, XPS valence photoelectron intensities are approximately an order of magnitude lower than those of the most intense core levels in a given specimen, but they are nonetheless high enough to be accurately measured and studied.

2.1.1. The Photoemission Process. For interpretation of photoemission experiments, Berglund and Spicer [21] proposed the three-step model for photoemission, utilized for analysis of photoemission studies in solids. Though a purely phenomenological approach, the model has proved to be extremely successful.

The complicated photoemission process can be broken up into three parts. In the first step, an electron below the solid surface is excited from an initial energy E_i to a final energy E_f greater by hv. The electron states involved are generally assumed to be characteristic of the bulk material. In the second step, the electron in the final state is

transported to the surface, and elastic and inelastic scattering events may occur during this step. In the third step, the electron passes across the surface into vacuum where it can be detected.

The final state in a photoemission experiment has a positive hole, and thus is distinctly different from the initial state. The transition of the electron from an initial state $|\psi_i\rangle$, to an excited state $|\psi_f\rangle$ by absorption of a photon of energy *hv*, to the final state $|\psi_{F^*}\rangle$ due to the electron's passage through the solid to the surface, will affect the kinetic energy distribution of detected electrons. The measured energy distribution curve (EDC) [6-8] can therefore be considered to be a result of the contribution of all the three steps, and can be expressed as:

$$E(E_k) \propto N_f(E_k) L_{tr}(E_k) S_{em}(E_k) \tag{2.3}$$

$N_f(E_k)$ represents the kinetic energy distribution of the electrons in the solid after the optical transition from the initial state $|\psi_i\rangle$ to the excited state $|\psi_f\rangle$. L_{tr} represents the effect on the EDC of the transport of the excited photoelectrons through the solid to the surface. $S_{em}(E_k)$ contains the effects of the emission of the photoelectrons through the surface into vacuum.

The first step is a simple optical transition with momentum being conserved (vertical transition), and the energy difference between the initial and final states being equal to that of the absorbed photon, as described in Equation 2.4, where E_i is the energy of the initial state, E_f is the energy of the final state, and *hv* is the energy of the absorbed photon:

$$E_f - E_i = h\nu \tag{2.4}$$

The probability of the optical transition, *w*, from an initial state $|\psi_i\rangle$ to a final state $|\psi_f\rangle$, calculated by the Fermi Golden Rule [22], and within the first order dipole

approximation[1] (according to which the wavelength of the incident radiation λ_{hv} is large compared to the dimensions of the excitation volume) is,

$$w \propto \frac{2\pi}{\hbar}\left|\left\langle \psi_j \mid \vec{r} \mid \psi_i \right\rangle\right|^2 \delta(E_j - E_i - h\nu) \tag{2.5}$$

Here $\vec{r}$ is the position operator; E_f, E_i, and $h\nu$ are the energies of the initial state, final state, and photon, respectively. The dipole approximation should be satisfactory for XPS as the core levels (since the energy levels of predominant interest in XPS are the core-level energies) are localized so that the average value of $\vec{r}$ is small, and λ_{hv}, the photon wavelength, is large.

The important assumption made in this model is the one-electron view for the initial and final state wave function [22]. To illustrate the point, assuming that the system under consideration has N electrons, we consider that the initial state $\psi_i(N)$ can be taken to be a product of the wave function of the orbital from which the electron is excited — φ_i^k, and the wave function of the remaining (N-1) electrons — $\psi_i^k(N-1)$, i.e.,

$$\psi_i(N) = C\varphi_i^k \psi_i^k(N-1) \tag{2.6}$$

C is an antisymmetrizing operator. Now, the remaining (N-1) orbitals are assumed to be the same in the final state after excitation as they were in the initial state. This renders the transition matrix element in the expression for the transition probability just a one-electron matrix which means that the electronic configuration in the photoelectron's environment is the same as it was before excitation except with a core hole. This also implies that the binding energy seen by the photoelectron, E_b, of the state it leaves is the same as it was prior to excitation, and hence all other electrons in the system are in the

[1] The dipole approximation is not completely valid for the photon energy ranges typically used in XPS ($h\nu$ ~ 1000-1500 eV) since in this case a_0/λ_{hv} ~ 0.5 Å/ 8 Å ~ 0.06 (a_0 = dimension of excitation region), but within the three-step model it is a sufficient first-order approximation.

same state as before the photoionization event. This energy is referred to as Koopman's energy [2]. The emergent kinetic energy, E_k, of the photoelectron is:

$$E_k = h\nu - E_b \tag{2.7}$$

The effect of the optical transition is to rigidly shift the energy of the distribution of electrons in the initial state by an amount equal to $h\nu$, such that the measured EDC reflects the initial density of states (DOS), $N_i(E_i)$. This EDC will then be modified and complicated by the transport and escape of the electron in the second and third steps, but will still retain information about the initial DOS.

In step one of the model, relaxation processes after the photoexcitation, which would bring about a reconfiguration of the remaining *N-1* charges for minimization of energy have been ignored. In reality, Koopman's energy is never observed. When the core hole is created, other electrons relax in energy to lower energy states to screen this hole partially and make more energy available to the outgoing photoelectrons. The kinetic energy will not simply be the difference between $h\nu$ and the initial atomic orbital binding energy, but will be altered due to the changed electronic environment after excitation. The result is that the measured EDC will not simply be a shift in the DOS modulated by transport and emission effects. The way to have a more complete representation of the excitation process would be to consider multi-electron effects on the excitation process. However, the many-electron picture will not be considered here.

The second step involves the effects of transport through the solid to the surface on the photoelectron. The features and shape of the EDC will be determined by both elastic and inelastic scattering processes. Inelastic scattering acts to diminish the no-loss photoelectron current; photoelectrons lose energy as they travel through the specimen, and many will not have sufficient energy to escape through the surface; still, others that do, will not reveal the required information on the density of states, and will simply contribute to a smooth background signal present within the EDC. In XPS studies of solid specimens, inelastic scattering in solids is generally discussed in terms of a characteristic length for decay of the no-loss intensity. Specifically, for a monoenergetic flux N_0

generated at energy E_{kin} at a given point, the no-loss flux N remaining after traveling a distance l is assumed to be given by an exponential decay law [23]:

$$N = N_0 \exp[-l / \lambda_{mfp}(E_{kin})] \tag{2.8}$$

Here λ_{mfp} is termed the electron attenuation length, inelastic mean free path, or penetration depth. In XPS, the photoelectrons have kinetic energies ranging from ~ 0 eV up to ~ hv (typically 250 -1500 eV), and the inelastic mean free path, λ_{mfp}, of electrons in this energy range is on the order of 5 – 20 Å. The probability of inelastic scattering during transport through from the sample is high enough that the mean depth of emission of no-loss electrons may be limited to few atomic layers. Only those photoelectrons arriving at the surface without losing energy will provide useful and direct information on the initial state of the system. Thus, any analysis based on these no-loss peaks is inherently providing information about a very thin layer near the specimen surface. This surface sensitivity of XPS is exploited for studying various aspects of surface physics and chemistry.

Figure 2.4 shows the compilations, by Seah and Dench [24], for elements and inorganic compounds, of inelastic mean free path measurements in nanometers as a function of electron kinetic energy. Figures 2.4(a) and 2.4(b) show the mean free path data for elements and inorganic compounds, respectively. As can be deduced from the graph, the mean free path values depend on both the electron kinetic energies and on the sample type. For the range of photon energies of interest in XPS involving solids, λ_{mfp} is as low as 5 Å, and as high as 20 Å. Thus if the photoelectron is to escape into vacuum and be detected, it must originate at or very near the surface of the solid.

The third step in the three-step model is the escape of the photoelectron from the surface. If, and only if, the photoelectron has energy sufficient to overcome the work function, will it escape into vacuum. Therefore, the kinetic energy, E_k, is not simply the difference between the atomic orbital binding energy, E_b, and the photon energy, hv, but the work function must also be taken into account, and Equation (2.1) describes the kinetic energy of the excited electron. In Equation 2.3, $S_{em}(E_k)$ affects the EDC by providing a cut-off value, ϕ (work function), for the kinetic energy of the photoelectrons.

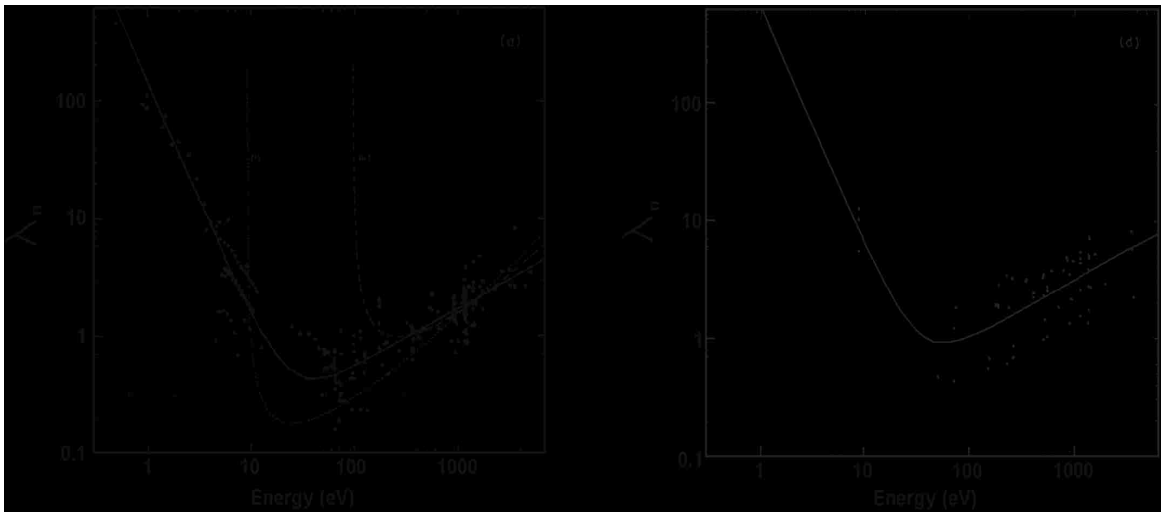

(a) **(b)**

Figure 2.4. Variation of inelastic mean free path in nanometers for (a) elements, and (b) inorganic compounds, as a function of electron energy (Reproduced by permission of John Wiley and Sons from Seah and Dench [24]).

The three-step model provides for a representation of the initial DOS through the EDC. This interpretation is distorted by effects of transport and emission of the photoelectron; however $L_{tr}\ (E_k)$ and $S_{em}\ (E_k)$ typically do not introduce significant structure into the measured EDC.

The schematic in Figure 2.5 represents the three-step model. The density of states, $N(E)$, is represented by a broad valence band at and just below the Fermi energy, E_F, and sharp core-level binding energies E_B. The energies are measured with respect to the energy zero, E_{vac}. In step 1, photons of energy hv are annihilated, and their energy absorbed to rigidly shift the electron energy distribution by hv. During step 2, the transport process, inelastically scattered electrons produce a smooth background, with the electron energy distribution superimposed on this background. In step 3, the photoelectrons must overcome the work function ϕ, in order for them to be emitted from the solid. This cuts off all electrons with energy less than ϕ. The measured EDC then reflects the initial DOS in the solid with the EDC shifted by an amount hν riding on top of a smooth background due to inelastic scattering and with a low energy cut-off of ϕ.

Figure 2.5. Schematic of EDC interpretation for solids from the three-step model. The measured EDC reflects the initial electron DOS in the solid. The three-step model is illustrated showing: (1) optical excitation, (2) transport, and (3) emission.

2.1.2. Core-Level X-Ray Photoelectron Spectroscopy. Compositional analysis of a surface can be obtained through core-level spectroscopy, in which the photoelectron emission of core-levels is measured and studied as a function of binding energy. Since core level energies are characteristic of the atomic species, the observation of certain binding energy peaks in an XPS spectrum can be taken as an indication of the presence in the surface region of a particular elemental species. In this way, core-level binding energies in an XPS spectrum can be used for identification of the specific elements under examination [25]. Photoemission produces a final state that is lacking one electron with

respect to the initial state. Therefore, according to Spicer's three-step model, photoemission (PE) studies measure final-state energies which can be related to initial-state energies as described by Equation 2.4. Additional information on exact peak positions can indicate the chemical state of some of the component elements. For photon energy in excess of 1 keV, photoemission from some energy levels of all elements is possible and in most cases several levels are accessible.

Figure 2.6 shows a plot of the EDC from a 3 ML Fe film deposited on Pd(001) at 300^{o}C using Mg K_{α} ($h\nu$ = 1254 eV) as an excitation source. The spectrum shows emitted electron intensity plotted as a function of both binding energy and kinetic energy. The main features are photoelectron and Auger peaks belonging to Pd and Fe. The photoelectron peaks appear less complex compared to the Auger peaks. These features appear at specific kinetic energies that ride on top of an inelastic background that increases with increasing binding energy. For Pd, the core-level peak at binding energy of 339.1 eV is due to the emission of the Pd $3d_{5/2}$ electrons from the Pd (001) substrate, and it is the most probable excitation for the excitation energy of 1254 eV, and therefore the level showing the largest peak intensity above the background. The value of 339.1 eV is about 4.1 eV above the actual value of binding energy of 335 eV, due to the fact that the XPS acquisition unit used to record the spectrum has not been set up to take into account the spectrometer work function. In fact, all the plots of the EDC spectra in this work reflect this constant shift. However, this does not affect the validity or utility of the data recorded in any way. Listed in Tables 2.1 and 2.2 are values for the kinetic and binding energy of electrons emitted from Fe and Pd, respectively, due to Mg K_{α} and Al K_{α} excitation. The most probable excitations for Fe and Pd are indicated by the shading.

Figure 2.7 shows an expanded view of the Pd 3d region for clean Pd(001). This narrow energy window of the scan, with smaller energy steps, provides finer peak details. The $3d_{3/2}$ and $3d_{5/2}$ peaks arise from the spin orbit splitting of the 3d level, and the occupancy of each of these two levels can be calculated as 2J+1. For the Pd 3d level, J = 3/2 and J = 5/2. Therefore, the relative intensity of the 3/2 level to the 5/2 level is [2(3/2) + 1]/[2(5/2) + 1] = 2/3.

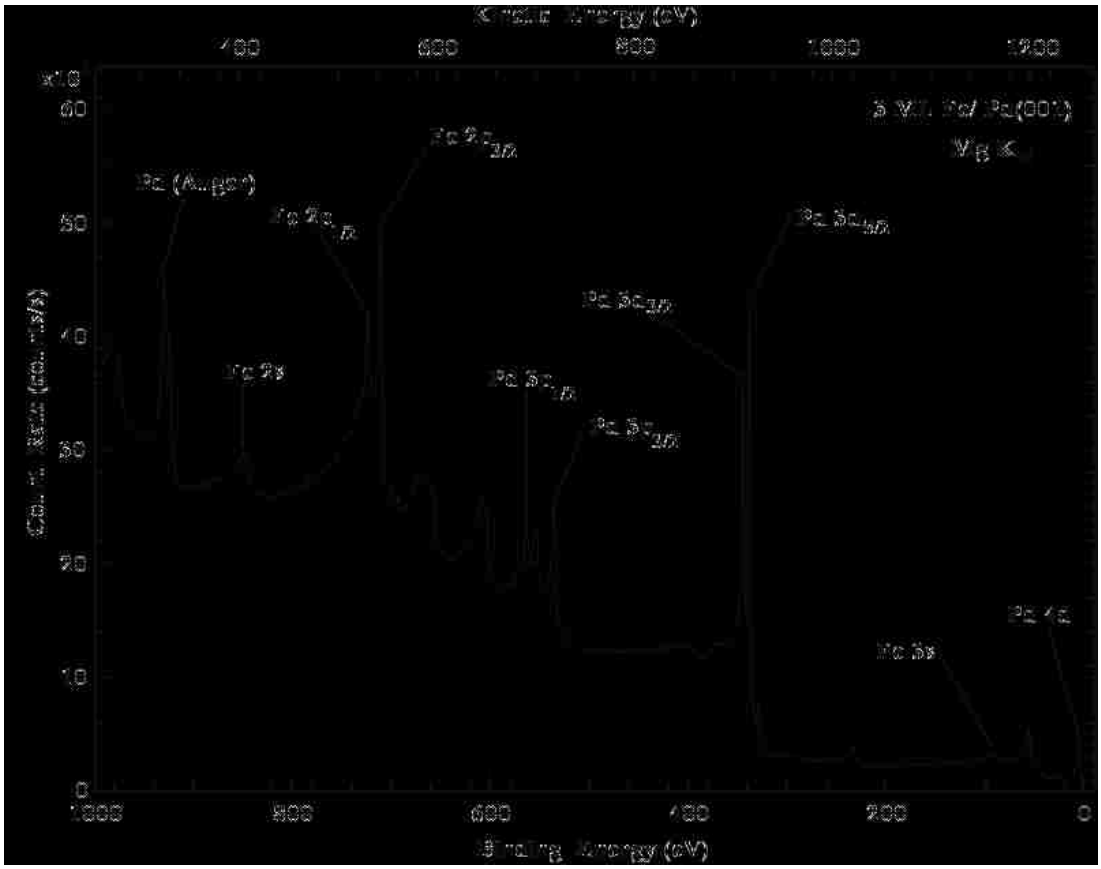

Figure 2.6. XPS spectrum of 3 ML Fe on Pd(001).

Table 2.1. Core-Level Line Positions for Fe

Energy Scale	Source	2s	$2p_{1/2}$	$2p_{3/2}$	3s	3p
Binding Energy(eV)	Mg	845	720	707	92	53
	Al	845	720	707	92	53
Kinetic Energy(eV)	Mg	409	534	547	1162	1201
	Al	642	767	780	1395	1434

Table 2.2. Core-Level Line Positions for Pd

Energy Scale	Source	3s	$3p_{1/2}$	$3p_{3/2}$	$3d_{3/2}$	$3d_{5/2}$	4s	4p
Binding Energy(eV)	Mg	671	560	533	340	335	88	52
	Al	671	560	533	340	335	88	52
Kinetic Energy(eV)	Mg	583	694	721	914	919	1166	1202
	Al	816	927	954	1147	1152	1399	1435

.

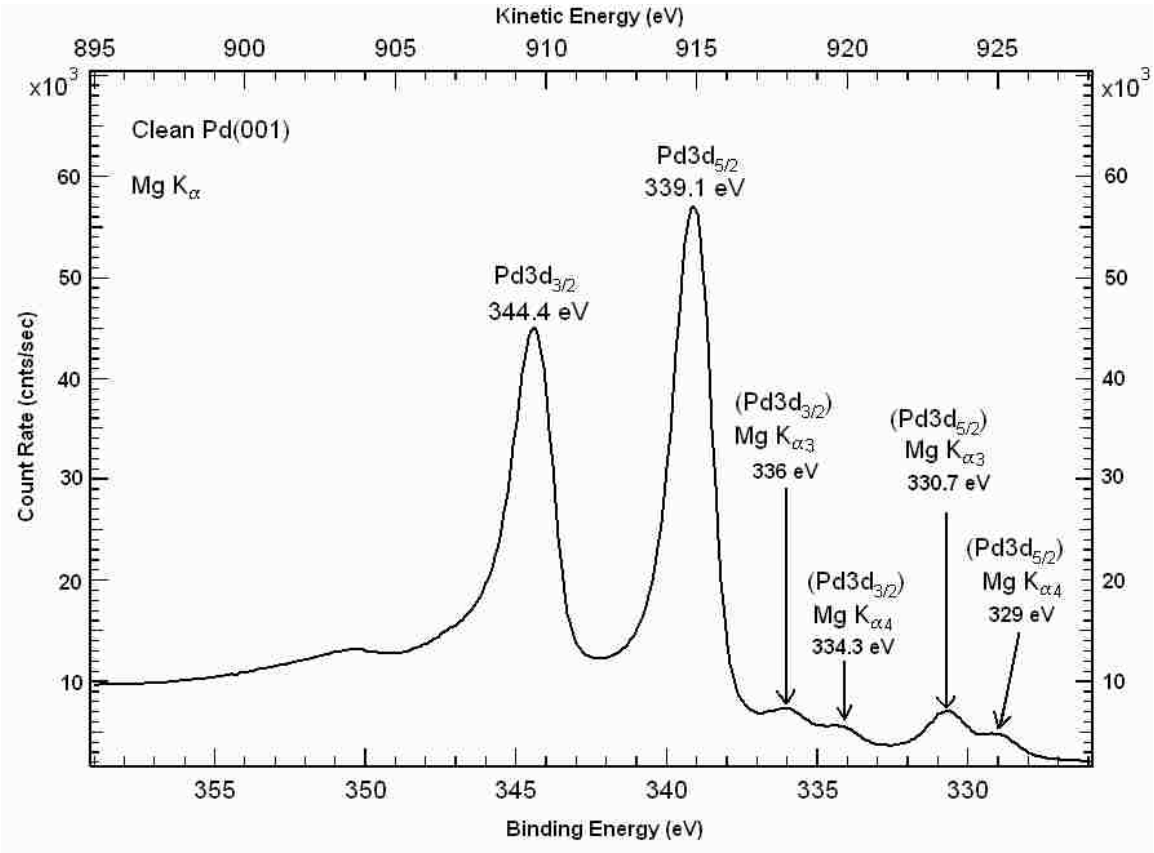

Figure 2.7. XPS spectrum of Pd 3d region for clean Pd(001).

Shown in Figure 2.8 is an expanded view of the Fe 2p region. This spectrum was collected for a 3 ML Fe film on Pd(001) at 300°C. Here, the large peaks are due to the emission of electrons excited from the spin-orbit split Fe $2p_{3/2}$ and Fe $2p_{1/2}$ core levels. For the Fe 2p level J = 3/2 and J = 1/2. Therefore the relative intensity of the Fe $2p_{1/2}$ level to the Fe $2p_{3/2}$ level is [2(1/2) + 1]/[2(3/2) + 1] = 1/2.

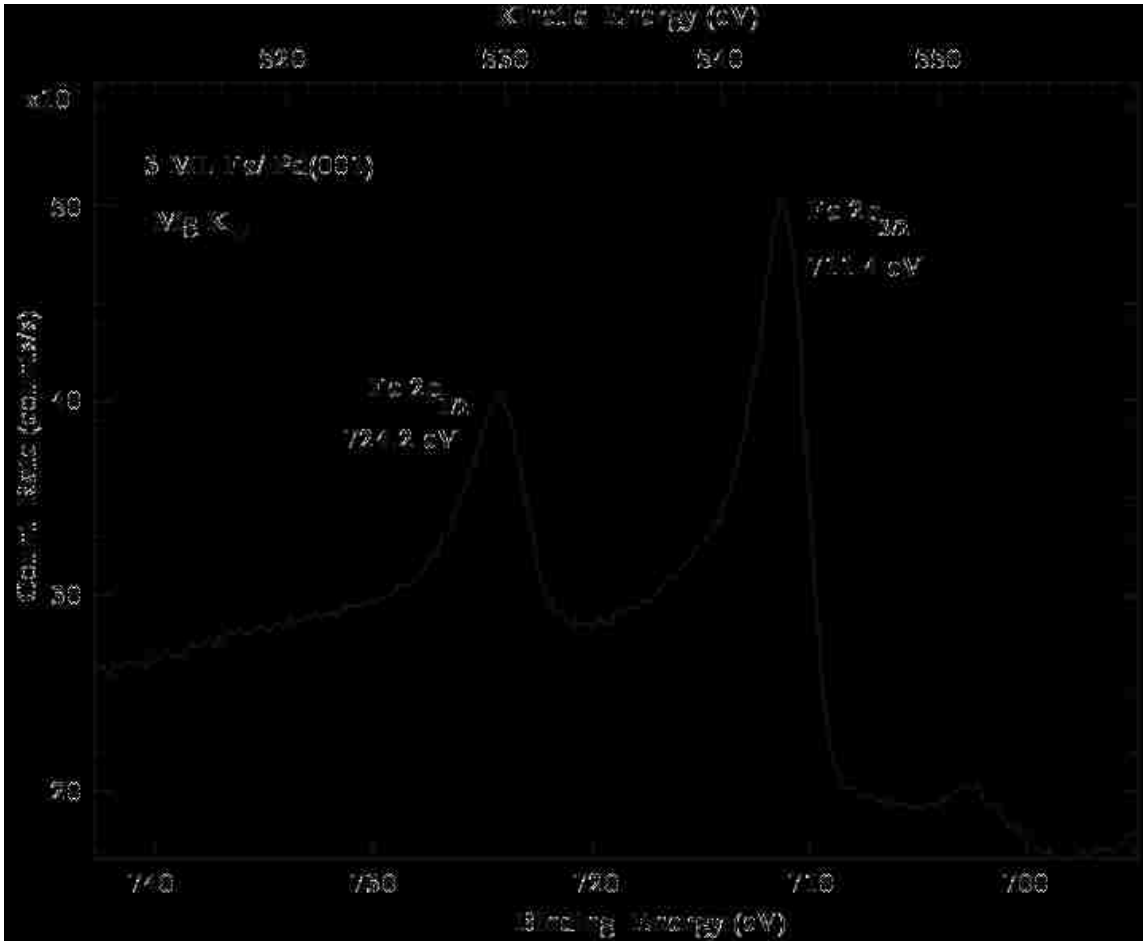

Figure 2.8. XPS spectra of Fe 2p region for Fe/ Pd(001).

The XPS photoemission spectrum also exhibits features called X-ray lines. These satellite features are due to different excitations of the x-ray source with lower probability. For each photoelectron peak that results from the routinely used Mg K_α and

Al K_α x-ray photons, there is a family of minor peaks at lower binding energies, with intensity and spacing characteristic of the x-ray anode material, and can thus be easily accounted for in analysis. In Figure 2.7, the two smaller peaks seen at binding energies of approximately 336 eV and 334.3 eV are satellite peaks of Pd $3d_{3/2}$ (344.4 eV) from excitation by x-rays of slightly higher energy than Mg K_α. Similarly, the photoelectron peak Pd $3d_{5/2}$ (339.1 eV) has satellite peaks at binding energies of 330.7 eV and 329 eV. The $K_{\alpha 3}$ and $K_{\alpha 4}$ lines, for each of the two photoelectron peaks, are at binding energies of 8.4 eV and 10.1 eV below the principle $K_{\alpha 1,2}$ line respectively. For the Mg x-ray source, the main x-ray line is the Mg $K_{\alpha 1,2}$ x-ray at $h\nu = 1254$ eV. The additional Mg $K_{\alpha 3}$ and Mg $K_{\alpha 4}$ x-rays are produced at energies of 1262.4 eV and 1264.1 eV, respectively. These $K_{\alpha 3}$ and $K_{\alpha 4}$ lines have intensities of 8% and 4.1% of the main $K_{\alpha 1,2}$ line. Therefore, the XPS spectrum shows peaks due to the excitation by the main Mg K_α line, as well as minor peaks due to excitation by a family of lower intensity x-ray lines.

2.1.3. Chemical Shifts, Shake-Up Lines. A chemically significant phenomenon is the difference in binding energy between two different chemical forms of the same atom. Although core-level electrons do not directly take part in chemical bonding, the binding energy of core-electrons will be affected by the change in charge distributions created by chemical bonds. The energy difference created is called the *chemical shift* [2, 22]. The existence of these chemical shifts associated with different local chemical and electronic environments is of considerable practical value in XPS studies. The presence of different chemical states can produce binding energy differences for electrons in different environments and will result in slight changes in the measured kinetic energies of the detected photoelectrons. For example, the binding energy of Fe $2p_{3/2}$ electrons in metallic Fe will differ from Fe $2p_{3/2}$ electrons in an iron oxide film. Such a shift, usually of a few electron volts, will be due to the changed electronic distribution, and the binding energy of the emitted electron will not simply be that of the atomic level. Another kind of more subtle energy shift is also observed. Surface features like the *surface core-level* shift arise from the difference in the core-level binding energies between bulk and surface atoms because of the changed potential at the surface. For the same material, the bulk valence DOS differs from the surface DOS. This difference is due to the difference in coordination number for the surface and bulk atoms. Thus the change in valence electron

density at the surface causes the core-level energy to change, and hence produce the chemical shifts of the core-levels. This effect can also change the position and width of d-bands in the transition metals or the f-bands in the rare-earth metals [2].

Excitation of a valence electron during primary photoemission results in what are known as *shakeup* peaks on the high binding energy side of the main peak in X-ray photoelectron spectra. When the photoelectric process does not simply lead to the formation of ions in the ground state, but instead to the ion being left in an excited state a few electron volts above the ground state, the kinetic energy of the emitted photoelectron is reduced by an amount equal to the energy difference between the ground and the excited state. The energy associated with relaxation may be sufficient to excite a valence level electron to higher energy. The electron receiving the energy ends up in a higher unoccupied state having discrete energy (shake-up) or an unbounded state (shake-off). Due to the kinetic energy losses, the shake peaks appear at higher binding energy relative to the main core-level peak. The shake-up satellite features normally appear within an energy range of 13.6 eV of the main photoelectron line lower in kinetic energy (higher in binding energy). Such multielectron excitations or shake-up satellites have been observed in the transition metal compounds, and are very helpful in XPS analysis since their positions and intensities convey information regarding important chemical properties of the compounds. Discrete shake-up losses are pronounced for metal oxides, and pronounced intensities are typically found for compounds having unpaired 3d or 4f electrons. For example, shake-up features show up in the XPS spectra of the core levels such as those of Fe 2p or Cr 2p in iron or chromium oxides respectively, providing noteworthy diagnostic tool for detecting the oxidation states of the Fe or Cr ions. By focusing on the energy separations between the main-line and satellite structures in the compounds of the 3d transition elements and on the chemical sensitivity of these relative energies, chemical information on the internal electron-level structure can be extracted.

2.1.4. Auger Electrons. In addition to photoelectron peaks, the XPS EDC also exhibits Auger electron peaks. These Auger electrons are created when an atom is ionized by the production of a core hole due to an incident photon or electron, and an electron from a higher energy level fills the core hole with the subsequent emission of an electron from an outer level for energy compensation. This energy may also appear in the form of

a photon and this process is dominated by the photon emission only for core-hole energies higher than ~10 keV [2].

The basis for nomenclature of the Auger transitions is illustrated in Figure 2.9. A vacancy in the K shell is filled by an electron from the L_1 shell. The excess energy is then transferred to an L_3 electron that is emitted from the atom. The process is denoted as a KL_1L_3 Auger transition. The transitions can also involve valence electrons and are denoted by the symbol V. Auger electron emission, being a three-level process, is intrinsically more complex than photoemission, and the Auger transition peaks are typically much broader and more complicated. Transitions involving valence electrons may produce complex line shapes due to the band of energies valence electrons occupy [2]. Figure 2.10 is an expanded view of the Pd Auger transition region. Based on the approximation of one-electron binding energies of the core levels involved in the Auger transition, one can write:

$$KE^{Z}_{ABC} = BE^{Z}_{A} - BE^{Z}_{B} - BE^{Z}_{C} \tag{2.9}$$

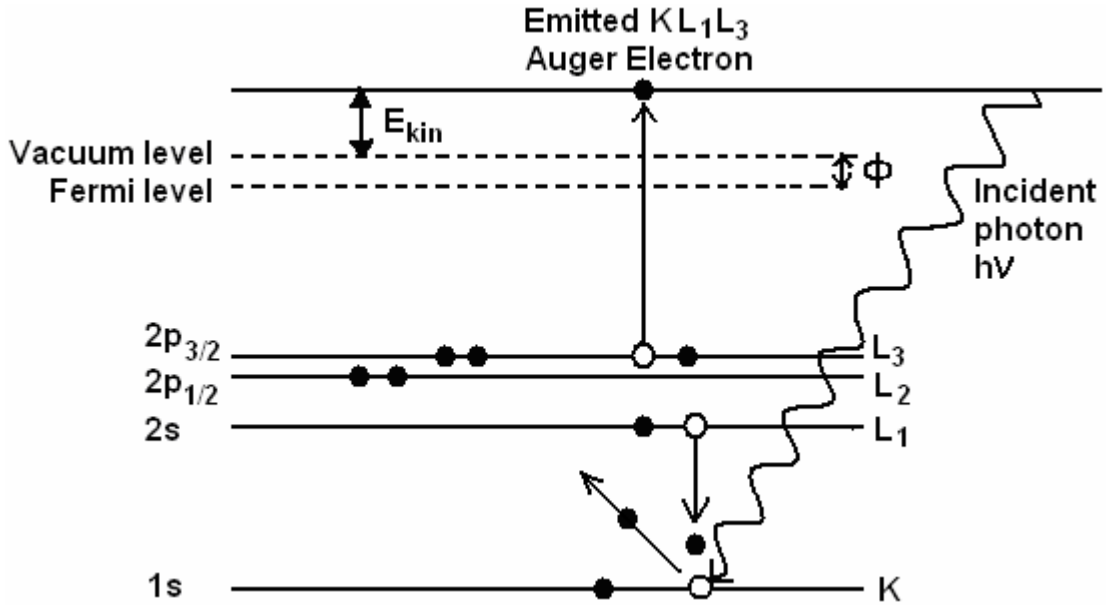

Figure 2.9. Schematic of the KL_1L_3 Auger transition process corresponding to an incident photon creating a hole in the K shell.

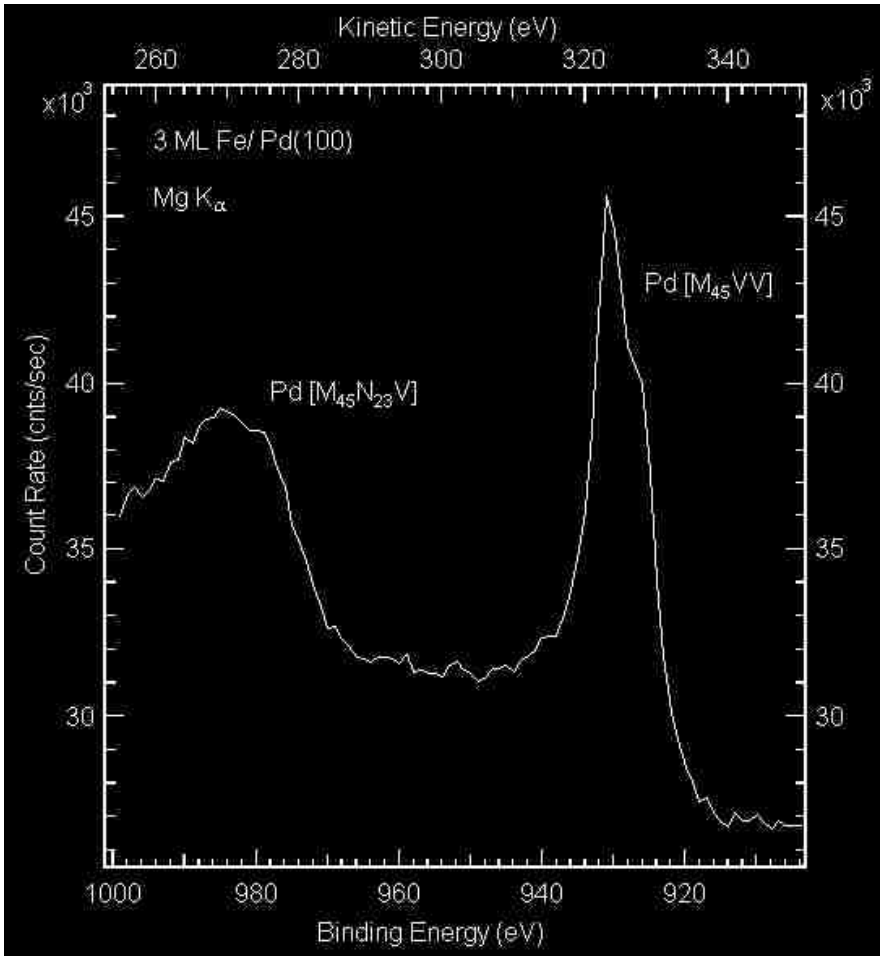

Figure 2.10. XPS spectrum of Pd Auger region for Fe/ Pd(001).

The drawback of Equation 2.9 is that it does not give a very accurate description of the energy, as it does not take into account the fact that the true energy is the difference between a one-hole binding energy state and a two-hole binding energy state. One way to account for the two-hole final state is to replace the binding energy of the *C* level for an atom of atomic number *Z* with the binding energy for an atom of atomic number (*Z+1*) [2]. The energy, KE^{Z}_{ABC} of an Auger electron of type *ABC* from an atom of atomic number (*Z+1*) can be given as:

$$KE^{Z}_{ABC} = BE^{Z}_{A} - BE^{Z}_{B} - BE^{Z+1}_{C} \tag{2.10}$$

Here, BE_A^Z, BE_B^Z, BE_C^{Z+1}, are the binding energies of the three electrons involved in the transition. The kinetic energy of the Auger electron during a particular Auger transition remains fixed for each element. This is because the Auger electron's kinetic energy depends on the energy difference between the levels involved in the transition, and these are independent of photon energy. Thus, the Auger electrons will always appear at constant kinetic energies for different photon energies. This situation is quite different from that of core-level electron emission where the kinetic energy of the photoelectron depends on the energy of the incident photon. By comparing the energy distribution curves obtained with two or more photon energies, peaks in a given EDC can be readily assigned to direct core-level emission or Auger emission. Tables 2.3 and 2.4 give values of the kinetic energies and binding energies for Auger transitions in Fe and Pd for Mg K_α and Al K_α excitation sources.

Table 2.3. Auger Line Positions for Fe

Energy Scale	Source	$LM_{23}M_{23}$	$L_3M_{23}M_{45}$	$L_3M_{45}M_{45}$
Binding Energy(eV)	Mg	655	606	551
	Al	888	839	784
Kinetic Energy(eV)	Mg	599	648	703
	Al	599	648	703

Table 2.4. Auger Line Positions for Pd

Energy Scale	Source	$M_{45}N_{23}V$	$M_{45}VV$
Binding Energy(eV)	Mg	978	926
	Al	1211	1159
Kinetic Energy(eV)	Mg	276	328
	Al	276	328

2.2. X-RAY PHOTOELECTRON DIFFRACTION (XPD)

In X-ray photoelectron diffraction (XPD), a photon excites an electron from a core-level, and the outgoing photoelectron wave is scattered from the atoms neighboring the emitter, producing an interference pattern. The modulations in the photoelectron intensity, due to the interference process, are observed as a function of either the direction of electron emission or the energy of excitation, leading to either scanned-angle or scanned-energy measurements. Used to probe the short-range order around the photoemitter, a large variety of surfaces (metals, semiconductors, oxides, systems exhibiting core-level shifts, adsorbed atoms and molecules, epitaxial overlayers, and atoms at buried interfaces) have been successfully studied using this local diffraction technique. By monitoring the photoelectron intensity of a particular core-level, information about atomic geometry in the vicinity of the emitting atom, local structure of multi-element samples, as well as structural information of an element in different chemical states can be obtained. For the parameters used in these experiments, the necessary information to be extracted from the samples is limited to depths of tens of angstroms, and as such, XPD is a very ideal structural probe technique for the kind of surface measurements that we are interested in.

The use of XPD to determine the structure of crystalline systems has been developed over the past 40 years after its first introduction by Siegbahn in 1970 [18, 19], with many subsequent reviews on the topic [14-15, 26-33]. Photoelectron diffraction is inherently atom-specific, since core level energies are always unique to a given atom. Thus, the local structure around each of the atomic types in a sample can be studied, and this is a key advantage compared to many other structural probes. As shown in the schematic diagram in Figure 2.11, the central atom acts as the localized source of probe electrons which bear no definite phase relationship to similar electrons generated at nearby atoms. The excitation source is a soft x-ray photon. The photoemitted electron can be described as a spherical outgoing wave modulated by a photoemission matrix element strongly dependent on the angle between the electric field vector associated with the incident photon and the outgoing electron wave vector. A portion of the outgoing wave propagates to the detector without undergoing any elastic scattering (the direct wave

portion), whereas other wave portions scatter elastically from ion cores in the vicinity of the emitter.

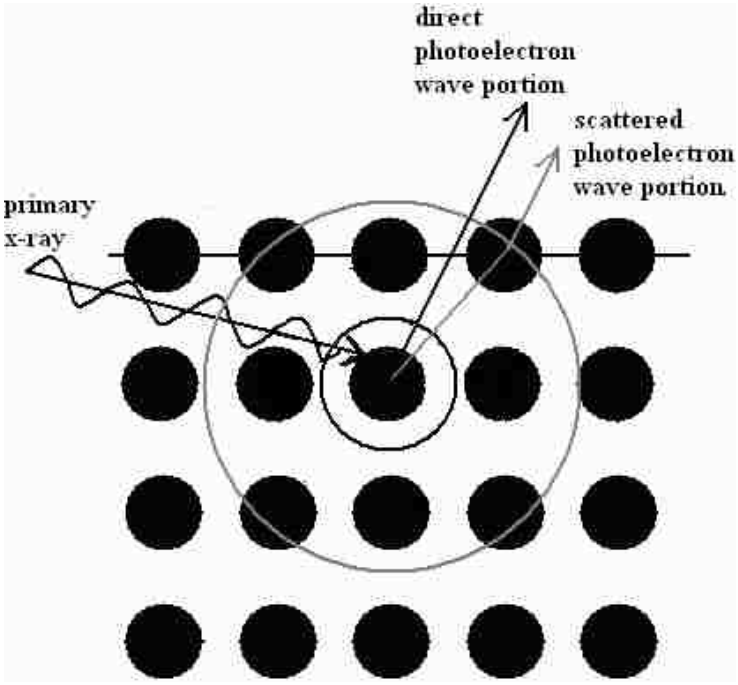

Figure 2.11. Schematic representation of XPD.

XPD occurs because of the temporal, spatial coherence between the portion of an outgoing photoelectron wave that passes directly to the detector, and those wave portions that undergo elastic scattering by ion cores in the vicinity of the emitter. The local structural environment of an emitting atom situated in a single crystal can be probed by XPD, without the necessity of long-range order. In fact, it is the very lack of coherence between the photoelectron waves emitted from different atoms that eliminates the requirement long-range order for observing diffraction effects. For example, adsorbates at submonolayer coverages will exhibit XPD intensity modulations that are characteristic of the adsorbate site, even though there is no long range order in the adlayer. Photoelectron intensity modulations are also produced with the inclusion of foreign atoms at lattice sites in a given sublattice of a single-crystal specimen, even if the specimen is a random alloy.

The modulations in intensity $I(\vec{k})$ shown by the photoelectron current can be as much as 50%, both as a function of photoelectron kinetic energy and emission direction. Here $\vec{k}$ is the photoelectron wave vector. The main area of focus here will be on the angle-scanned mode (Figure 2.12) where the emission direction of the photoelectron is varied in relation to the axes of the crystalline system, and the photoelectron intensity modulations are recorded as a function of these angles. In the energy scanned mode, intensity modulations are measured as a function of the energy of the exciting photons; therefore a tunable photon source is necessary in this case. Common laboratory x-ray sources are limited to a few select photon energies, such as Mg K_α and Al K_α, and are thus unsuitable for the energy scanned mode of XPD.

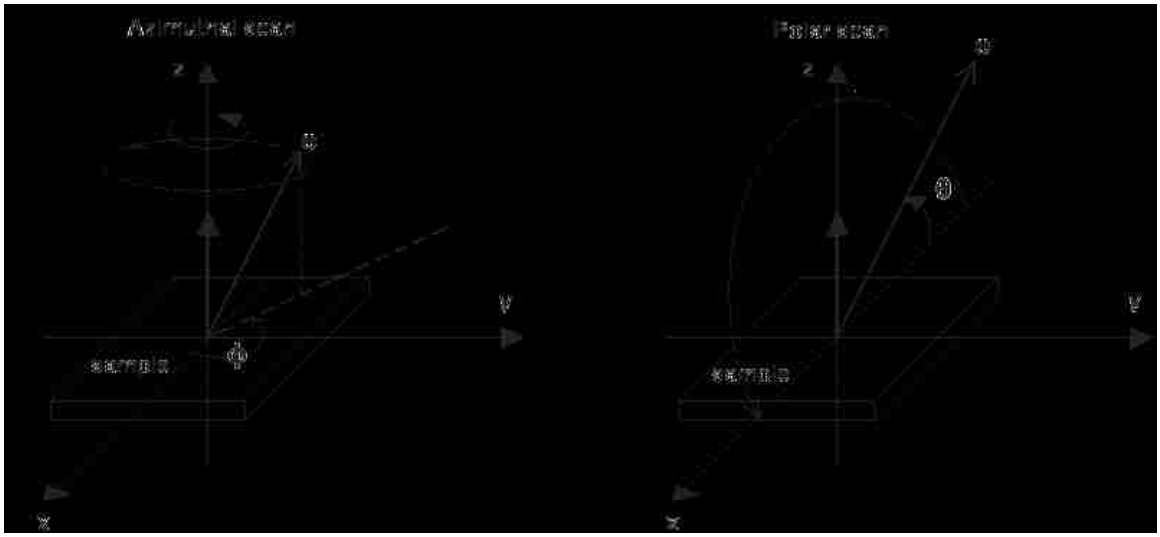

Figure 2.12. Schematic of XPD azimuthal scan at a constant polar angle (left) and polar scan at constant azimuthal angle (right).

Angular distribution measurements of Auger electrons will reveal the structural information in much the same way as photoelectron diffraction angular distributions. But, due to the greater complexity of Auger electron diffraction data, interpretation is more difficult. However, it has been found that studies with high kinetic energy Auger electrons using forward scattering [14, 28], can be useful in epitaxial growth

investigations. At energies greater than 500 eV, Auger electrons from elemental solid surfaces produce distributions essentially similar to those of photoemission peaks at similar energies. At high energies, the narrow forward elastic scattering dominates over other effects, making interpretation of Auger data possible.

2.2.1. X-Ray Photoelectron Diffraction Theory. To be able to discuss XPD effects quantitatively, a detailed model of the scattering and interference phenomena is required, and a good model to start with is a straightforward single-scattering approach, leading up to more complex treatments incorporating some degree of multiple scattering. As mentioned earlier, elastic scattering of an emitted photoelectron wave by neighboring atoms will lead to modulations in the intensity of detected electrons as emission angle is varied due to the interference of scattered and unscattered wave portions. The scattering process changes the amplitude, phase and shape of the electron wave. Referring back to the three-step model of photoemission in XPS, the process of x-ray photoelectron diffraction can be viewed similarly, with a modification in step two. During the transport process of step two, in addition to the inelastic scattering of the photoelectrons which brings about attenuation of the initial photoelectron signal, elastic scattering also takes place which introduces modulations in the photoelectron intensity due to the interference between the directly emitted and elastically scattered photoelectron wave portions.

The schematic diagram in Figure 2.13 exhibits photoabsorption of energy hv by the emitting atom, with the consequence that a direct photoelectron wave Ψ_0 is produced. It is detected at a distance r from the emitting atom with an angle of α between the detector and the incident photon directions. A portion of Ψ_0 is also scattered by atoms around the emitter, and $\Psi_j\,(r_j,\, \alpha_j,\, \theta_j)$ represents the scattered wave portion generated at the jth atom which is at a distance r_j from the emitter, θ_j is the scattering angle between the emitter-scatterer direction and the scatterer-detector direction, and α_j is the angle between the incident radiation and emitter-scatterer direction. Photoemission from non-s orbitals necessitates calculations of more complex forms, and to simplify matters, the XPD formalism in this work is limited to s-wave excitation [26]. The direct portion of the outgoing photoelectron wave can be described as an outgoing spherical wave, centered at the emitting atom, with an amplitude that is modulated by a matrix element for the ionization event, and is given by:

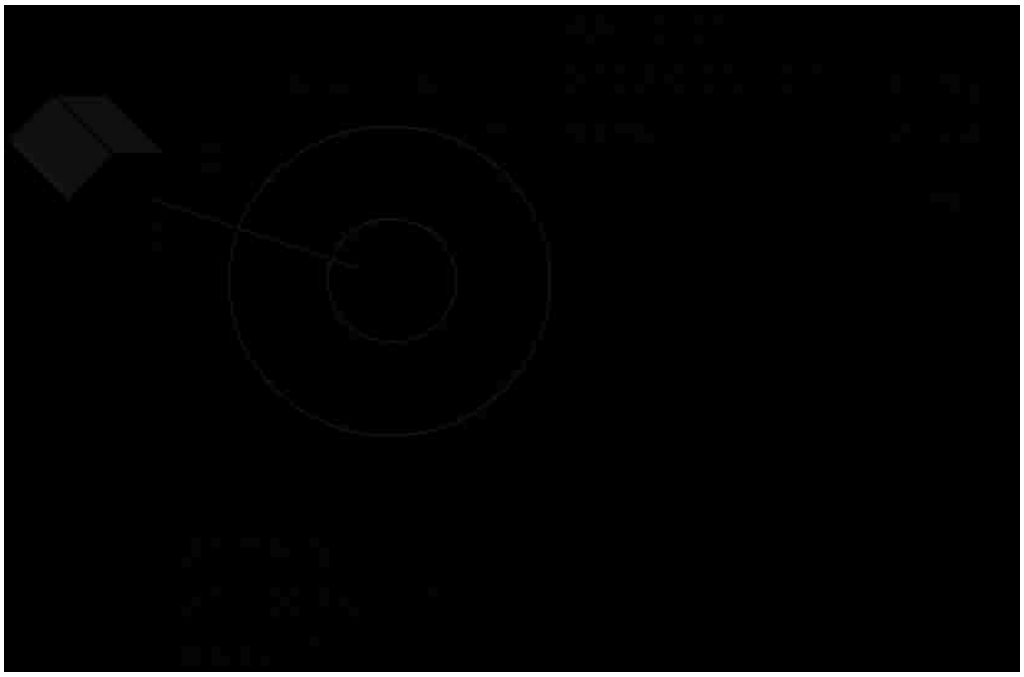

Figure 2.13. Schematic of the x-ray photoelectron diffraction process. Interference between the direct photoelectron wave, Ψ_0, and the elastically scattered photoelectron wave, Ψ_j, will produce intensity fluctuations at the detector. The scattering plane is defined by the incident photon direction and the detected photoelectron direction.

$$\Psi_0(r,\alpha) \propto M_{fi} \frac{\exp(ikr)}{r} \tag{2.11}$$

M_{fi} is the photoemission transition matrix element for transition from initial state Ψ_i to final state Ψ_f. The scattered wave portion, $\Psi_j(r_j, \alpha_j, \theta_j)$, is also a spherical wave centered at the *j*th atom and, at the detector point, is given by:

$$\Psi_j(r_j,\alpha_j,\theta_j) \propto \Psi_0(r_j,\alpha_j)\left|f(\theta_j)\right| \frac{\exp[i\{\vec{k}\cdot(\vec{r}-\vec{r}_j)+\gamma(\theta_j)\}]}{\left|\vec{r}-\vec{r}_j\right|} \tag{2.12}$$

Here, the amplitude of the scattered wave is proportional to both the amplitude of the direct wave portion at the jth atom $\Psi_0(r_j, \alpha_j)$ and the magnitude of the complex scattering factor $\left|f(\theta_j)\right|$. The parameter $\gamma(\theta_j)$ is the phase shift undergone by the scattered wave in

relation to the direct wave. The length $\left|\vec{r}-\vec{r}_j\right|$ is the distance from the *j*th scatterer to the detector. This distance represents the path length difference to the detector for the direct and scattered waves. This appears in the exponential term in Equation 2.12, and is the reason for the structural sensitivity in XPD experiments. Therefore, the overall wave amplitude at the detector will be given by:

$$\Psi(r,\alpha)=\Psi_0(r,\alpha)+\sum_j \Psi_j(r_j,\alpha_j) \tag{2.13}$$

Therefore, the photoelectron intensity $I(\vec{k})$ at the detector is then given by:

$$I(\vec{k})\propto\left|\Psi_0(r,\alpha)+\sum_j \Psi_j(r_j,\alpha_j)\right|^2 \tag{2.14}$$

2.2.2. Single-Scattering Cluster Model. Equation 2.14 represents the situation for single scattering events. The scattering amplitudes at high kinetic energies tend to be very small for large scattering angles, so that the probability for multiple scattering is negligibly small for approximately $\theta_j \geq 30°$. Thus the scattering process for Auger or photoelectrons interaction with a lattice is well approximated by the single-scattering formalism for all emission directions except those coincident with chains of atoms (in which case multiple-scattering is dominant).

For x-ray photoemission at high kinetic energies, the amplitude modulation, M_{fi}, can be approximated by the square root of a differential cross-section for the ionization event $[d\sigma_{n,l}\{\varepsilon, k\}/d\Omega]^{1/2}$ [26]. The scattering factor $|f(\theta_j)|$ falls off rapidly with θ_j at high electron kinetic energy, and therefore, the square root of the differential photoemission cross-section does not contribute much unless $\alpha = \alpha_j$, and can be factored out of the scattered photoelectron wave portions. Thus, with the approximations incorporated, the simplified equation for $I(\vec{k})$ valid for high kinetic energies (>500 eV) and limited to single scattering becomes:

$$I(\vec{k}) \propto \left| \frac{\exp(ikr)}{r} + \sum_j \frac{\exp(ikr_j)}{r_j} \left| f(\theta_j) \right| \frac{\exp[i\{\vec{k}\cdot(\vec{r}-\vec{r}_j)+\gamma(\theta_j)\}]}{\left|\vec{r}-\vec{r}_j\right|} \right|^2 \qquad (2.15)$$

Attenuation of the detected photoelectron wave intensity due to thermal vibrational effects and inelastic scattering must also be included, in order to be able to realistically simulate XPD at a surface or thin epitaxial film. The thermal vibrational correction is included by multiplying the scattered wave terms by a Debye-Waller factor, which can be written as [26]:

$$W_j = e^{-\Delta k^2 \overline{U_j^2(T)}} = e^{-2k^2(1-\cos\theta_j)\overline{U_j^2(T)}} = \exp\left[-2k^2(1-\cos\theta_j)\frac{\hbar T}{m\Theta_T^2 k_B} \right] \qquad (2.16)$$

Here Δk is the magnitude of the change in wave vector produced by the scattering, the bulk Debye temperature of the jth scatterer is given by Θ_T, and $\overline{U_j^2(T)}$ is the temperature dependent one-dimensional mean-squared vibrational displacement of the *j*th atom with respect to the emitter. $\overline{U_j^2(T)}$ is assumed to be isotropic in space and any correlations in movements of near-neighbor atoms are neglected. As in the case of the photoelectric differential cross-section, the rapid fall off of $|f(\theta_j)|$ with θ_j selects out only those W_j factors for which $\theta_j \approx 0$, to yield W_j's very close to unity for all important scattered waves.

Inelastic attenuation can be approximated by a simple exponential damping factor for both unscattered and scattered terms. Intensity falls off as $\exp(-L/\lambda)$ (or, $\exp(-L_j/\lambda)$), where L is the distance from the emitter to the surface, L_j the distance from the jth scattering atom to the surface, along the detector emission direction, and λ is the inelastic mean free path. So, the amplitude falls off as the square root of this, or $\exp(-L/2\lambda)$. Each wave Ψ_0, or Ψ_j can thus be multiplied by such a factor involving an L value. The measured photoelectron intensity, multiplied by the Debye-Waller factor W_j, that corrects for thermal vibrations and the inelastic damping term can be written as:

$$I(\vec{k}) \propto \left| \frac{e^{ikr}}{r} \exp(-L/2\lambda) + \sum_j \frac{e^{ikr_j}}{r_j} \left| f(\theta_j) \right| e^{-\frac{L}{2\lambda}} W_j \frac{e^{i\{\vec{k}\cdot(\vec{r}-\vec{r}_j)+\gamma(\theta_j)\}}}{\left|\vec{r}-\vec{r}_j\right|} \right|^2 \qquad (2.17)$$

In addition to being scattered inside the solid, the electron wave is also refracted when crossing the solid interface. This causes the de-Broglie wavelength of the electron inside the solid to differ from the value measured by the electron spectrometer. Even at the relatively high energies of XPS, for emission near grazing, the emission angle can be changed by a few degrees by refraction. Thus, especially for adsorbate studies, a proper allowance for refraction is necessary, at least for θ values $\leq 10^o$. Refraction is taken into account by assuming the solid to have an 'inner potential V_0' [23] (typical values of V_0 can be from 5-25 eV for clean surfaces) , which changes E_{kin} of any electron traversing the surface. The polar angle θ' inside the solid is related to the detected polar angle θ by the expression:

$$\theta' = \cos^{-1}\left[\left(\frac{E_k - V_0}{E_k} \right) \cos\theta \right] \qquad (2.18)$$

Here, E_k is the electron kinetic energy outside the solid. This correction is negligible at kinetic energies of about 1000 eV for all polar angles except those near grazing emission and amounts to about 1-2^o at $\theta \leq 10^o$ at this energy.

Equation (2.17) is thus the basic starting point of the single scattering cluster model. Such a cluster makes no explicit use of the 2- or 3- dimensional translational periodicities that may be present, thus neither surface- nor bulk-reciprocal lattice vectors are explicitly involved, though the atomic co-ordinates $\vec{r}_j$ used as inputs may implicitly incorporate such periodicities.

2.2.3. Forward-Scattering. In all photoelectron studies, electron scattering by atoms is predominantly in the forward direction, into small scattering angles measured between the incident and the scattered electrons. The peak in the scattering amplitude will produce strong intensity enhancements in the forward scattering direction, corresponding to low-index crystal directions. These peaks coincide with the directions of internuclear

axes for the emission site and its neighbors [34]. The intensity enhancement in the forward direction is due to scattering of the high-energy electrons by an attractive (Coulomb) potential. This is referred to as forward-scattering and is included as part of XPD even though it is not a true interference effect. Therefore, by monitoring the emission angle of these large intensity enhancements, termed 'forward-scattering' peaks, the bond directions in the crystal can be determined.

The location of forward-scattering peaks indicate bond directions that can be used to determine the structure of the film, and due to the element specificity of XPD, film properties can be distinguished from the substrate. The phenomenon of forward-scattering can be observed from a polar angle XPD scan (Figure 2.14) taken with the scattering plane corresponding to the (100) azimuthal plane for a clean annealed Pd(001) sample. The scan was acquired by monitoring the Pd $3d_{5/2}$ photoemission intensity. The forward-scattering peaks can be seen at $\theta = 0^o$ and at approximately $\theta = 45^o$. The $\theta = 0^o$ forward-scattering peak corresponds to the [001] direction and the $\theta = 45^o$ forward-scattered peak corresponds to the [101] direction.

The forward-scattering effect also shows dependence on the energy of the photoelectron. Egelhoff has explained this energy dependence [27]. While forward-scattering dominates at high electron kinetic energies, below 100 eV the scattering is somewhat more isotropic. Figure 2.15 illustrates the reason for the behavior. The potential of the scattering atom varies much more rapidly than 1/r in the outer regions with the effective charge of the atom, Z_{eff}, increasing steadily with decreasing r as the screening orbitals are penetrated. Two things happen simultaneously- first, an electron with low energy, such as 50 eV, cannot make it past the outer regions of the atom, as it does not possess sufficient energy to penetrate substantially deep into the screening orbitals, and it gets deflected significantly from its incident trajectory due to the relatively small force required. Second, due to the very rapid variation of the potential in the outer regions of the atom, it does not take a large change in the impact parameter to affect a significant scattering. A small change in the incident trajectory makes a large change in the scattering angle, and depending upon the incident direction, the electron can be deflected in multiple directions, and not necessarily in the forward direction. As such, the scattering, with respect to direction, becomes more isotropic below 100 eV.

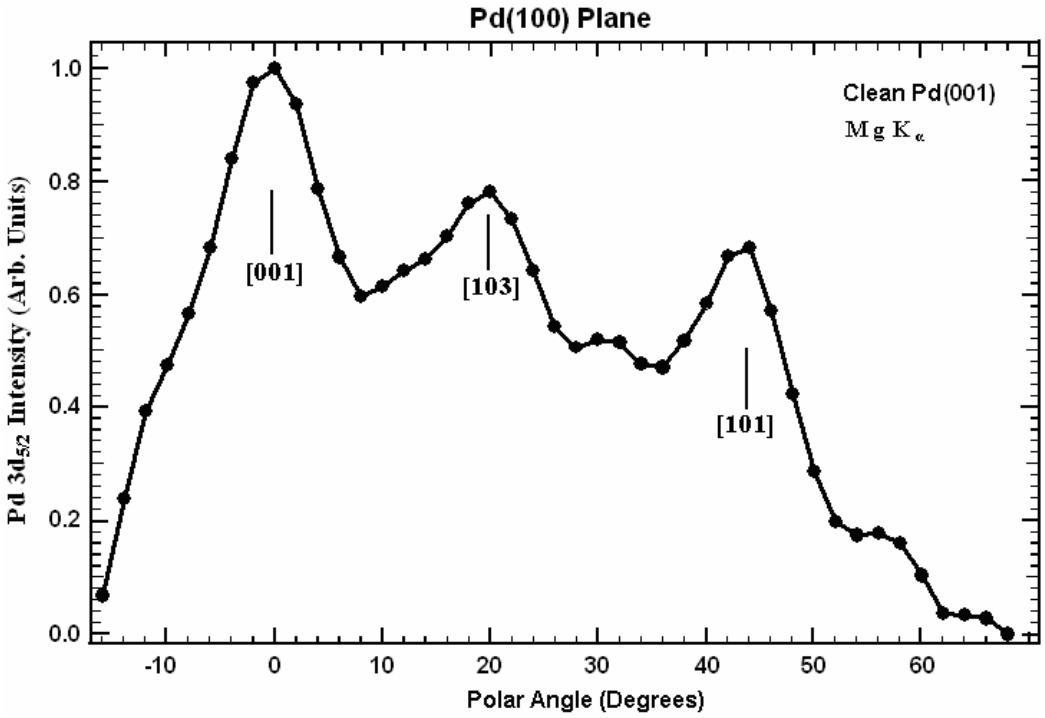

Figure 2.14. Pd $3d_{5/2}$ XPD polar scan for the Pd(100) azimuthal plane.

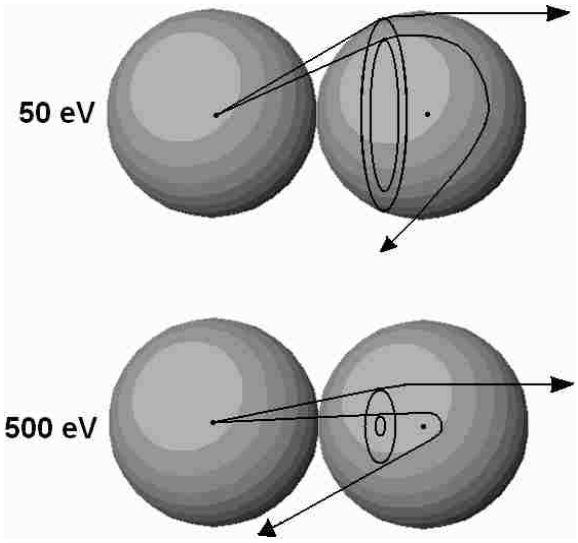

Figure 2.15. A schematic illustration of electron trajectories indicating the energy dependence of the impact parameters giving forward scattering and large-angle back scattering.

Scattering becomes much more simplified above a few hundred electron volts, which permits the forward scattering effect to be so useful. At high energies, the electron makes it past the rapidly varying potential in the outer region of the atom, the screening orbitals are largely penetrated, and the electron sees more or less the actual nuclear charge. Here, in the inner regions of the atom, with most of the screening orbitals penetrated, the potential varies more slowly, that is, more like 1/r. Thus, the deflections produced are less dramatic, and consist mostly of forward scattering. For the electron to be scattered to large scattering angles, there must be a large change in impact parameter, subjecting the electron to large forces found only near the nucleus of the scattering atom.

Thus, the electron must pass very close to the nucleus to be deflected by a relatively large angle. In the high energy range of interest in XPS studies, forward scattering is by far the predominant effect. Forward-scattering in angle scanned XPD can be used to determine the crystal structure and growth morphology of thin films of only a few monolayers in thickness. The use of forward-scattering effects in angle-scanned XPD can be illustrated with a few examples. For a 1 ML film deposited on a single crystal substrate, whether there will be any forward-scattering peaks observed from film atoms will be decided by the type of film growth, as shown in Figure 2.16. If on one hand, the growth of the 1 ML film is two-dimensional, i.e., layer-by-layer growth as illustrated in Figure 2.16(a), then no forward-scattering peaks will be observed as there are no atoms above the film layer that lie between an emitter and the detector. On the other hand, if the same amount of film is deposited in a three-dimensional cluster, as illustrated in Figure 2.16(b), there will be multiple layers of atoms and forward scattering from overlayer atoms can be observed. Thus, observation of forward-scattering peaks in angle-scanned XPD for the film material implies that the possibility of clustering must be considered. However, the presence of forward-scattering peaks alone does not confirm the presence of clustering. Another possibility is the interdiffusion of the film and substrate material (Figure 2.16(c)) – substrate atoms are now in positions to cause forward-scattering from overlayer atoms.

Structural information about a crystal under investigation can also be determined using the forward–scattering effect. Figure 2.17 shows a schematic of the (100) azimuthal plane of the face-centered cubic (fcc) crystal structure, that has the [001] direction normal

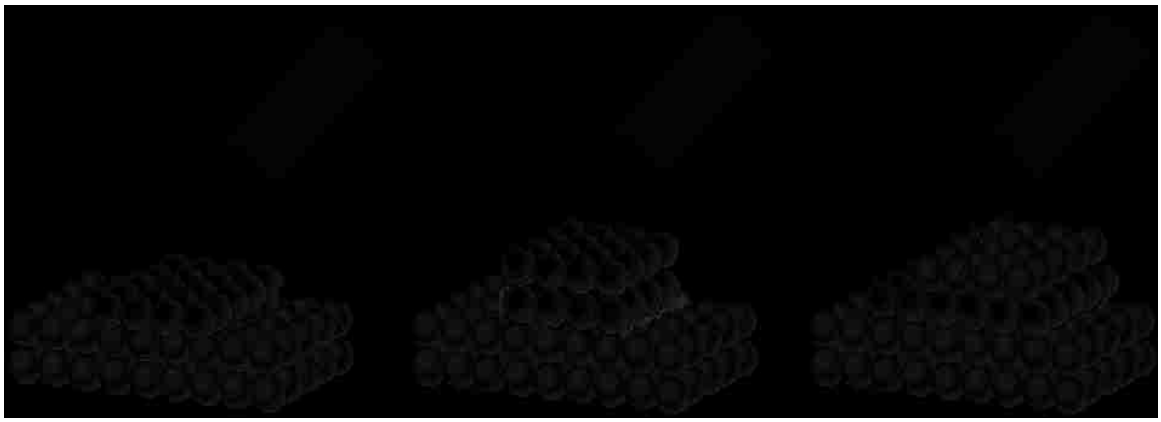

(a) **(b)** **(c)**

Figure 2.16. Film growth mode determinations using angle-scanned XPD. Forward-scattering from overlayer atoms (white spheres) will not be observed in (a) because no atoms lie between the emitter and the detector. Forward-scattering from overlayer atoms will be observed in (b), from overlayer atoms in a cluster, and in (c), from substrate atoms (grey spheres) after interdiffusion of film-substrate atoms.

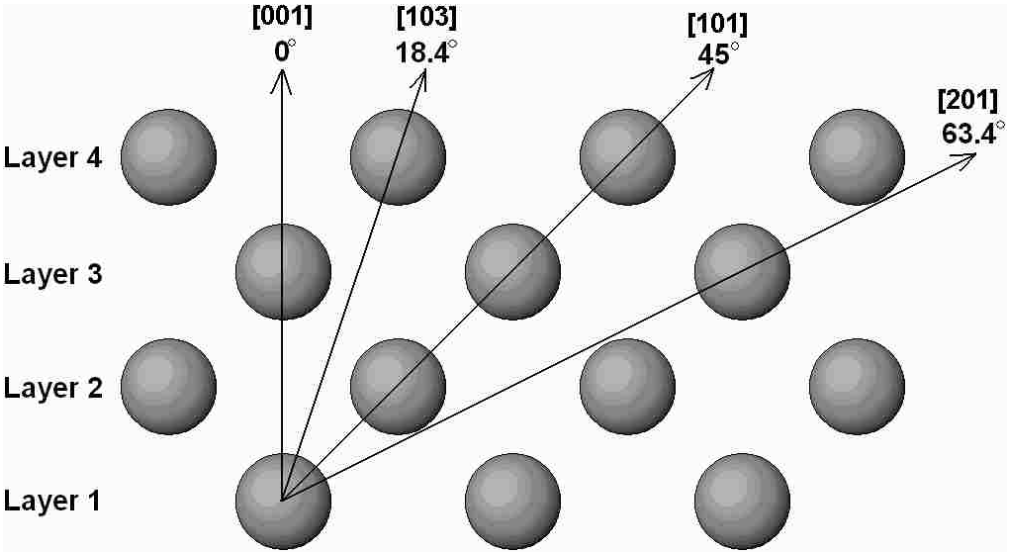

Figure 2.17. Forward-scattering angles for the (100) azimuthal plane of an fcc crystal lattice. The forward-scattering angles are taken with respect to the sample normal, [001] direction, and are labeled for some of the low-index directions.

to the surface. If the crystal has an fcc structure, then the forward-scattering peaks will lie along the fcc crystal lattice's bond directions, which in the (100) plane, are at polar angles of 0^o, 18.4^o, 45^o, and 63.4^o. These angles correspond to the [001], [103], [101], and [210] directions, respectively. The polar angle XPD scan for the Pd(100) azimuthal plane in Figure 2.14 corresponds to the schematic of Figure 2.17. In Figure 2.14, the peak at $\theta \sim 30^o$ is probably due to higher-order diffraction effects associated with interference with more intense forward-scattering events at other angles.

Figure 2.18 shows a schematic of the fcc crystal for the (110) azimuthal plane, for which the bond directions are at polar angles of 0^o, 19.5^o, 35.3^o, and 54.7^o corresponding to the [001], [114], [112], and [111] directions, respectively. When azimuthal planes of an fcc structure coincide with the scattering plane, forward-scattering peaks would be expected at the indicated angles. This is manifested in the polar XPD curve taken for the Pd(110) azimuthal plane in Figure 2.19, for a clean annealed Pd(001) sample.

XPD can also be used for verification of film thickness determinations. Referring to Figure 2.17, for a film deposited with a fcc crystal lattice, at least 2 layers of material in the film must be present in order to be able to observe the forward-scattering peak at 45^o, and at least 3 layers for obtaining the 0^o, and 63.4^o. Similarly, from Figure 2.18, forward-scattering peaks at 0^o, 35.3^o, and 54.7^o will be observed only if there are at least 3 layers in the film.

Certain other more subtle details, such as tetragonal distortions of the crystal lattice from an ideal structure, can be determined using angle-scanned XPD. Figure 2.20 illustrates the expansion along the c-axis by 3.6% for an ideal fcc Cu lattice in the (100) plane [26, 35]. This 3.6% expansion in the c-axis from 3.61Å to 3.74Å produced in response to the compressive strain in the plane of the interface produces a shift in the measured forward-scattering peak location of 1.0^o. This strain will remain up to some critical thickness, at which point the strain energy can no longer be accommodated by the lattice, and strain relief by misfit dislocation generation is expected to occur. The measurable shift in forward-scattering peak location allows for small expansions or contractions in film crystal structure to be investigated and quantified.

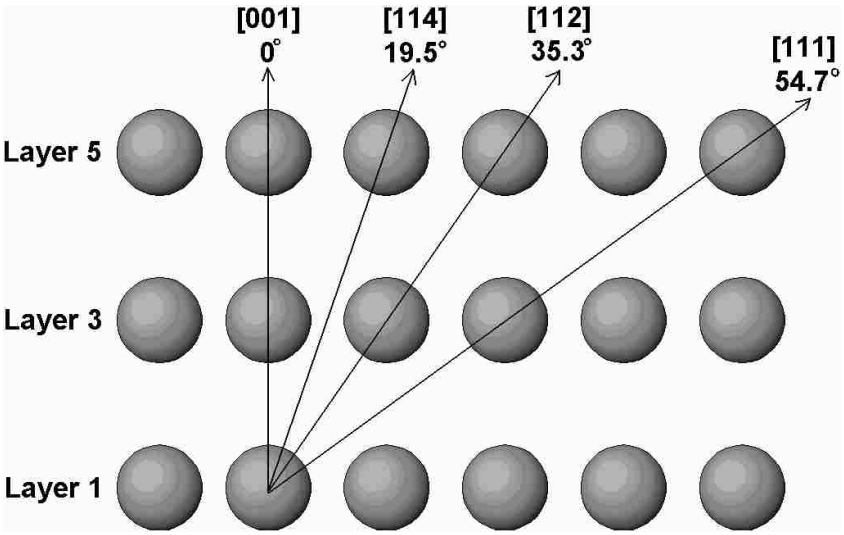

Figure 2.18. Forward-focusing angles for the (110) azimuthal plane of an fcc crystal lattice. The forward-scattering angles are taken with respect to the sample normal, [001] direction, and are labeled for some of the low-index directions.

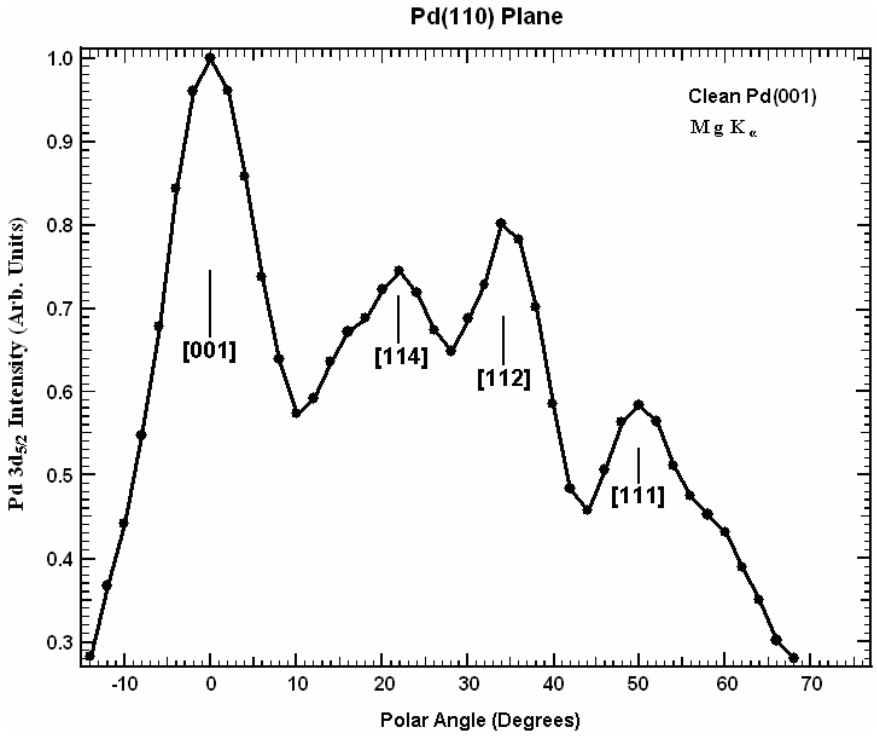

Figure 2.19. Pd $3d_{5/2}$ XPD polar scan for the Pd(110) azimuthal plane.

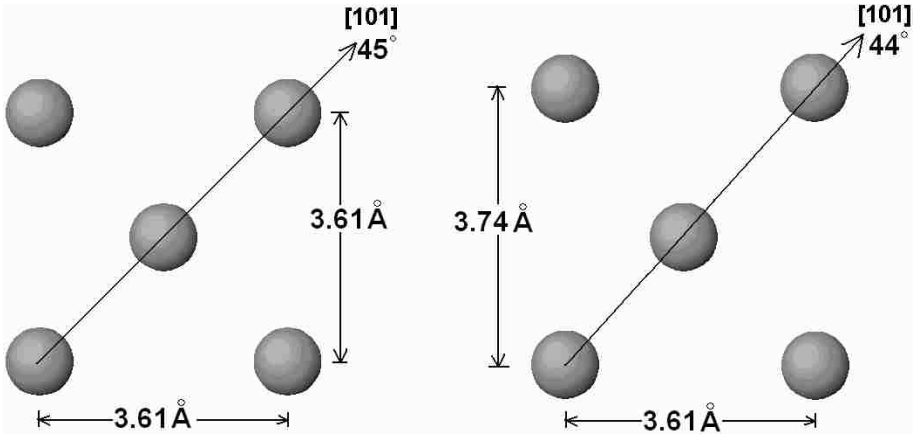

Figure 2.20. Tetragonal distortion in an fcc crystal lattice. The forward-focusing angle for the [101] direction is shifted by 1.0º toward lower angles due to an expansion of the c-axis (sample normal direction).

2.2.4. Multiple Scattering and the MSCD Program. The strength of the single-scattering cluster model lies in its simplicity and computational convenience, with only modest computing power needed for clusters large enough to insure proper convergence. This theory generally yields results with greater accuracy for photoelectron diffraction experiments at scattering angles greater than ~ 30º and for kinetic energies ~500 eV or higher. As is evident from the plot for scattering strength vs. scattering angle of Ge in Figure 2.21, the degree of forward scattering increases with increasing electron kinetic energy [26]. For energies in excess of several hundred electron volts, the scattering strength $|f(\theta_j)|$ is strongly peaked in the forward direction, and there is almost no phase shift between the scattered and unscattered wave portions at low scattering angles. As a result, at high energies constructive interference takes place and multiple scattering is negligible except for small scattering angles (the forward-scattering regime) at low electron kinetic energies.

However, at low kinetic energies, less than about 500 eV, many of the assumptions and approximations made in arriving at Equation 2.17 break down. Effects due to the initial state (s, p, d, f) of the photoelectron wave prior to scattering also must be included in calculations of photoelectron diffraction at lower kinetic energies. The exclusion of multiple scattering is no longer valid for low kinetic energies since the

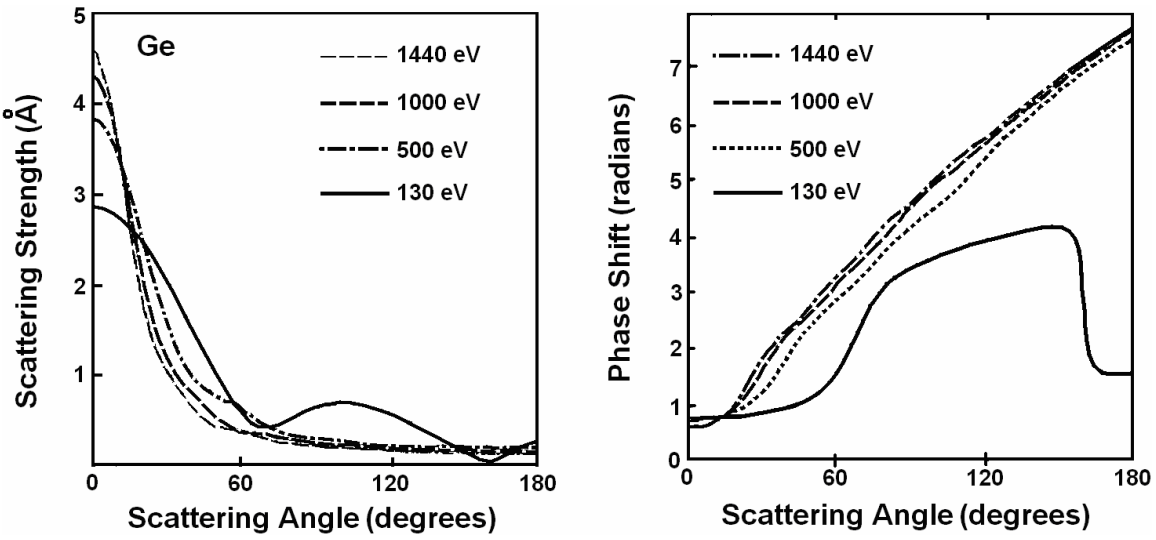

Figure 2.21. Scattering strengths and phase shifts as a function of scattering angle and electron kinetic energy for a Ge ion core in bulk Ge. The scattering strength falls off rapidly with increasing scattering angle at high kinetic energies, and the phase shifts are small for small scattering angles. (Reproduced by permission of Taylor and Francis from S. A. Chambers [26]).

scattering amplitude $|f(\theta_j)|$ is no longer as strongly peaked in the forward direction, so that taking the differential cross-section $[d\sigma_{n,l}\{\boldsymbol{\varepsilon}, \mathbf{k}\}/d\Omega]^{1/2}$ to be the same for both scattered and unscattered wave portions is no longer appropriate.

Even in the high energy regime the single-scattering cluster (SSC) model cannot reproduce some experimental spectra. Again, effects due to the initial state (s, p, d, f) of the photoelectron wave prior to scattering have to be accounted for. Single-scattering theory gives an overestimation of the forward-scattering intensity along close-packed, low-index directions [28], and the multiple-scattering theory predicts intensities that are in much better agreement with experiments. The large elastic scattering cross-sections $|f(\theta)|^2$ at small θ and high kinetic energies result in an increased probability for multiple scattering along close-packed low-index directions involving more than two atoms. Due to the Coulomb attraction of the electron by the ion core, secondary scattering of the electrons by atoms along rows lying next to the emitting atom will take place, resulting in a 'defocusing effect' [26] as shown in Figure 2.22. This interaction occurs as the wave portion that is forward scattered by the atom directly adjacent to the emitter passes

through the potential centered on the secondary scattering site. For example, if we consider a film of 3 ML thickness (Figure 2.22), an electron emitted from a third-layer atom, after being focused into the forward direction by a second-layer atom, is further deflected (defocused) to directions other than forward by a first-layer atom. In multiple-scattering theory, such electrons are discarded from the forward-direction peak. Likewise, the effect occurs at subsequent scattering sites along the chain, such that forward scattering along the chain is completely eliminated for sufficiently long chain length. This phenomenon cannot be modeled without recourse to multiple scattering theory.

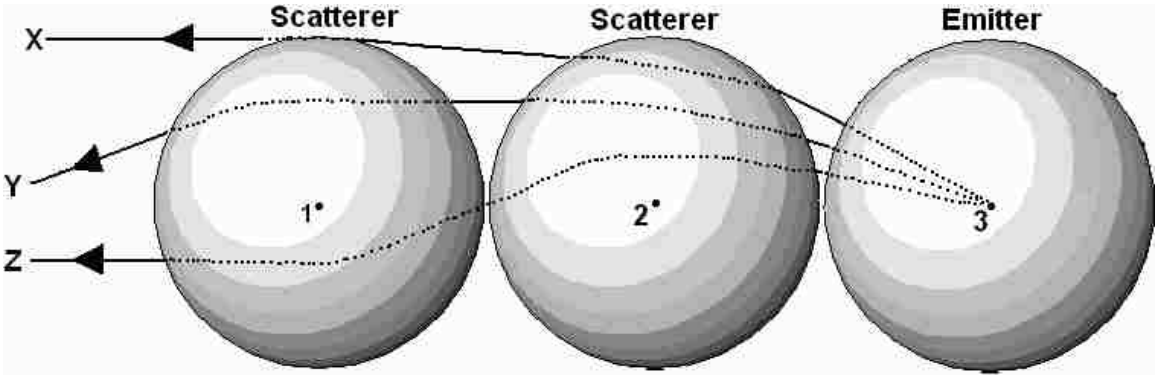

Figure 2.22. Schematic diagram showing the defocusing effect that accompanies multiple scattering along a chain of atoms.

Multiple-Scattering Calculation of Diffraction (MSCD) is a multiple scattering photoelectron diffraction program that has been used to compare XPD experimental results with theoretical predictions, and is currently the program of choice for all such comparisons with the experiments. This program was developed by Yufeng Chen and Michael Van Hove of the Materials Sciences Division of Lawrence Berkeley National Laboratory [36]. Multiple scattering calculations in both the angle-scanned mode as well as the energy-scanned mode, can be performed in the MSCD program, and this program simulates the elemental and state-specific core-level photoelectron diffraction pattern from an atomic cluster. It is based on multiple scattering theory with the Rehr-Albers

(RA) separable representation of spherical-wave propagators, and is used to produce structures yielding best fits to the experimental data [37].

To model the use of unpolarized radiation, the results of MSCD for two orthogonal polarizations were averaged. The program code features the multiple scattering approach developed by Rehr and Albers [37], the TPP-2 inelastic mean free path formula developed by Tanuma, Powell, and Penn [38], and the correlated temperature effect developed by Sagurton, Bullock, and Fadley [39]. The program incorporates curved-wave multiple-scattering contributions with the use of formalism similar to that based on the plane-wave approximation. In this approximation, termed the 'small-atom approximation', the wave curvature is considered negligible over the dimensions of the scattering potential associated with the scattering site, thereby allowing the direct wave portion incident on a given scatterer to be approximated by a plane wave. However, due to non-negligible wave curvature for dimensions of a few angstroms from the emitter, scattering by the nearest neighbors (for distances less than 5 Å from the emitter) calculated using the small-atom approximation is not very accurate, and some level of curved-wave correction is incorporated.

Various parameters, incorporated into the program, include the multiple-scattering order n_{max} — the degree of multiple scattering events which can be varied from zero to eight, the Rehr-Albers (R-A) order $|\mu|_{max}$ (size of the scattering matrices), the initial angular momentum state (s, p, d, f), photoelectron kinetic energy, sample orientation, sample properties (density, molecular weight, lattice constant, number of valence electrons, Debye temperature, sample temperature), and the crystal structure of the sample under investigation. The number of atoms in the cluster used for the calculation can also be varied, and often, the results of calculations depend strongly on the size and shape of the cluster.

2.2.5. Instrumentation for XPS and XPD. All experiments in this work were performed in an ultra-high vacuum (UHV) chamber equipped with a low energy electron diffraction (LEED) unit, XPS unit consisting of an electron energy analyzer and x-ray source, a residual gas analyzer (RGA), a sample manipulator, a sputter gun, a film evaporation facility, an ion pump, and a Titanium sublimation pump. A schematic of the experimental set-up is shown in Figure 2.23. The x-ray generator (PHI model 04-548) is

equipped with Al and Mg anodes which are the sources for Al K_α ($h\nu$ = 1486.6 eV) and Mg K_α ($h\nu$ = 1253.6 eV) soft x-ray. The full width at half maximum (FWHM) is less than 1 eV for both anodes. The FWHM is normally the major contributor to the observed peak widths in the XPS spectrum.

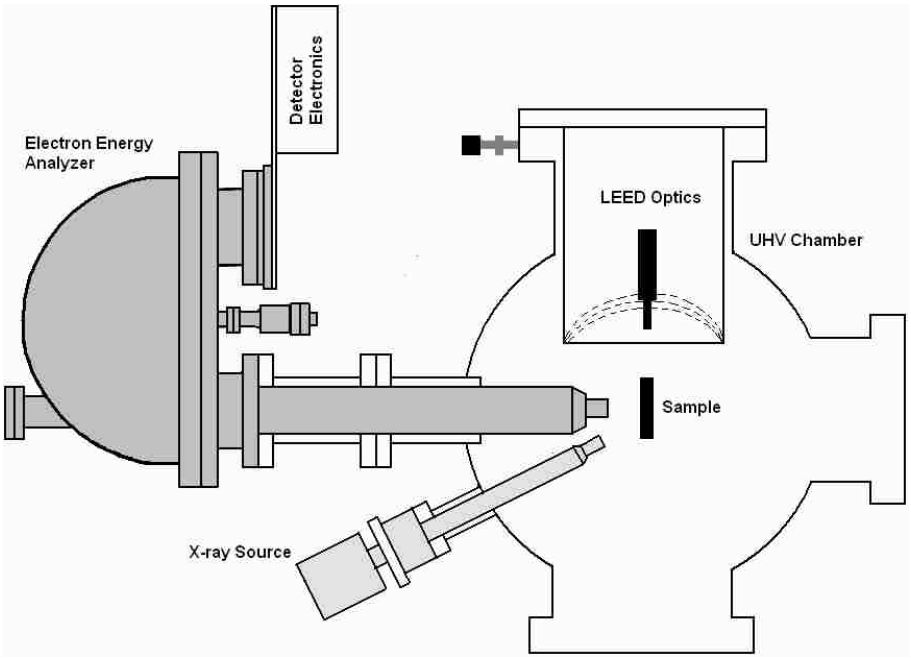

Figure 2.23. Schematic of the Ultra-High Vacuum facility showing XPS/XPD and LEED at the upper level of the chamber. The sputter gun and evaporator are located in the lower level of the chamber.

In the employed configuration, the angle between the analyzer and the x-ray source was 55°. The kinetic energy of the emitted electrons was measured by a hemispherical energy analyzer (VSW model 125), and the energy dispersion of the electrons entering through the input slit took place between two concentric hemispherical electrodes of 125 mm mean radius. A potential difference is applied between the inner and outer surfaces of the two concentric hemispheres. This potential difference, known as the pass energy, determines the kinetic energy of the electrons that are passed to the

electron detector. For electrons at a specific energy E_0, the finite analyzer energy resolution ΔE_a of the analyzer is given approximately by:

$$\Delta E_a = E_0 \left(\frac{d}{2R_0} + \alpha^2 \right) \tag{2.19}$$

Here, d = slit width, R_0 = mean radius of the hemispheres, α = half angle of electrons entering the analyzer at the entrance slit. Thus, the energy resolution depends on the electron pass energy E_0, the slit width and the acceptance angle of the lens system. This mode of operation of the analyzer is known as the fixed analyzer transmission mode (F.A.T.) in which the analyzer pass energy is held constant, and the retarding voltage is changed, thus scanning the kinetic energy of the detected electrons. The resolution obtained in the F.A.T. mode is constant throughout the whole kinetic energy range.

The sample analysis area and the acceptance angle of the detected electrons can be changed by varying the magnification mode of the lens system, and by changing the entrance slit size. Three magnification operating modes of the lens system are available - low, medium, and high with acceptance angles of ±1°, ±4°, and ±8°, respectively. A variable slit mechanism with 5 different linked pairs of entrance and exit apertures is available which can be selected from outside the vacuum system by a rotary drive. The slits vary from 1mm diameter up to 6 mm x 12 mm in size. For normal XPS scans high magnification and 6 mm x 12 mm entrance slit settings are adequate. The product of the slit area and the acceptance angle is a conserved quantity for a fixed energy [40]. The arriving electrons are detected by a channel electron multiplier placed at the exit of the analyzer. The pulses from the electron multiplier are detected by a charge sensitive pulse pre-amplifier and passed to a pulse counter for processing and production of an electron energy spectrum.

For resolving small chemical shifts or other closely spaced spectroscopic features the analyzer should be operated in high resolution mode. High resolution will provide the narrowest peaks, with reduced sensitivity, and accurate peak positions, making it possible to derive chemical information in XPS from narrow scan spectra. For this purpose, the

analyzer is operated at low magnification mode, in which ±1° acceptance angle and 2mm diameter entrance slit settings are selected.

2.3. LOW ENERGY ELECTRON DIFFRACTION

Low energy electron diffraction is one of the oldest but also one of the most widely used methods in surface analysis. The technique involves the elastic backscattering of well-defined (but variable) low energy (50-300eV) electrons from a well ordered crystal surface leading to formation of diffraction spots on a fluorescent screen. For an electron with an energy E with respect to the zero of the crystal potential, the de-Broglie wavelength is given by:

$$\lambda = \frac{h}{\sqrt{2m_e E(eV)}} = \sqrt{\frac{150.4}{E(eV)}} \tag{2.20}$$

Here, m_e is the mass of an electron, E is the electron energy, and h is the Planck's constant. Main applications of this method lie in surface quality characterization during sample preparation prior to other UHV experiments, and structure determination of clean and adsorbate covered crystal surfaces, and thin films. The sensitivity of this technique to the geometrical structure of the atoms at the surface of a crystal lies in the fact that electrons interact strongly with matter and so cannot penetrate deeply.

For energies between 30 and 500 eV, the wavelengths (2.7 Å> λ > 0.6 Å) are comparable to the lattice spacing of typical crystals. The inelastic mean free path of electrons in the noted energy range is approximately ~ 5 Å, and therefore, only the upper-most atomic layers of a surface are sampled. Therefore, the low penetration depth and suitable wavelength, as well as the fact that it is easy to change the electron energies make LEED a powerful and versatile crystallographic probe for surface analysis. In this work, the use of LEED for surface analysis is confined to qualitative characterization of surface ordering and the quantitative determination of the two-dimensional surface lattice parameters (e.g. superstructures).

Diffraction results from the interaction of electron waves scattered from a periodic array of scattering centers. Scattering from individual centers may be very small, but if the scattered waves from successive centers are in phase, then the net result may be significant. Due to the periodicity of the waves and scatterers, different possible conditions of strong in-phase scattering may occur resulting in the production of a whole series of diffracted beams. For single crystal surfaces, the interference results in a sharp maximum in the intensity of scattered electrons for certain directions in space. Roughly 1 to 5 percent of the incoming electrons are elastically scattered, and this fraction is allowed to impinge on a fluorescent screen. The LEED pattern reveals surface symmetry as well as imperfections of the surfaces such as steps, and it can be used to determine the lattice constants of ordered overlayer films.

2.3.1. Instrumentation for LEED. The experimental LEED setup is constructed within a UHV chamber. The LEED optics is of the "rear view" type. On the atmospheric side the LEED flange is equipped with a UHV window. Inside the vacuum the LEED system consists of an electron gun, fluorescent screen, and retarding grids. The system used in this work is Model ErLEED 100/150, made by Vacuum Science Instruments. A schematic of the LEED system is shown in Figure 2.24.

The fluorescent screen can be viewed through a glass window on an 8" flange. The screen is metal-coated on both sides, and the grid side of the screen is coated with cadmium free phosphor. This four-grid LEED system has a 2" motion provided by a linear drive attachment. Prior to LEED analysis the x-ray source can be retracted, and the LEED system is extended in such a way that the sample to electron gun distance is approximately 1.25". The highly compact electron gun consists of the cathode, the Wehnelt cylinder, a double anode, an electrostatic single lens, and the drift tube. The cathode is a Lanthanum hexaboride (LaB_6) filament with specially cut microfaces. Within the standard LEED operation the electron energy can be varied between 0 and 300 eV. The Wehnelt cylinder acts as an electrostatic aperture between the cathode and the anode. It is kept on the same or negative potential with respect to the cathode and regulates the sharpness of the diffraction spots – an increase of the Wehnelt voltage leads to a narrowing of the electron beam. The anode is always at a positive potential with respect to the cathode, and is responsible for accelerating the electrons emitted by the filament

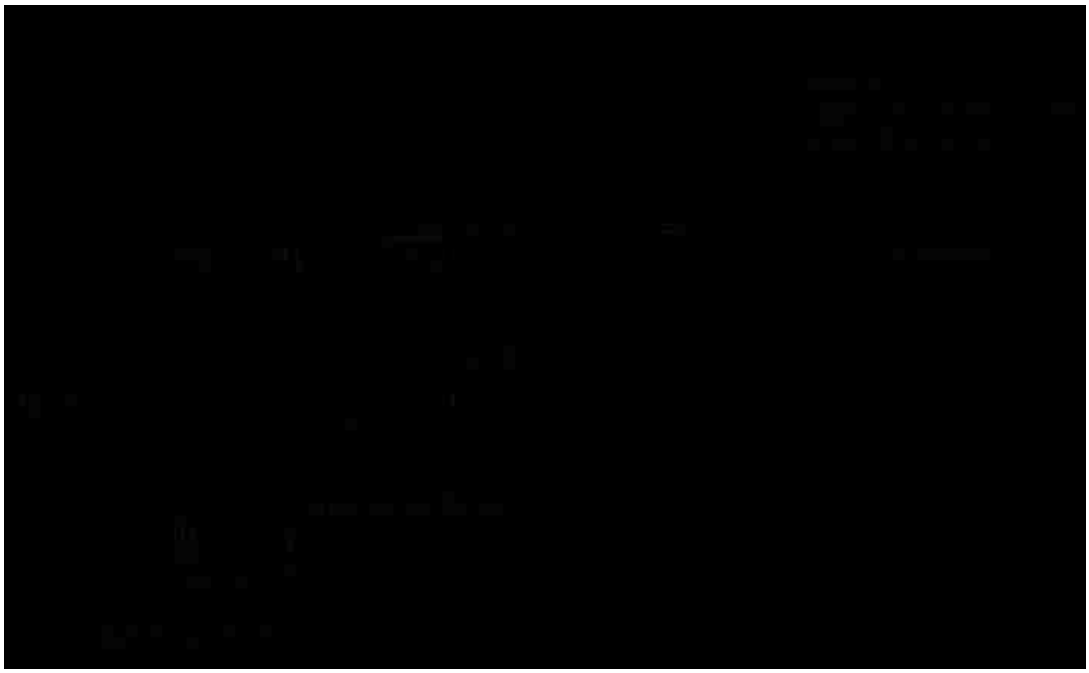

Figure 2.24. Schematic of LEED apparatus.

into the direction of the lens elements. The lens elements constitute an electrostatic single lens that shapes and focuses the electron beam onto the sample. In practice, the electron beam energies typically lie between 50-500 eV, and the electron beam spot size at the sample is less than 300 μm in diameter at 1 μA and 100 eV. The diameter of the electron gun is 0.6" and thus covers only a small area of the viewing screen. The grids of the LEED optics are fabricated out of molybdenum, and gold coated to avoid potential changes due to work function differences. By applying a negative voltage to the grids, secondary electrons and inelastically scattered electrons can be kept away from the fluorescent screen, so that only elastically scattered electrons and electrons with small energy losses contribute to the diffraction pattern.

2.3.2. Overlayer Structures. The most direct information obtained from LEED is the periodicity and intermediate range order, and this can be gathered by visual inspection of the diffraction pattern and by relatively simple mathematical transformation of the spot profiles. Within its bulk, a crystal will be periodic in three dimensions and can be described in terms of a three-dimensional lattice. If $\vec{a}_1$, $\vec{a}_2$, and $\vec{a}_3$ are the primitive

vectors of the crystal lattice, then the three primitive vectors $\vec{a}_1^*$, $\vec{a}_2^*$, $\vec{a}_3^*$, of the reciprocal lattice are given by:

$$\vec{a}_1^* = 2\pi \frac{\vec{a}_2 \times \vec{a}_3}{\vec{a}_1 \cdot \vec{a}_2 \times \vec{a}_3} \tag{2.21a}$$

$$\vec{a}_2^* = 2\pi \frac{\vec{a}_3 \times \vec{a}_1}{\vec{a}_1 \cdot \vec{a}_2 \times \vec{a}_3} \tag{2.21b}$$

$$\vec{a}_3^* = 2\pi \frac{\vec{a}_1 \times \vec{a}_2}{\vec{a}_1 \cdot \vec{a}_2 \times \vec{a}_3} \tag{2.21c}$$

At the surface, the layers may not be equally spaced and $\vec{a}_3$ is ill-defined. Moreover the electrons do not penetrate into the crystal far enough so the periodicity of the structures beyond the top few layers is relatively weakly explored in the direction normal to the surface. The diffracting structure can be considered to be a two-dimensional lattice in which the unit cell is extended in the third dimension. In general, a surface structure may have real space lattice vectors $\vec{b}_1$ and $\vec{b}_2$ which differ from the substrate real space lattice vectors $\vec{a}_1$ and $\vec{a}_2$.

The Bragg condition for constructive interference can be represented by the equation:

$$(\vec{k}' - \vec{k}_0) = \vec{G} = h\vec{a}_1^* + k\vec{a}_2^* + l\vec{a}_3^* \tag{2.22}$$

where $\vec{k}_0$ is the incident wave vector and is related to the wavelength λ, by the relation $k_0 = 2\pi/\lambda$, $\vec{k}'$ is an elastically scattered wave vector, $\vec{G}$ is a reciprocal lattice vector, and h, k, l are integers (h, k, l = 0, 1, 2…). The Ewald sphere construction, as shown in Figure 2.25, can be used to envisage a geometrical interpretation in reciprocal space which would simulate the diffraction process. The wave vector $\vec{k}_0$ is so positioned that one end

touches a reciprocal lattice line, and the other end provides the center for a sphere of radius $k_0=2\pi/\lambda$, the Ewald sphere. For diffraction from surfaces we let $\vec{a}_3 \to \infty$, while the other two basis vectors remain unchanged. As the lattice vector in any direction is increased, the corresponding reciprocal lattice vector will decrease. If the separation $\vec{a}_3$ between the planes is increased towards infinity, the two dimensional situation is approached as the reciprocal points given by $\vec{a}_3^*$ converge towards zero, thereby forming a continuous line.

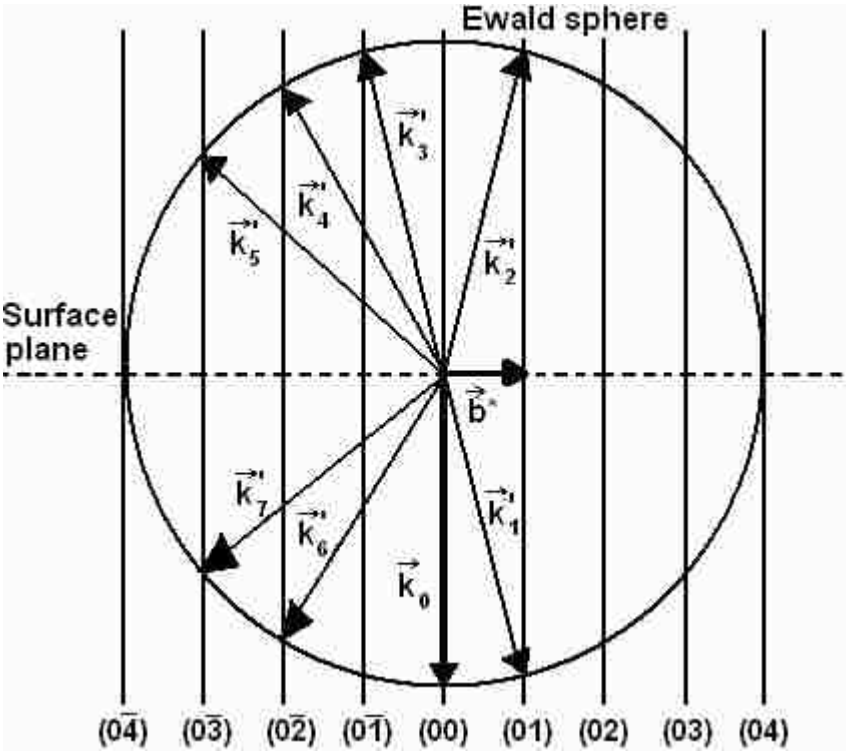

Figure 2.25. Ewald sphere construction for surface with diffracted beams and reciprocal lattice rods as shown. Here $\vec{b}^*$ is in the plane of the paper.

The reciprocal lattice is given by a discrete two-dimensional mesh defined by $h\vec{a}_1^* + k\vec{a}_2^*$ with continuous lines or rods in the third dimension (normal to the real space plane), passing through this two-dimensional array. Wherever the Ewald sphere intersects

these rods a diffracted beam will be observed. In Figure 2.25, the origin of the crystal is at the center of the Ewald sphere. The incident beam wave vector touches a reciprocal lattice rod at one end, and this point of intersection is designated as the reciprocal space origin. All possible diffracted beams are given by those vectors which have length $2\pi/\lambda$ about the other end of the incident beam vector and meet reciprocal lattice rods. This locus of beam vectors with the same energy as the incident beam defines the Ewald sphere. The incident beam, diffracted beams, and the reciprocal lattice rods are shown for $\vec{a}_2^*$ in the plane of the paper. The (*hk*) indices represent the reciprocal lattice rods associated with each surface net point.

The back scattered beams, $\vec{k}_2'$, $\vec{k}_3'$, $\vec{k}_4'$, $\vec{k}_5'$ are observed in a LEED experiment, while $\vec{k}_1'$ is insignificant since it's directed into the sample and hence not observed. As the incident energy is increased, the radius of the Ewald sphere will also increase. Consequently, the number of rods intersected by the sphere increases, which increases the number of diffraction beams and the angle between each diffraction beam decreases. In the experiment, this leads to the diffracted beams moving towards the (00) beam with increasing incident energy.

2.3.3. Overlayer Notation. The lattice vectors $\vec{b}_1$ and $\vec{b}_2$ can always be described in terms of the substrate lattice vectors $\vec{a}_1$ and $\vec{a}_2$. While this method of notation enables rapid identification of the resulting diffraction pattern, it is rather inconvenient to always write down in matrix notation and it is not always straightforward to recognize special features. Another common nomenclature proposed by Wood [41] is often preferable. This notation defines the structure of an ordered overlayer by specifying the unit cell of the overlayer in terms of the ideal unit cell of the underlying substrate.

If the lengths of the overlayer unit cell are $|\vec{b}_1| = m|\vec{a}_1|$, and $|\vec{b}_2| = n|\vec{a}_2|$ and the angle between $\vec{b}_1$ and $\vec{b}_2$ is the same as that between $\vec{a}_1$ and $\vec{a}_2$, the complete Wood's notation for a surface structure formed by the adsorption of an atomic or molecular species *E* on an (*hkl*) surface of a substrate *M* is given by $M(hkl)\text{-}{}_c^p(mxn)E$, with either *p* (primitive) or *c* (centered) used as appropriate. If the overlayer lattice vectors are subtended by the same angle as the substrate vectors, but the whole lattice is rotated

through an angle α with respect to the lattice vector $\vec{a}_1$, the lattice is described as $M(hkl)-{}^{p}_{c}(mxn)R\alpha^{o}-E$. Figure 2.26 shows an example of an overlayer on a clean fcc(001) surface and its reciprocal space. Figure 2.26(a) shows the clean fcc(001) surface

Real Space Reciprocal Space

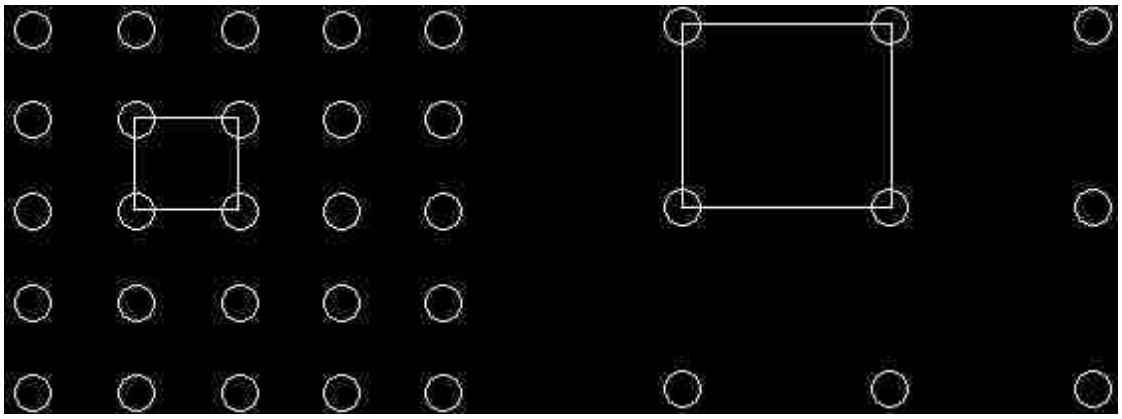

(a) **(b)**

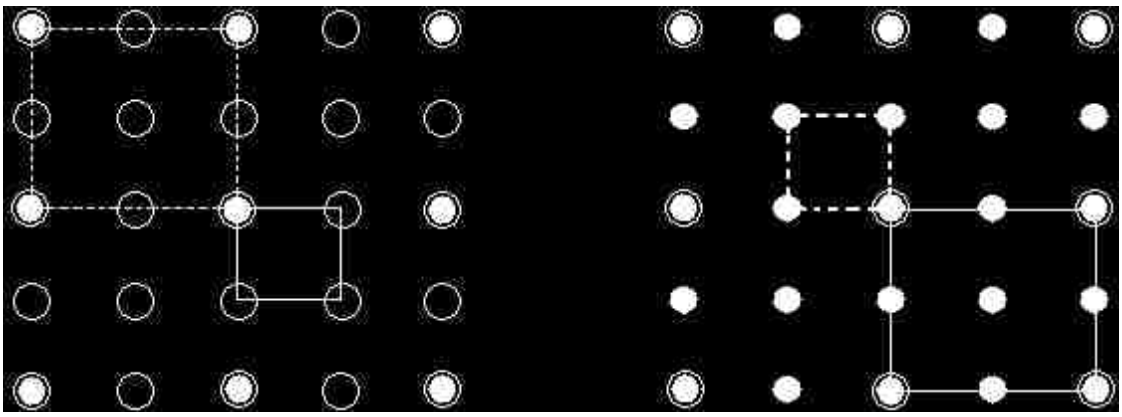

(c) **(d)**

Figure 2.26. Schematic of an overlayer structure. Open circles indicate the substrate atoms and their corresponding diffraction spots, and the filled circles indicate the overlayer atoms and their corresponding diffraction spots. The upper panels (a) and (b) are for clean fcc(001) substrate, and the lower panels (c) and (d) show the addition of a p(2 x 2) overlayer structure.

in real space with its primitive cell outlined by solid lines, while Figure 2.26(c) shows the overlayer (filled circles) in real space with dashed lines indicating the overlayer primitive cell. On the right panel, Figures 2.26(b) and 2.26(d) show the corresponding reciprocal space structures (LEED pattern) for the clean fcc(001) surface and the overlayer respectively. For a Ni substrate with an adsorbed overlayer of O, the LEED pattern can be denoted as Ni(001)-p(2 x 2)-O in Wood's notation.

Often multiple orientations of the overlayer may exist on the surface, as shown in Figure 2.27. These regions of different orientations comprising a particular overlayer structure are called *domains*. If typical domain sizes are small compared with the coherence length of the incident electron beam, interference may occur between the diffracted waves from regions of different type. For domains much larger than the coherence length of the electron but smaller than the total beam area, the resulting diffraction pattern will be superposition of the patterns that would be expected from each domain individually.

A schematic of single and multiple domain diffraction patterns is shown in Figure 2.27. The diffraction pattern consists of 2 domains with the surface net in real space given by $a_1 = a_2 = 2.2361a_0$, and $\varphi_0 = 53.1°$, where a_0 denotes the substrate surface lattice constant. The existence of domain structures adds more features to the observed LEED pattern.

2.4. SAMPLE PREPARATION

The samples were and analyzed in a custom built UHV chamber (Figure 2.28). A well oriented and polished single-crystalline Pd substrate was obtained commercially (Monocyrstals Co.). The substrate was washed with acetone and methanol before being placed into the substrate holder. Once it was mounted on the manipulator and put in vacuum, the substrate was cleaned by Ar^+ sputtering (20 mA emission, 1.5 kV beam voltage) for 20 minutes in the UHV chamber at a partial argon pressure of approximately ~$2x10^{-5}$ Torr, treated with oxygen at partial pressure of $5x10^{-7}$ Torr and substrate temperature of 150-200°C for 2 minutes to remove carbon contaminants, and subsequently annealed at 420°C for 30 minutes.

Real Space Reciprocal Space

(a) **(c)**

(b) **(d)**

Figure 2.27. Effects of multiple domains in a diffraction pattern on an fcc(001) surface. The figures (a) and (b) are real space structure for two domain rotated by 90° with respect to each other, (c) is diffraction pattern from a single domain, and (d) is the diffraction pattern from superposition of two domains rotated by 90° with respect to each other.

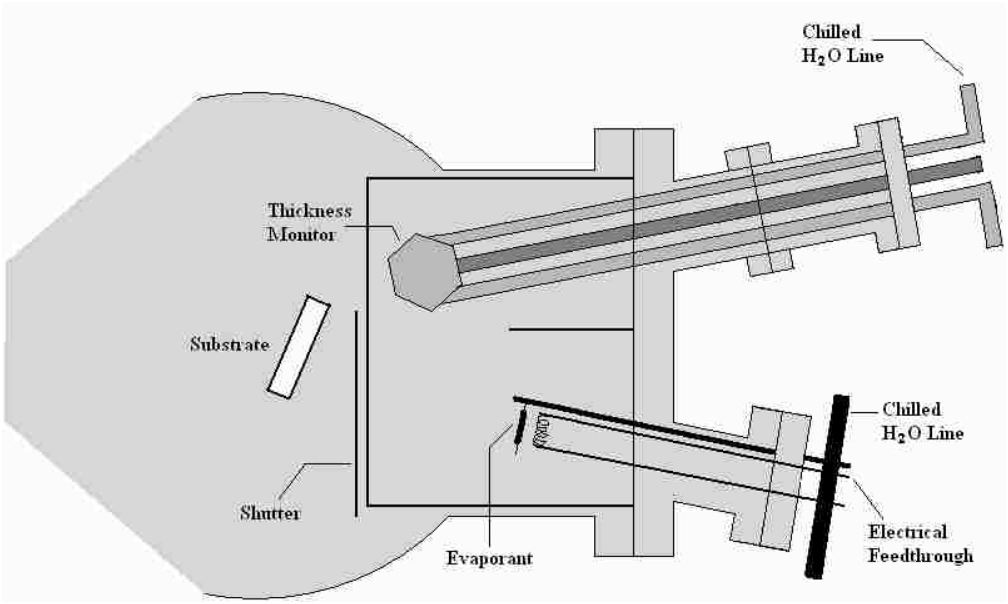

Figure 2.28. Schematic of the evaporator assembly. The shutter is used to control the time of exposure to the evaporant flux and the selection between the two evaporant sources (Cr and Fe). One of the evaporators is shown.

The metal films are evaporated by electron beam bombardment in which an electron beam, emitted from a Ta filament, is accelerated towards the evaporant by applying a bias voltage of 600-1500 V to the metal pellet with respect to the filament. The thermionically emitted electrons bombard and heat up the evaporant charge. The evaporant flux can be controlled by adjusting the electron emission current. The UHV based evaporation facility was built on an 8" flange with four feedthroughs to support the thickness monitor, shutter, and two evaporators. The evaporators are separated from one another by a partition, and are housed inside a distilled water cooled stainless steel jacket.

Film evaporation rates for both Fe and Cr were typically kept at ~0.5 Å/ minute in this study. For determination of evaporation rate and estimation of the thickness of the film deposited on the Pd substrate a crystal thickness monitor (INFICON thickness monitor) was used. The base pressure of the UHV chamber during evaporation was maintained at approximately ~ 10^{-9} Torr. Oxidation of the deposited transition metal films was done by exposing the films to molecular oxygen (Matheson 99.995% purity) at

a partial pressure of approximately $2x10^{-5}$ Torr. A variable leak valve was used to introduce O_2 into the UHV chamber. Two basic procedures were involved in the fabrication of the transition metal oxide (TMO) films. In one of the methods, termed Multilayer Deposition Technique, a multilayer thick metal film was deposited on the palladium substrate. This was followed by oxidation at elevated substrate temperatures for 10-20 minutes so that the entire film gets oxidized. After the oxidation, the film was annealed for 20-30 minutes to obtain a well ordered sample. In the second growth method, termed Sequential Deposition Technique, films of submonolayer - one monolayer (ML) thickness is equivalent to one atomic layer of evaporated film - thickness were deposited sequentially, followed by oxidation and annealing after each deposition. The oxygen partial pressure was kept the same as in the case of multilayer film oxidation, but the exposure time was limited to 3-5 minutes during each sequence. More detailed discussions of each technique and growth conditions are provided in the following two sections.

The UHV chamber was equipped with an ion pump and a titanium sublimation pump (TSP), Physical Electronics (PHI) model TNBX pump station, to maintain the base pressure in the low 10^{-10} Torr range. An ion gauge monitored the vacuum chamber pressure, and a residual gas analyzer model RGA100 enabled the characterization of the vacuum environment.

3. CHROMIUM-OXIDE THIN FILM GROWTH ON Pd(001)

3.1. BACKGROUND

The oxides of chromium are technologically important due to their use in areas such as in magnetic recording media, as catalysts, and as passivating overlayers for stainless steel. Several stable phases of chromium-oxide exist over a wide range of temperatures. The most stable phase of chromium-oxide is Cr_2O_3 and it crystallizes in the corundum structure. It is an anti-ferromagnetic insulator with a band gap of 3.2 eV, and is also used as an important polymerization catalyst and for passivating stainless steel. Chromium-oxide also forms a tetragonal CrO_2 phase which exhibits the property of a ferromagnet with a Curie temperature of $T_C = 386$ K. CrO_2 is the only ferromagnet in the family of transition metal oxides with the rutile structure. It is used in magnetic recording media due to its corrosion resistance and high coercivity. Above 280 °C, CrO_2 decomposes to Cr_2O_3. The tetragonally distorted Cr_3O_4 spinel phase exists at temperatures above 1600 °C. Some of the oxide phases have geometrically incomplete structures [42] that have deficiencies (voids) in the oxygen close-packing or an incomplete filling of the possible metal positions. These deficit structures also have the cubic spinel-like structure and are known as the γ-oxides.

Epitaxial growth of chromium-oxide by oxidation of the surface region of chromium crystals has been reported on the (100), (110), (111), and (113) surfaces [43-46]. For oxidation of the Cr(011) surface, most studies report the formation of Cr_2O_3(0001) [43, 44, 47-49]. Michel and Jardin [43] reported LEED, RHEED, and scanning microscopy studies done on the oxidation of clean Cr(100) and Cr(110) surfaces. They observed that oxygen exposure of about 10^{-7} Torr at room temperature yielded a c(2x2) structure on the surface, and they suggested oxygen atoms being adsorbed into the octahedral sites of the surface with half of the sites being occupied. The diffraction pattern disappeared when the oxygen exposure was increased to 10^{-6} Torr and the temperature to 500 °C, and RHEED observations suggested the occurrence of a thin polycrystalline film of Cr_2O_3. After heating the Cr(110) surface at 400 °C and at an O_2 pressure of 10^{-7} Torr, a streaked diffraction pattern was observed, and was attributed to the faceting of the (110) surface. Additional oxygen exposure to the Cr(110) surface at

500 °C and 10^{-6} Torr O_2 resulted in a new c(3x1) diffraction pattern with streaks and diffraction spots, and further exposure of 10^{-6} Torr O_2 at about 900 °C led to the formation of a sharp six-fold diffraction pattern, and it was concluded that the stable structure was rhombohedral $Cr_2O_3(0001)$. Ekelund and Leygraf [44] also carried out investigations on the initial oxidation stages of Cr(110) and Cr(100) surfaces using LEED and Auger electron spectroscopy. Adsorption of oxygen on the Cr surfaces at room temperature was detected through AES, and short heat treatment resulted in an ordered surface structure. For Cr(110) surfaces, higher oxygen exposures led to the growth of strained $Cr_2O_3(001)$ films, and the strain was attributed to the misfit of the $Cr_2O_3(001)$ surface with the Cr(110) surface along $[1\,\bar{1}\,0]$. Further oxygen exposure resulted in lattice contraction along the $[1\,\bar{1}\,0]$ direction with the oxide film structure matching the lattice of bulk Cr_2O_3. Oxidation of Cr(001) led to the formation of a $Cr_2O_3(310)$ surface parallel to the Cr(001) surface. Another study by Watari and Cowley [45] reported the formation of both Cr_2O_3 and spinel oxides upon oxidation of the Cr(111) surface.

Investigations on the growth of surface structures of ultra-thin chromium-oxide films on metal and metal oxide substrates have also been reported in the literature [50-54]. The growth of Cr_3O_4- and Cr_2O_3-like oxides has been reported on various substrates [50, 55]. Studies of chromium oxides prepared on Cu(110) [52, 53], assuming a structure of CrO(111) at monolayer coverage and $Cr_2O_3(111)$ at a coverage of more than two layers, have also been reported. Du et al. [51] prepared chromium-oxide films on a MgO(001) substrate by molecular beam epitaxy at a substrate temperature of 600 °C. Ozone was used as an oxidizing agent and the Cr films were oxidized at a pressure of $2x10^{-4}$ mBar. XPS and XRD studies revealed the formation of thin single-phase epitaxial chromium oxide films with a body-centered orthorhombic unit cell. The crystalline structure of the chromium-oxide was determined to be a defect NaCl-type structure with ordered Cr vacancies. These ordered Cr vacancies were believed to be crucial in the formation of the defect NaCl-type structured chromium-oxide which does not exist in bulk form. Ultrathin chromium-oxide films on Cu(110) were investigated by Maetaki and Kishi [53] using XPS and LEED. The oxide films were prepared by evaporating Cr onto Cu(110) and exposing the metal film to O_2 (20 L) and heating at 400-500 °C in vacuum, and the oxide was found to grow into two types of structures depending on the coverage.

At monolayer coverage, they observed that the LEED pattern had a hexagonal symmetry and the oxide consisted mostly of CrO(111) containing both Cr^{2+} and Cr^{3+} ions. At coverages of two layers, the LEED pattern developed to a $(\sqrt{3} \times \sqrt{3})R30°$ pattern and was ascribed to a $Cr_2O_3(111)$ surface. Both surfaces were found to be stable to oxygen exposure up to 1000 L at room temperature. However, above 200°C both surface oxides were unstable to oxygen pressure (~1.3×10^{-5} Pa), and a copper oxide layer with Cu^+ ions was found to segregate to the top of the chromium oxide with most of the chromium atoms reduced to Cr^{2+}. The growth and oxidation of chromium films on W(100) were studied by Guo et al. [54] using low energy electron microscopy (LEEM) and LEED. The Cr films were first deposited at 357 °C and were then exposed to oxygen at pressures between 1.3×10^{-9} and 1×10^{-8} Torr and at temperatures between 102 and 667 °C. They observed a Stranski-Krastanov growth mode for the Cr films, and that 1 and 2 ML Cr films were unstable during oxidation. The formation of 3D clusters resulted in the production of complex diffraction features and this was attributed to the formation of Cr_2O_3 during oxidation of a monolayer of Cr at temperatures ≥ 517 °C. They also observed that the single layer Cr film remained intact during oxidation at T ≤ 357 °C, with 3D bulk Cr clusters being formed during oxidation of the 2 ML Cr film. Priyantha and Waddill [56] reported on the growth and characterization of ultrathin chromium-oxide films on Ag(111) using XPS, LEED, and XPD. The oxide films were grown using the sequential deposition technique, in which each submonolayer deposition of Cr was followed by an oxidation step, and this process was repeated until films of desired thickness were obtained. They observed that the chromium-oxide films with thickness ≤ 5 Å exhibited a $p(2 \times 2)$ LEED which, based on similar results obtained by other studies on the growth of chromium oxide on Pt (111) [50, 57] in which a p(2x2) LEED pattern was also observed, they suggested could be indicative of $Cr_3O_4(111)$ growth. However, they could not conclusively confirm the low coverage structure from the XPD results. For the chromium oxide films with thickness greater than approximately 12 Å, they observed a $(\sqrt{3} \times \sqrt{3})R30°$ LEED pattern that was found to consistent with α-$Cr_2O_3(0001)$. Their XPD results confirmed this and they further identified the surface termination as a single Cr layer with an inward relaxation of 50% from its bulk value. For films between 5 and 12 Å in thickness they observed a LEED pattern which was a superposition of the p(2x2)

and $(\sqrt{3} \times \sqrt{3})R30°$ patterns. XPS, LEED and XPD studies were also done on the growth of chromium oxide films on Ag(001) by Ozturk and Waddill [58]. The oxide films were grown using the sequential and the multilayer deposition techniques. They observed that while the multilayer growth technique resulted in the growth of α-Cr_2O_3(210) on Ag(001), the sequential growth technique yielded an α-Cr_2O_3(111) structure on Ag(001). They noted that the α-Cr_2O_3(111) oxide, which was formed from the initial deposition step in the sequential deposition method, persisted to the thickest oxide film (about 30 Å) grown on Ag(001).

3.2. EXPERIMENT AND RESULTS

The Cr_xO_y films were grown by thermal evaporation of Cr metal and subsequent oxidation of the deposited metal. The oxide films were characterized for surface crystallographic order, composition, film thickness, and surface structure determination by XPS, LEED, and XPD. All experiments were done inside an ultra high vacuum chamber with a base pressure of ~ $1x10^{-10}$ Torr. The thicknesses of the analyzed Cr_xO_y films ranged from approximately 4 to 23 Å. Two techniques were used to grow the Cr_xO_y films on Pd(001) – the multilayer deposition and the sequential deposition techniques.

3.2.1. Chromium Film Growth. It is important to characterize Cr films grown on Pd(001) in order to understand the structure the structure of chromium oxide films on Pd(001). A brief summary of the findings of growth of Cr on Pd(001) is reported here.

In the present study, Cr films were grown on Pd(001) at substrate temperatures of 300-350 °C. The diffraction patterns for the clean Pd substrate and the Cr films grown on Pd(001) are shown in Figure 3.1. Figures 3.1(a), (b), and (c) show the observed LEED patterns for clean Pd(001), a 5 Å thick Cr film, and a 16 Å thick Cr film grown on Pd(001) respectively. Figure 3.1(d) is a schematic representation of the relationship of the overlayer with respect to the substrate. The absence of additional LEED spots for the Cr films compared to the Pd(001) pattern suggests that the Cr films have the same surface mesh as the Pd substrate. The observed LEED pattern for Cr deposition on Pd is p(1x1) which is consistent with the growth of bcc Cr(001) films, and this structure persists to the highest coverages investigated. The LEED spots following Cr deposition show an initial

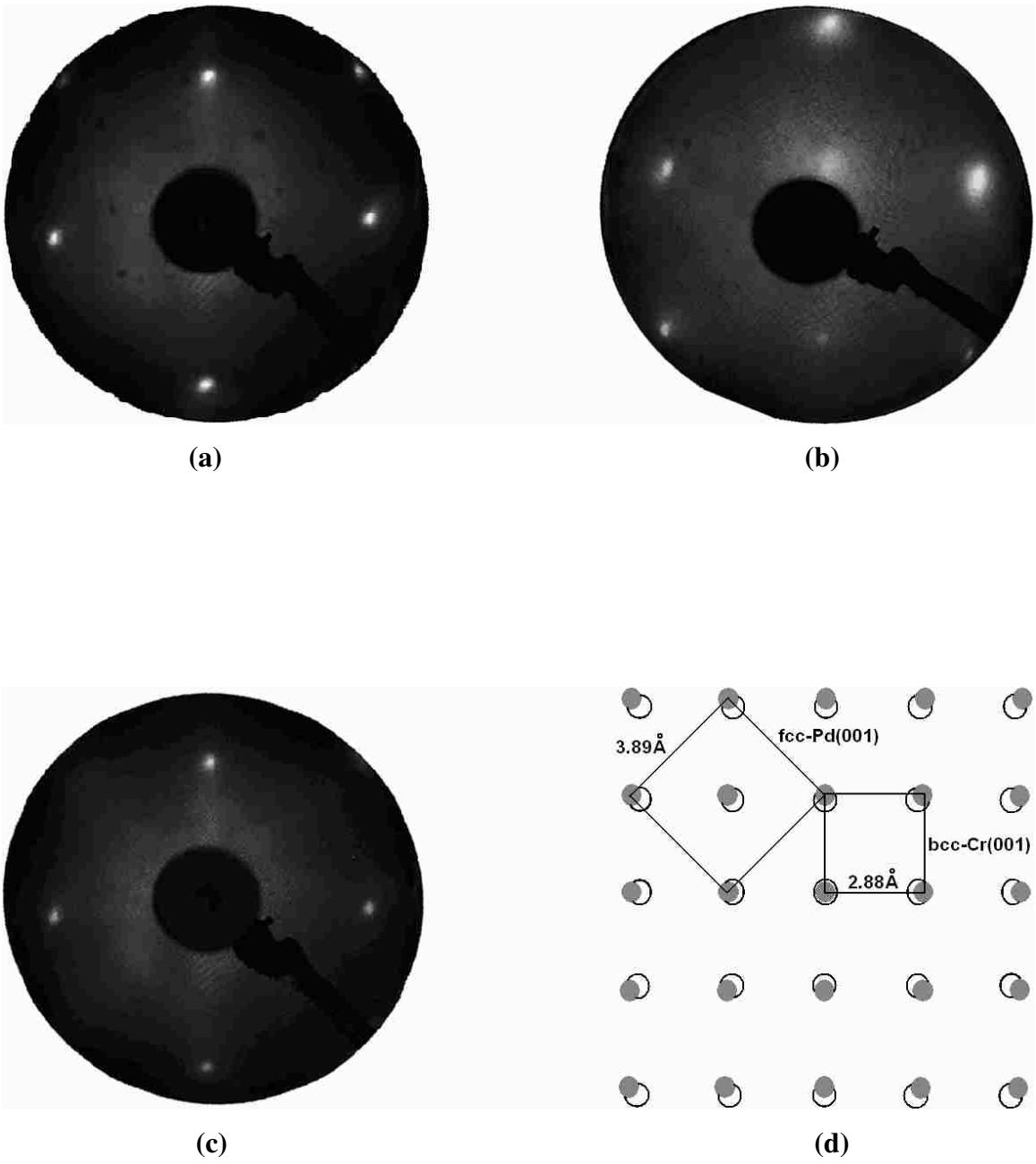

Figure 3.1. LEED patterns observed for (a) clean Pd(001), (b) a 5 Å thick Cr film on Pd(001), (c) a 16 Å thick Cr film on Pd(001), respectively, recorded at 72 eV electron energy, and (d) a schematic representation of the real space lattice match between the Cr (001) surface mesh (filled circles) and the Pd(001) (open circles) substrate.

broadening at around 5 Å. However, there is an improvement in LEED pattern at higher coverages with a decrease in spot size, as is evident from the 16 Å film. The significant broadening of the LEED spots at low coverages is an indication of the presence of disorder in the Cr films, and strain from trying to fit the substrate. However as the thickness increases the films become more ordered, and at high coverages the Cr film is more or less bulk-like as the interaction with the Pd substrate is no longer in effect, and the topmost layers no longer have to fit the substrate lattice. The structural relationship between the bcc(001) and fcc(001) surfaces is shown in Figure 3.1(d). There is a 4.5% misfit between bcc Cr (a_0 = 2.88 Å) and fcc Pd (a_0 = 3.89 Å, a = 2.75 Å), 'a' being the primitive surface unit cell side, and the unit cell of Cr is rotated by 45° with respect to the underlying Pd(001) substrate.

There are several studies of Cr film growth on (100) surfaces reported in the literature. A SEXAFS study of ultrathin Cr films on Pd(001) is reported by Cook et al. [59]. Films with thickness between 1 and 20 ML were grown at three different substrate temperatures of -123 °C, 27 °C, and 127 °C. They observed that the substrate temperature made no difference in the growth mode of the Cr films, and proposed the growth to be layer- by-layer. They also studied the Cr films at three different thicknesses of < 3 ML, between 3 ML and 6 ML, and > 6 ML. Films grown with a thickness > 6 ML were found to be bcc with no change in phase observed after annealing to ~227 °C. Films with a thickness between 3 and 6 ML were reported to have bcc structure which after annealing bore a strong resemblance to that of the fcc Pd(001) SEXAFS spectra. Films grown with a thickness < 3 ML were reported to be fcc both before and after annealing to ~227 °C. They attributed the formation of the fcc phase at the lowest coverages (< 3 ML) and between 3 and 6 ML thickness after annealing to the formation of a Cr-Pd surface alloy with an fcc structure within the first layer. Studies on the epitaxial growth of chromium on other (001) surfaces have also been reported [60-62]. Steadman et al. [60] report a study, using surface x-ray diffraction, of the growth of ultrathin Cr films on Ag(001) at substrate temperatures between -173 °C and 197 °C, and found that the growth of the films was highly sensitive to the variation in the substrate temperature. At low temperatures (around -173 °C) and between 2 ML and 5 ML, they observed a poorly ordered layer-by-layer growth mode of the Cr film on the substrate. At room temperature,

a disordered growth mode was found, and this was attributed to progressive roughening of the growing layer. In contrast, the growth at higher temperatures (around 157 °C) was found to be more complex. For the high temperature growth, they proposed a model in which initial growth of the film involved the formation of a bilayer on top of the Ag substrate followed by an overcoating of the initial Cr islands with Ag. In addition, subsequent growth would involve growth of Cr monolayers with some intermixing between the Cr overlayer and the Ag atoms that diffused vertically to reduce surface energy. The growth of ultrathin Cr films on Cu(001) over the temperature range of 12-302 °C is reported by Lawler et al. [61]. Film formation was studied using scanning tunneling microscopy, Auger electron spectroscopy, and low-energy electron diffraction. The LEED patterns for all the films exhibited the presence of only the (1x1) surface structure. From STM and AES studies it was observed that 0.6 ML-3.0 ML Cr deposition at 12 °C led to three-dimensional growth with the formation of irregular multilayer islands of varying sizes (2-15 nm). For film growth at elevated temperatures of 152 °C and 302 °C, a reduction in the number of islands and an increase in their size and height was observed, implying more particulate formation of Cr. This type of formation of particulate features was also observed for films deposited at 12 °C and subsequently annealed at elevated temperatures. The phenomenon was attributed to an increase in interlayer mass transport, as annealing caused agglomeration of the films to become more particulate in form.

3.2.2. Sample Preparation. The chromium-oxide films were deposited using two different techniques – the multilayer and the sequential deposition techniques.

3.2.2.1 Multilayer growth of chromium-oxide film. Samples of Cr_xO_y films were prepared in the UHV chamber with a base pressure of approximately $1x10^{-10}$ Torr. Prior to being mounted onto the sample holder, the substrate was cleaned with acetone and methanol. Inside the UHV chamber, the substrate was cleaned by Ar^+ sputtering (20 mA emission current, 1.5 kV beam voltage) for 15 minutes at an argon partial pressure of $2x10^{-5}$ Torr, and then the substrate was annealed at 420 °C for 30 minutes. Surface carbon contamination of the sample was observed from XPS, and LEED — a c(4x2) pattern was observed. Somorjai [11] has reported this LEED pattern to result from surface carbon contamination of Pd(001). This kind of surface contamination observed

after sputtering has also been reported by others [63-64]. This carbon contamination was eliminated by heating the Pd sample at 150-200 °C in an ambient oxygen environment at a partial pressure of $5x10^{-7}$ Torr for 2 minutes [65]. This procedure led to a clean Pd surface as determined by XPS and a well-ordered sharp p(1x1) LEED pattern.

Multilayer Cr films were first deposited at room temperature on the clean Pd(001) substrate at a rate of approximately 0.5 ML per minute. However, it was not possible to obtain ordered oxide samples by first oxidizing Cr films at room temperature and then annealing the oxide films to 420-450 °C after metal film deposition. Oxidation at room temperature yielded samples of very poor quality and order. Also, the quality of the multilayer Cr films deposited on Pd(001) deteriorated rapidly with thickness. As such, Cr was deposited at an elevated substrate temperature of around 300 °C, and the sample temperature was maintained at 300 °C during oxidation with an oxygen partial pressure of $2x10^{-5}$ Torr for 5 minutes. The oxidized sample was then annealed at 490-500 °C for 30 minutes to get an ordered film. 99.2% pure Cr, and Matheson 99.995% purity O_2 were used for Cr_xO_y film growth. The maximum pressure during evaporation of Cr was $\leq$ $5x10^{-9}$ Torr. A water-cooled Leybold Inficon XTM/2 thickness monitor was used to measure the metal deposition rate and to estimate the thickness of the epitaxial film. Film thickness was also determined by measuring the attenuation of the Pd $3d_{5/2}$ photoemission signal and using the TPP formula proposed by Tanuma, Powell and Penn [66] for electron inelastic mean free paths to calculate the thickness of the Cr_xO_y epitaxial films.

XPS data was taken using Mg K_α radiation ($h\nu$ = 1253.6 eV) and an electron energy analyzer angular acceptance of ±8°. All measurements were made with the samples at room temperature. The sample manipulator is equipped with x, y, and z movement and rotation of both polar angle (θ), and azimuthal angle (φ). The sample manipulator is capable of 360° polar angle rotation and ~200° azimuthal rotation, with an angular resolution of ±1° for polar rotation and approximately ±0.5° for azimuthal rotation. XPD data was taken at an analyzer angular acceptance of ±1°. XPD scans were obtained for Cr 2p core level (Cr $2p_{3/2}$ binding energy = 574 eV, Cr $2p_{1/2}$ binding energy = 584 eV) and , and O $KL_{23}L_{23}$ Auger level. From the XPS spectra for clean Pd(001) and Cr_xO_y film (Figure 3.2) it can be observed that the O 1s (binding energy = 531 eV)

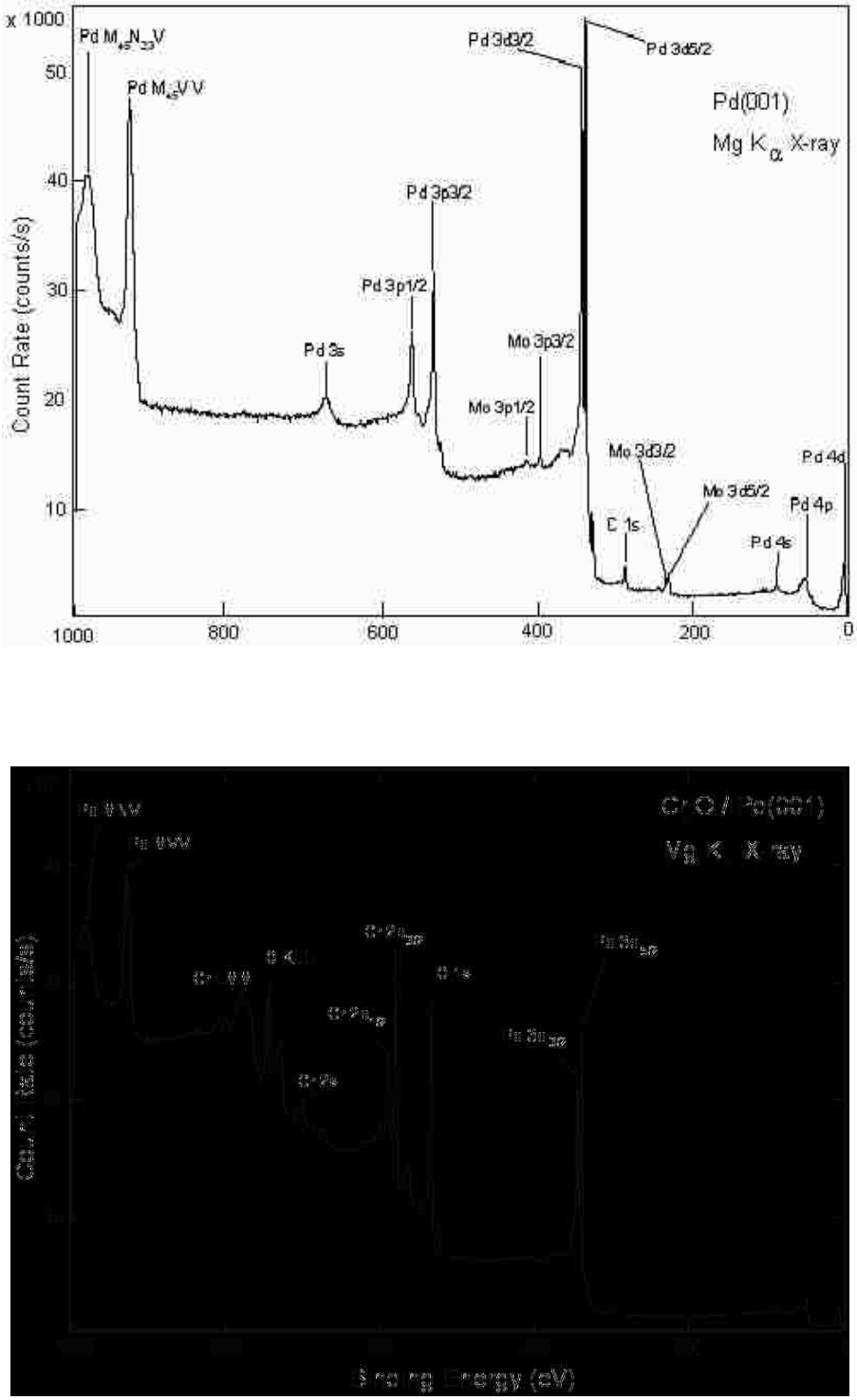

Figure 3.2. XPS survey from clean Pd(001) substrate (top) and from a 15 Å Cr_xO_y film (bottom).

overlaps with the Pd $3p_{3/2}$ core level (binding energy = 533 eV), and as such it was not possible to obtain XPS and XPD data for the O 1s peak. The integrated area of these energy levels after proper background subtraction was used to generate XPD polar and azimuthal curves.

3.2.2.2 Sequential growth of chromium-oxide films. The second method of growing chromium-oxide is the sequential deposition method. Sequentially deposited chromium oxide films were grown on a clean Pd(001) substrate using thermal evaporation. Samples were prepared by repeated cycles of 0.5 ML or less chromium deposition at 300 °C substrate temperature, followed by oxidation. The Cr films were oxidized for 5 minutes at $2x10^{-5}$ Torr oxygen partial pressure and 300 °C substrate temperature in each cycle. This was followed by annealing for 1 minute at temperatures of 400-420 °C initially. This process was repeated until the desired film thickness was achieved. The final oxidized samples were then annealed at temperatures of 400-420 °C. This process was repeated until the desired film thickness was achieved. As will be discussed in detail in Section 3.2.5.2, stable LEED patterns were not observed for the oxide films when the substrate was cooled to room temperature after the anneal at 400-420 °C. The idea was then to grow another set of Cr_xO_y films annealed to higher temperatures of 490-500 °C to observe whether stable films are obtained or not. The same process of repeated cycles of metal deposition and oxidation at elevated temperatures was followed as before. The final oxidized samples of desired thickness were then annealed at of 490-500 °C for about 15 minutes. Film thickness was determined by measuring the attenuation of the Pd $3d_{5/2}$ photoemission signal from the sample.

XPS and XPD data were taken using Mg K_α radiation ($h\nu$ = 1253.6 eV). The integrated area of these peaks after proper background subtraction was used to generate polar and azimuthal XPD curves. LEED studies of chromium oxide films were performed on oxide films ranging in thickness from 3 Å to 23 Å.

3.2.3. Chromium-Oxide Film Thickness Determination. The intensities of the emitted photoelectron signal from the overlayer and the substrate can be used to calculate the thickness of the epitaxial Cr_xO_y film. The attenuation of the Pd $3d_{5/2}$ photoelectron signal was monitored as a function of the oxide film coverage. Assuming a layer-by-layer

growth mode for the epitaxial Cr_xO_y film, the attenuation of the substrate photoemission signal will be represented by a simple exponential decay. The photoelectron intensity and the thickness of the overlayer film are related by:

$$I^s = I_0^s \exp(-x/\lambda_s) \tag{3.1}$$

The intensity from the clean Pd substrate is I_0^s, and the intensity from the substrate covered by the overlayer is I_s. Ideal exponential decay is possible only for a layer-by-layer growth of the overlayer, and as such the calculated oxide coverages are only rough estimates – this is true for both the oxide deposition methods used. Figure 3.2 shows the XPS survey scans of the clean Pd surface (top curve) and from a 15 Å Cr_xO_y film on the Pd(001) substrate (bottom curve). The most intense peaks of Pd are at binding energies of 335 eV and 340 eV and correspond to the Pd $3d_{5/2}$ and Pd $3d_{3/2}$ core levels, respectively. Equation 3.1 was used to determine the thickness of the Cr_xO_y films. Figure 3.3 shows the exponential attenuation curves of the Pd substrate signal as a function of Cr film thickness and chromium oxide film thickness. Both the curves are consistent with layer-by-layer growth. However the inelastic mean free path for Pd $3d_{5/2}$ electrons with kinetic energy of ~919 eV (Mg K_α excitation) is approximately 17.09 Å, which is much larger than the interlayer separations of the ultra-thin oxide film samples. This attenuation plot, therefore, does not necessarily reflect the actual experimental film growth mode, and the thicknesses provided should be viewed only as approximate coverages.

3.2.4. Film Morphology and Composition. XPS can provide information on the chemical composition, morphology, and valence of Cr in the growth of Cr_xO_y samples. One of the key questions in the surface analysis of oxide compounds is the chemical state of the active metal ions on the surface. For transition metal oxides, chemical state analysis is often complex, and a reliable quantitative determination requires a detailed analysis of the photoelectron spectrum. Chemical shifts are, of course, observed in XPS lines - sometimes very small (2 eV or less) and sometimes dramatically significant (10 eV or more). The information about the degree to which a metal film has been oxidized can be obtained through an analysis of the chemical shifts observed in the XPS spectrum

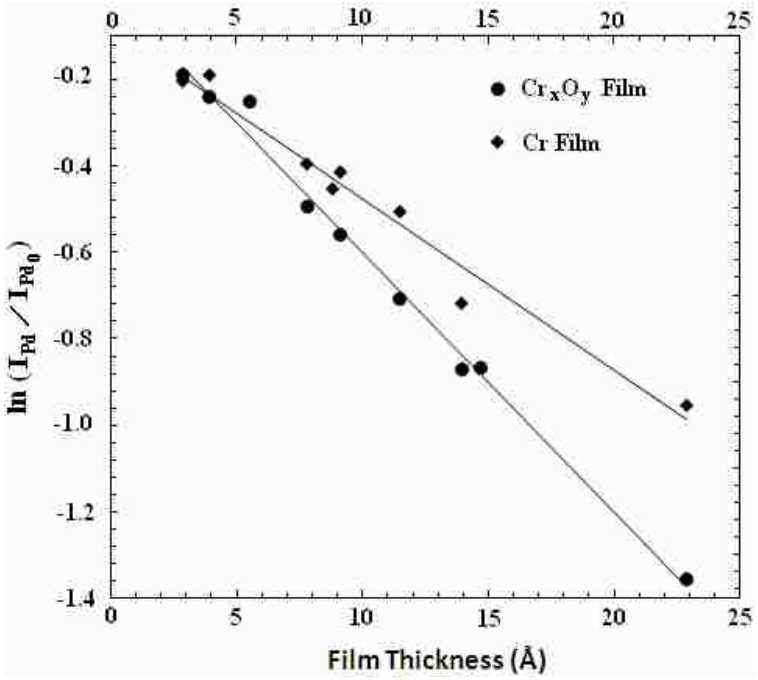

Figure 3.3. The attenuation of Pd 3d photoemission intensity for the chromium oxide film (circles) and for chromium film growth (diamonds).

of the oxide sample. Table 3.1 shows a list of binding energies for the Cr $2p_{3/2}$ core level in different chromium oxide compounds, and it can be seen that in all cases the binding energy shifts for the Cr $2p_{3/2}$ core level observed in the oxide compounds as compared with chromium metal is close to 3 eV for the Cr^{3+} oxidation state, and around 2 eV for the Cr^{2+} oxidation state [52-53, 67-68].

Table 3.1. List of Cr $2p_{3/2}$ Binding Energies in Various Chromium Oxide Compounds

Chromium compound/ion	Cr $2p_{3/2}$ BE (eV)	BE shifts as compared with Cr metal
Cr_2O_3 as single crystal	576.96	2.94
ref. [68]Cr^{3+}	577.2	3.2
ref. [67], [52], [53]Cr^{3+}	577	2.8
ref. [67], [52], [53] Cr^{2+}	576	1.8

For the Cr_2O_3 single crystal, the binding energy shift due to the Cr^{3+} oxidation state is 2.94 eV. For Cr metal, the binding energies for the Cr $2p_{3/2}$ level and for the Cr $2p_{1/2}$ level are 574 eV and 584 eV respectively. In Figure 3.4, similar binding energy shifts of approximately ~ 3 eV can be observed for both Cr $2p_{3/2}$ and Cr $2p_{1/2}$ core levels for the thicker Cr_xO_y samples (15-29 Å). This is an indication of the presence of Cr^{3+} oxidation state in the chromium-oxide samples, though that does not rule out the existence of the Cr^{2+} oxidation state. For the 7 Å thick film, a prominent shoulder on the lower binding energy side of the Cr $2p_{3/2}$ peak (at metallic Cr binding energy) suggests incomplete oxidation of the Cr film. The binding energy separation of the Cr^{2+} and Cr^{3+} oxidation states has been reported to be ~1 eV [52, 53]. Equation 2.20 gives the value for finite energy resolution of the analyzer, ΔE_a. For the *High Magnification* operating mode of the electron energy analyzer, the energy resolution is around ~1.57 eV, and for the *Low Magnification* operating mode the current energy resolution of the electron analyzer is ~0.62 eV. In theory, line width ΔE of a single oxidation state observed in an XPS spectrum is a convolution of three components:

$$\Delta E = \sqrt{\Delta E_n^2 + \Delta E_p^2 + \Delta E_a^2} \tag{3.2}$$

Here ΔE_n is the natural line-width of the core level, ΔE_p is the width of the photon source, and ΔE_a is the analyzer resolution width. The x-ray photon line width for standard Mg K_α source is 0.7 eV, and the natural line width for the Cr 2p core level is around 0.29 eV. This gives ΔE values of ~1.75 eV and ~1 eV for the Cr 2p core level in the *High Magnification* and *Low Magnification* operating modes respectively. Hence, it is quite challenging to resolve the different peaks of Cr^{3+} and Cr^{2+} if both the oxidation states are present in the sample. As such the ~2 eV binding energy shift for the Cr 2p core-level peaks, which will correspond to the Cr^{2+} oxidation state from the Cr metal, is difficult to observe. However, the development of a shoulder (Figure 3.4) on the low binding energy side of the 2p peaks in the oxide sample could be an indication that there are Cr^{2+} ions present too.

XPS measurements for core-level electrons in cations of transition series insulators also commonly show shake-up satellite features in the vicinity of the main

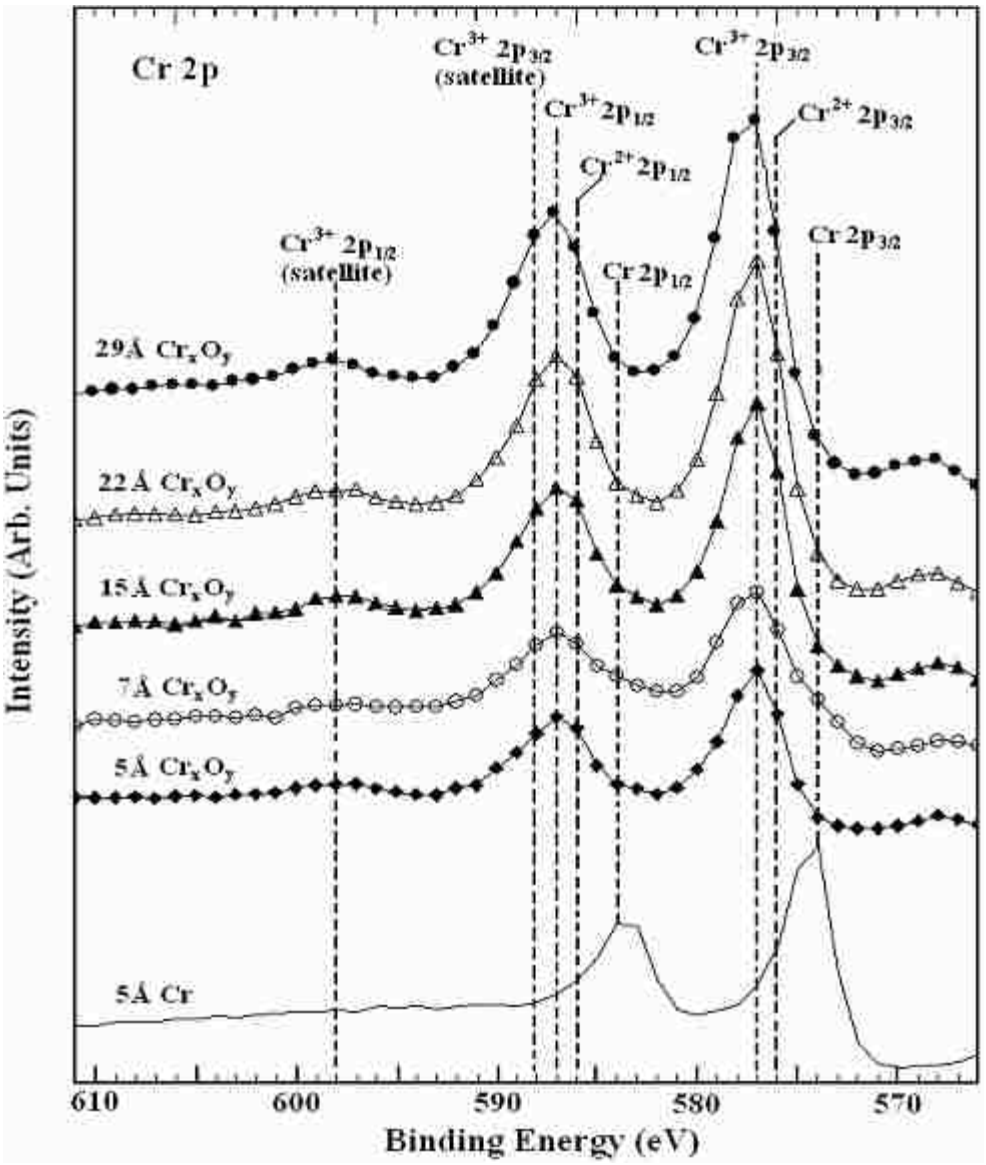

Figure 3.4. Cr 2p XPS as a function of oxide film thickness. The observable shake-up satellites are consistent with the presence of Cr^{3+} in these films.

photoelectron peaks caused by the configuration interaction due to relaxation of the valence electrons. Chromium is the first element of the transition series to show a satellite. The analysis of the energy separations between the photoelectron main-line and these shake-up satellite structures can provide information on the different chemical environments of the ions in the compound, and the sensitivity to chemical change can be

monitored in the observed. main-line to satellite separation. For the Cr 2p core-level these shake-up satellites are seen as discrete peaks on the low kinetic energy (high binding energy) side of both of the 2p peaks. The separation between the 2p main peaks and the satellites for Cr^{3+} has been reported to be of the order of 11 eV [69, 70]. Aronniemi et al. [70] also studied the effect of three background subtraction methods on the analysis results for Cr_2O_3, Fe_2O_3, and Fe_3O_4. Table 3.2 shows some of the results obtained by Aronniemi et al. for chromium oxide.

Table 3.2. Results of the Cr 2p Curve Fit

	"Tougard"[70] for Cr^{3+}	"Seah"[70] for Cr^{3+}	"Shirley"[70] for Cr^{3+}
BE $2p_{3/2}$ (eV)	576.5	576.5	576.5
BE $2p_{3/2}$- BE $2p_{1/2}$ (eV)	9.9	9.8	9.9
$2p_{3/2}$ satellite shift	11.6	11.5	12.0
$2p_{1/2}$/ $2p_{3/2}$ intensity ratio	0.54	0.55	0.40

Referring to Figure 3.4, the binding energy for the Cr $2p_{3/2}$ level is 577 eV, and for the Cr $2p_{1/2}$ level it is 587 eV. The spin-orbit splitting between the Cr $2p_{3/2}$ and the Cr $2p_{1/2}$ core level in the chromium oxide sample is 9.8 eV. In the case of Cr metal, the shake-up satellite of the Cr $2p_{3/2}$ strongly overlaps the Cr $2p_{1/2}$ peak, and for the chromium oxide samples the case should be no different. In addition, these peaks cannot be experimentally resolved due to the 1 eV energy resolution limit of the apparatus. As such the only observable shake-up satellite in the XPS spectrum of the chromium oxide sample is for the Cr^{3+} $2p_{1/2}$ peak, for which the shift of the Cr^{3+} $2p_{1/2}$ satellite from the Cr $2p_{1/2}$ main line is 11 eV. The $2p_{1/2}$/ $2p_{3/2}$ intensity ratio calculated for the Cr_xO_y film was found to be 0.51 after a Shirley background subtraction. All these are indications of the presence of Cr^{3+} ions. For the Cr^{2+} oxidation state, the Cr 2p satellite separation from the

main line is ~ 13 eV [69]. Again, due to the fact that there is some broadening due to the overlapping of shake-up satellites with the main line peaks and the fact that these peaks have very low intensities, discerning the 2p satellite positions for Cr^{2+} ions is extremely difficult. Thus, the XPS spectrum, under the current experimental conditions, provides insufficient information to definitively determine the precise Cr^{3+}:Cr^{2+} ratio in the oxide film. To further address this issue, XPD and MSCD calculations have been carried out to explore the structure of these chromium oxide surfaces.

3.2.5. LEED Results for Cr_xO_y Film Growth on Pd(001). This section presents the LEED results for the chromium-oxide samples obtained from the two deposition methods.

3.2.5.1 Films grown using the multilayer deposition technique. The LEED patterns for the clean Pd substrate and the Cr_xO_y films grown on Pd(001) are shown in Figure 3.5. The LEED pattern for clean Pd(001) is shown in Figure 3.5(a), and Figures 3.5(b), (c), and (d) show the photographs of the LEED patterns obtained from 2 Å, 7.3 Å, and 23 Å thick chromium oxide films respectively. These films were grown on Pd(001) using the multilayer deposition technique. All the LEED patterns were recorded using a primary electron beam energy of 72 eV and at room temperature. Figure 3.5(a) exhibits a sharp p(1x1) LEED pattern for the clean substrate with low background intensity. Figures 3.5(b), (c) and (d) all exhibit a p(1x1) LEED pattern for the overlayer with respect to the Pd(001) substrate. The LEED patterns do not change with film coverage, however the diffuse background intensity increases at higher film coverages (Figure 3.5(d)). The consistent p(1x1) LEED pattern of the overlayer at all coverages is an indication of a strong interaction between Pd and the oxide overlayer.

3.2.5.2 Films grown using the sequential deposition technique. For the films grown using the sequential deposition technique, room temperature deposition and oxidation of Cr films only led to disordered films and no LEED patterns were observed. Films were annealed at two different temperature ranges of 400-420 °C and 490-500 °C, and two different kinds of observations were made for these two annealing temperature ranges.

Figure 3.6 shows the diffraction patterns for clean Pd and the chromium-oxide films grown on Pd(001). Figures 3.6(a), (b), (c), and (d) show the LEED patterns for

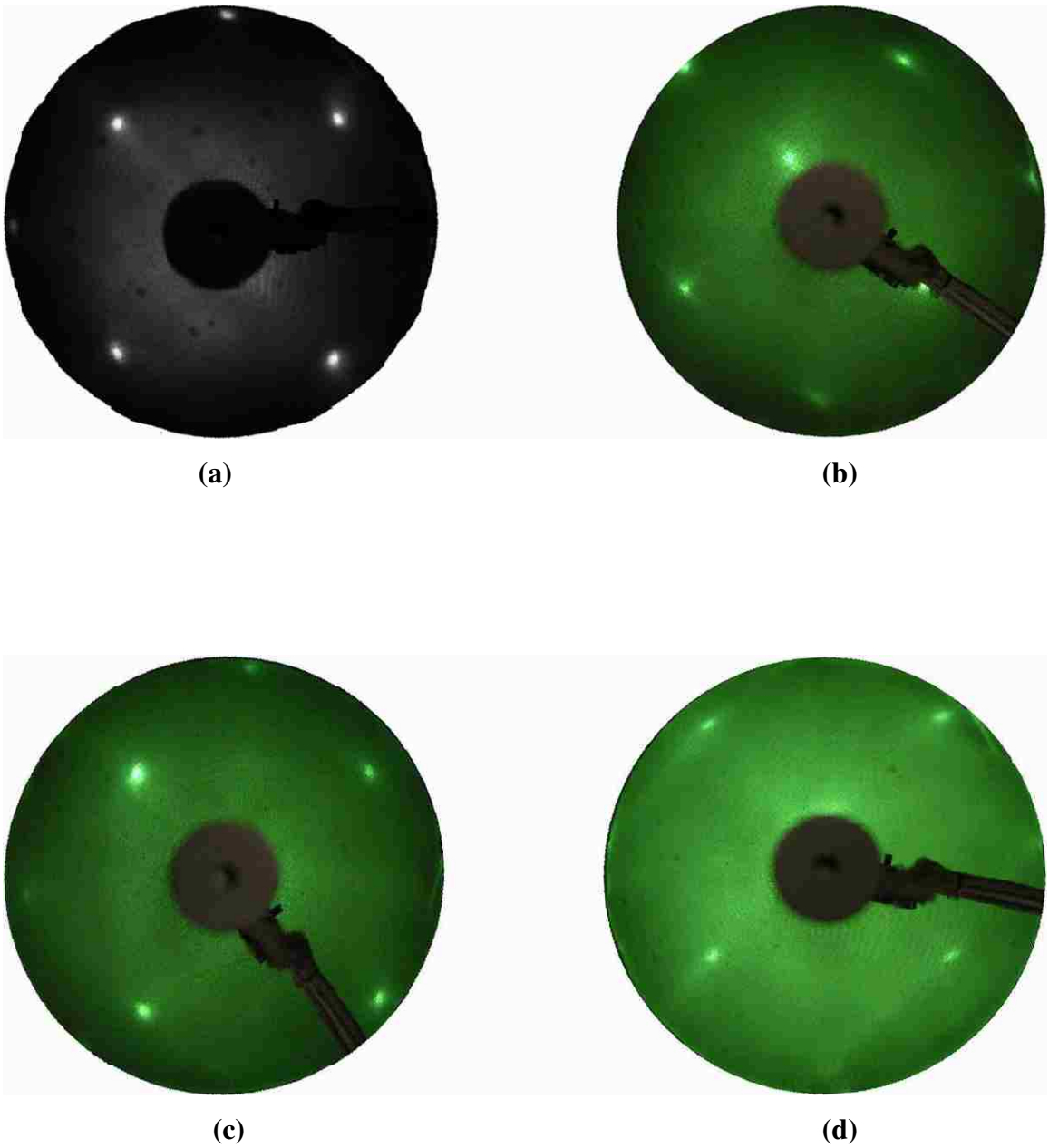

(a) **(b)**

(c) **(d)**

Figure 3.5. LEED patterns for Cr_xO_y films grown by multilayer deposition technique: (a) clean Pd(001), (b) 2 Å thick Cr_xO_y film, (c) 7.3 Å thick Cr_xO_y film, and (d) 23 Å Cr_xOy film at primary electron energy of approximately 72 eV.

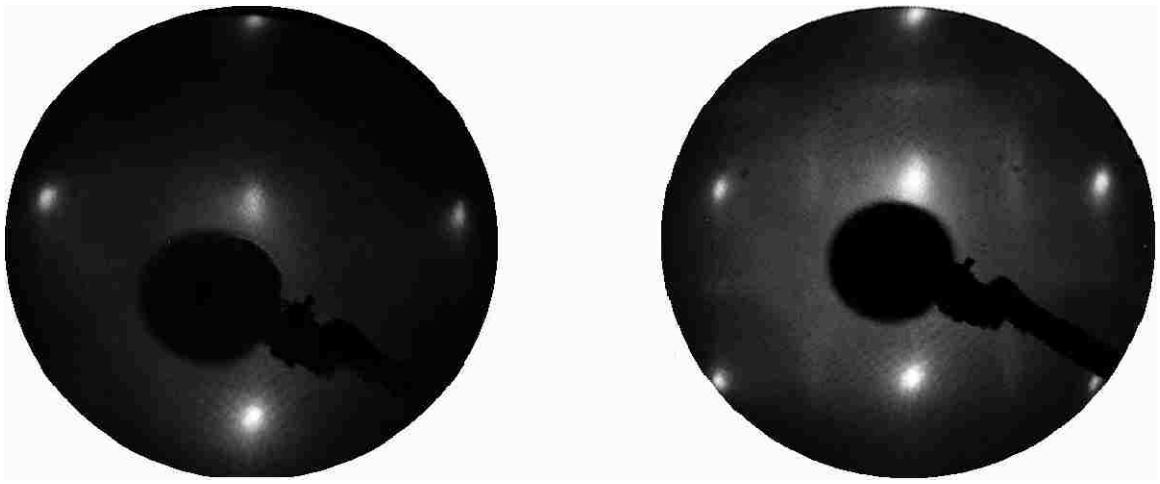

(a) **(b)**

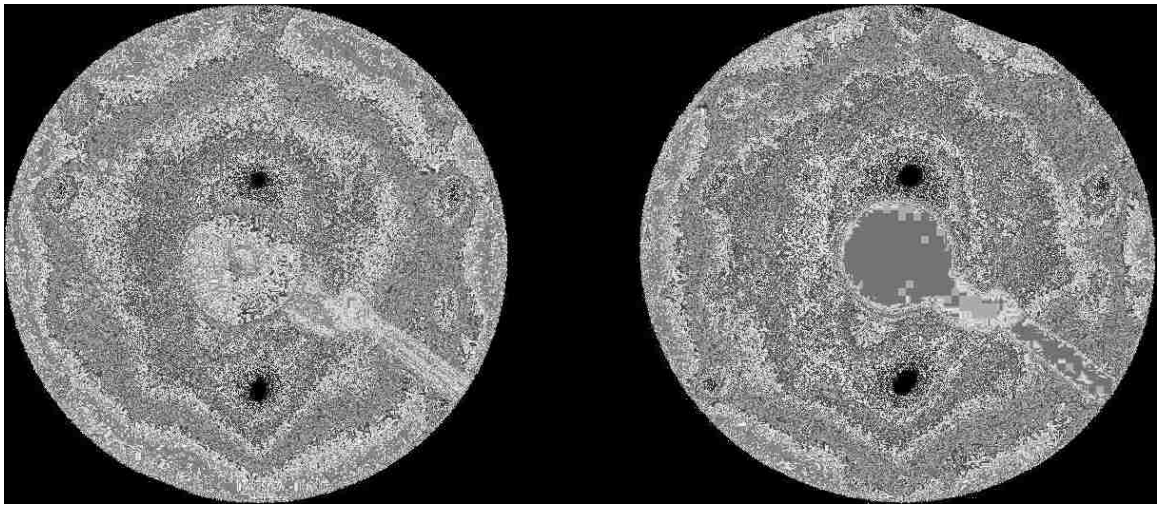

(c) **(d)**

Figure 3.6. LEED patterns for Cr_xO_y films grown by sequential deposition technique: (a) clean Pd(001), (b) 2.2 Å thick Cr_xO_y film, (c) 4 Å thick Cr_xO_y film, (d) 6 Å Cr_xO_y film, at primary electron energy of approximately 63 eV.

for clean Pd(001), and 2.2 Å, 4 Å, and 6 Å Cr_xO_y films respectively at a primary electron energy of approximately 63 eV. These oxide films were annealed at 400-420 ºC. The oxide films with coverages around 2 Å (Figure 3.6 (b)) have a streaked LEED pattern indicating that oxide island growth, as well as step and terrace formations. By 4 Å (Figure 3.6(c)), slightly broadened spots appear indicating increased disorder. At around coverages of 6 Å (Figure 3.6(d)), the LEED pattern develops dramatically and beams that are well ordered are observed with appreciable intensity, implying a crossover point at which the films start growing with marked order.

This pattern has a c(4x2) overlayer orientation with respect to the Pd(001) substrate. However the c(4x2) structure is unstable, and the LEED pattern changes and deteriorates within a span of a few hours after the annealing. Figure 3.7 charts the deterioration over time of the LEED pattern for the sequentially deposited films that were annealed at 400-420 °C. Figure 3.7(a) shows the LEED pattern immediately after annealing, and it shows well ordered LEED beams. After 45 minutes (Figure 3.7(b)) however, the pattern changes to a c(2x2) which is also well-ordered with sharp LEED spots. After 75 minutes (Figure 3.7(c)) streaks develop in the c(2x2) pattern, and the streaking becomes more pronounced after 2 hours (Figure 3.6(d)) and the LEED spots become less distinct. By 2.5 hours (Figure 3.7(e)), the complex overlayer LEED pattern has disappeared and is replaced by a p(1x1) pattern. Finally, after 18 hours (Figure 3.7(f)), the LEED pattern looks deteriorated with poor intensity. It looks like a (4x4) but has not developed into either a p(4x4) or a c(4x4) as additional spots are missing. After 20 hours, there was almost no LEED pattern visible, implying complete disorder.

For the oxide films annealed at 490-500 °C, the LEED patterns were indiscernible and blurry, and also changed with time, as shown in Figure 3.8. Figure 3.8(a) shows the LEED pattern from clean Pd(001), and Figures 3.8(b), (c) and (d), and (e) show the photographs for the LEED patterns obtained from 6.5 Å, 11 Å, and 17 Å thick chromium oxide films respectively. At 6.5 Å (Figure 3.8(b)), the faint LEED pattern for Cr_xO_y film shows blurry and streaked spots, and even after the film thickness has been increased to 11 Å (Figure 3.8(c)), the streaking remains and the LEED pattern does not improve and resolve into a clearer pattern. When the 11 Å film (Figure 3.8(d)) is left undisturbed for

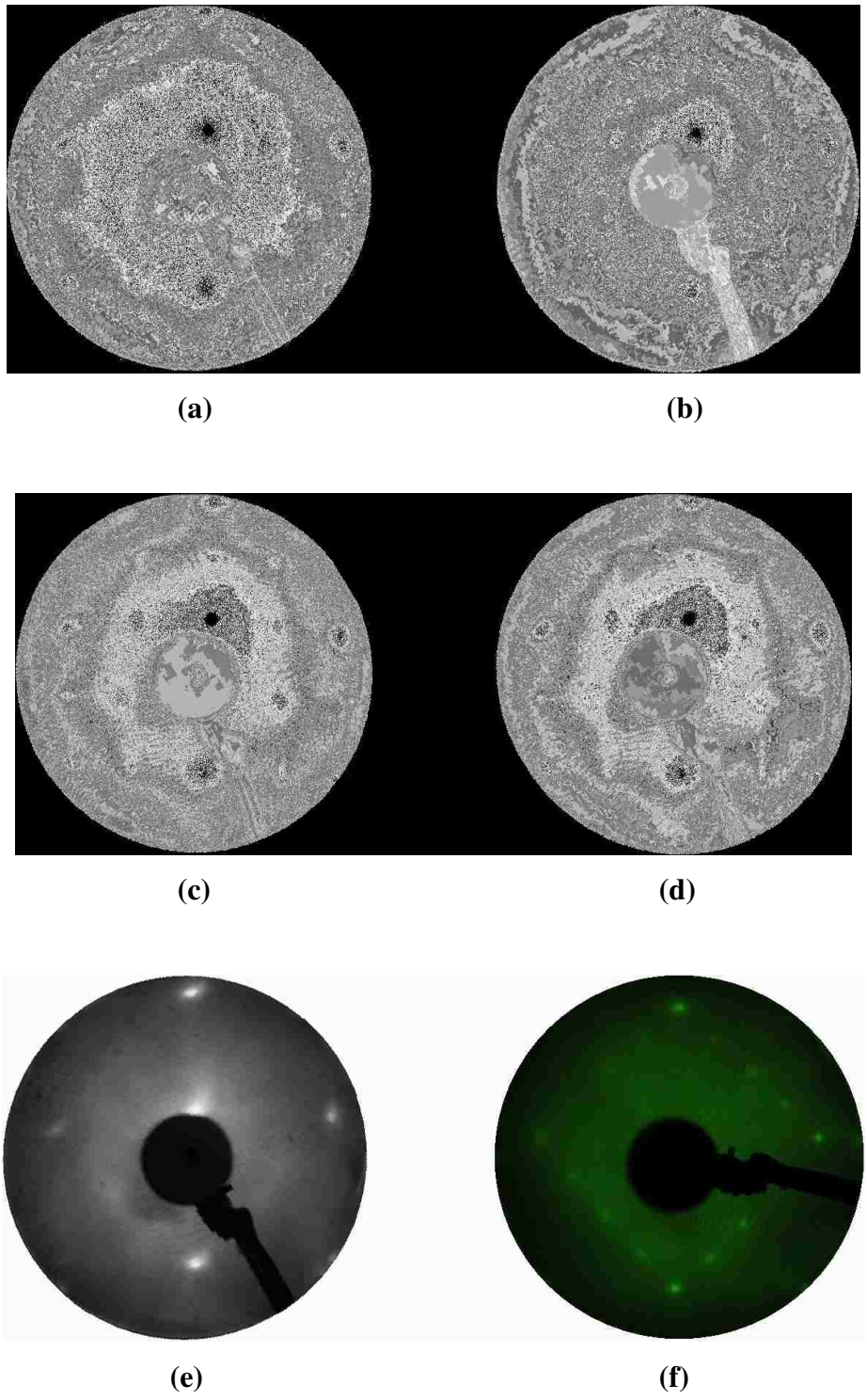

(a) **(b)**

(c) **(d)**

(e) **(f)**

Figure 3.7. LEED patterns for a 7 Å thick Cr_xO_y film grown by sequential deposition technique at electron energy of approximately 64 eV after: (a) annealing (b) 45 minutes, (c) 75 minutes (d) 2 hours (e) 2:5 hours (f) 18 hours.

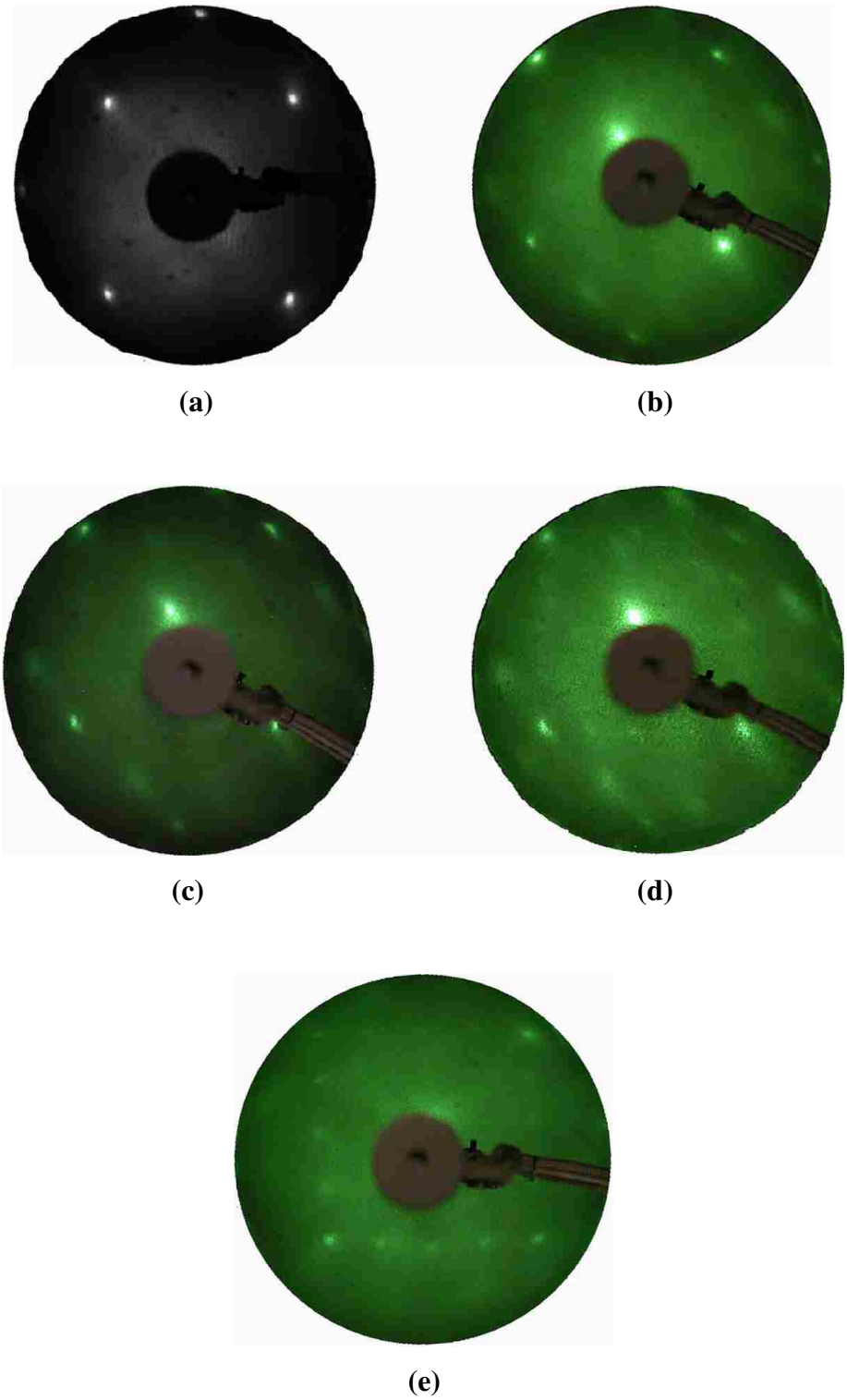

Figure 3.8. LEED patterns for Cr_xO_y films grown by sequential deposition technique: (a) clean Pd(001), (b) 6.5 Å, (c) 11 Å, (d) 11 Å (after 24 hours) (e) 17 Å thick Cr_xO_y film, respectively, at primary electron energy of approximately 72 eV.

24 hours, additional spots are observed to have developed afterwards while the pattern still remains streaked. The spots are now brighter but the pattern still remains indistinct and the spots blurry. Finally, when the film thickness is increased to 17 Å (Figure 3.8(e)) and left overnight, the LEED pattern again changes. The pattern has an overall 4-fold symmetry similar to Figure 3.7(f), but it still does not fit any of the known four-fold diffraction patterns. In addition, this phase deteriorates further after a few hours as observed from the LEED pattern, and it was not possible to take any XPD data for even this high coverage film.

From the LEED results, it can be concluded that the chromium oxide phases obtained from the sequential deposition technique are very much temperature sensitive. At lower annealing temperatures of 400-420 °C, the films produced are ordered, but are not stable at room temperature. At higher annealing temperatures of 490-500 °C the film growth is not well-ordered, and also unstable at room temperature. Therefore stable and well-ordered sequentially deposited chromium oxide films could not be obtained, and as such it was concluded that further characterization of these films was not justified.

3.2.6. XPD and MSCD Results. For further investigation of the structure of the chromium-oxide films grown using the multilayer deposition technique, XPD polar and azimuthal scans for the Cr 2p core level and the O $KL_{23}L_{23}$ Auger level were performed for the p(1x1) LEED patterns. Since quantitative LEED I(V) analysis needs to be performed to determine possible lattice structural variations in the sample, and the qualitative LEED analysis in this study does not furnish that kind information, XPD polar scans were conducted in the Pd(100) and Pd(110) scattering planes, for film coverages ranging from 5 Å to 23 Å. Based on LEED and previous studies of Cr_xO_y [50-53, 55, 57], two possible surface structure tests have been made for the chromium oxide structure on Pd(001) grown using the multilayer deposition technique — a CrO(001) surface, and a reconstructed Cr_3O_4(001) surface. There is also a third possibility that the resulting Cr_xO_y overlayer could be a mixed phase of CrO and Cr_3O_4. All three possibilities will be explored in greater detail in the following discussion. Experimental results will be presented for both the low and high coverage oxide phases, and the model calculations for the CrO(001) and reconstructed Cr_3O_4(001) phases, which also the current LEED results do not distinguish between.

The LEED results indicate that oxidation of the Cr(001) films at elevated temperatures followed by annealing results in the formation of ordered surfaces, and no ordered structures are observed for oxidation at room temperature. The attenuation of the substrate photoemission signal can be studied to distinguish the layer-by-layer growth mode from the cluster growth mode, given correct experimental conditions. This is, however, possible only when the inelastic mean free path of the photoelectrons emitted from the substrate is comparable to the interlayer spacing in the film. The inelastic mean free path for Pd $3d_{5/2}$ (kinetic energy ~ 919 eV) for Mg K_α excitation is approximately 17.09 Å, which is much larger than the interlayer separation in the oxide structure. As such, the examination of the attenuation of the substrate signal will more or less produce an exponential decay of the photoemitted signal, which is typical for a layer-by-layer growth, irrespective of the actual experimental growth mode. Consequently this method cannot distinguish between the possible growth modes of the oxide films, and the coverages quoted throughout the discussion are only to be viewed as 'effective coverages'. The XPS results exhibit a chemical shift of the Cr 2p photoemission peaks after oxidation of the Cr films indicating the formation of chromium oxide. The photoemission peaks for the Cr 2p core levels in oxide phase show a significant shift towards the higher binding energy side (~ 2.9 eV) with respect to the metallic Cr 2p line positions suggesting complete oxidation of the Cr film. Among known values, the binding energy shift for the Cr 2p core levels in Cr_2O_3, which contains only the Cr^{3+} oxidation state, from the metallic Cr 2p line positions is ~ 3 eV [25]. Zhang, Kuhn and Diebold [50] observed that the Cr $2p_{3/2}$ feature in their low coverage Cr_3O_4 sample on Pt(111) could be fitted properly using two assigned peaks at 576.5 eV and 577 eV supporting the presence of both Cr^{2+} and Cr^{3+} cations respectively. This would correspond to chemical shifts of ~ 2.5 eV and 3 eV for the Cr^{2+} and Cr^{3+} oxidation states respectively. As discussed earlier in Section 3.2.4, while the determination of the presence of Cr^{3+} ions in the oxide sample is possible, determining whether Cr^{2+} ions are present or not is more challenging due to the limits in the experimental energy resolution

A comparison of the XPD polar angle curves for thicknesses of 23 Å (closed circles) and 5.1 Å (open circles) acquired in the Pd(100) scattering plane is shown in Figure 3.9. Experimental polar XPD scans were carried out in the $\varphi = 0°$ and $\varphi = 45°$

scattering planes with respect to Pd(100) surface (φ = 0° corresponds to the Pd[100] direction, and φ = 45° corresponds to the Pd[110] direction), and compared to model calculations. For the XPD polar scans in the Pd(100) scattering plane, the oxide film thicknesses for the low and high coverage systems are 5.1 Å and 23 Å, respectively. For the XPD polar scans in the Pd(011) scattering plane, the oxide film thicknesses for the low and high coverage films are 7 Å and 16 Å respectively. The left panel shows the Cr 2p results and the right panel shows the O $KL_{23}L_{23}$ results. Other than slight variations in intensity and shape of the individual peaks, there are no appreciable differences in the features of the XPD curves for the low and high coverages, implying that no structural transformation takes place with increasing oxide film thickness.

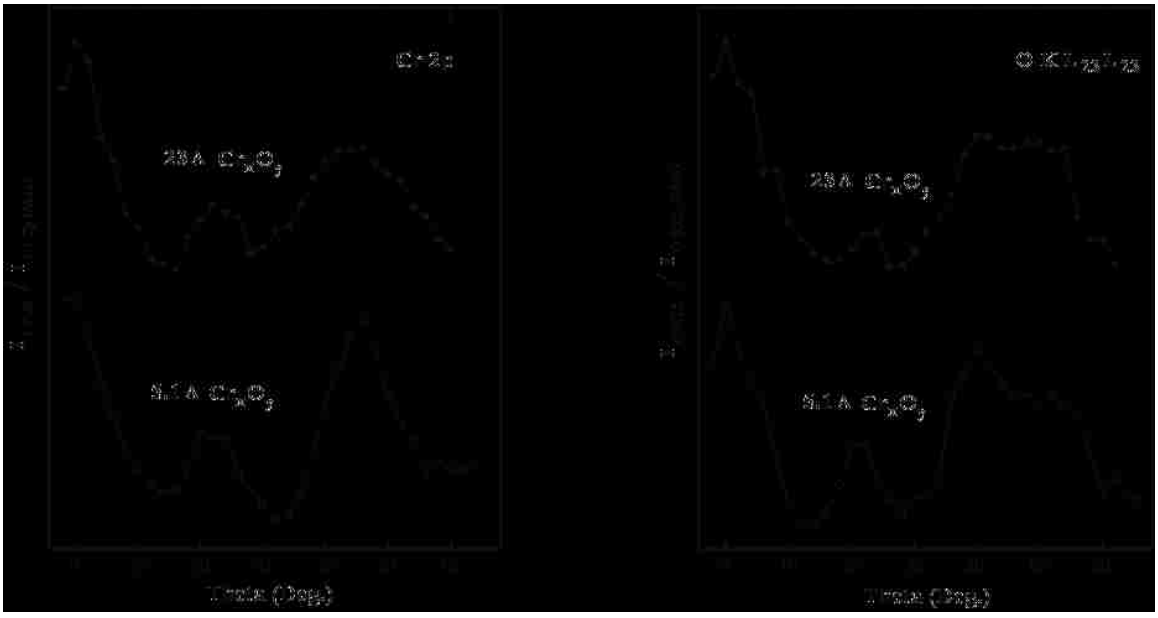

Figure 3.9. XPD polar scans for Cr 2p (left panel) and O $KL_{23}L_{23}$ (right panel) for a chromium oxide coverage of 23 Å (top curve) and 5.1 Å (bottom curve). The scans were acquired for the Pd(001) scattering plane.

Figure 3.10 shows azimuthal XPD scans obtained for the Cr 2p core level and O $KL_{23}L_{23}$ Auger level. The right panel shows data for Cr 2p data and the left panel shows data for $OKL_{23}L_{23}$ data. Both experimental XPD azimuthal scans for polar scattering

angles at θ = 45° for Cr 2p, and at θ = 22° for O $KL_{23}L_{23}$ exhibit photoelectron intensity fluctuations with peaks that are 45° apart, but with apparent four-fold symmetry. The azimuthal scans and the LEED patterns therefore suggest that the Cr_xO_y films have a 4-fold symmetry and cubic structure. In the following sections, discussions on the model calculations and their comparison with the experimental XPD data will follow.

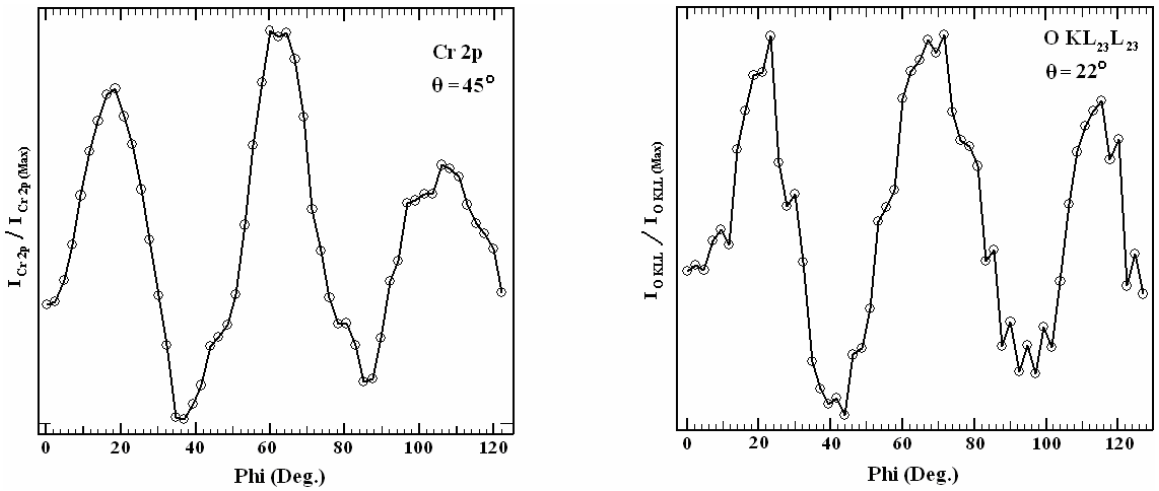

Figure 3.10. XPD azimuthal scans for Cr 2p at polar scattering angle of 45° (left), and for O $KL_{23}L_{23}$ at polar scattering angle of 22° (right).

3.2.6.1 MSCD calculations for CrO(001). No known literature has been found that might give an indication of the existence of CrO as a bulk material in nature. The chemical composition for stoichiometric phases of CrO has one Cr atom and one O atom, and the expected crystal structure for CrO would be rocksalt, since all transition metal monoxides, barring copper monoxide, have this crystal structure arrangement. In the case of bulk ionic oxides such as CrO and VO, the polar surfaces of CrO(111) and VO(111) are inherently unstable due to the divergence of the electrostatic surface potential [13, 52, 71]. Rogojanu [72] described efforts to stabilize CrO as a thin epitaxial film using MBE on three different (100) surfaces – MgO(100), MnO(100), and $SrTiO_3$(100). Using NO_2 gas to oxidize the evaporated chromium beam resulted in the formation of non-stoichiometric chromium monoxide with a substantial amount of

nitrogen built into the films. When O_2 and O_3 gases were used as oxidizing agents at low gas pressure, nearly stoichiometric CrO was formed and the rock salt crystal structure was obtained, but with substantial disorder. For high gas pressures, the CrO showed a rock salt structure with ordered defects. Du et al. [51] did X-ray diffraction studies on the growth of a NaCl-type CrO defect structure on the Mg(001) substrate. The film exhibited a body-centered orthorhombic unit cell rotated by 45° around the c-axis with respect to that of the MgO unit cell, and they observed the out-of-plane lattice constant c of the structure to be 3.892 Å along the MgO[001] direction, with a = 8.94 Å along MgO[110] and b = 2.98 Å along Mg $[\bar{1}10]$. Schmid et al. [73] studied the oxygen-covered Cr(100) surface using STM, quantitative LEED, and low-energy ion scattering. For the CrO structure that they obtained, they did comparison studies with other NaCl-type oxides and nitrides of elements neighboring Cr in the periodic table and estimated that a hypothetical NaCl-type CrO should have a lattice constant of approximately 4.08 Å. Deductions from the growth of CrO on other substrates like Cu(100) and Cu(111) [52, 53, 55] have also led to different lattice constants for the overlayer. For instance, Maetaki et al. [52] estimated the lattice constant for CrO(111), observed at the monolayer coverage, grown on Cu(100) to be 3.01 Å.

Due to such a lack in general consensus over the lattice constant of CrO, it is assumed here that the CrO(001) surface adopts the Pd surface lattice parameters (a_0 for Pd = 3.89 Å), and the overlayer surface mesh to be defined by a_1 = 2.75 Å, a_2 = 2,75 Å, and φ = 90°. Figure 3.11 show the reciprocal and real space lattice representations for the CrO(001) surface. Figure 3.11(a) represents the resultant expected diffraction pattern for the overlayer film on the Pd substrate, and Figure 3.11(b) represents the structural relationship of the overlayer lattice with respect to the substrate fcc lattice in real space. In order to produce the observed LEED pattern, the unit cell of the CrO superlattice is rotated by 45° with respect to the underlying Pd(001) substrate. This CrO(001) surface is non-polar, which means that the surface does not have a divergent surface potential, and all the excess charge on the surface from the cation-derived dangling bonds compensates the anion-derived dangling bonds. Figure 3.12 shows top and side views of CrO(001).

The *Multi-Scattering Calculation of Diffraction* (MSCD) package developed by Yufeng Chen and Michael Van Hove of the Materials Sciences Division of Lawrence

CrO(001) Reciprocal Space CrO(001) Real Space

(a) **(b)**

Figure 3.11. Top views of the CrO(001) surface. Panel (a) is the expected LEED pattern of the overlayer at a_0^{CrO} = 2.75 Å, and (b) is schematic representation of the real space lattice match between surface mesh for the CrO superlattice (filled circles) at a_0^{CrO} = 2.75 Å (in-plane lattice constant of overlayer) and the Pd(001) (open circles) substrate. Open circles represent the substrate lattice, and filled circles represent the overlayer lattice.

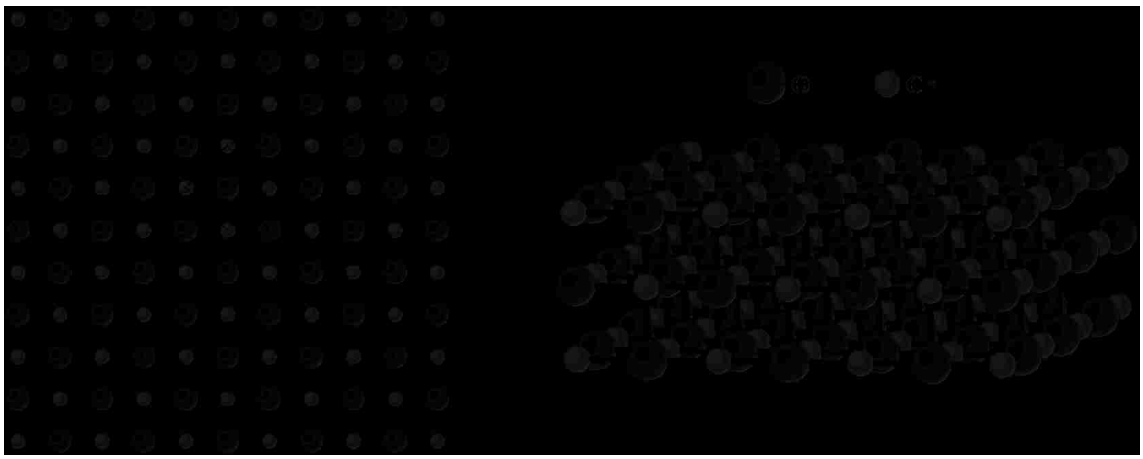

(a) **(b)**

Figure 3.12. Atomic structure of CrO(001). Panel (a) is top view, (b) is side view of the CrO surface.

Berkeley National Laboratory [36] is used for the analysis of the XPD data. MSCD simulations for the $Cr_xO_y(001)$ surface were carried out for the scattering planes corresponding to φ = 0° and φ = 45°, which correspond to the experimental Pd(100) and Pd(110) scattering planes for the polar XPD scans. Cluster sizes of about 55-200 atoms were used for modeling of the oxide surface. To better compare the angle-scanned curves in this work and find the best agreement between experiment and theory, reliability factor calculations were carried out. First the photoemission intensities of different polar and azimuthal angles are normalized to form the χ function,

$$\chi = (I - I_0) / I_0 \tag{3.3}$$

where I is the photoemission intensity at specific polar and azimuthal angles (θ and φ), and I_0 is the background subtracted from the intensity. For polar θ angle-scanned curves, $I_0(\theta)$ is obtained is obtained by using a cubic spline fitting method. The misfit between theory and experiment is then quantified with a reliability factor (R-factor) defined as [73-74],

$$R = \frac{\sum_i (\chi_{ci} - \chi_{ei})^2}{\sum (\chi_{ci}^{\ 2} + \chi_{ei}^{\ 2})} \tag{3.4}$$

where χ_{ci} and χ_{ei} are calculated and experimental χ curves respectively. This R-factor is the sum of R-factors for all polar angles and for both Cr and O. The R-factor calculations involved the investigation of the surface lattice constant of the film (a_0^{CrO}). No known values for the lattice constant of CrO exist in literature. Therefore, for a hypothetical CrO single crystal, an investigation of the film lattice constant was performed in order to see whether the substrate lattice has any influence. For this analysis, a series of calculations were carried out assuming different values of a_0^{CrO} from 2.63 Å (4.4% compression compared to 2.75 Å) to 3.08 (12% expansion compared to 2.75 Å) in steps of 0.03 Å ($\approx 1\%$). For each value of the lattice constant a_0^{CrO}, the scattering phase shifts were calculated by adjusting the muffin-tin radius of the elements in accordance with the

relation, $r_{muf}^{O} + r_{muf}^{Cr} = d_{nn}$, where r_{muf}^{O} and r_{muf}^{Cr} are the oxygen and the chromium muffin-tin radii, respectively, and d_{nn} is the nearest neighbor distance. In addition, the effects of possible interlayer relaxations was also investigated. The separation between the i^{th} and j^{th} layer is defined by d_{ij}. The distances d_{12} and d_{23} were varied simultaneously by keeping d_{13} constant, which had the net effect of moving the 2nd layer between the 1st and 3rd layer. The R-factor calculation as a function of the lattice constant a_0^{CrO} is shown in Figure 3.13, and variation of the R-factor as a function of d_{12} is shown in Figure 3.14.

The variation of the R-factor as a function of the lattice constant (Figure 3.13) shows a minimum for the lattice constant a_0^{CrO} at 2.75 Å, implying that the chromium oxide adopts the surface lattice parameter of the substrate. The simulations for the relaxed surface (at d_{12} = 2.334 Å) do not show any significant difference or improvement from the simulations for the unrelaxed surface (d_{12} = 1.945 Å), and the broad minimum in Figure 3.14 shows that R-factor curve is pretty much insensitive to the variations in d_{12} for a wide range of values around that of the unrelaxed value.

XPD scans for Cr 2p (left panels) and O $KL_{23}L_{23}$ (right panels), and MSCD curves for the CrO(001) structure are shown in Figures 3.15 and 3.16. The top two curves in each figure are experimental results for high and low coverage systems respectively, and the curves below the experimental curves represent results from the model calculations for the CrO(001) surface. For the XPD data in the Pd(100) scattering plane (Figure 3.15), the oxide film thicknesses for the low and high coverage systems are 5.1 Å and 23 Å, respectively. For the XPD data in the Pd(110) scattering plane (Figure 3.16), the oxide film thicknesses for the low and high coverage films are 7 Å and 16 Å respectively. The MSCD curves have also been included for the CrO(001) structure with a surface lattice constant of 2.75 Å, with and without interlayer relaxations incorporated into the MSCD calculations. For the lowest R-factor at d_{12} = 2.33 Å (20% expansion), the MSCD simulations again do not show any significant difference from the bulk value. Based on these results, nothing definitive can be said about the presence or absence of strain in the film.

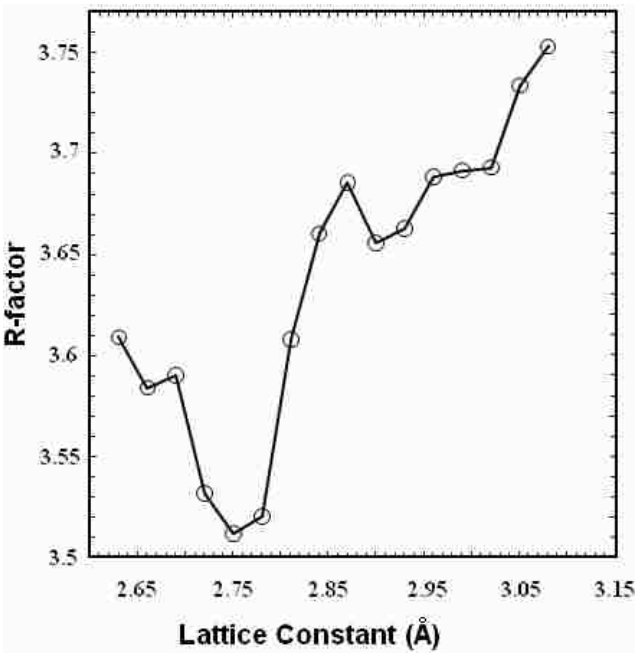

Figure 3.13. Behavior of the total R-factor as a function of CrO surface lattice constant.

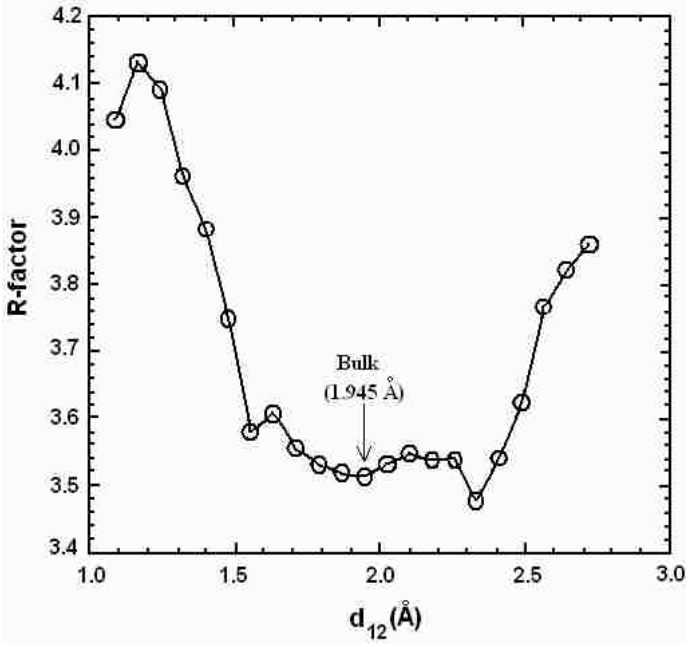

Figure 3.14. Behavior of the total R-factor for CrO as a function of the interlayer spacing d_{12}, for surface lattice constant of 2.75 Å.

High coverage: XPD and MSCD for 23 Å Cr_xO_y in the Pd(100) plane

Low coverage: XPD and MSCD for 5.1 Å Cr_xO_y in the Pd(100) plane

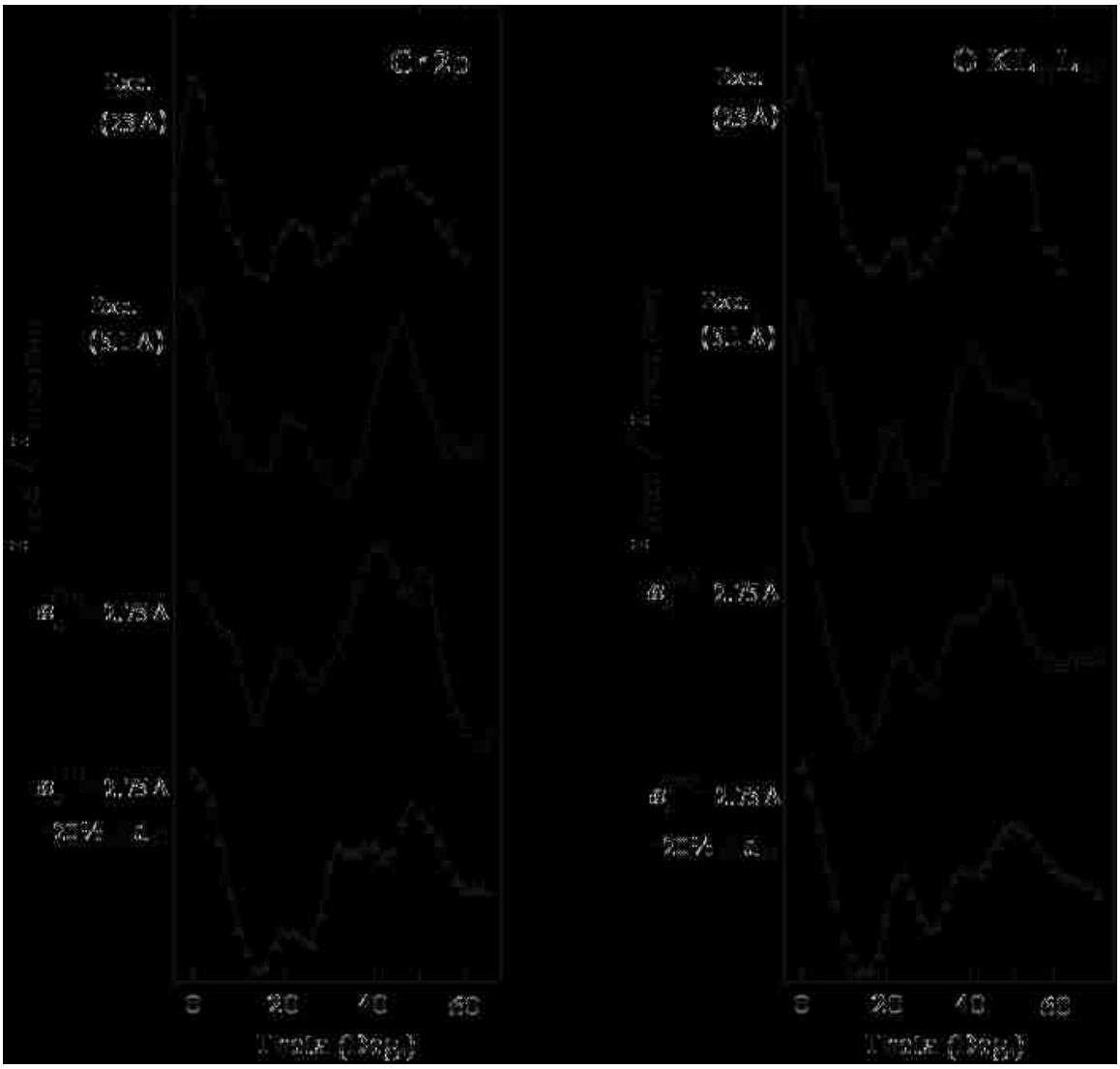

Figure 3.15. Polar scan XPD and MSCD curves for the CrO(001) surface. Results for Cr 2p (left) and O $KL_{23}L_{23}$ (right) are for the scattering plane corresponding to φ = 0°. The top two curves are for the experimental high coverage (filled circles) and experimental low coverage (empty circles) films, respectively. The bottom two curves are MSCD curves (triangles).

High coverage: XPD and MSCD for 16 Å Cr_xO_y in the Pd(110) plane

Low coverage: XPD and MSCD for 7 Å Cr_xO_y in the Pd(110) plane

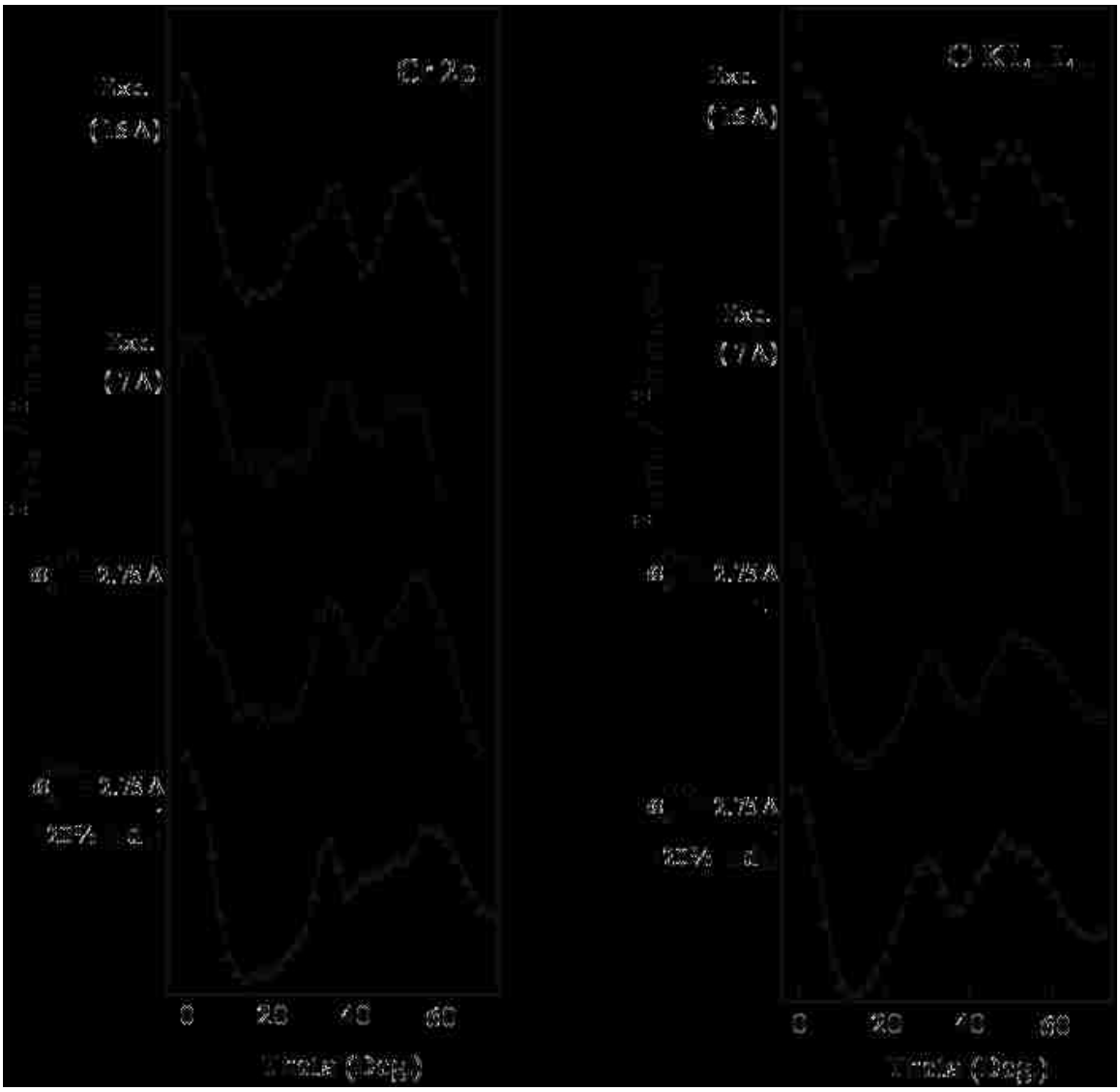

Figure 3.16. Polar scan XPD and MSCD curves for the CrO(001) surface. Results for Cr 2p (left) and O $KL_{23}L_{23}$ (right) are for the scattering plane corresponding to φ = 45°. The top two curves are for the experimental high coverage (filled circles) and experimental low coverage (empty circles) films, respectively. The bottom two curves are MSCD curves (triangles).

3.2.6.2 MSCD calculations for $Cr_3O_4(001)$. The cubic spinel structure of Cr_3O_4, as shown in Figure 3.17, is essentially a cubic close-packing of anions, bound together by suitably placed interstitial cations. The larger oxygen anions form a fcc lattice and the chromium cations occupy tetrahedrally (A type) and octahedrally (B type) coordinated interstitial sites. The valence of the various atoms is described by the chemical formula (Cr^{3+}) $(Cr^{3+}Cr^{2+})$ $(O^{2-})_4$. Half of the Cr^{3+} cations occupy tetrahedral A sites, and the other half reside at octahedral B sites, as do the Cr^{3+} cations. As shown in Figures 3.17(b) and 3.17(c), the structure can also be viewed as a stack of (001) layers containing either oxygen and chromium ions in octahedral B sites or chromium ions in tetrahedral A sites. Within a mixed Cr(B)/oxygen layer, the chromium ions are arranged in rows along the [110] direction, and these rows are rotated in neighboring B layers. Two terminations are possible for the bulk-truncated surface of $Cr_3O_4(001)$. In one termination, the topmost layer consists of oxygen and chromium ions in octahedral B sites located in the same plane (Figure 3.17(c)). In the other termination, the surface can consist of a monolayer of tetrahedral A chromium ions (Figure 3.17(b)). Neither of these terminations is autocompensated, or non-polar. Thus $Cr_3O_4(001)$ tends to reconstruct.

Based on the experimental LEED results, the p(1x1) pattern is possible for a reconstructed B layer. Figure 3.18 shows schematic diagrams for the unreconstructed and reconstructed $Cr_3O_4(001)$ surfaces. The reconstructed $Cr_3O_4(001)$ surface has a square unit cell with a lattice constant of 2.86 Å (Figure3.18(b)), which is also the oxygen interatomic distance. Figure 3.18(c) represents the structural relationship of the overlayer lattice with respect to the substrate fcc lattice in real space – the filled circles represent the Cr_3O_4 superlattice, and the open circles represent the Pd001) substrate – and the surface mesh can be defined by $a_1 = 2.86$ Å, $a_2 = 2.86$ Å, and $\varphi = 90°$. The unit cell of the Cr_3O_4 superlattice is rotated by 45° with respect to the underlying Pd(001) substrate. This surface is fully autocompensated as will be shown. A useful model, particularly for covalent bonded materials, for predicting stable surface terminations is the surface autocompensation model [12]. The most stable surfaces are those in which the excess charge from cation-derived dangling bonds compensates anion-derived dangling bonds. The net result is a zero dipole moment along the surface normal. All stable metal oxide surfaces for which the structure is known fulfill the autocompensation criterion.

(a)

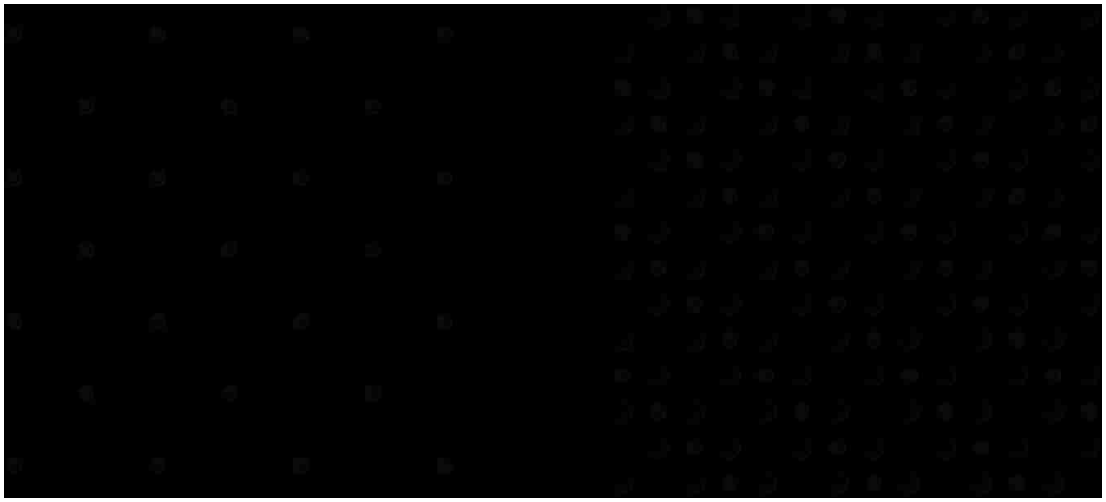

(b) **(c)**

Figure 3.17. Atomic structure of Cr_3O_4(001). Panel (a) is side view, (b) is top view of tetrahedral Cr terminated surface (A-layer), and (c) is top view of the mixed octahedral Cr surface and O surface (B-layer). Filled spheres represent Cr, and white spheres represent O.

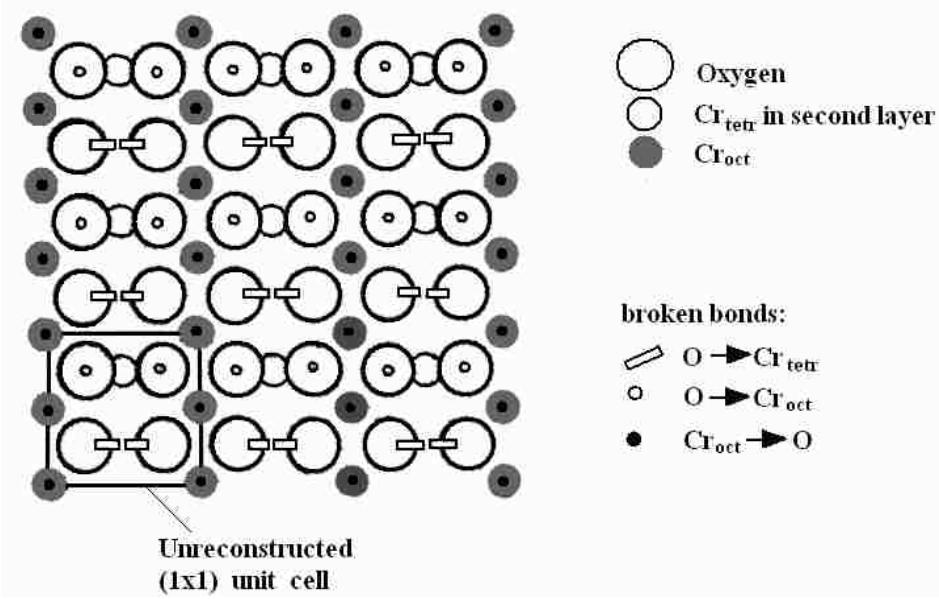

(a)

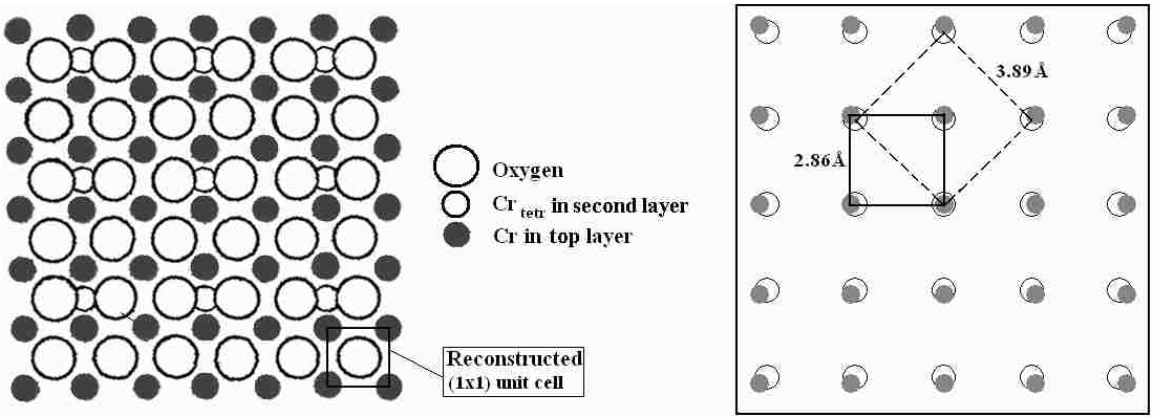

(b) **(c)**

Figure 3.18. Top views of the $Cr_3O_4(001)$ surfaces. Panel (a) is top view of the B-layer terminated, unreconstructed surface, (b) is top view of the reconstructed mixed Cr and O surface in Cr_3O_4, (c) is schematic representation of the real space lattice match between surface mesh for the Cr_3O_4 superlattice (filled circles) at $a_0^{Cr_3O_4}$ = 2.86 Å (in-plane lattice constant of overlayer) and the Pd(001) (open circles) substrate. Open circles represent the substrate lattice, and filled circles represent the overlayer lattice.

In Cr_3O_4, one tetrahedral Cr^{3+} ion contributes 3 electrons to a total of 4 bonds to neighboring oxygen atoms in bulk Cr_3O_4. Therefore, each bond contains $3/4e^-$ that are donated from the tetrahedral chromium ions [75]. Above the Verwey transition [76], each octahedral Cr ion has an average oxidation state of 2.5 and contributes $2.5e^-$ to a total of six bonds to oxygen ions. Each Cr(oct)-O bond contains $(2.5/6)e^- = 5/12e^-$ contributed from chromium ions. Assuming 2 electrons per bond, each oxygen contributes $[2 – (3/4)]e^- = 5/4e^-$ to each Cr(tet)-O bond, and $[2 – (5/12)]e^- = 19/12e^-$ to each Cr(oct)-O bond. These numbers can be used to determine dangling bonds charges when different surface structures are created. Turning to the (1x1) unit cell in the unreconstructed B-layer terminated surface, as shown in Figure 3.18(a), 2 bonds from surface octahedral $Cr^{2.5+}$ ions to oxygen ions are broken in creating this surface resulting in $2x(5/12e^-) = 5/6e^-$ excess charge. In addition there are 2 dangling bonds associated with surface oxygen ions that would bond to octahedral chromium ions if a new layer was added and that contribute $2x(19/12e^-) = 19/6e^-$ excess charge, and 2 oxygen dangling bonds that would connect to tetrahedral chromium in the next layer and that contribute $2x(5/4e^-) = 5/2e^-$ excess charge. Summing up charges ($19/6e^- + 5/2e^- + 5/6e^- = 39/6e^-$) in these broken bonds and transferring electrons from chromium-derived dangling bonds to oxygen-derived dangling bonds leaves the latter deficient by $(8 – 39/6)e^- = 1.5e^-$. Now, in order to obtain the experimental p(1x1) LEED pattern for the oxide overlayer on Pd(001), the starting point would be a tetrahedral A-layer terminated surface which has chromium ions in a reduced oxidation state of Cr^{2+}, instead of the Cr^{3+}. If a B-layer is added next on top of the tetrahedral layer, per unreconstructed unit cell of this layer now has a deficiency of $2.5e^-$. This deficiency can be compensated by adding 2 extra chromium ions per unit cell of the unreconstructed B-layer unit cell in the vacant rows between the adjacent oxygen atoms. For the surface to be electrically neutral we must have per unit cell,

$$\begin{aligned} 2.5 + 2y &= 8 \\ y &= 2.75 \end{aligned} \tag{3.5}$$

where 'y' represents the charge on each of the extra chromium ions added to the surface. Therefore, the reconstructed B-layer terminated surface (Figure 3.18(b)) can be

autocompensated by raising the effective average oxidation state of each chromium ion on the surface to 2.75^{+}, and this can be accomplished with a surface distribution of Cr^{3+} and Cr^{2+} ions in the ratio of Cr^{3+}:Cr^{2+} = 3:1. This reconstructed surface is identical to the CrO(001) surface, with the exception of the oxidation state of the Cr ions.

The R-factor calculations were performed for the Cr_3O_4(001) structure, as shown in Figures 3.19 and 3.20, and in each case the R-factor is the sum total for both Cr and O, and for both the Pd(100) and Pd(110) scattering planes. A series of calculations were carried out to study the variation of the R-factor as a function of the lattice constant, assuming different values of $a_0^{Cr_3O_4}$ from 2.63 Å (7.3% compression compared to 2.86 Å) to 3.08 Å (4.2% expansion compared to 2.86 Å) in steps of 0.03 Å ($\approx$1%). A minimum was obtained for the lattice constant $a_0^{Cr_3O_4}$ = 2.77 Å (Figure 3.19). This value of the lattice constant is very close to the Pd surface lattice constant of 2.75 Å (a difference of 0.73% from 2.75 Å). The R-factor calculation, for $a_0^{Cr_3O_4}$ = 2.77 Å, did not exhibit sensitivity to the variations in d_{12}. R-factor calculations were also carried out for variation in d_{12} for the bulk Cr_3O_4 structure ($a_0^{Cr_3O_4}$ = 2.86 Å, bulk d_{12} = 1.011 Å), and a minimum was observed at d_{12} = 0.647 Å which is a 36% contraction with respect to the bulk value (Figure 3.20).

Figures 3.21 and 3.22 include the polar scan XPD curves (for Cr 2p and $OKL_{23}L_{23}$) in Pd(100) and Pd(110) scattering planes respectively, and the MSCD curves for the Cr_3O_4(001) structure at surface lattice constants of 2.86 Å (without and with relaxations in d_{12}) and at 2.77 Å (without any relaxations in d_{12}). The top two curves in each figure are the experimental results for high and low coverage systems respectively, and the curves below the experimental curves represent results from the model calculations for the reconstructed Cr_3O_4(001) surface. The XPD curves in the Pd(100) scattering plane are for oxide film thicknesses of 5.1 Å and 23 Å, and the XPD curves in the Pd(110) scattering plane are for oxide film thicknesses of 7 Å and 16 Å.

3.2.6.3 MSCD calculations for mixed CrO(001)-Cr_3O_4(001). By comparing the reliability factor calculations for CrO(001) and Cr_3O_4(001), the R-factor for the reconstructed Cr_3O_4(001) surface with lattice constant of 2.77 Å is seen to have a lower value, even though the minimum R-factor values for both the surfaces do not vary by

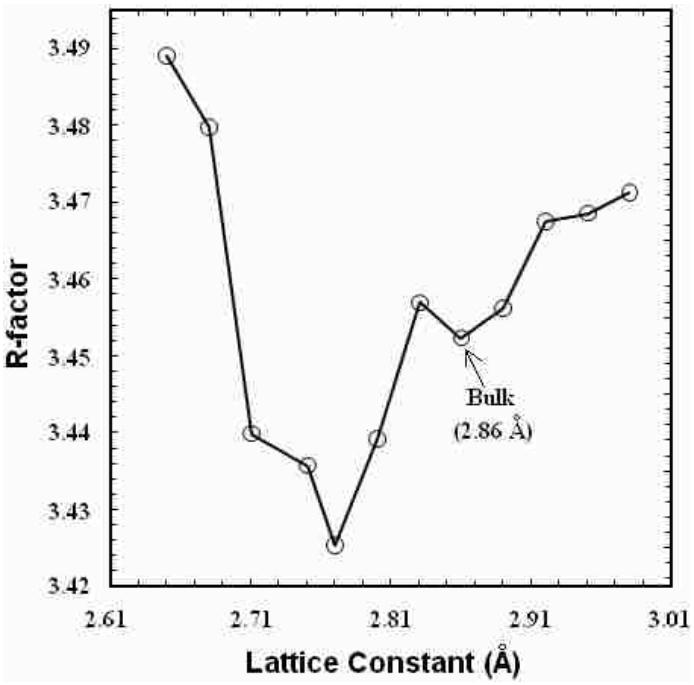

Figure 3.19. Behavior of the R-factor as a function of Cr_3O_4 surface lattice constant.

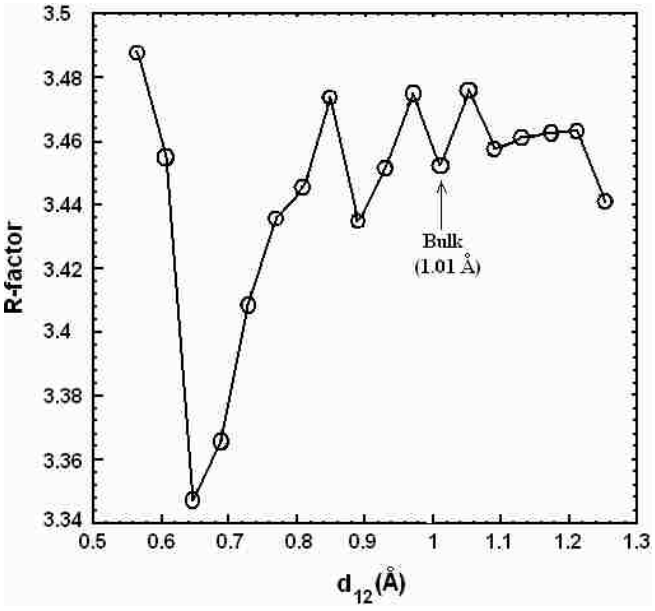

Figure 3.20. Behavior of the R-factor for Cr_3O_4 as a function of the interlayer spacing d_{12}. Surface lattice constant is $a_0^{Cr_3O_4}$ = 2.86 Å.

High coverage: XPD and MSCD for 23 Å Cr_xO_y in the Pd(100) plane

Low coverage: XPD and MSCD for 5.1 Å Cr_xO_y in the Pd(100) plane

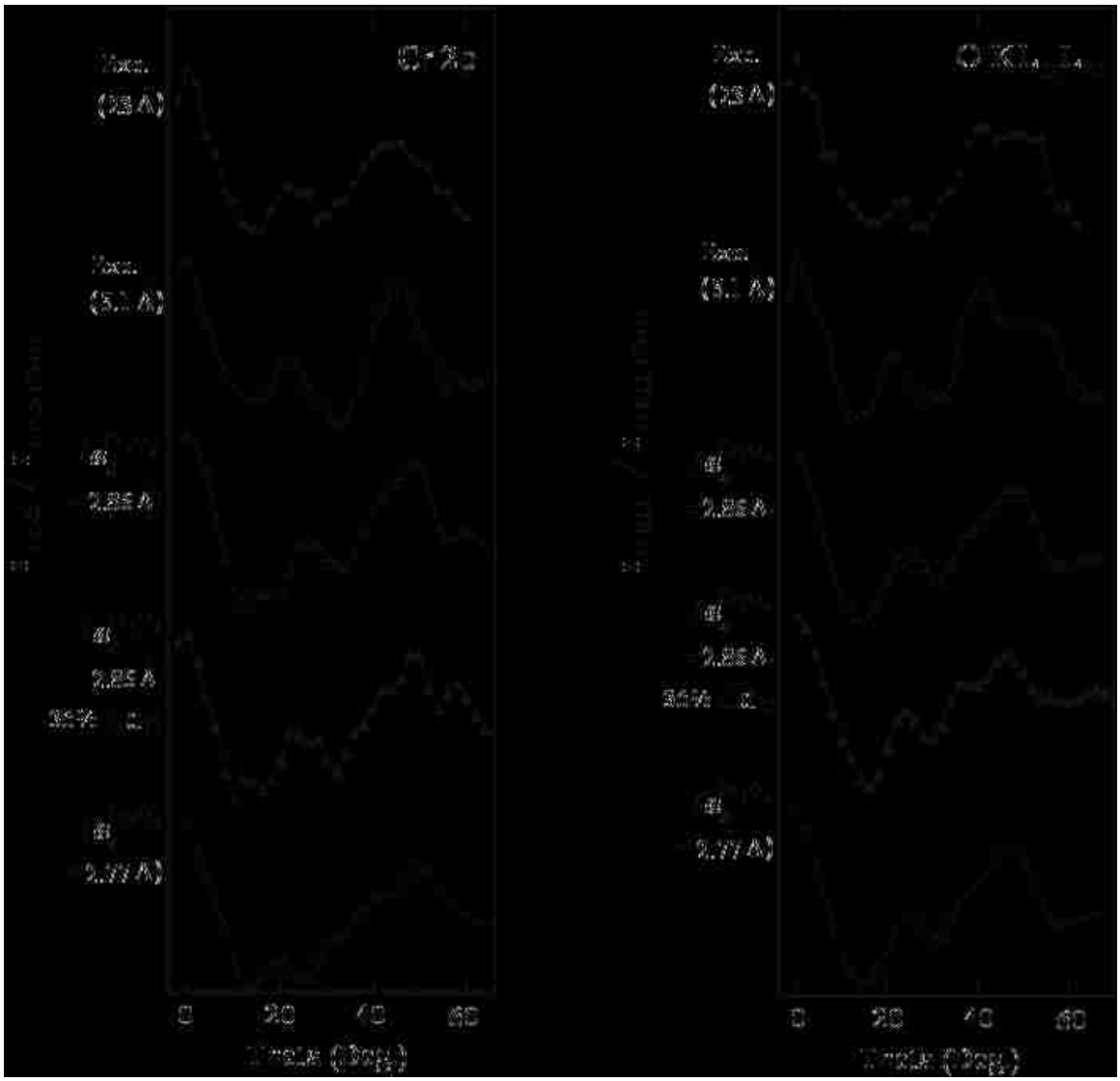

Figure 3.21. Polar scan XPD and MSCD curves for the reconstructed $Cr_3O_4(001)$ surface. Results for Cr 2p (left) and O $KL_{23}L_{23}$ (right) are for the scattering plane corresponding to $\varphi = 0°$. The top two curves are for the experimental high coverage (filled circles) and experimental low coverage (empty circles) films respectively. Rests of the curves are MSCD curves (triangles and diamonds).

High coverage: XPD and MSCD for 16 Å Cr_xO_y in the Pd(110) plane

Low coverage: XPD and MSCD for 7 Å Cr_xO_y in the Pd(110) plane

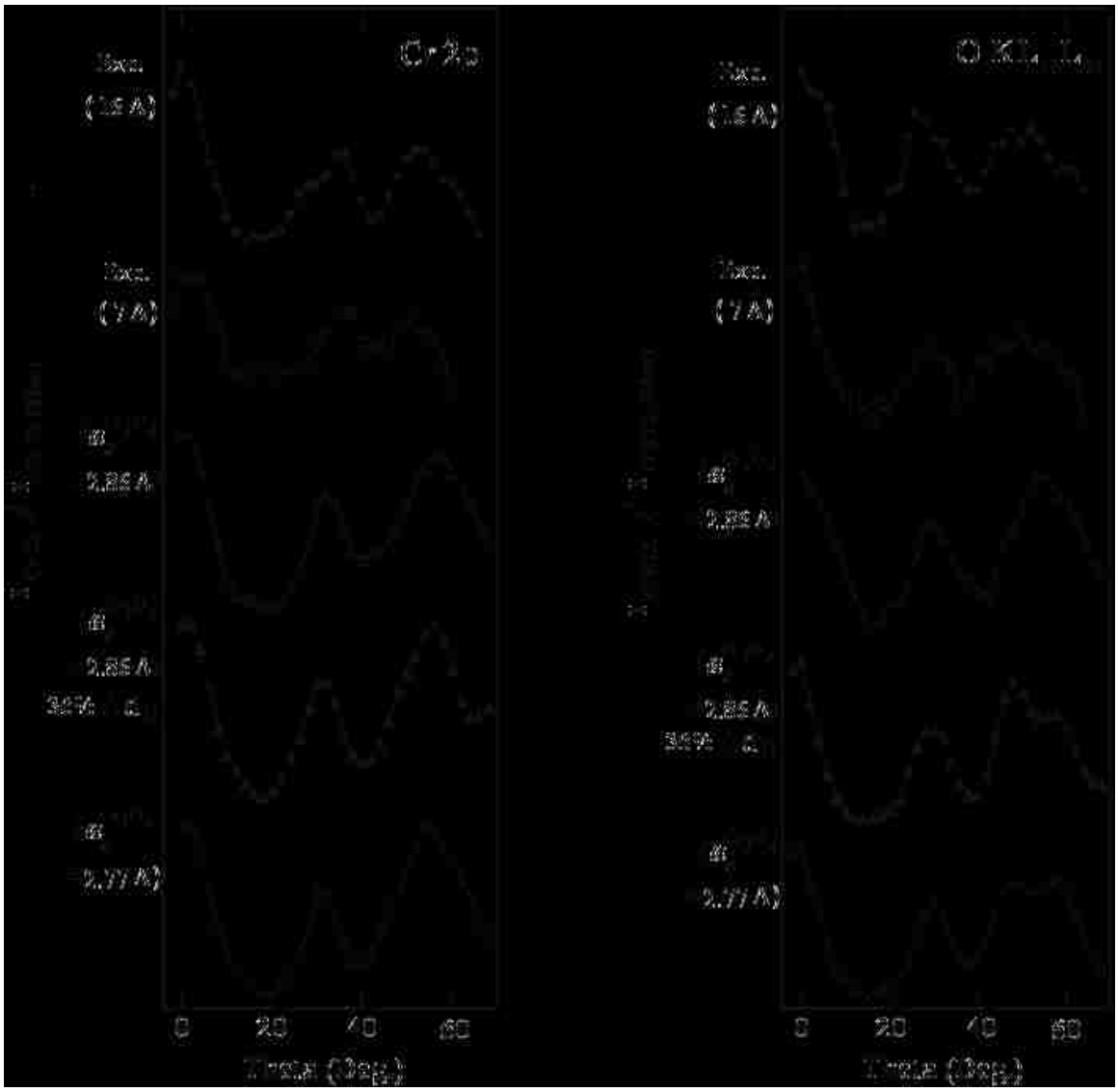

Figure 3.22. Polar scan XPD and MSCD curves for the reconstructed $Cr_3O_4(001)$ surface. Results for Cr 2p (left) and O $KL_{23}L_{23}$ (right) are for the scattering plane corresponding to $\varphi = 45°$. The top two curves are for the experimental high coverage (filled circles) and experimental low coverage (empty circles) films respectively. Rests of the curves are MSCD curves (triangles).

much. Also, the MSCD simulations do not show any significant effect of interlayer relaxations in both CrO and Cr_3O_4. Based on these results, it is tempting to conclude that the chromium oxide surface on Pd(001) has lattice parameters close to that of the substrate lattice, and is a reconstructed Cr_3O_4(001) surface. However, it is also possible that rather than a single phase, a mixed phase oxide with both CrO and Cr_3O_4 phases is present in the film.

R-factor analysis was done for the mixed phase for different percentage compositions of CrO and Cr_3O_4, the R-factor calculations in each case being the total for all polar angles and for both Cr and O. The variation of the R-factor as a function of the percentage composition of CrO (a_0^{CrO} = 2.75 Å), when the lattice constant of Cr_3O_4 is taken to be 2.86 Å is shown in Figure 3.23. This figure shows a minimum at a composition ratio of CrO:Cr_3O_4 = 3:7 (30%:70%). Figure 3.24 shows the variation of the R-factor in relation to the percentage CrO (a_0^{CrO} = 2.75 Å) composition when the Cr_3O_4 lattice constant is taken to be 2.77 Å, and it shows a minimum at a composition ratio of CrO:Cr_3O_4 = 11:7 (55%:45%). While the R-factor for the composition ratio of CrO:Cr_3O_4 = 3:7 shows the lowest minimum among all the R-factor calculations, one has to consider with reservation the absolute quantitative certainty of this result, since the difference between the R-factor minima of the CrO:Cr_3O_4 = 3:7 (30%:70%) and the CrO:Cr_3O_4 = 11:7 (55%:45%) phases is not dramatic. Also, the similarity between the CrO(001) and the reconstructed Cr_3O_4(001) surfaces makes distinction between the two almost impossible. However, XPS results do exhibit the presence of Cr^{3+} ions, and thus the presence of Cr_3O_4.

Figures 3.25 and 3.26 show the polar XPD scans and MSCD curves for Cr 2p (left panels) and O $KL_{23}L_{23}$ (right panels). The top two curves in each figure are experimental results for high and low coverage systems, respectively, and the curves below represent results from weighted composition calculations for the mixed CrO-Cr_3O_4 film. For the XPD data in the Pd(100) scattering plane, the oxide film thicknesses for the low and high coverage systems are 5.1 Å and 23 Å, respectively. For the XPD data in the Pd(110) scattering plane, the oxide film thicknesses for the low and high coverage films are 7 Å and 16 Å, respectively.

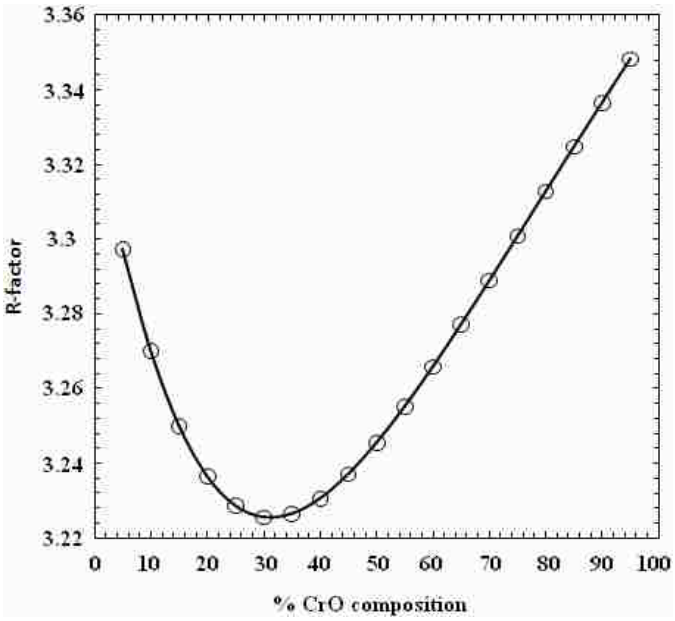

Figure 3.23. Behavior of the R-factor for variation of CrO-Cr_3O_4 composition. Surface lattice constants are $a^{Cr_3O_4}$ = 2.86 Å, and a^{CrO} = 2.75 Å.

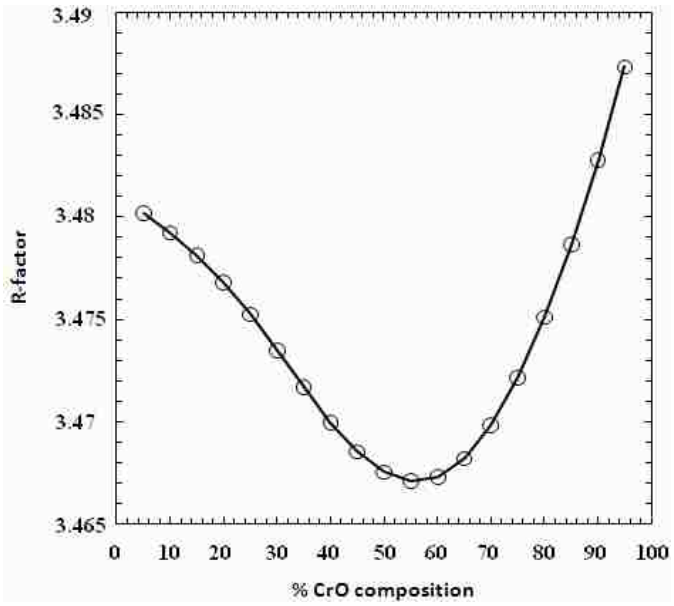

Figure 3.24. Behavior of the R-factor for variation of CrO-Cr_3O_4 composition. Surface lattice constants are $a^{Cr_3O_4}$ = 2.77 Å, and a^{CrO} = 2.75 Å.

High coverage: XPD and MSCD for 23 Å Cr_xO_y in the Pd(100) plane

Low coverage: XPD and MSCD for 5.1 Å Cr_xO_y in Pd(100) plane

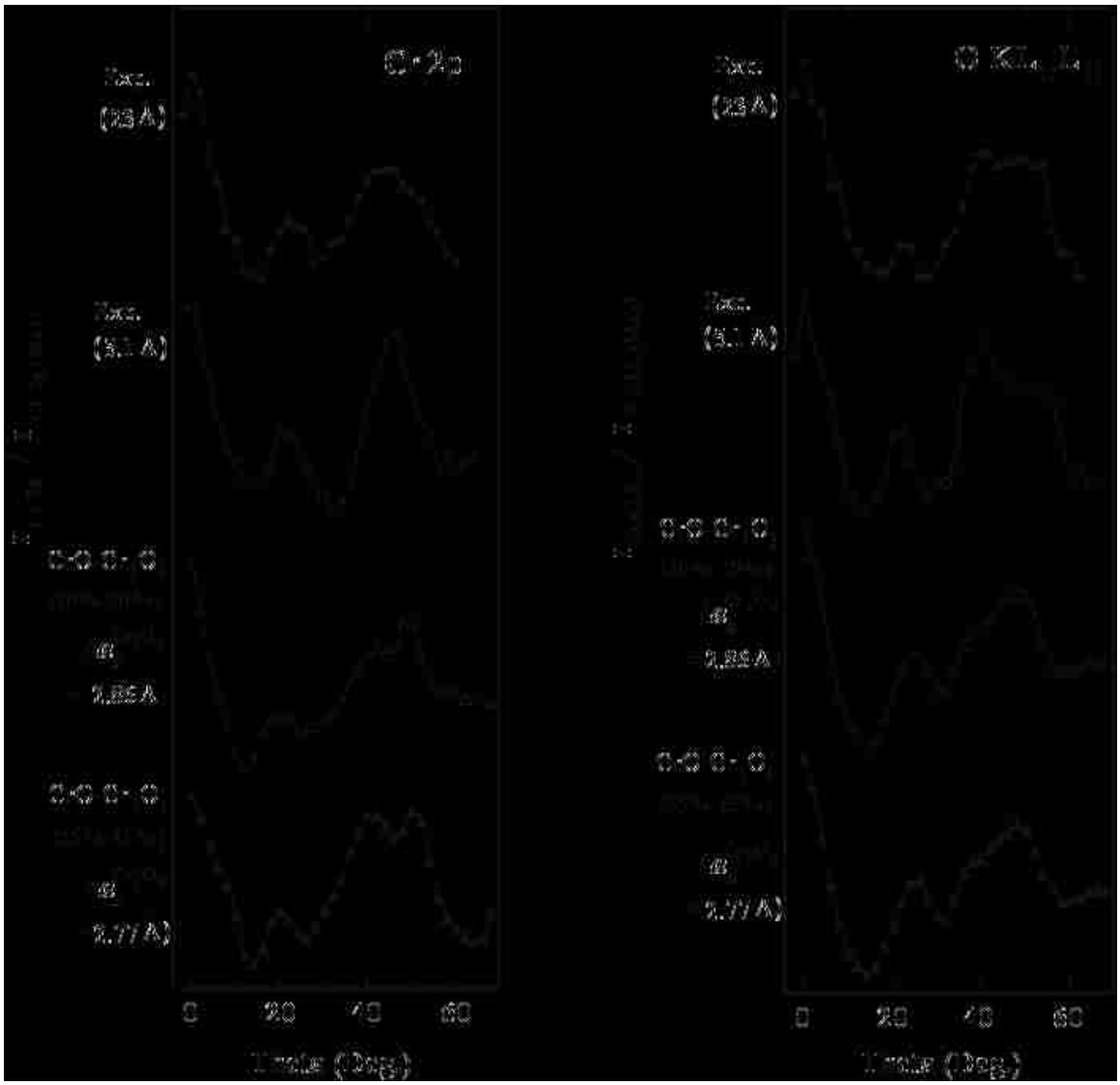

Figure 3.25. Polar scan XPD curves, and MSCD curves for the CrO-Cr_3O_4 mixed phase. Results for Cr 2p (left) and O $KL_{23}L_{23}$ (right) are for the scattering plane corresponding to φ = 0°. The top two curves are for the experimental high coverage (filled circles) and experimental low coverage (empty circles) films respectively. The bottom two curves are MSCD curves (triangles).

High coverage: XPD and MSCD for 16 Å Cr_xO_y in the Pd(110)

Low coverage: XPD and MSCD for 7 Å Cr_xO_y in the Pd(110)

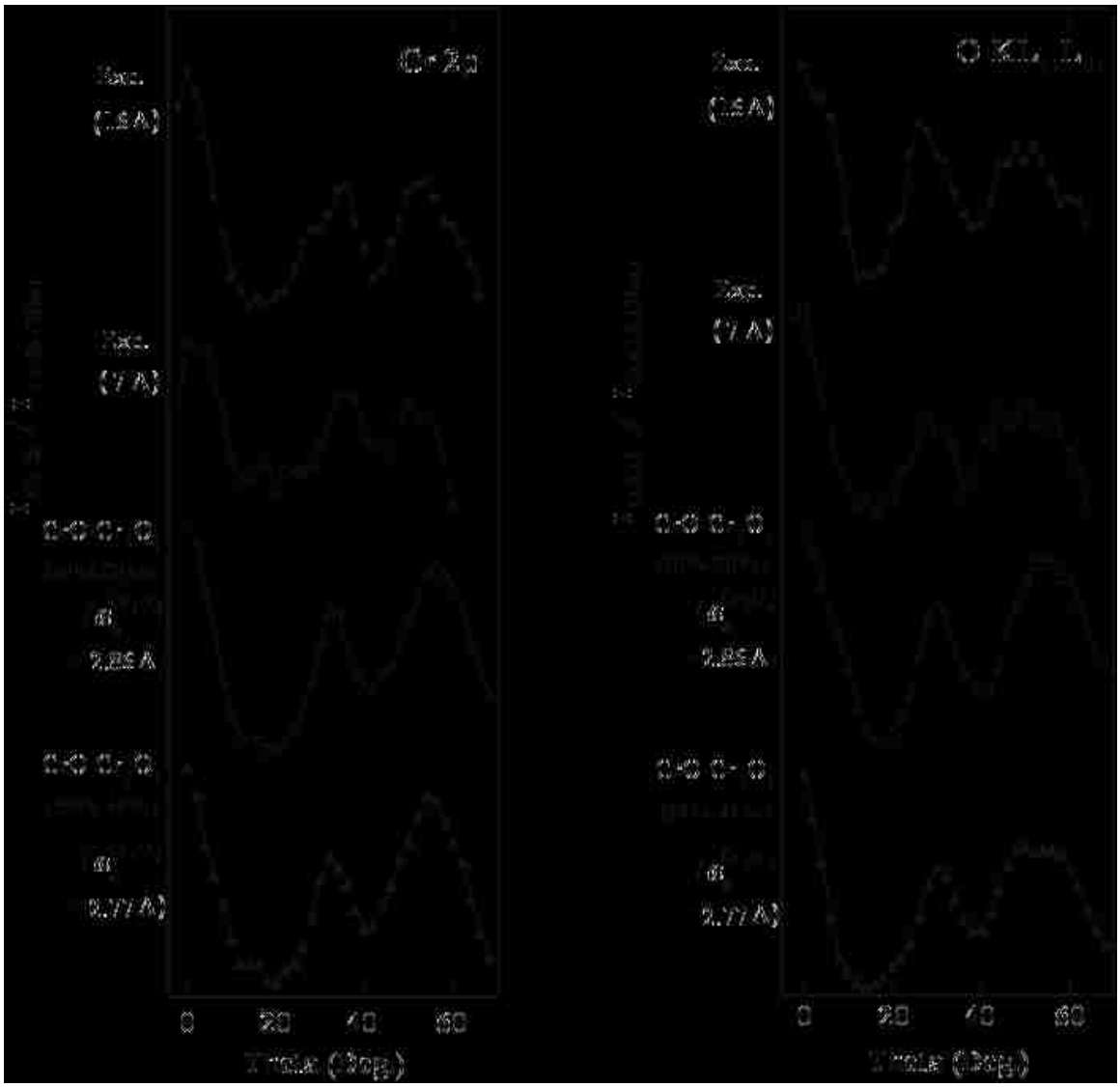

Figure 3.26. Polar scan XPD curves, and MSCD curves for the CrO-Cr_3O_4 mixed phase. Results for Cr 2p (left) and O $KL_{23}L_{23}$ (right) are for the scattering plane corresponding to φ = 45°. The top two curves are for the experimental high coverage (filled circles) and experimental low coverage (empty circles) films respectively. The bottom two curves are MSCD curves (triangles).

3.2.7. Summary and Conclusions. This work has shown that well-ordered chromium-oxide films may be grown on Pd(001) using the multilayer deposition technique. However, only metastable Cr_xO_y films resulted from the sequential deposition technique, and no final stable well-ordered oxide structures were obtained.

The thickness of the Cr_xO_y films was estimated by monitoring the attenuation of the Pd $3d_{5/2}$ core-level photoemission signal. However, the film coverage estimates are to be viewed only as approximates due to the much larger inelastic mean free path of the Pd $3d_{5/2}$ core-level electrons (λ_{mfp} = 17.09 Å) compared to the interlayer separations of the ultra-thin oxide film samples. The exponential decay of the Pd photoemission signal with Cr, and Cr_xO_y film coverages on Pd(001) would suggest layer-by-layer growth modes for both, but that determination would only be reasonable for comparable Pd $3d_{5/2}$ photoelectron inelastic mean free path and film lattice spacings. As such the precise growth mode for these oxide films is not known. Section 3.2.1 discussed results of some studies in the existing literature done on the growth of Cr on (001) substrate surfaces. Cook et al. [59] proposed layer-by-layer growth for Cr films grown on Pd(001) at three different temperatures of -123 °C, 27 °C and 127 °C. They also observed a bcc phase for films of thicknesses > 3 ML, and while the films greater than 6 ML remained bcc after annealing at 227 °C, the films between 3 and 6 ML turned to a fcc phase after the anneal at 227 °C. Films grown with a thickness < 3 ML were reported to be fcc both before and after annealing to ~227 °C. All the Cr films deposited in our experiment were done at a substrate temperature of 300 °C, and they remained bcc at all coverages.

An attempt was made to determine the oxidation state of Cr in the Cr_xO_y films by observing the chemical shift of the Cr 2p photoemission peak. Binding energy shifts of approximately ~3 eV have been observed for both Cr $2p_{3/2}$ and Cr $2p_{1/2}$ core levels in the Cr_xO_y samples, and therefore it can be safely conclude that the Cr films were completely oxidized during the sample preparation process. Resolution of the Cr^{3+} and Cr^{2+} oxidation states however remains difficult due to the small energy binding energy separation of ~ 1eV, and limits to the experimental energy resolution. Presences of shake-up satellites do however confirm the presence of Cr^{3+} ions.

For the chromium oxide films grown using the multilayer deposition technique, sharp p(1x1) LEED patterns are observed at all coverages from ~2 Å to 23 Å. The

absence of extra LEED spots suggests that the Cr_xO_y overlayer has the same surface mesh as the Pd(001) substrate. No ordered oxide surface structures were obtained at room temperature deposition, and all the Cr_xO_y films were made at elevated substrate temperatures. The p(1x1) LEED pattern associated with the oxide films is consistent with the growth of a CrO(001) surface. This pattern is also consistent with the growth of a reconstructed Cr_3O_4(001) surface structure. Model calculations from each of these two different structures provided reasonable agreement with the experimental XPD curves. Results from the incorporation of possible interlayer relaxations for both the CrO and Cr_3O_4 surfaces remain inconclusive. Attempts to match XPD results with MSCD calculations from a mixed phase of CrO(001) with Pd lattice parameters, and reconstructed Cr_3O_4(001) with its bulk lattice parameters, with weighted compositions from each individual phase also provided satisfactory fit between experiment and theory, and it may very well be that we have a mixed oxide film composed of both CrO and Cr_3O_4 phases on the Pd(001) substrate. XPS certainly does confirm the predominance of the Cr^{3+} oxidation state in the oxide sample, as do the R-factor calculations (Figure 3.23).

For the chromium oxide films obtained from the sequential deposition technique, no XPD measurements were possible since no stable and well-ordered oxide structures were observed at room temperature. The oxide films that were annealed to 400-420 °C initially produced a well-ordered c(4x2) LEED pattern which however was not stable, and the LEED pattern not only changed with time but it also deteriorated. For the oxide films annealed to higher temperatures of 490-500 °C, the LEED patterns were not well-ordered and they also deteriorated with time.

Obviously, the deposition technique does have an effect on the stability and order of the chromium oxide films grown on Pd(001). From previous studies done on the growth of chromium-oxide films on Ag(001) using the multilayer and sequential growth techniques [58], ordered oxide structures were obtained from both the deposition methods, and it was observed that the deposition technique influences the symmetry of the oxide formed. While multilayer growth of Cr_xO_y on Ag(001) resulted in structures with four-fold symmetry and the oxide proposed was α-Cr_2O_3(210), sequential growth of Cr_xO_y on Ag(001) resulted in 3-fold symmetry structures and the oxide proposed was α-Cr_2O_3(111). This aspect of the dependence of growth of the Cr_xO_y films on the Pd(001)

and Ag(001) substrates on the deposition method will be explored further in Section 5. A comparison study between the Cr_xO_y/Pd(001) and Cr_xO_y/Ag(001) systems will also be performed.

4. IRON-OXIDE THIN FILM GROWTH ON Pd(001)

4.1. BACKGROUND

The oxides of iron are technologically important due to their use in high density magnetic recording media or as pigments, and as catalysts for oxidation and dehydrogenation reactions. Heteroepitaxially grown oxide films have been found to be useful model catalyst systems for systematic investigation of catalytic properties. Iron oxides are also of great interest in corrosion and oxidation processes of iron metal and steel. These processes are mediated by the surface whose structure depends greatly on environmental factors like temperature, oxygen, or water pressure. Iron ions can readily exist in either a Fe^{2+} or Fe^{3+} ionization state while forming compounds, and as such several stable crystallographic forms of iron oxides exist in bulk phase.

The three most stable forms of iron oxide are FeO or wustite, α-Fe_2O_3 or hematite, and Fe_3O_4 or magnetite. FeO crystallizes in the NaCl structure, and is stable at temperatures above 550 °C. In actuality, wustite is always deficient in iron with an average composition of $Fe_{0.9}O$ to $Fe_{0.95}O$ [77]. Hematite crystallizes in the corundum structure, and for stoichiometric, non-defective α-Fe_2O_3, all of the iron ions are in a Fe^{3+} state. Magnetite crystallizes in the inverse-spinel structure and is the most stable form of iron oxide. In the inverse-spinel structure the tetrahedrally-coordinated metal ions are all in a Fe^{3+} state and the octahedrally-coordinated metal ions are half Fe^{2+} and half Fe^{3+} states. The oxides of iron exhibit a variety of electronic and magnetic properties. Wustite and hematite are anti-ferromagnetic semiconductors, and magnetite is a conducting ferromagnetic material.

Thin films of Fe and Fe oxides have been successfully grown epitaxially on several metal and metal oxide substrates. Fe/Ag(100) and Fe/Cu(100) systems have been extensively studied [78-84]. Due to the fact that there are several stable phases of iron oxide, identifying the crystal structure and surface termination of an epitaxial iron oxide overlayer is not always easy. At the surface, the lattice parameters may differ significantly from the bulk. For example, due to the polar nature of the FeO(111)surface, it is expected that it may undergo a surface reconstruction. Several studies of controlled oxidation of Fe(100) and Fe(110) surfaces have been conducted [85-90]. The observed

ordered phases have been found to depend critically on the temperature and oxygen pressure during oxide formation. In a LEED and AES study of the oxidation of the Fe(001) surface, Simmons and Dwyer [87] observed an initial c(2x2) LEED pattern when the Fe(001) surface was oxidized at room temperature at initial oxygen exposure of below 10 L. At 10 L oxygen exposure, the c(2x2) pattern disappeared and reverted to a (1x1), and above 20 L oxygen exposure no diffraction features were visible. Mild heating to ~200 °C and at oxygen exposures between 20 L and 40 L, produced a diffraction pattern which they claimed to be due to the growth of FeO(001), with a lattice parameter 4.5% smaller than bulk FeO. In addition, they observed a complex diffraction pattern upon further oxidation at 75-100 L and after annealing at 200 °C, which they claimed to be FeO(111). Leygraf and Ekelund [88] conducted LEED and AES studies on the initial stages of oxidation of the Fe(110) and Fe(100) single crystal surfaces at 27 °C and 127 °C. They reported that on the Fe(110) surface, a FeO-like structure formed with a lattice parameter 4% larger than that of bulk FeO. For oxidation of the Fe(100) surface, they observed that oxygen initially occupied four-fold sites on the Fe(100) surface, and this fcc(100) face initially contracted and later expanded with increased oxygen doses (~800 L) at room temperature and formed a spinel-like structure. Heat treatment caused the spinel-like structure to transform to FeO(100), however this FeO-like structure was observed to be metastable and it transformed back to the spinel phase after a few hours. Busch et al. [89] prepared ultrathin iron oxide layers by exposing the atomically clean Fe(110) surface to atomic and molecular oxygen at partial pressures of several times 10^{-8} mbar and at a constant temperature of 147 °C, as well as through oxidation by reactive Molecular Beam Epitaxy (MBE). Through LEED, AES, and grazing ion scattering studies, they reported formation of well-ordered FeO(111) films with low defect density if atomic instead of molecular oxygen exposure of between 1 and 2 L was used for oxidation. Compared to bulk, the FeO lattice was found to be laterally compressed by about 5-6%. Also due to the large mismatch between FeO(111) and Fe(110), they claimed that independent of the preparation method, the long range structural order was possible only for a limited thickness of about 3 layers. Fe substrate oxidation or reactive MBE with molecular oxygen was found to lead to poor film quality over the entire range of oxygen exposures of up to 145 L.

Studies have also been performed on the growth of epitaxial iron oxide on substrates other than iron. These include Mo(100), Pt(100), Pt(111), Ag (100), Ag(111), Mg(100), Cu(001), NiFe(100), and α-Al_2O_3(0001). MgO(001) is a commonly used substrate to prepare epitaxial films of Fe_xO_y. Results of investigation through XPD, LEED and STM studies done by Chambers et al. [91] on the surface structure of oxygen-plasma assisted MBE-grown Fe_3O_4(001) on MgO(001) suggest that the reconstructed $\left(\sqrt{2}x\sqrt{2}\right)R45°$ surface is terminated with a ½ of monolayer tetrahedrally coordinated Fe^{3+} autocompensated layer, with the first four interlayer spacings relaxed by -14, -57, -19, and +29% of the respective bulk value. Gao and Chambers [92] prepared iron-oxide films on MgO(001) by oxygen-plasma MBE, and their RHEED, LEED, and XPS studies revealed layer-by-layer growth for γ-Fe_2O_3(001) and Fe_3O_4(001) on Mg(001). The γ-Fe_2O_3 films were grown at rates of 0.2-0.3 Å/s at oxygen partial pressures of $4x10^{-5}$ Torr, while the Fe_3O_4 films were grown at rates of 0.6-0.8 Å/s and at oxygen partial pressures of $3x10^{-6}$ Torr; during growth the substrate was held at 250-500 °C. The γ-Fe_2O_3(001) LEED pattern was observed to be a (2x2) pattern with respect to the MgO(001) substrate and the film surface autocompensated. The Fe_3O_4(001) LEED pattern revealed, as in previous studies, a (2√2x√2)R45º pattern with respect to the MgO(001) substrate or alternatively, a (√2x√2)R45º reconstructed surface with respect to the bulk-terminated Fe_3O_4. Again this reconstruction of Fe_3O_4 was attributed to the formation of a ½ ML tetrahedrally coordinated Fe^{3+} surface layer termination.

Growth of iron oxide films on metal substrates have also been reported in several studies. Among the various low index surfaces of FeO, the FeO(111) surface has been structurally investigated in most studies of iron oxide growth on Pt substrate [93-96]. Vurens et al. [93] reported layer-by-layer iron oxide growth on both Pt(111) and Pt(100), and the ordered FeO structures were reported to have (10x10) and c(2x10) epitaxial relationships with Pt(111) and Pt(100) substrates respectively. Iron oxide films were prepared by first evaporating Fe onto the Pt substrate, followed by oxidation at $5x10^{-7}$ Torr oxygen, and finally annealing to 830 K in an oxygen atmosphere. On Pt(111), for monolayer oxide coverage they reported a complex hexagonal LEED pattern and for multilayer coverages, after annealing to 1040 K, a (2x2) LEED pattern relative to the monolayer structure. On the Pt(100) substrate, they reported a diffuse (1x1) LEED

pattern for monolayer oxide coverage, which after annealing in $5x10^{-7}$ Torr of O_2 to 830 K resulted in a c(2x10) structure. From ISS studies, the oxide films on Pt(100) and Pt(111) were found to be stable up to 1000 K, and beyond 1000 K the overlayers dissolved into Pt. Photoelectron diffraction measurements revealed formation of FeO(111) bilayers on both substrates, with lower oxygen content of the monolayer on Pt(100) as deduced from AES. Galloway et al. studied growth of iron oxide films on Pt(111) [95] and observed that for coverages ≤ 1 ML, the iron oxide is FeO with a large lattice mismatch between the oxide and Pt substrate. The FeO was referred to as a 9x9 structure. At higher coverages, the oxide films were ascribed to α-Fe_2O_3 and Fe_3O_4 phases. Ritter et al. [96] observed well-ordered FeO monolayers on Pt(100) substrate. STM images revealed buckling of the top oxygen layer caused by an interaction with Pt atoms, and the existence of two superstructures described as the FeO(111)/Pt(100) — c(2x10) and c(2x9) coincidence structures. LEED studies on the growth of FeO(001) on Ag(001) were performed by Lopes et al. [97]. The FeO(001) films were made by evaporating Fe on to the Ag(001) surface and oxidizing it at an oxygen partial pressure of 10^{-7} mbar, then annealing the oxidized sample at 600 °C for 10 minutes. A c(2x2) LEED pattern was observed, and from their LEED-I(V) analysis, they proposed a FeO(001) structure with a rumpled surface termination layer with oxygen atoms lying outwards; the oxide film in-plane lattice constant was estimated to have expanded by 1.6%. Waddill and Ozturk reported on the growth and characterization of ultrathin iron-oxide films on Ag(111) using XPS, LEED, and XPD [98]. The epitaxial iron-oxide films were grown by two methods. The first growth method involved the deposition of Fe films, ranging in thickness from 1-10 ML, on Ag(111) and then oxidizing these films at 10^{-5} Torr O_2 pressure and 350 ºC substrate temperature (multilayer growth technique). This led to the growth of poorly ordered FeO(111) films. The second method involved the sequential deposition of submonolayer Fe films (typically ≤ 0.5 ML) followed by oxidation, and the cycles was repeated until films of desired thickness were obtained (sequential growth technique). The second method resulted in FeO(111) films below ~ 10 Å, with the growth of Fe_3O_4(111) for thicker films. Also, the iron-oxide films grown by the sequential deposition method were found to have much better crystallographic order than those grown by oxidizing thicker iron films. XPS, LEED and XPD studies were also done

on the growth of iron oxide films on Ag(001) by Priyantha and Waddill [99]. For the iron-oxide films grown using the multilayer deposition technique, a (2√2x2√2)R45º LEED pattern was observed, and they proposed the oxide structure to be Fe_3O_4(100). For the sequentially deposited iron-oxide films, while the iron-oxide thin films were found to be FeO(111), growth of the thicker films resulted in the formation of Fe_3O_4(111).

4.2. EXPERIMENT AND RESULTS

The Fe_xO_y films were grown by thermal evaporation of Fe metal and subsequent oxidation of the deposited metal. The oxide films were characterized for surface crystallographic order, composition, film thickness, and surface structure determination by XPS, LEED, and XPD. All experiments were done inside an ultra high vacuum chamber with a base pressure of ~ $1x10^{-10}$ Torr. The thicknesses of the analyzed Fe_xO_y films ranged from approximately 7 to 43 Å. Two techniques were used to grow the Fe_xO_y films on Pd(001) – multilayer deposition and sequential deposition.

4.2.1. Iron Film Growth. Before starting on an investigation of the structure of oxide films produced by oxidizing Fe, it is important to first characterize the Fe films on Pd(001). There is a 4.2% misfit between bcc Fe (a_0 = 2.87 Å) and fcc Pd (a_0 = 3.89 Å, a = 2.75 Å), 'a' being the primitive surface unit cell side, and a -8.4% misfit between fcc Fe (a_0 = 3.59 Å) and Pd.

In the present study, the Fe films on Pd(001) were grown at a rate of approximately 0.6 Å/ minute and at a substrate temperature of 300 °C, resulting in a p(1x1) LEED pattern that is consistent with the growth of bcc Fe(001). Figure 4.1 shows the diffraction patters for clean Pd and Fe film grown on the Pd substrate. Figures 4.1(a), (b), and (c) show the LEED patterns for clean Pd(001), 3.5 Å, and 14 Å thick Fe films on Pd(001), respectively, for an electron energy of 74 eV. The p(1x1) LEED pattern does not change with Fe film coverage. Figure 4.1(d) shows a schematic of the epitaxy of Fe(001) on Pd(001). The unit cell of Fe is rotated by 45° with respect to the underlying Pd(001) substrate. The LEED pattern for the 3.5 Å Fe film as well as the 14 Å are consistently p(1x1) and are well-ordered.

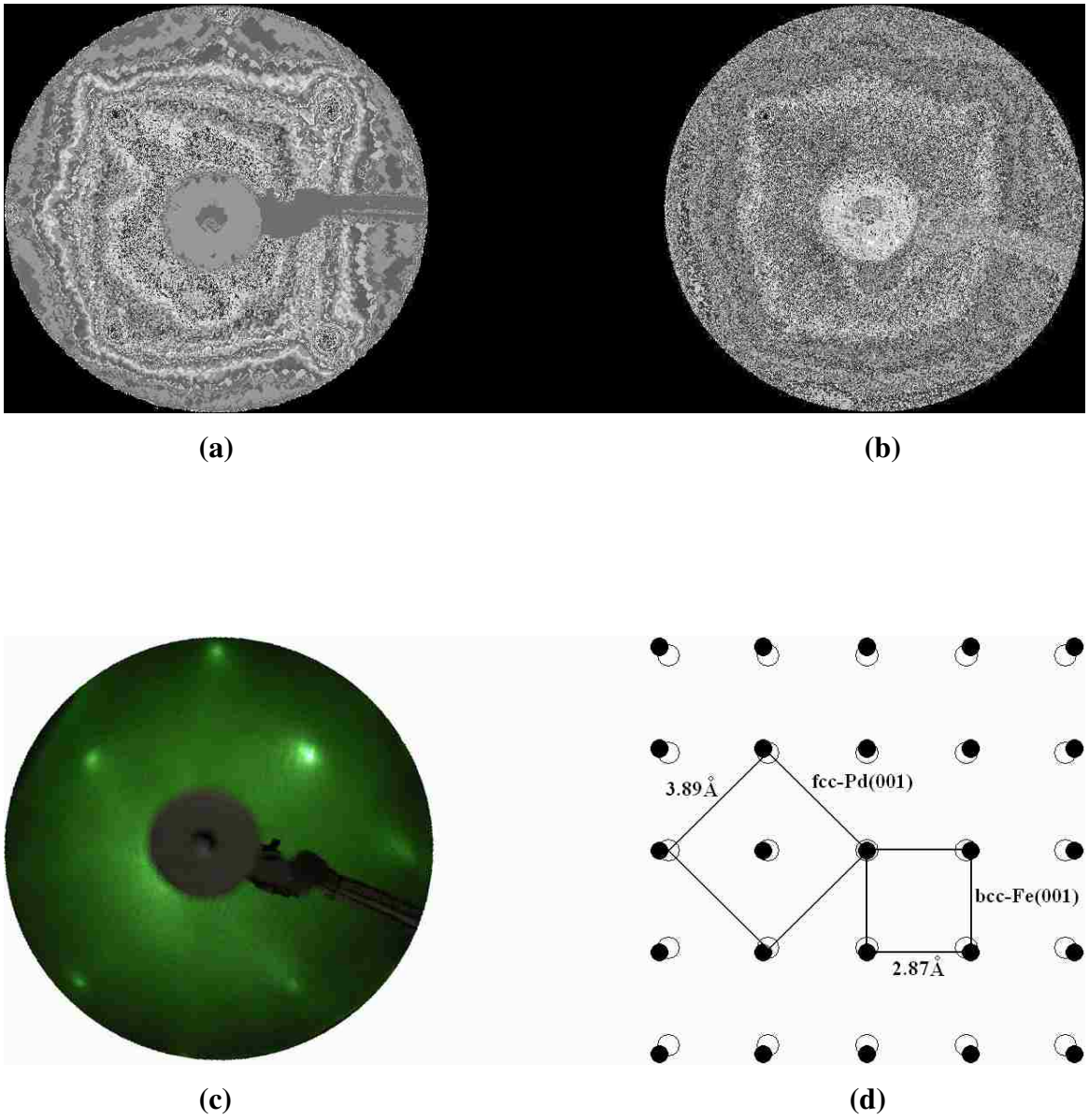

Figure 4.1. LEED patterns observed for (a) clean Pd(001), (b) a 3.5 Å thick Fe film on Pd(001), (c) a 14 Å thick Fe film on Pd(001), respectively, recorded at 72 eV electron energy. Figure (d) is a schematic representation of the real space lattice match between the Fe (001) surface mesh (filled circles) and the Pd(001) (open circles) substrate.

This section also briefly discusses some studies done on the growth of Fe on Pd(001) as reported in existing literature. Quinn et al. [65] studied Fe films grown on Pd(001), and based on LEED and ARPES studies, found no evidence for layer-by-layer growth in the Fe/Pd(001) system in the early growth stages. For slow deposition (0.5 Å/min) of metal at room temperature, a (1x1) LEED pattern was observed which deteriorated as thickness increased to 5 layer equivalents (LE), but improved upon further deposition, and the LEED pattern contrast increased steadily up to about 20 LE. The (1x1) LEED patterns were reported to be noticeably sharper when the substrate was cooled to 120 K, with similar kind of initial worsening and successive improvement of the patterns with increasing thickness. For fast deposition of Fe, the (1x1) LEED pattern was noticeably worse than with the slow deposition, and the in-plane lattice constant was found to be larger than that of the Pd(001) substrate. During the early stages of growth for slow deposition, the films grow as epitaxial flat-topped (001) islands of unequal heights. The growth mode during slow deposition of both low and high coverage films was claimed to be pseudomorphic, irrespective of whether the substrate was at room temperature or whether it was cooled. Structure of the thick films (up to 65 LE) grown at a slow rate was reported to be body-centered-tetragonal, while very thick films grown at a fast rate (10 Å/min) were not pseudomorphic and had essentially a bcc structure. Lee et al. [66] also observed a (1x1) LEED pattern for Fe films (up to 3 ML) on Pd(001) at room temperature, and claimed the growth mode to be pseudomorphic. Like Quinn et al. [65], they also observed the initial worsening and successive improvement of LEED pattern for thickness up to 3 ML. Their LEED I(V) analysis suggested the possibility of the formation of randomly substituted binary alloy near the surface rather than films formed purely of Fe atoms. Liu and Bader [100] contended through AES and photoemission adsorbed Xe (PAX) studies that at the submonolayer regime, the formation of randomly distributed Fe atoms or small clusters on Pd(001) surface took place without forming extended 2-dimensional islands, so essentially a layer-by-layer growth mode, and also that at room temperature there was some degree of Fe-Pd intermixing in the Fe growth. Jin et al. [101] observed through RHEED and STM studies that the initial growth stage of Fe on Pd(001) at room temperature is in the layer-by-layer mode, however at early stages it soon changed to the island growth mode. At 0.5 ML, the

growth of Fe on Pd(001) was in the 2D-layer mode, and the 2D film consisted of a large amount of randomly distributed Fe atoms or clusters of atoms. This was observed up to 1.4 ML, beyond which the morphology started to become rough, and they proposed an island growth mode after 3 ML. Boeglin et al. [102] examined the growth and interface of Fe/Pd(100) ultrathin films at room temperature, and for 1-4 ML Fe/Pd(001) films, they observed a (1x1) LEED pattern and claimed the structure to be a face-centered tetragonal (fct) Fe-Pd alloy. Beyond 4 ML, LEED I(V) and EXAFS studies supported a structural transition from a fct to bct (body-centered tetragonal) Fe. The Fe/Pd(100) interface at room temperature was described as a disordered Fe-Pd alloy. The growth mode of the Fe films on Pd(001), thus, remains controversial.

4.2.2. Sample Preparation. The iron-oxide films were deposited using two different techniques – the multilayer and the sequential deposition techniques.

4.2.2.1 Multilayer growth of iron-oxide films. The samples were prepared in an ultra-high vacuum chamber with a base pressure of ~ $1x10^{-10}$ Torr. The well oriented and polished single-crystalline substrate of Pd(001) was commercially obtained (Monocrystals Co.). Prior to being mounted onto the sample holder, the substrate was cleaned with acetone and methanol. Inside the UHV chamber, the substrate was cleaned by Ar^+ sputtering (20 mA emission current, 1.5 kV beam voltage) for 15 minutes at an argon partial pressure of $2x10^{-5}$ Torr, and then the substrate was annealed at 420 °C for 30 minutes. The substrate was then heated for 2 minutes at 150-200 °C at oxygen partial pressure of $5x10^{-7}$ Torr for to remove the surface carbon contamination. This procedure led to a clean Pd surface as determined by XPS, and a well-ordered sharp p(1x1) LEED pattern with sharp LEED spots and low background intensity was then obtained. Initially multilayer Fe films were grown at room temperature on the clean Pd(001) substrate at a rate of approximately 0.5 ML per minute. No diffraction features were observed when the multilayer Fe films were oxidized at room temperature. Therefore, Fe films of desired multilayer thickness were first deposited at 300 °C substrate temperature, and the sample temperature was maintained at 300 °C during oxygen exposure at a partial pressure of $2x10^{-5}$ Torr for 5 minutes. The oxidized sample was then annealed at 420 °C for 30 minutes so that a well-ordered film could be obtained. 99.98% pure Fe and Matheson 99.995% purity O_2 were used for Fe_xO_y film growth. The maximum pressure during the

evaporation of Fe was $\leq 5x10^{-9}$ Torr. A water-cooled Leybold Inficon XTM/2 thickness monitor was used to measure the metal deposition rate and thickness of film. The film thickness was also determined by measuring the attenuation of the Pd $3d_{5/2}$ core-level photoemission signal by the deposited film. In calculating the thickness of the Fe_xO_y films, the TPP formula proposed by Tanuma, Powell, and Penn [66] for electron inelastic mean free path was used.

XPS data was gathered using Mg K_α radiation (hv = 1253.6 eV) and at an analyzer angular acceptance of ±8°, while XPD data was taken at an angular acceptance of ±1°. XPD scans were obtained for Fe $2p_{3/2}$ (binding energy = 707 eV) and Fe $2p_{1/2}$ (binding energy = 720 eV) core energy levels, and O $KL_{23}L_{23}$ Auger line. The integrated area of these features after proper background subtraction was used to generate XPD polar and azimuthal curves. From the XPS spectra for clean Pd(001) and Fe_xO_y film (Figure 4.2) it can be observed that the O 1s (binding energy = 531 eV) overlaps with the Pd $3p_{3/2}$ core level (binding energy = 533 eV), and as such it was not possible to obtain XPS and XPD data for the O 1s peak.

4.2.2.2 Sequential growth of iron-oxide films. The second method of growing iron-oxide films on Pd(001) is by the sequential deposition method. In this method, the Fe_xO_y films were grown on clean Pd(001) substrates using repeated cycles of thermal evaporation of Fe of 0.5 ML or less at 300 °C substrate temperature. The deposited Fe metal was then oxidized at 300 °C substrate temperature and at ~$2x10^{-5}$ Torr oxygen partial pressure for 2-5 minutes, followed by annealing for 2 minutes at 420 °C. These steps were repeated until the desired film thickness was achieved. The oxidized sample was then annealed at 420 °C for 20-30 minutes to obtain a well-ordered oxide sample. Film thickness was again determined by measuring the attenuation of the Pd $3d_{5/2}$ photoemission signal by the deposited film. XPS and XPD data were taken using Mg K_α radiation (hv = 1253.6 eV). The integrated area of the Fe $2p_{3/2}$ and O $KL_{23}L_{23}$ peaks after proper background subtraction was used to generate polar and azimuthal XPD curves. LEED and XPD studies of sequentially deposited iron oxide films were performed for thicknesses ranging from 5 Å to 20 Å.

4.2.3. Iron-Oxide Film Thickness Determination. The thickness of the epitaxial Fe_xO_y films can be calculated by using the photoelectron emission intensities from the film and the substrate. The attenuation of the Pd $3d_{5/2}$ photoelectron signal can be monitored as a function of the Fe_xO_y film coverage. Assuming a simple exponential decay of the substrate signal with increasing coverage of the epitaxial Fe_xO_y film for an ideal layer-by-layer growth mode, the attenuated photoelectron intensity of the substrate at a particular film coverage is given by:

$$I^s = I_0^s \exp(-x/\lambda_s) \tag{4.1}$$

Here λ_s refers to the value of the photoelectron inelastic mean free path for Pd taken from the TPP method [66]. The inelastic mean free path for Pd $3d_{5/2}$ electrons with kinetic energy ~919 eV (Mg K_α excitation) is approximately 17.09 Å. The thickness of the overlayer film is represented by the variable *x*, the intensity from the clean Pd substrate is I_0^s, and the intensity from the overlayer covered substrate is I^s. Thus, information on the thickness of the epitaxial Fe_xO_y layer can be obtained by measuring the Pd $3d_{5/2}$ photoelectron intensity. Figure 4.2 shows the XPS spectrum for a clean Pd substrate and for a 15 Å Fe_xO_y film on the Pd surface. The two most intense energy peaks for clean Pd are at binding energies of 335 eV and 340 eV and correspond to Pd $3d_{5/2}$ and Pd $3d_{3/2}$ core levels respectively. With a Fe_xO_y overlayer on the Pd substrate, the relative intensity of the two core level peaks is reduced.

Ideally, exponential decay is possible only if the epitaxial films grow layer-by-layer. Figure 4.3 shows the exponential attenuation curves of the Pd substrate signal as a function of Fe film thickness and iron-oxide film thickness. Both curves are consistent with layer-by-layer growth. However the inelastic mean free path for Pd $3d_{5/2}$ electrons with kinetic energy of ~ 919 eV (Mg K_α excitation) is approximately 17.09 Å, which is much larger than the interlayer separations in our ultra-thin oxide film samples. This plot for the attenuation of the Pd substrate photoemission signal as a function of the overlayer thickness therefore, does not necessarily reflect the experimental film growth mode of the oxide films, and the thicknesses provided should be viewed only as approximate coverages.

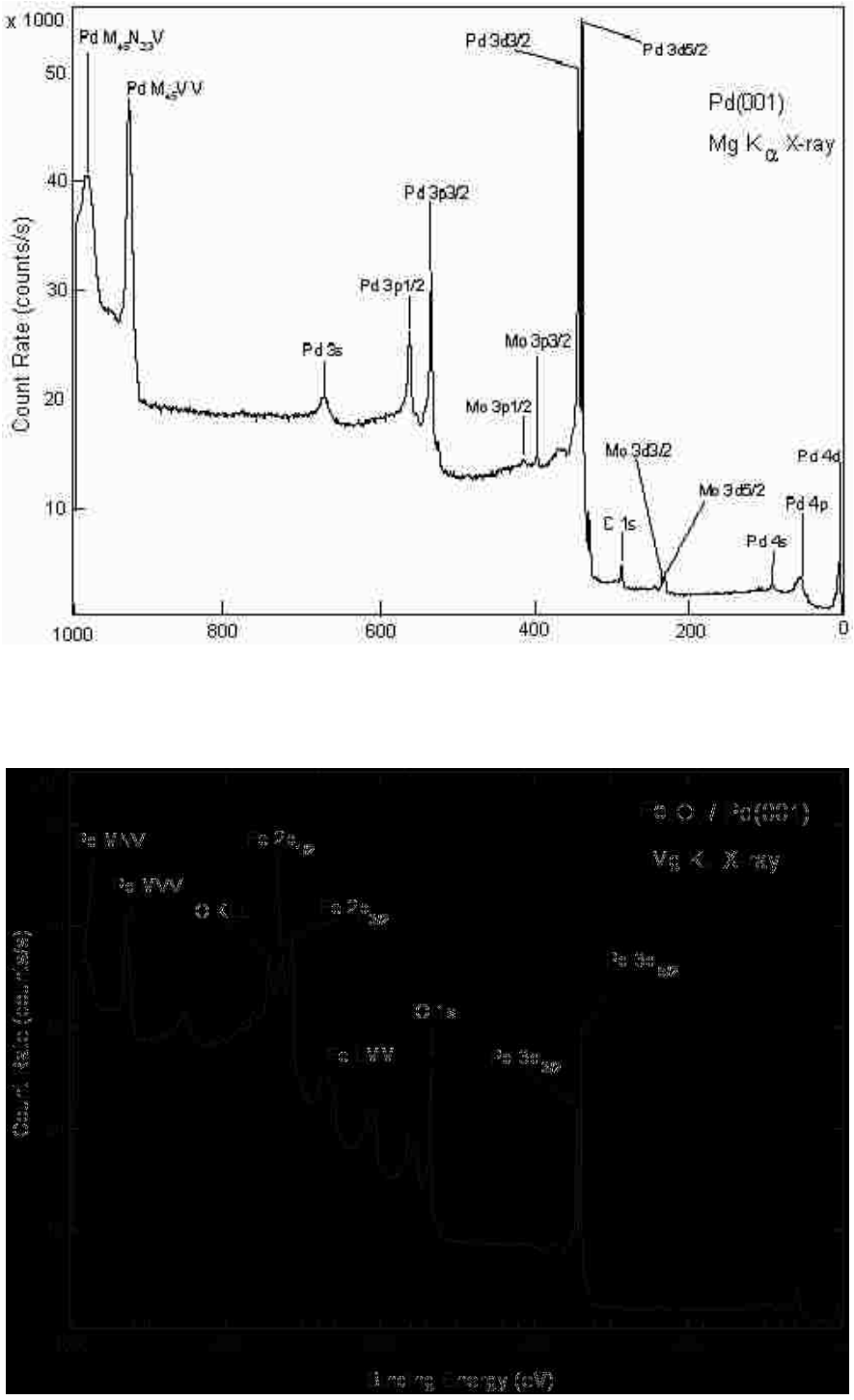

Figure 4.2. XPS survey from clean Pd(001) substrate (top) and from a 15 Å Fe_xO_y film (bottom).

Figure 4.3. The attenuation of Pd 3d photoemission intensity for the iron oxide film (circles) and for chromium film growth (triangles).

4.2.4. Film Morphology and Composition. Information on the chemical composition, film morphology, and valence of Fe in the growth of Fe_xO_y samples can be obtained from XPS. Chemical shifts observed in XPS spectra of the oxide samples provide information about the degree to which a metal film has been oxidized, and Fe valencies present in the oxide sample. The binding energy shifts for the Fe $2p_{3/2}$ core level observed in the oxide compounds as compared with Fe metal is close to 3 eV for the Fe^{3+} oxidation state, and 2 eV for the Fe^{2+} state [70]. In Figure 4.4, similar binding energy shifts of approximately ~ 3 eV were observed for both Fe $2p_{3/2}$ and Fe $2p_{1/2}$ core levels, implying that the Fe films were oxidized during the sample preparation process with no metallic Fe left unoxidized, as well as indicating that Fe^{3+} ions are present in the sample. The evidence for the presence of Fe^{2+} ions in the Figure 4.4 is less obvious in terms of observable chemical shifts. The binding energy separation of the Fe^{2+} and Fe^{3+} oxidation states has been reported to be ~1 eV [70], and given the limit to the experimental energy

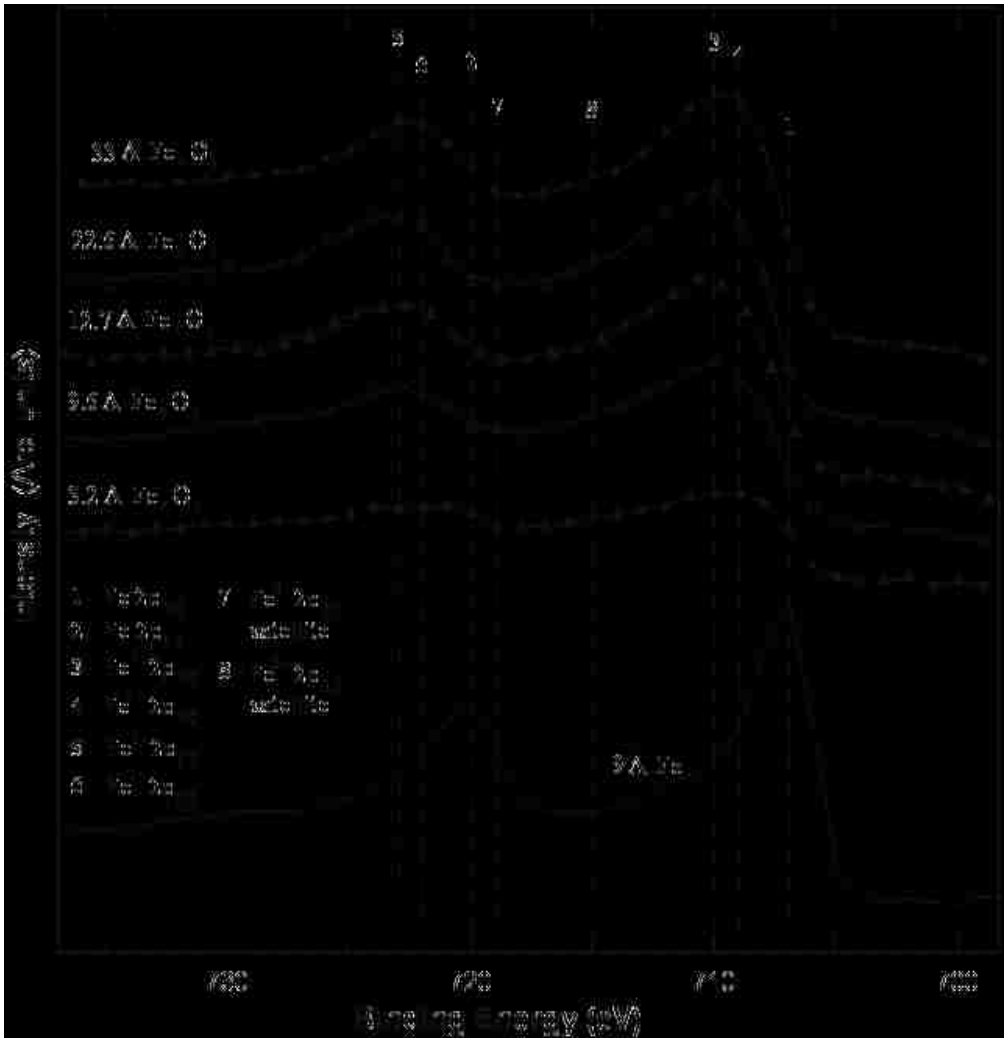

Figure 4.4. XPS of Fe 2p core level as a function of iron oxide film thickness. The observable shake-up satellites are consistent with the presence of Fe^{3+} and Fe^{2+} in these films.

resolution of the electron analyzer (Section 3.2.7), it is difficult to resolve the different peaks corresponding to the two different Fe valencies.

Aronniemi et al. [70] studied the effect of three different background subtraction methods on the analysis results for Cr_2O_3, Fe_2O_3, and Fe_3O_4. Table 4.1 shows some of the results obtained by Aronniemi et al. for iron-oxide. The presence of shake-up satellites features in the vicinity of the main photoelectron peaks can be examined for further analysis on the different chemical environments of the ions in the compound. For the Fe

2p core-level, the shake- up satellites are seen as discrete peaks on the low kinetic energy (high binding energy) side of both of the 2p peaks, and the energy separation between the 2p main peaks and the satellites is of the order of 6 eV for Fe^{2+} and 8 eV for Fe^{3+} [70, 103]. In Figure 4.4, the development of a pronounced shoulder (at 715 eV), especially at higher coverages of 22.6 Å and 33 Å, on the higher binding energy side of the Fe $2p_{3/2}$ level corresponds to the Fe^{2+} $2p_{3/2}$ satellite (energy separation from the Fe^{2+} $2p_{3/2}$ core-level peak = 6 eV). All these are indications of the presence of Fe^{2+} ions in the iron-oxide sample. The development of the shoulder corresponding to the Fe^{3+} $2p_{3/2}$ satellite is more difficult to observe. Broadening due to the overlapping of the shake-up satellites with the main line peaks, very low intensities of these features, and limit to the experimental energy resolution (as discussed in Section 3.2.7), make identification of the specific oxidation states of Fe in the oxide samples difficult, and the XPD and MSCD calculations have therefore been carried out to further understand the structure of these iron oxide surfaces.

Table 4.1. Chemical Information for Fe 2p

	"Tougard" [70] for Fe^{3+}	"Seah" [70] for Fe^{3+}	"Shirley" [70] for Fe^{3+}	"Tougard" [70] for Fe^{2+}	"Seah" [70] for Fe^{2+}	"Shirley" [70] for Fe^{2+}
BE $2p_{3/2}$ (eV)	710.6	710.6	710.4	709.2	709.2	709.0
$2p_{3/2}$ satellite shift	8.2	8.2	8.7	6.0	6.7	5.7

4.2.5. LEED Results for Iron-Oxide Film Growth on Pd(001). The stable LEED patterns observed for the ultrathin iron-oxide films grown using multilayer and sequential deposition techniques are the same. Figure 4.5 shows the diffraction patterns for clean Pd and the multilayer iron-oxide films grown on the Pd substrate. Figure 4.5(a) shows the LEED pattern of a clean Pd(001) substrate, and Figures 4.5(b) and 4.5(c) show

LEED patterns recorded from multilayer iron oxide surfaces with thicknesses 8.4 Å and 43.3 Å, respectively. All were observed at a primary electron energy of 96 eV. The films were given a final anneal at 420 °C for 30 minutes to obtain well-ordered surfaces and were cooled to room temperature before LEED analysis. The LEED patterns for the Fe_xO_y films grown using the multilayer deposition technique exhibit a c(8x2) pattern, and this pattern is observed at all coverages.

Figure 4.6 shows the diffraction patterns for clean Pd and the sequentially grown iron-oxide films grown on the Pd substrate. Figure 4.6(a) shows the LEED pattern for clean Pd(001), and Figures 4.6(b), 4.6(c), and 4.6(d) show LEED patterns recorded from sequentially grown Fe_xO_y surfaces with thicknesses 3.1 Å , 11.6 Å and 20 Å, respectively, using a primary electron energy of approximately 84 eV. The sequentially deposited films were also given a final anneal at 420 °C for 30 minutes to obtain well-ordered surfaces and cooled to room temperature before LEED analysis. For the sequentially deposited Fe_xO_y films, the LEED pattern obtained at all coverages is also a c(8x2). In Figure 4.6(b), the LEED pattern for a 3.1 Å oxide film shows a broadening of the diffraction spots implying that some amount of disorder is present during the initial growth of the films. With increasing thickness, the spot sizes decrease, as does the intensity. However, the diffraction patterns remains well-ordered all the way up to the highest coverages studied, and the c(8x2) structure does not change. The structure that is proposed for the iron oxide is a reconstructed FeO(001). The c(8x2) LEED pattern is actually the resultant of the superposition of the diffraction patterns arising from two different domains of the oxide film, and these domains are rotated by 90º with respect to each other. Figure 4.7 represents the structural relationship of the overlayer lattice with respect to the substrate fcc lattice in reciprocal and real space. Figure 4.7(a) shows the diffraction pattern from one orientation of the overlayer film on the Pd substrate, and Figure 4.7(c) the real space lattice structure of that overlayer orientation – the open circles represent the substrate and the filled squares represent the overlayer. Figure 4.7(d) shows the other overlayer orientation in real space, and Figure 4.7(b) represents the expected LEED pattern resulting from the two domain film.

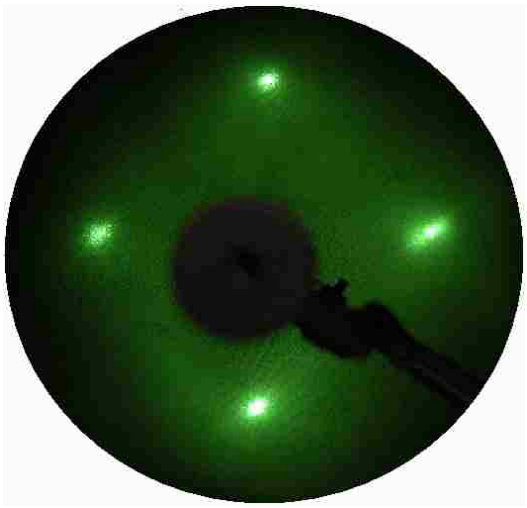

(a)

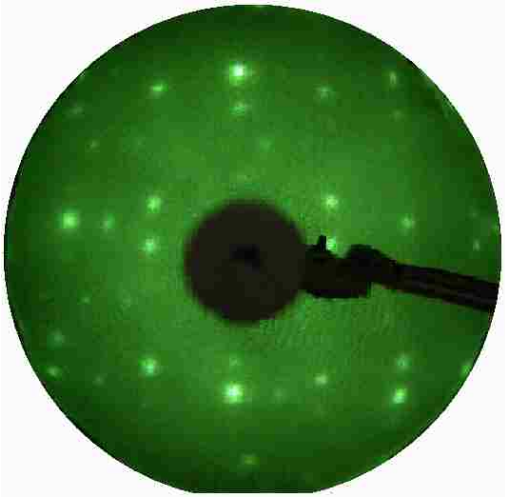

(b)

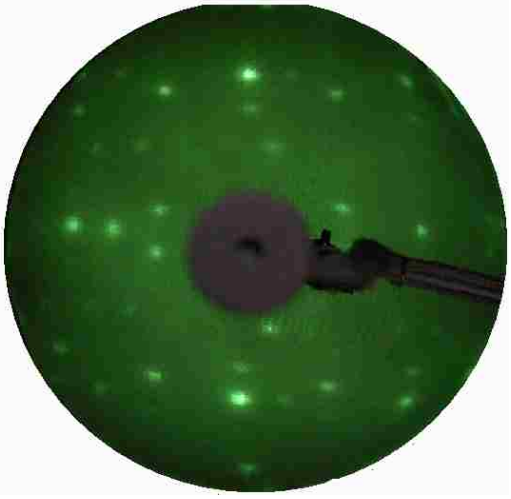

(c)

Figure 4.5. LEED patterns for Fe_xO_y films grown by multilayer deposition technique: (a) clean Pd(001) (b) 8.4 Å thick Fe_xO_y film, and (c) 43 Å Fe_xO_y film at electron energy of 96 eV.

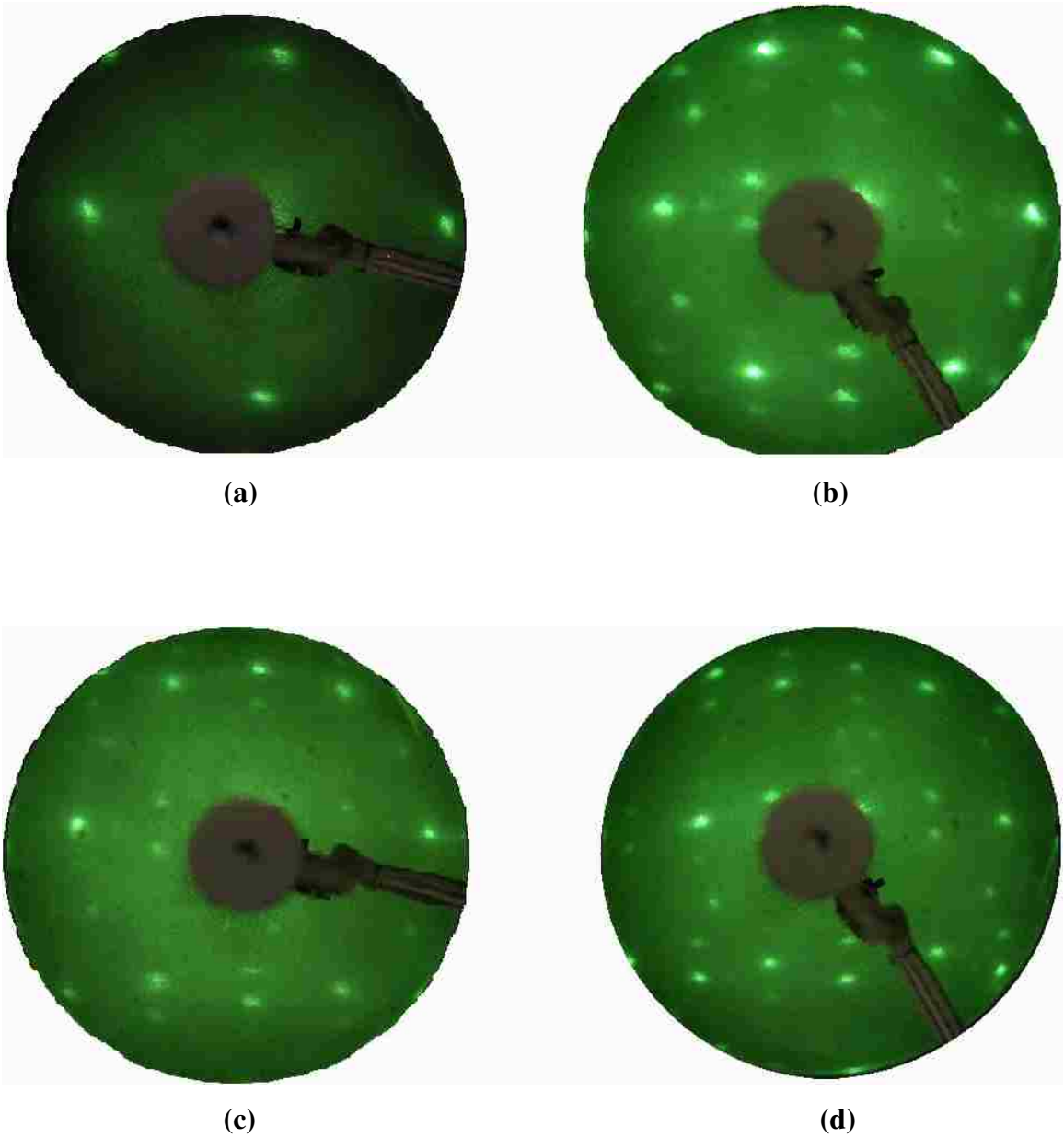

Figure 4.6. LEED patterns for Fe_xO_y films grown by sequential deposition technique: (a) clean Pd(001) at electron energy of 84 eV, (b) 3.1 Å thick Fe_xO_y film, (c) 11.6 Å thick Fe_xO_y film, and (d) 20 Å Fe_xO_y film at primary electron energy of approximately 84 eV.

Fe_xO_y Reciprocal Space Fe_xO_y Real Space

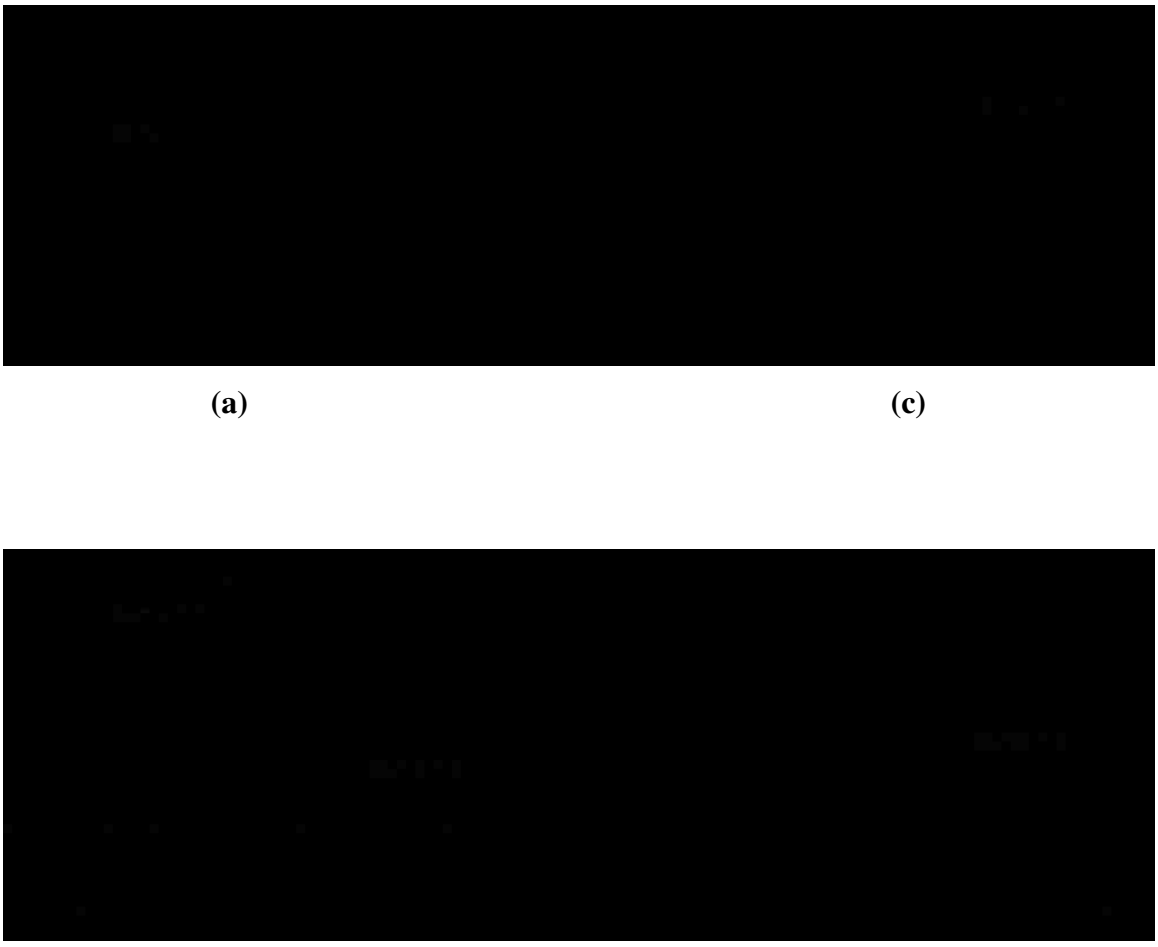

(a) **(c)**

(b) **(d)**

Figure 4.7. Top views of the Fe_xO_y surfaces. Panel (a) is the expected LEED pattern from a single domain of the overlayer, (b) is expected LEED pattern from the superposition of two overlayer domains rotated by 90° with respect to each other respectively; (c) is the real space structure of one overlayer domain, and (d) is real space structure of the other overlayer domain rotated by 90°. Open circles represent the substrate lattice, filled squares and filled circles represent domains of the overlayer.

4.2.6. XPD and MSCD Results. For further investigation of the structures of the iron-oxide films grown using the multilayer and sequential deposition techniques, XPD polar and azimuthal scans for the Fe $2p_{3/2}$ core level and the O $KL_{23}L_{23}$ Auger level were performed for the c(8x2) LEED patterns. The polar scans were conducted in the Pd(001) and Pd(110) scattering planes and for film coverages ranging from ~8 Å to 43 Å.

While the LEED patterns do not show any change with coverage, the XPD curves exhibit differences for the low and high coverage systems – this reflects a change in the lattice structural parameters from the low to high coverage films. In the remaining discussion of the multilayer and sequentially deposited iron oxide films, XPD experimental results will be presented for the both the low and high coverage oxide phases and the model calculations for the reconstructed FeO(001) surface. No XPD measurements were performed for the very low coverages (1-3 Å) due to the difficulty of acquiring good XPD data from a very thin film.

A comparison of the XPD polar angle curves for multilayer oxide films (circles) and sequential oxide films (triangles) acquired in the Pd(100) scattering plane is shown in Figure 4.8. The Figure 4.8(a) shows the Fe $2p_{3/2}$ results and Figure 4.8(b) shows the O $KL_{23}L_{23}$ results. It can be observed that while the deposition technique has little effect on the XPD curves, the results for the low coverage films (open circles and open triangles) differ from those for the high coverage films (filled circles and filled triangles).

Figure 4.9 shows azimuthal XPD scans obtained for the Fe $2p_{3/2}$ core level and O $KL_{23}L_{23}$ Auger level. Figure 4.9(a) shows experimental XPD azimuthal scans for Fe $2p_{3/2}$ data for multilayer and sequential oxide films, and Figure 4.9(b) shows data for O $KL_{23}L_{23}$ data for multilayer and sequential oxide films. The azimuthal scans for Fe $2p_{3/2}$ and O $KL_{23}L_{23}$ are taken at polar scattering angles of $\theta = 34°$ and $\theta = 40°$, respectively, and the scans exhibit photoelectron intensity fluctuations with peaks that are approximately 45° apart. These, along with LEED patterns, therefore suggest that the Fe_xO_y films have a 4-fold symmetry and cubic structure.

Based on the LEED and XPD results, a reconstructed FeO(001) surface is proposed for the films. FeO has a NaCl-type structure and a bulk lattice constant of 4.31 Å. For the observed c(8x2) LEED pattern, the overlayer lattice parameters for the bulk unit cell with respect to the substrate surface are defined by $a_1 = 11.33$ Å, $a_2 = 11.33$ Å,

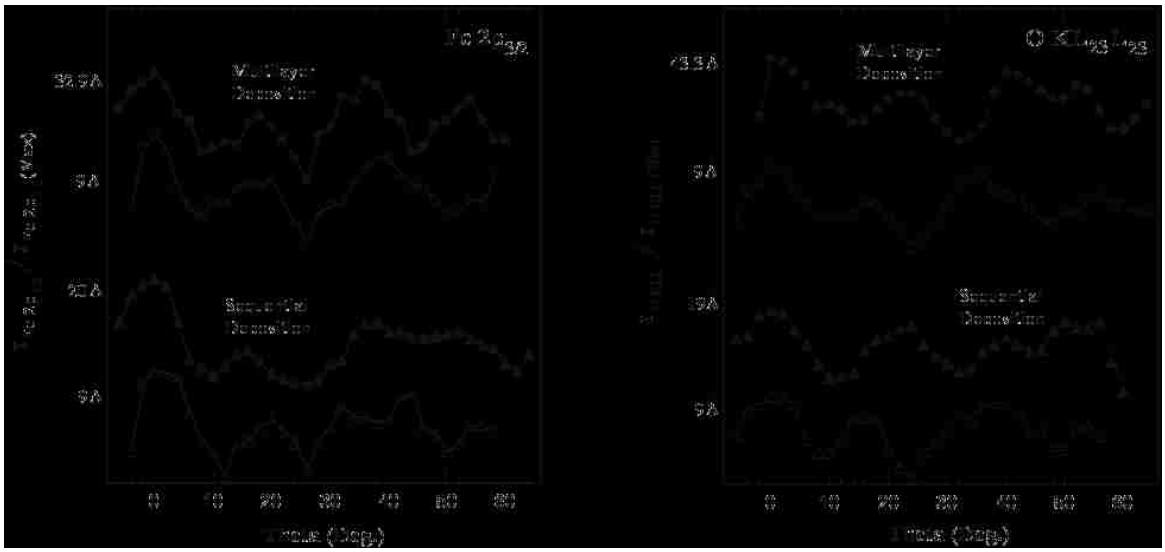

(a) **(b)**

Figure 4.8. XPD polar scans in the Pd(100) scattering plane for (a) Fe $2p_{3/2}$, and (b) O $KL_{23}L_{23}$ for iron oxide films grown using the multilayer deposition technique (top two curves), and the sequential deposition technique (bottom two curves).

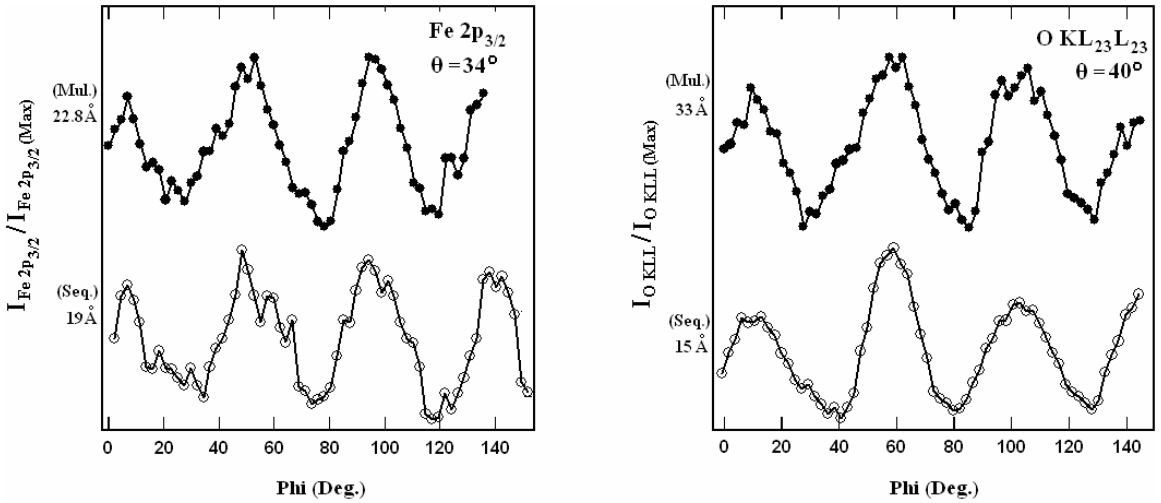

(a) **(b)**

Figure 4.9. XPD azimuthal scans for (a) Fe $2p_{3/2}$ at polar scattering angle of 34°, and for (b) O $KL_{23}L_{23}$ at polar scattering angle of 40°. [Mul. – multilayer oxide films, Seq. – sequential oxide films].

and φ = 28°. The (001) plane in bulk FeO has a surface lattice constant of 3.048 Å and a Fe-O distance of 2.155 Å. The unreconstructed FeO(001) surface is autocompensated and the nearest neighbor distance in the (001) plane is 2.155 Å. However, this unreconstructed Fe(001) surface does not produce the expected LEED pattern, and therefore an autocompensated reconstruction of the (001) surface has to take place, as will be discussed soon.

Figure 4.10 shows the unreconstructed and reconstructed surfaces of the FeO(001) surface. In the unreconstructed bulk FeO unit cell shown in Figure 4.10(a), one Fe^{2+} ion contributes 2 electrons to 6 bonds to neighboring oxygen atoms. Therefore each bond contains $(2e^-)/6 = 1/3e^-$, that are donated from the Fe^{2+} ions. Assuming two electrons per bond, each oxygen contributes $(2\text{-}1/3)e^- = 5/3e^-$ to each Fe-O bond. These numbers can be used to determine dangling bond charges when different surface terminations are created. For the c(8x2) overlayer surface unit cell in Figure 4.10(c), if two oxygen ions are removed per unit cell from the surface, the number of broken bonds that result is 10. The charge contribution due to the formation of the dangling bonds associated with the surface Fe^{2+} ions and the Fe^{2+} ions in the layer below when the two surface oxygen ions are removed is $10x(1/3e^-) = 10/3e^-$. Transferring electrons from iron-derived dangling bonds to oxygen-derived dangling bonds in the overlayer surface unit cell leaves the latter deficient by $(6\text{-}10/3)e^- = 8/3e^-$. This charge could be supplied by adding one Fe ion per unit cell in a new layer above the surface which had the oxygen ions removed, and by raising the average oxidation state of these Fe ions in the termination layer to 2.67^+. This can be obtained from a surface distribution of Fe^{3+} and Fe^{2+} ions in the ratio of Fe^{3+}:Fe^{2+} = 4:2. This would explain the prevalence of Fe^{3+} in our XPS results.

4.2.6.1 MSCD calculations for the low coverage films. In the low coverage films in the experiment, interaction between the oxide layer and the substrate results in a strained overlayer, and the film is forced to adopt the surface lattice parameters of Pd (a_0^{Pd} = 2.75 Å). As discussed in Section 3.2.6.1, R-factor calculations are also performed for optimization of the surface lattice constant of the reconstructed FeO(001) structure, and for the interlayer separation d_{12}. In each case the R-factor is the total for all polar angles and for both Fe and O. For low coverage iron oxide films (in the range of 3-13 Å),

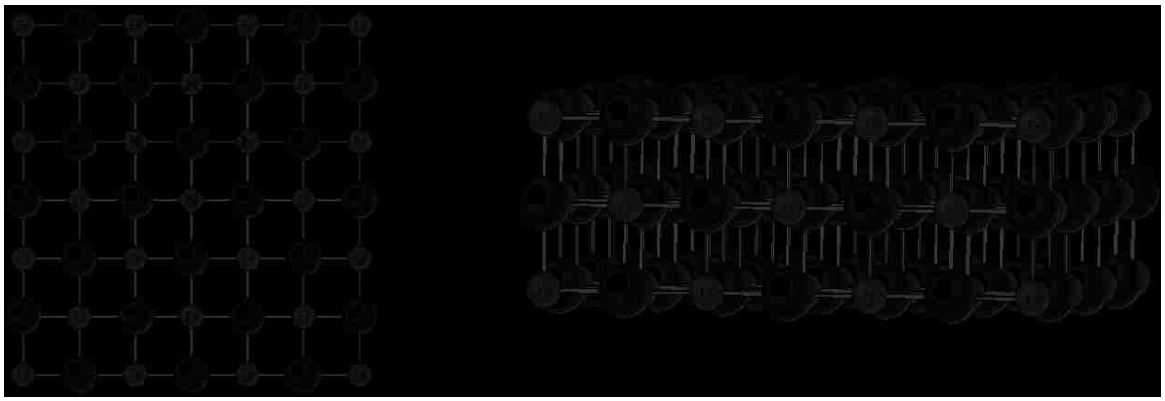

(a) **(b)**

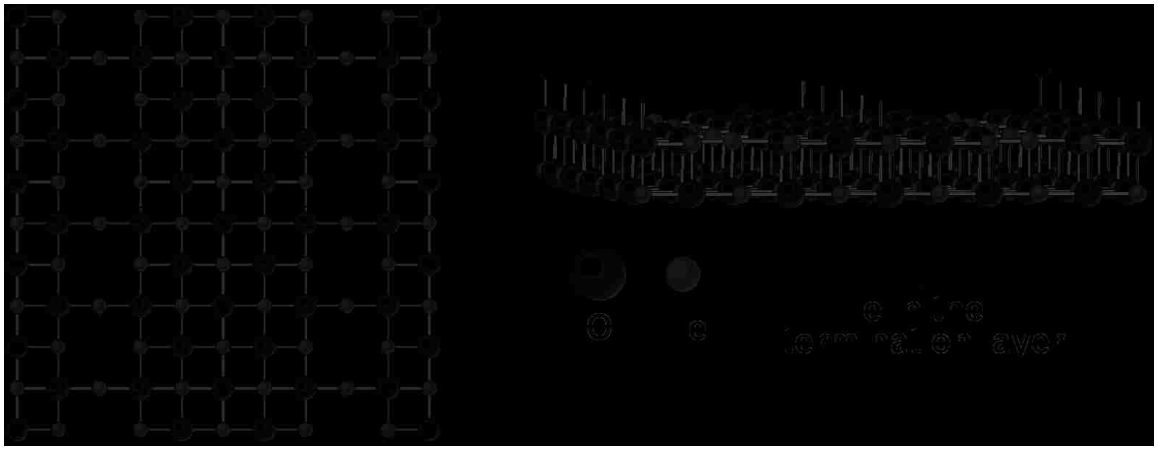

(c) **(d)**

Figure 4.10. Atomic structure of FeO(001). Panel (a) is top view of the unreconstructed surface, (b) is side view of FeO, (c) is top view of the reconstructed top two layers, and (d) is side view of the top three layers of reconstructed FeO(001).

the R-factor analysis for the surface lattice constant was carried out through a series of calculations assuming different values of a_0^{FeO} from 2.60 Å (14.5 % compression compared to 3.05 Å) to 3.11 Å (3.6 % expansion compared to 3.05 Å) in steps of 0.03 Å ($\approx 1\%$). As shown in Figure 4.11, a minimum for the R-factor is obtained at a surface lattice constant of a_0^{FeO} = 2.75 Å. This exactly matches the Pd(001) surface lattice constant. Thus, due to a strong interaction between the metal oxide and the substrate at the initial stages of growth, the FeO structure is forced to adopt the lattice parameters of Pd. The behavior of the R-factor as a function of the interlayer separation between the first and second layer, d_{12}, with a surface lattice constant value of 2.75 Å (Figure 4.12) shows a minimum at d_{12} = 1.56 Å which is a 20% contraction of with respect to the bulk value of d_{12}. However the deviations are very small over a wide range of d_{12}, indicating insensitivity of our results to this parameter.

Experimental polar XPD scans were carried out in the φ = 0° and φ = 45° scattering planes with respect to Pd(001) surface (φ = 0° corresponds to the Pd[100] direction, and φ = 45° corresponds to the Pd[110] direction). Figures 4.13 and 4.14 include the XPD polar scans, and the MSCD curves for the Fe $2p_{3/2}$ core level (left panels) and the O $KL_{23}L_{23}$ Auger level (right panels) for the low coverage iron oxide films. The top two curves in each figure are XPD experimental results (open and filled circles) for oxide films grown using the multilayer and sequential deposition techniques respectively, and the curves below the experimental curves represent the model calculations (open and filled triangles) for the reconstructed FeO(001) surface.

4.2.6.2 MSCD calculations for the high coverage films. For the high coverage iron-oxide films, the R-factor calculation, shown in 4.15, for the surface lattice constant shows a minimum at 2.96 Å. This is considerably larger than the Pd lattice constant of 2.75 Å, and is closer to the bulk-FeO value of 3.05 Å. For this value of lattice constant the R-factor for optimization of d_{12} has a minimum value at 1.76 Å (Figure 4.16), which is a 16% contraction with respect to the unrelaxed value of d_{12} = 2.093 Å of for surface lattice constant of 2.96 Å.

R-factor calculations were also performed for optimization of the separation between the first and second layers at the value of the bulk lattice constant of 3.05 Å (Figure 4.17), and the minimum R-factor was obtained at d_{12} = 1.81 Å which signifies a

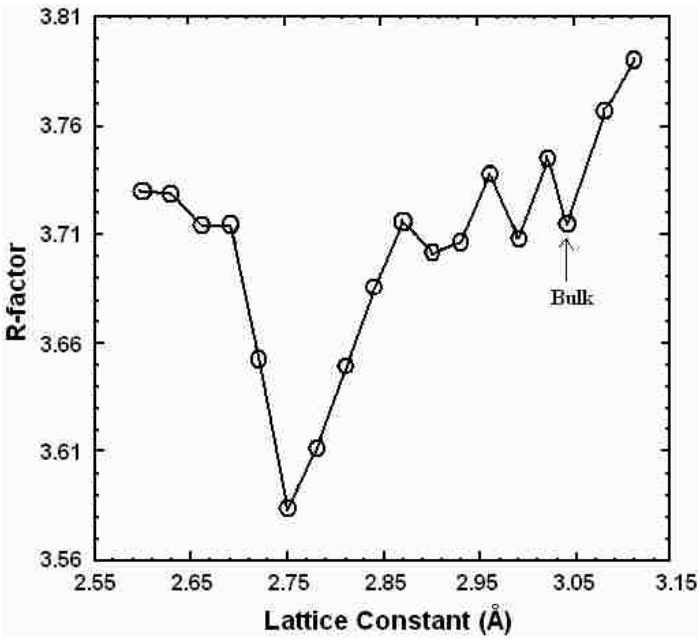

Figure 4.11. Behavior of the R-factor for FeO as a function of the surface lattice constant for the low coverage oxide films.

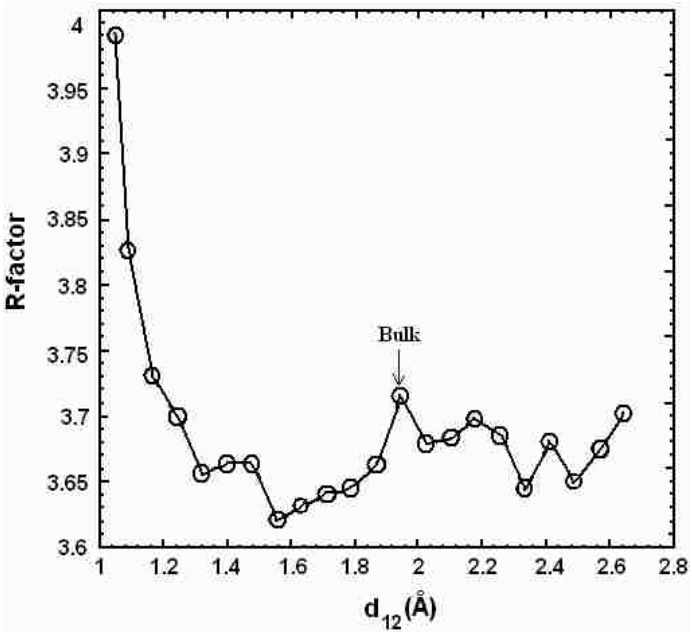

Figure 4.12. Behavior of the R-factor for FeO as a function of d_{12} for the low coverage oxide films with surface lattice constant of 2.75 Å.

Low coverage: Fe_xO_y(001)/ Pd(001)

Pd(100) scattering plane

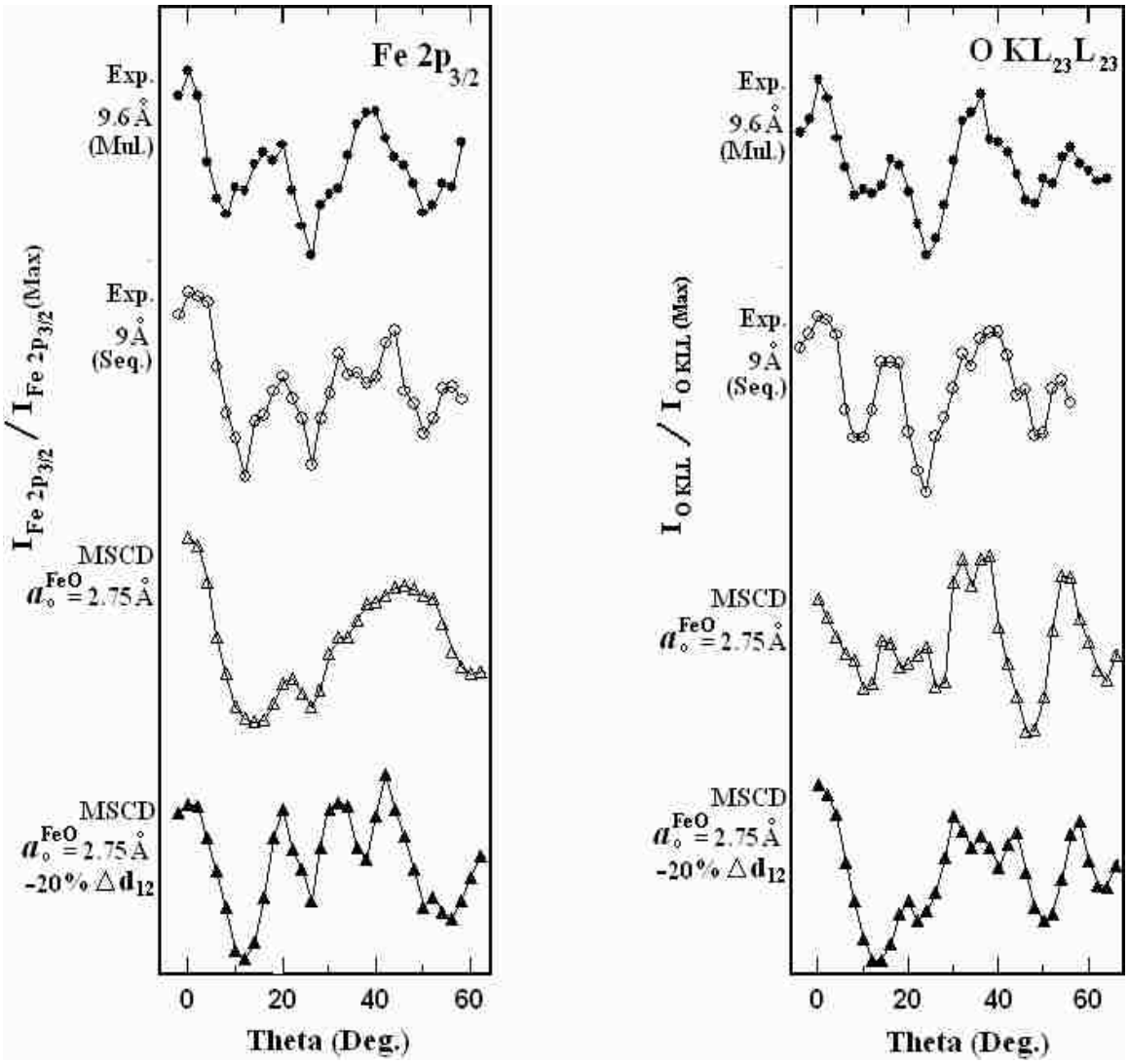

Figure 4.13. Polar scan XPD curves, and MSCD curves for low coverage iron oxide films. Results for Fe $2p_{3/2}$ (left) and O $KL_{23}L_{23}$ (right) are for the scattering plane corresponding to $\varphi = 0°$. The top two curves are for the experimental multilayer oxide (filled circles) and sequential oxide (empty circles) films respectively. The bottom two curves are MSCD curves (triangles).

Low coverage: $Fe_xO_y(001)$/ Pd(001)

Pd(110) scattering plane

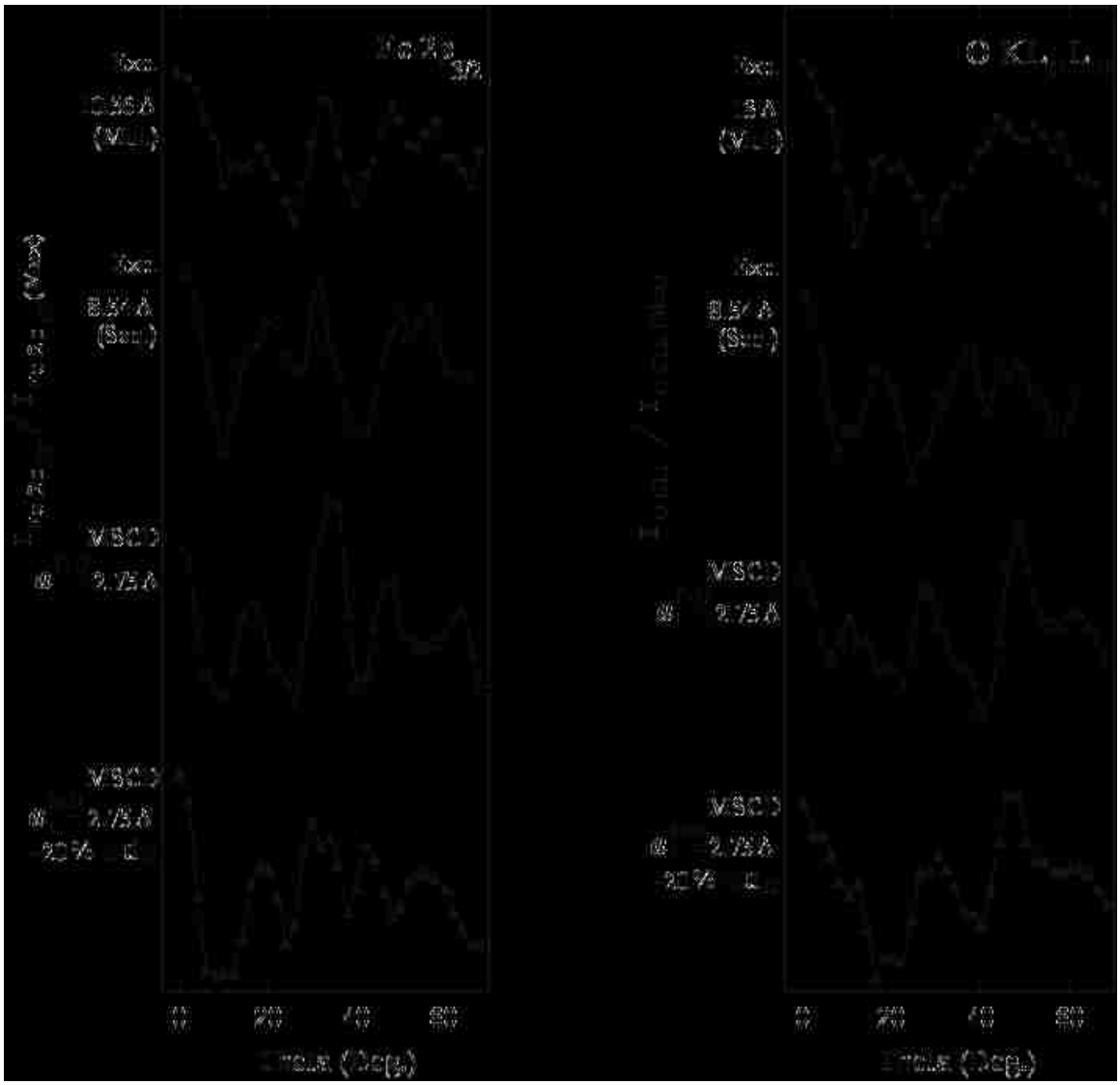

Figure 4.14. Polar scan XPD curves, and MSCD curves for low coverage iron oxide films. Results for Fe $2p_{3/2}$ (left) and O $KL_{23}L_{23}$ (right) are for the scattering plane corresponding to $\varphi = 45°$. The top two curves are for the experimental multilayer oxide (filled circles) and sequential oxide (empty circles) films respectively. The bottom two curves are MSCD curves (triangles).

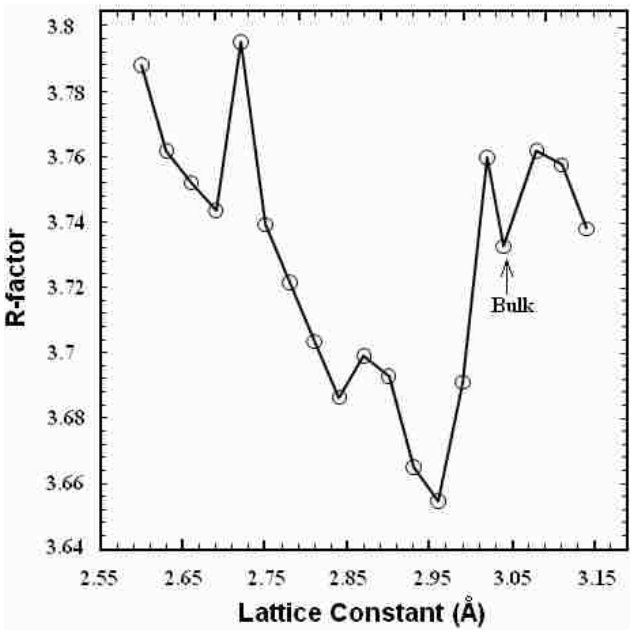

Figure 4.15. Behavior of the R-factor for FeO as a function of the surface lattice constant for the high coverage oxide film.

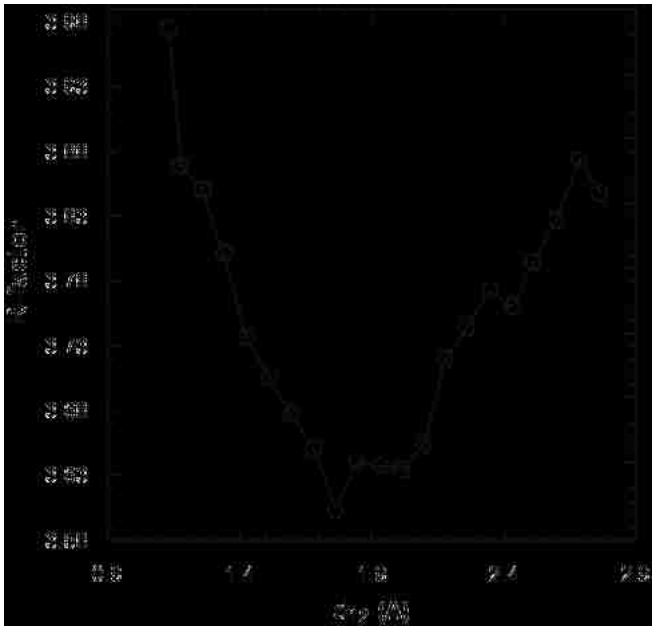

Figure 4.16. Behavior of the R-factor for FeO as a function of d_{12} for the high coverage oxide films with surface lattice constant of 2.96 Å.

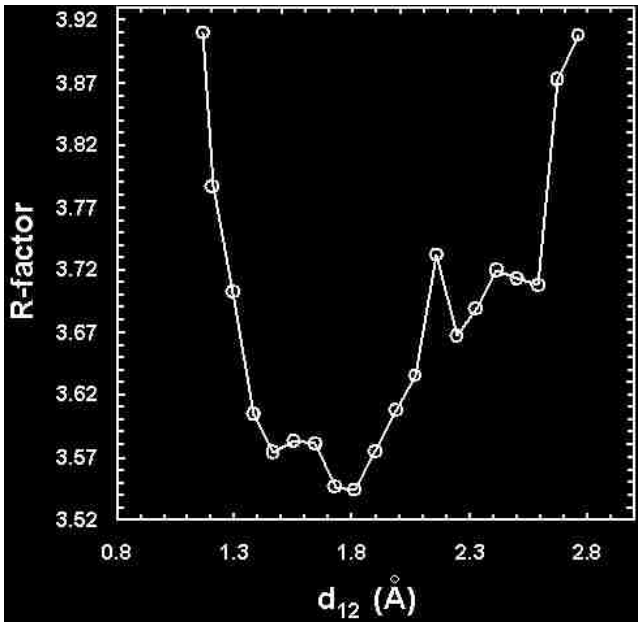

Figure 4.17. Behavior of the R-factor for FeO as a function of d_{12} for the high coverage oxide films with surface lattice constant of 3.05 Å.

16% contraction. Out of all the R-factors calculated for the high coverage systems, the lowest R-factor is obtained for a_0^{FeO} = 3.05 Å with a 16% contraction of the first interlayer spacing. Thus with increasing coverage of the Fe_xO_y films, the effect of the Pd substrate on the film structural parameters is reduced, and the oxide film approaches bulk parameters, though there is strain present in the film as is evident from the R-factor calculation for the optimization of d_{12}.

Figures 4.18 and 4.19 show the experimental polar XPD scans were carried out in the φ = 0° and φ = 45° scattering planes with respect to Pd(001) surface (φ = 0° corresponds to the Pd[100] direction, and φ = 45° corresponds to the Pd[110] direction), and the corresponding MSCD curves for the Fe $2p_{3/2}$ core level (left panels) and the O $KL_{23}L_{23}$ Auger level (right panels) for the high coverage iron oxide films. The top two curves in each figure are XPD experimental results (open and filled circles) for oxide films grown using the multilayer and sequential deposition techniques respectively, and the curves below the experimental curves represent the model calculations (open and filled triangles) for the reconstructed FeO(001) surface.

High coverage: Fe_xO_y(001)/ Pd(001)

Pd(100) scattering plane

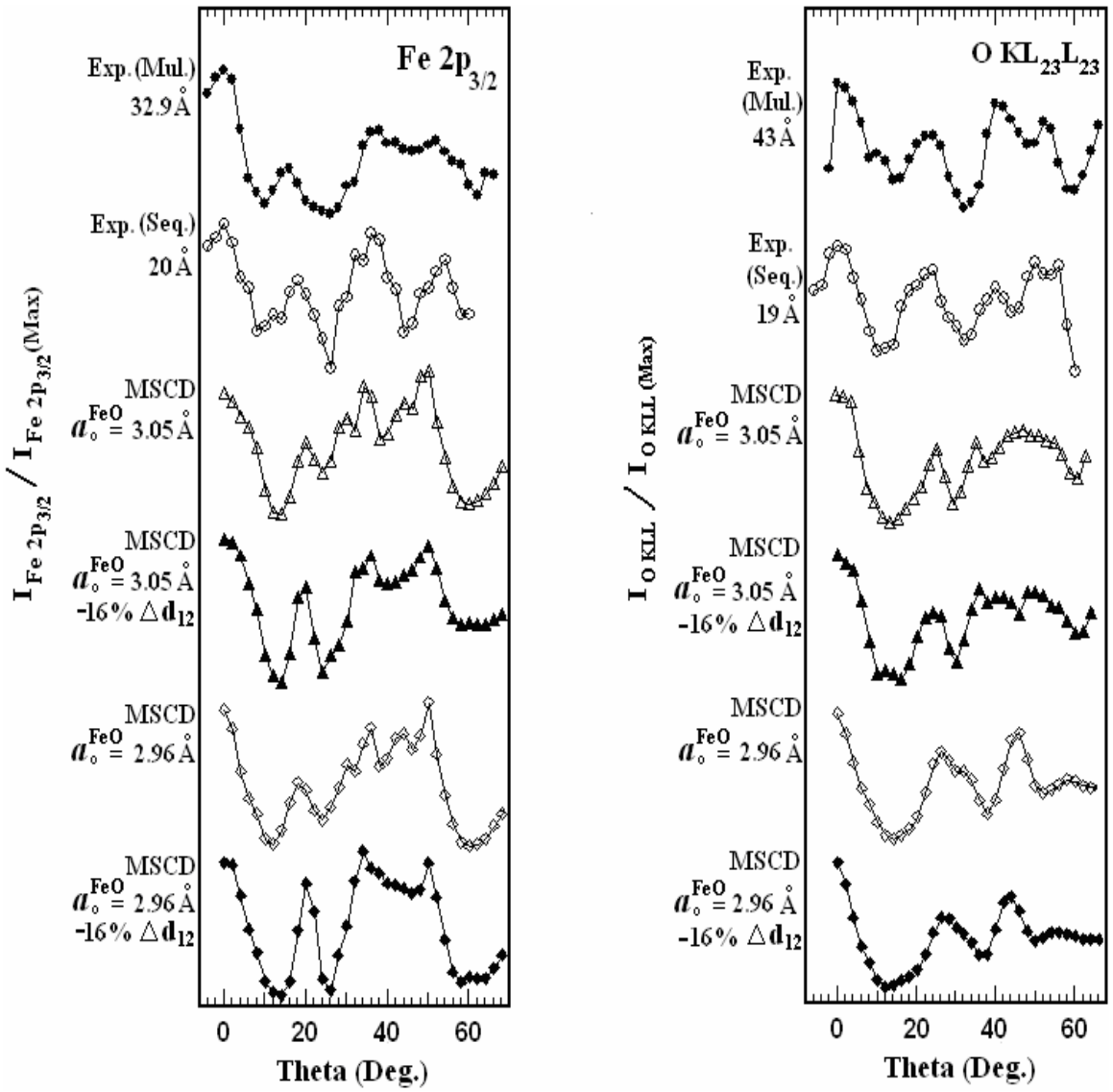

Figure 4.18. Polar scan XPD curves, and MSCD curves for the high coverage iron oxide films. Results for Fe $2p_{3/2}$ (left) and O $KL_{23}L_{23}$ (right) are for the scattering plane corresponding to $\varphi = 0°$. The top two curves are for the experimental multilayer oxide (filled circles) and sequential oxide (empty circles) films respectively. The bottom four curves are MSCD curves (triangles and diamonds).

High coverage: $Fe_xO_y(001)$/ Pd(001)

Pd(110) scattering plane

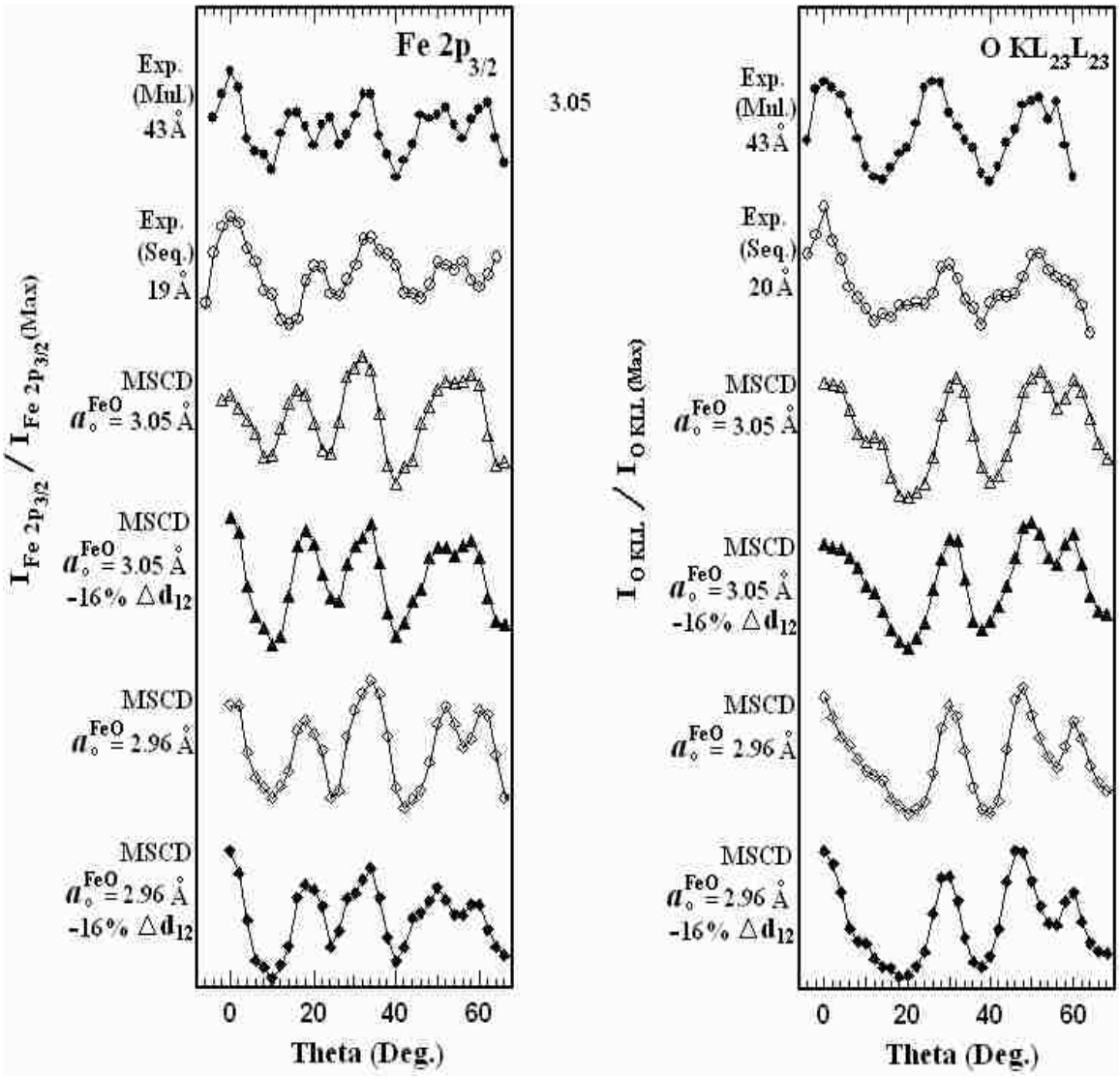

Figure 4.19. Polar scan XPD curves, and MSCD curves for the high coverage iron oxide films. Results for Fe $2p_{3/2}$ (left) and O $KL_{23}L_{23}$ (right) are for the scattering plane corresponding to $\varphi = 45°$. The top two curves are for the experimental multilayer oxide (filled circles) and sequential oxide (empty circles) films respectively. The bottom four curves are MSCD curves (triangles and diamonds).

4.2.7. Summary and Conclusions. High quality iron-oxide films were obtained from both the multilayer and sequential deposition techniques. Both methods also yielded similar oxide structures, though there are structural differences observed between the low and high coverage systems for both methods of deposition from the XPD results, the crossover point being somewhere around 13 Å. While the LEED patterns do not reveal any difference in the surface structure of the films obtained from either deposition technique, the LEED results do exhibit poorer order for the sequentially deposited films at very low coverages (Figures 4.6(b)).

An attempt was made to determine the oxidation state of Fe using XPS scans. Chemical shifts of ~ 3 eV (towards the higher binding energy side) in the photoemission peak positions of Fe 2p peaks in the iron oxide samples with respect to metal Fe were observed in the XPS scan. The 3 eV chemical shift is consistent with the presence of Fe^{3+} ions in the oxide samples. However detecting the presence of Fe^{2+} was more challenging. Distinguishing the chemical shift for the Fe^{2+} oxidation state was not possible due to the small energy difference of ~1 eV between the Fe^{3+} and Fe^{2+} oxidation states, and the limit to the experimental energy resolution as discussed in Section 3.2.4. The observation of prominent Fe^{2+} $2p_{3/2}$ satellites, however, suggests the presence of Fe^{2+} ions. This would make sense given the fact that a FeO(001) structure with a reconstructed surface has been suggested and modeled with an iron terminated layer having both Fe^{2+} and Fe^{3+} ions.

For the thin iron oxide films, a c(8x2) LEED pattern is observed. The LEED pattern shows an initial broadening of the diffraction spots implying that some amount of disorder is present during the very early stages of growth of the films. With increasing thickness, the spot sizes decrease and the LEED pattern becomes more ordered, and it remains a c(8x2) at all the coverages studied. This LEED pattern is believed to be consistent with the growth of a reconstructed FeO(001) surface with an iron terminated layer. XPD analysis of the c(8x2) structure for the multilayer and sequential deposition techniques at both low and high coverages was performed. R-factor calculations suggest that while no phase change occurs with increase in oxide coverage, there is definitely a transition in the values of the lattice structural parameters in going from the low to high coverage systems. The thin films adopted the surface lattice parameter of Pd, $a_0^{FeO} = a_0^{Pd} =$ 2.75 Å. From the rather modest agreement of the MSCD curves for the low coverage

unstrained structure with the XPD curves for $OKL_{23}L_{23}$, and the still poorer agreement of the O $KL_{23}L_{23}$ XPD curves with the MSCD results with strain incorporated (Figures 4.13 and 4.14), makes it difficult to comment on the presence or absence of strain in the film. There, however, is satisfactory agreement of the MSCD curves for the Fe $2p_{3/2}$ core level with the experimental XPD curves with somewhat better agreement for the models with relaxed d_{12}. For the thicker films, the R-factor calculations show that the oxide structure for the high coverage systems is still a reconstructed FeO(001) but with more bulk-like FeO in plane lattice parameters. The best agreement for the high coverage XPD curves is obtained for a_0^{FeO} = 3.05 Å with a first interlayer separation ~16% less than the bulk value.

In the case of the growth of Fe_xO_y films on Pd(001), the deposition technique has little effect on the growth of the iron oxide films, while the interaction of Pd substrate with the overlayer at low coverages is strong enough to force the oxide to adopt the substrate lattice parameters. From previous studies done on the growth of iron-oxide films on Ag(001) using the multilayer and sequential growth techniques [102], ordered oxide structures were obtained from both the deposition methods, and it was observed that the deposition technique influences the symmetry of the oxide formed. While multilayer growth of Fe_xO_y on Ag(001) resulted in structures with four-fold symmetry and the oxide proposed was Fe_3O_4(100), sequential growth of Fe_xO_y on Ag(001) resulted in 3-fold symmetry structures and the oxide proposed was Fe_3O_4(111). This aspect of the growth of the Fe_xO_y films on the Pd(001) and Ag(001) substrates with respect to the method of deposition and the substrate-overlayer interaction will be explored further, as well as a comparison study made between the Fe_xO_y/Pd(001) and Fe_xO_y/Ag(001) systems in Section 5.

5. METAL AND METAL-OXIDE GROWTH

5.1. BACKGROUND

The ultrathin iron- and chromium-oxide films in this study were grown by thermal oxidation under specific experimental conditions. By thermal oxidation, it is implied that the investigations involved will be for the growth of the basic system of metal substrate/oxide film/oxygen gas, from room temperature upwards. The term "film" would imply a layer of oxide ranging from sub-monolayer to tens of angstroms thick, and the growth of such a film would be preceded by the adsorption of the gas molecules (oxygen, in this case), their dissociation and ionization, rearrangement to form the oxide nuclei, possible reconstructions for surface energy minimization, and the lateral growth of the oxide nuclei (following oxygen solution in which the oxide precipitates in oxygen-saturated regions of the metal surface) to form complete oxide layers. In the scope of the present discussion, it will not be possible to make a comprehensive review of such a complex subject, and so the idea here is to *qualitatively* isolate some factors that might give a better insight into understanding the observations that were made for the iron- and chromium-oxides formed under the given conditions of the present experiment.

The overall chemical reaction involved in the oxidation of a metal is represented by a simple equation,

$$x\mathrm{Me} + \tfrac{1}{2}\, y\mathrm{O}_2 \rightleftarrows \mathrm{Me}_x\mathrm{O}_y \qquad (5.1)$$

where 'Me' represents the metal involved in the oxidation process. The deceptive simplicity of the overall chemical reaction belies the complexity of the diffusion processes and phase boundary reactions that determine the progress of the oxidation processes. The reaction will involve the change in the free energy associated with the formation of oxide from the reactants. The reaction mechanism will also in general depend on temperature, oxygen pressure, surface orientation, crystal structure, and physical and chemical properties of the metal, metal oxide, and the substrate. The current discussion will not consider the detailed thermodynamics and diffusion processes that govern such reactions, but rather present a general overview, and will be more concerned

with a discussion of the experimental studies in the current study and others similar to this study in the existing literature that might provide a greater *qualitative* insight into the metal oxidation process. Another objective of this discussion will be to explore the differences observed in the growth of the ultrathin iron- and chromium-oxide films on Ag(001) and on Pd(001) using the two techniques of sequential deposition and multilayer deposition.

5.2. A REVIEW OF RESULTS

A brief review of the results on the growth of iron- and chromium- oxide films on Ag(001) and Pd(001) are presented in this section.

5.2.1. Chromium-Oxide Film Growth on Ag(001). Ozturk and Waddill [58] studied the growth of ultrathin chromium-oxide films on Ag(001) using the multilayer and sequential deposition techniques. The multilayer Cr(001) films on Ag(001) were exposed to 10^{-5} Torr of O_2 at 350-400 °C substrate temperature. The oxidized samples were then annealed at 400 °C for 30 minutes. Figure 5.1 shows the diffraction patterns for clean Ag and the chromium-oxide films grown on Ag(001). Figure 5.1(a) shows the LEED pattern for clean Ag, and Figure 5.1(b) shows the LEED pattern for a chromium oxide film of thickness 18 ML. All LEED patterns were recorded using an electron energy of approximately 90 eV. The LEED pattern for the chromium oxide film at 18 ML has been proposed to be due to the growth of two domains of α-Cr_2O_3(210) that has a surface net defined by a_1 = 5.35 Å, a_2 = 8.58 Å, and φ = 74.5°. The oxide film obtained from the multilayer deposition technique has 4-fold symmetry.

The LEED pattern observed for the chromium oxide film grown using the sequential deposition technique is dramatically different from that obtained with the previous growth technique. In the sequential method, Cr was deposited in 0.5 ML steps and oxidized at 150 °C. Following the final deposition-oxidation step, the films were annealed at 400 °C for 30 minutes. Figure 5.1(c) shows the LEED pattern for an annealed 13 Å film. It is obvious that the LEED pattern displays an oxide structure with three-fold symmetry and has been attributed to be consistent with 2 domains of α-Cr_2O_3(111) with a surface net defined by $a_1 = a_2$ = 4.90 Å, and φ = 60°.

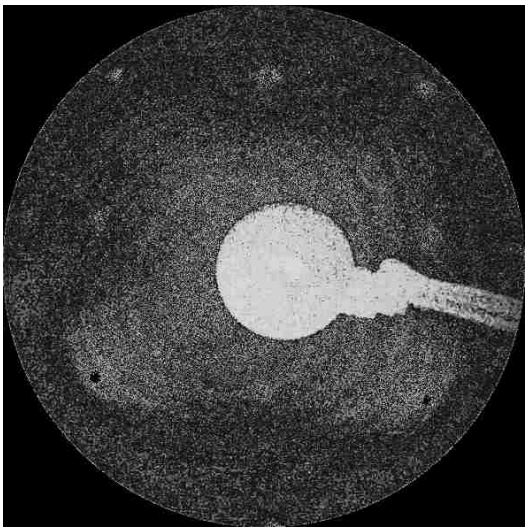

(a)

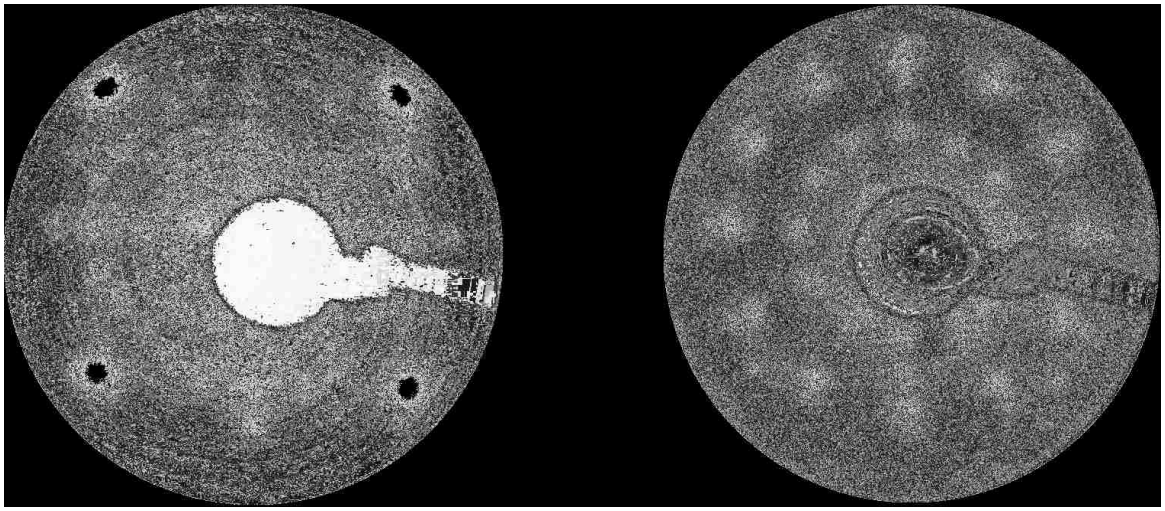

(b) **(c)**

Figure 5.1. LEED patterns for (a) clean Ag(001), (b) 18 ML of α-Cr_2O_3(210) grown by multilayer deposition technique, and (c) 13 Å of Cr_2O_3(111) grown by sequential deposition technique, on Ag(001), for primary electron energy of approximately 90 eV [58].

5.2.2. Iron-Oxide Film Growth on Ag(001). Priyantha and Waddill [99] studied the growth of ultrathin iron-oxide films on Ag(001) using the multilayer and the sequential deposition techniques. Figure 5.2 shows the diffraction patterns for clean Ag and the iron-oxide films deposited on Ag(001).

Figure 5.2(a) shows the LEED pattern for the clean Ag(001) substrate at an electron energy of 67 eV. Figure 5.2(b) shows the LEED pattern taken from a 15 Å thick iron oxide film obtained from the oxidation of a multilayer Fe(001) film. The LEED pattern was observed at an electron energy of approximately 67 eV. The film was annealed at 420 °C for 30 minutes, and the LEED analysis was done at room temperature. This oxide film has 4-fold symmetry, and the diffraction pattern has a $(2\sqrt{2}x2\sqrt{2})R45°$ overlayer orientation with respect to the Ag(001) substrate. This pattern has been attributed to a $Fe_3O_4(001)$ surface.

Figure 5.2(c) shows the LEED pattern recorded from a 28 Å thick sequentially grown iron oxide surface on Ag(001), at primary electron energy of 67 eV. After repeated cycles of submonolayer deposition of iron oxide, the film was given a final anneal at 420 °C for 30 minutes to get ordered surfaces and was the cooled to room temperature before the LEED analysis. The ring LEED pattern with 3-fold symmetry observed for the sequentially grown oxide has been attributed to a $Fe_3O_4(111)$ surface.

5.2.3. Chromium-Oxide Film Growth on Pd(001). In the present study, the chromium-oxide films on Pd(001) were grown using both the multilayer and sequential deposition techniques.

Oxide film growth through multilayer deposition technique was achieved by depositing multiple layers of Cr metal on Pd(001) at 300 ºC, followed by oxidation at O_2 pressure of $2x10^{-5}$ Torr for 5 minutes and subsequent annealing for 30 minutes at 490-500 ºC. The LEED patterns recorded at approximately 72 eV of electron energy exhibit a p(1x1) pattern at all coverages of the chromium oxide film (refer to Figure 3.5 in Section 3.2.5). This pattern has been attributed to the most probable growth of a mixed phase of both CrO(001) and $Cr_3O_4(001)$.

In the sequential deposition technique, submonolayer deposition of Cr metal on Pd(001) at 300 ºC was followed by oxidation at $2x10^{-5}$ Torr O_2 pressure and 300 ºC substrate temperature, followed by annealing at 400-420 ºC for 1 minute (refer to Figures

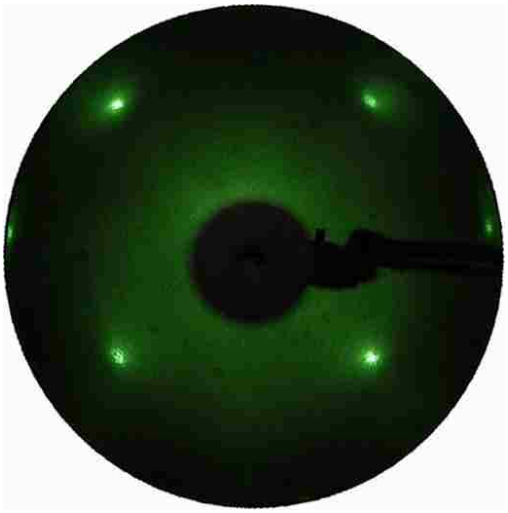

(a)

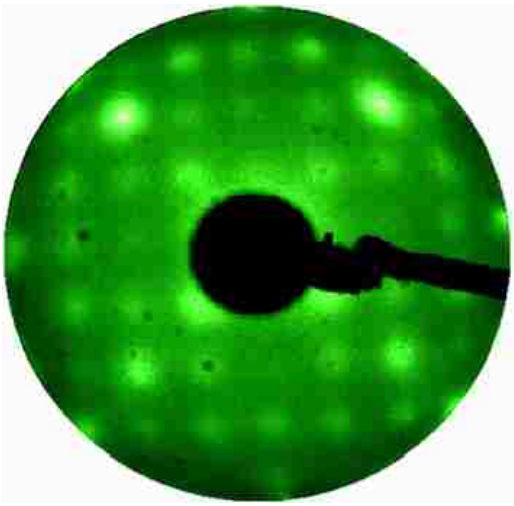

(b)

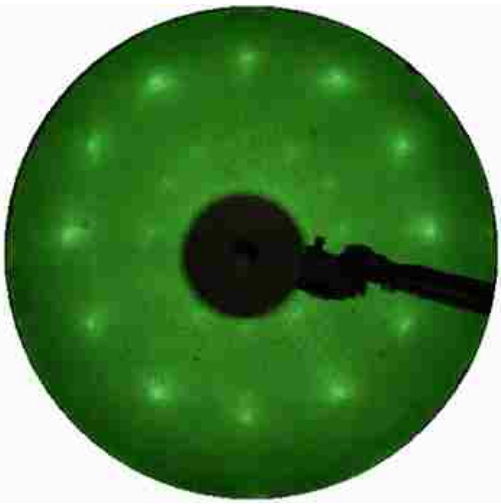

(c)

Figure 5.2. LEED patterns for (a) clean Ag(001), (b) 15 Å thick Fe_3O_4(001) film on Ag(001) (multilayer deposition technique), (c) 28 Å thick Fe_3O_4(111) film on Ag(001) (sequential deposition technique), for primary electron energy of 67 eV [99].

3.6 and 3.7 in Section 3.2.5). The whole process was repeated over and over again until the desired thickness was achieved, and then a final anneal was given at 400-420 ºC. However, no stable structures were obtained at room temperature. Another set of oxide films was then prepared using the same procedure, with the exception of the annealing temperature which was now raised to 490-500 ºC. Again, however, no well-ordered structures were observed from the LEED results (Figure 3.8).

5.2.4. Iron-Oxide Film Growth on Pd(001). In the present study, the iron-oxide films on Pd(001) were grown using both the multilayer and sequential deposition techniques.

For the multilayer deposition technique, multilayer Fe metal films were deposited on Pd(001) at 300 ºC, followed by oxidation at O_2 pressure of $2x10^{-5}$ Torr and substrate temperature of 300 ºC, and then annealed at 400-420 ºC for 30 minutes. Figure 4.4 in Section 4.2.5 shows a c(8x2) LEED pattern for the iron oxide films. The LEED patterns were recorded at electron energy of 96 eV. The c(8x2) structure has been attributed to a FeO(001) structure with a reconstructed surface.

For the sequential deposition technique, submonolayer deposition of Fe metal on Pd(001) at 300 ºC was followed by oxidation at $2x10^{-5}$ O_2 pressure and 300 ºC substrate temperature, followed by annealing at 400-420 ºC for 1 minute. The cycle was repeated until the desired thickness was achieved, and then a final anneal was given at 400-420 ºC. Figure 4.5 in Section 4.2.5 exhibits a c(8x2) LEED pattern recorded at 84 eV electron energy, and this structure has also been attributed to FeO(001) with a reconstructed surface.

5.2.5. Discussion. The multilayer deposition technique, irrespective of the substrate, always leads to the growth of oxide structures with four-fold symmetry. However, the structures obtained on Ag(001) and Pd(001) are different.

On the other hand, the growth of oxide films using the sequential deposition technique has been observed to depend on the substrate. While chromium-oxide and iron-oxide deposition on Ag(001) led to the growth of structures with three-fold symmetry, deposition of iron-oxide on Pd(001) led to the growth of structures with four-fold symmetry. Even the chromium-oxide deposition on Pd(001), while it did not yield any final ordered films, led to metastable structures that were observed to possess four-fold

symmetry. Also, while the iron-oxide growth on Pd(001) was found to be relatively independent of the deposition technique, chromium-oxide growth on Pd(001) was very much affected by the deposition technique.

The discussion in the following sections will therefore try to isolate parameters that impact oxide growth, and attempt to explain the differences mentioned above.

5.3. FACTORS AFFECTING FILM GROWTH

In thermodynamic equilibrium, all processes in opposite directions occur at equal rates. For example, in equilibrium adsorption, the surface processes of condensation and re-evaporation, decay and binding of 2D clusters are all in balance, so that there is no net growth. The macroscopic variables remain unchanged, while microscopically the system changes continuously through these various surface processes. In contrast, crystal growth is a non-equilibrium kinetic process. Some of the surface processes may be kinetically forbidden, some may be in local thermodynamic equilibrium, and others may kinetically rate-limiting. In the usual methods for deposition of metals or semiconductors, such as molecular beam epitaxy, chemical vapor deposition, etc., the incident flux is high enough for the growth mode to be far from equilibrium.

For vapor deposition from an ideal gas, the arrival rate of the metal vapor atoms can be given by [104],

$$R = p/\sqrt{2\pi mkT} \tag{5.2}$$

where R is the arrival rate, p is the vapor deposition pressure, m is the molecular weight, k is the Boltzmann constant, and T is the source temperature. The molecules arriving at the substrate may diffuse over the surface. They can also undergo processes such as re-evaporation, solution, nucleation of 2D and 3D clusters, capture by existing clusters, dissolution into the substrate, and capture at defect sites (Figure 5.3). If it is assumed that the molecular beam or evaporation source creates single atoms on the surface, the lifetimes of each of these processes depends on the single-atom concentration and/or coverage. In addition, if any of these processes are thermally activated, there may also be

Figure 5.3. Schematic diagram of processes in nucleation and growth on surfaces.

activation barriers to surmount like the activation energies for diffusion, binding of small clusters, and formation of nuclei of critical size. Processes like re-evaporation depend on the substrate temperature and the characteristic surface vibration frequency. Also, real substrate surfaces may be far from perfect and may have kinks, dislocations, point defects, ledges, and terraces. The clusters which initially form at these defect sites are not necessarily the most stable, and can undergo rearrangement like alloying, shape changes through surface diffusive processes, coalescence, etc.

After the atoms of the vapor phase have impinged on the surface and undergone a period of thermal accommodation, they can randomly diffuse over the surface to give rise to 2D nuclei (Figure 5.4). The first few molecules of the overlayer can also interact with the clean, often unreconstructed substrate, undergoing chemical reaction to form a chemisorbed species with properties that may differ from either the overlayer material *A* or the substrate *B* (Figures 5.4(a) and 5.4(b)). As more and more molecules are deposited, the interface reaction saturates, and subsequent molecules of *A* are deposited on the resulting interface compound resulting in the nucleation of the first layer and formation of islands (Figures 5.4(c) and 5.4(d)). These molecules then nucleate a new epitaxial layer by capturing the incident molecules from the vapor phase, from heterogeneous sites

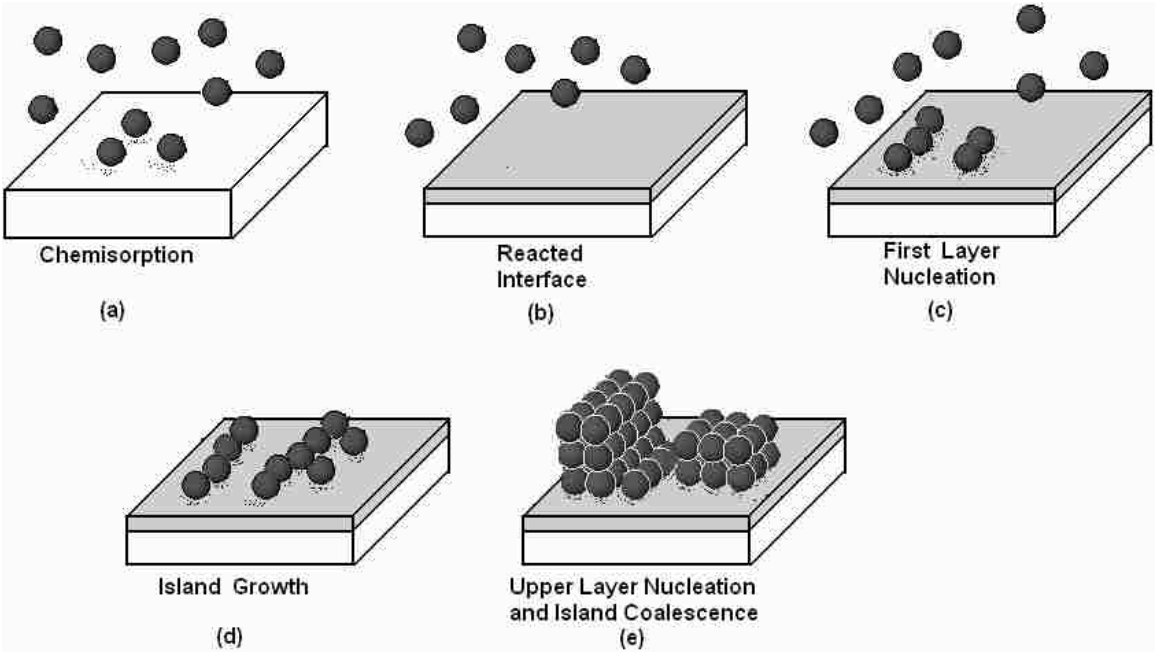

Figure 5.4. Molecules of the overlayer chemisorb on the substrate, eventually forming a reacted first layer (interfacial region) that serves as the substrate for subsequent growth. Islands nucleate with second layer nucleation occurring either before or after coalescence.

on the substrate, and/or intercepting other molecules diffusing on the surface. After the upper layers of *A* have nucleated, the islands of the new layer grow both laterally and vertically, with molecules diffusing to join the edges of the islands and new layers nucleating on top of the islands (Figure 5.4(e)). How fast these processes take place will be depend on the arrival rate of the vapor atoms and the energy barriers for diffusion on the substrate, across the reacted interface layer, and across the overlayer. The islands will eventually coalesce to completely cover the substrate and reacted layers (Figure 5.4(e)).

Finally, to achieve homoepitaxy, the material *A* of coalesced film must achieve its equilibrium lattice structure. This typically occurs through the introduction of misfit dislocations. As the overlayer thickness increases, so does the strain energy, and these misfit dislocations occur where the strain energy is the largest or at points where islands coalesce. Whether the obtained heterostructure is stable or not depends on whether the chemical reactions that take place when an isolated molecule approaches a bare substrate are stable or not. Due to the presence of stress or electronic states characteristic of the

formed crystalline interface, the chemical reactions may be unstable, and metastable structural defects in the film or interface present may prevent the molecules from attaining minimum energy configurations.

Some of the important factors affecting film growth are discussed below in detail.

5.3.1. Surface Energy. The properties of surfaces depend strongly on the surface energy and its minimization. In addition, during formation of ultra-thin surfaces on substrates, strain may also develop in the first few layers of the film as it tries to match the substrate structure. For a superlattice consisting of the metals *A* and *B*, where *B* is the substrate, the relative orientation of the two components is determined by the condition for minimization of the total system's free energy under the geometrical constraint imposed for formation of the superlattice. Homogeneous strain arising from the crystal *A* being forced to adopt the lattice of *B*, and locally varying periodic strains due to misfit dislocations arising when pseudomorphic growth becomes energetically unfavorable, can affect the growth of the superlattice. However, in general, surface energy effects are often found to dominate the strain energy effects.

Near equilibrium, thin crystalline films grow by one of the three mechanisms: the Volmer-Weber (VW), the Stranski-Krastanov (SK), and the Frank-van der Merwe (FM) mode, depending on the relative magnitudes of γ_s, γ_f, and γ_{in}, where γ_s and γ_f are the surface energies of the substrate and film, and γ_{in} is the interfacial energy. Monolayer-by-monolayer, or FM growth occurs when $\Delta\,\gamma_n = \gamma_{fn} + \gamma_{in} - \gamma_s \leq 0$ for all n. Here n represents the number of monolayers in the film. The n-dependant strain energy in the films has been absorbed in γ_{in}. The values of γ_f and γ_s are for the semi-infinite crystal. For zero misfit, which is possible only for growth of A on A (homoepitaxy), we get $\gamma_f \equiv \gamma_s$ and $\gamma_{in} \equiv \gamma^0_{in}$, where the strain contribution γ^{ϵ}_{in} to γ_{in} is zero, and $\Delta\,\gamma_n = \gamma_{fn} + \gamma^0_{in} - \gamma_s \leq 0$. Here γ^0_{in} is the zero strain contribution to γ_{in} which depends on the specific chemical interaction between film and substrate atoms and rapidly approaches zero within the first few monolayers. In the SK mode of growth, the increase of the strain energy with n leads to an increase of γ_{in} until at a given $n = n^*$ the FM condition is no longer fulfilled and three-dimensional crystals form. If the FM condition is not fulfilled from the very beginning ($n = 1$), then three-dimensional crystals form immediately on the substrate (VW mode).

In the present study, it is not possible to determine the growth modes of the oxide films with the current experimental techniques available. Based on selective surface energy data available in the existing literature for the various surfaces of interest, one could speculate on the types of growth morphologies that could be expected on Ag(001) and Pd(001), but nothing can be predicted in definite terms due to the complexity of the processes involved, lack of data on interfacial energies, and experimental limitations.

5.3.2. Lattice Match. An important consideration while choosing a substrate for film growth is the lattice mismatch, which should be as small as possible to reduce strain in the film, unless it is specifically the effects of strain in the film that form the subject of interest and study. Strain energy initially builds up rapidly with thickness resulting in misfit dislocation generation, film buckling, morphological transformation from 2D layer-by-layer to 3D island growth, or coincidence lattice formation. Depending on the film growth kinetics and the energetics of the different processes, different mechanisms of strain come into play.

A quantitative comparison of in-plane lattice parameters of the substrate and film can also be defined by [105]:

$$f = \frac{\Delta a}{a} = \left| \frac{a_{film} - a_{sub}}{a_{sub}} \right| \tag{5.3}$$

Here both lattice parameters are in the growth plane. In order to reduce strain in the film, f should be as small as possible. If a_{film} < (>) a_{sub}, the film will be in tension (compression) prior to relaxation.

The feasibility of the growth of superlattices may be characterized by a compatibility factor that would represent the surface energy mismatch [106]:

$$\Gamma_{AB} = 2\left|(\gamma_A - \gamma_B)/(\gamma_A + \gamma_B)\right| \tag{5.4}$$

From the experimental data on some classical systems, a critical value of $\Gamma^{c}_{AB} \approx ½$ has been calculated. For $\Gamma_{AB} < \Gamma^{c}_{AB}$ superlattice formation should be possible and for $\Gamma_{AB} > \Gamma^{c}_{AB}$ it should not.

5.3.3. The Interfacial Region. The epitaxial interface is the boundary between the film crystal and the substrate crystal, the former being in epitaxial orientation with the latter. This boundary, between two single crystals, determines the extent of the "reaction" region between the film and the substrate, and it can have structures that are uniquely characterized by the nature of chemical bonds due to phenomena like surface adsorption, alloying, interdiffusion or chemical reactions, the crystal lattices and lattice parameters, homogeneous strain due to lattice misfit and/or periodic strain due to misfit dislocations, the chemical properties of both materials, etc. For example, the remarkable catalytic activity observed for V_2O_5 when supported on a TiO_2 substrate is not evident for either the unsupported V_2O_5 or the TiO_2 support. The degree of stability of these interfaces along with how accommodation of the misfit and other interactions across the boundary plane is achieved, may lead to structural modifications of the thin film.

The interface plays a dominant role in the overlayer-substrate interactions during growth of an overlayer on a substrate. Extensive literature exists on interaction studies between iron (or chromium) and a platinum group metal (Ru, Rh, Pd, Ir, or Pt). The Pt group metals exhibit remarkable reactivity and selectivity especially in the presence of more electropositive elements like Fe and Cr [107]. In addition to the formation of novel structures, alloying can also induce magnetic moments, and specific magnetic properties in both binary systems of Pd-Fe and Pd-Cr alloys have been observed [108-111].

Bulk phase diagrams cannot be considered to be accurate predictors of what happens at the surface region, but referring to them can enable us to form ideas about what to expect from the deposition of Fe (or Cr) metal with the Pd and Ag substrates under the given conditions of temperature and atomic % composition in our experiment.

From the established thermodynamic studies on the Pd-Fe system it has been observed that, under similar experimental parameters to those in our study (such as temperature and atomic percentage of palladium), two ordered phases of (γFe, Pd) exist – $FePd_3$ and FePd – as shown on the Pd-rich side of the Fe-Pd phase diagram [112] in

Figure 5.5. The crystal structure of FePd is AuCu type which is a tetragonal distortion of the fcc structure, and that of $FePd_3$ is cubic $AuCu_3$ type where all the atoms are located on the sites of a plain face centered cubic lattice. The boundaries between FePd and $FePd_3$ are quite ambiguous as achieving equilibrium between the two phases requires migration of atoms at low temperatures. For the AuCu-type FePd phase, the reported values of the lattice parameters *a* and *c* are 3.852 Å and 3.706 Å respectively at around 50 atomic % Pd. The lattice parameter *a* for the $AuCu_3$-type $FePd_3$ phase has a reported value of 3.848 Å at 75 atomic % Pd [112].

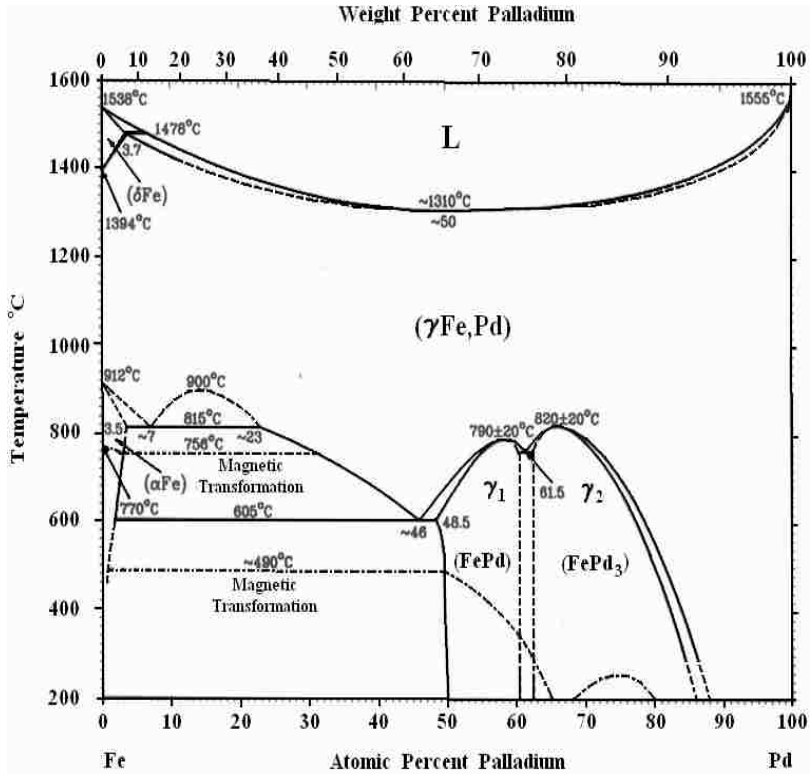

Figure 5.5. The Fe-Pd phase diagram (reprinted with permission of ASM International [112]).

Figure 5.6 shows the phase diagram for the Pd-Cr system with experimental points [113]. The area of interest in the phase diagram is the Pd-rich side between temperatures of 400-600 K and at Pd mole fractions lying between 1.0 and 0.5, where

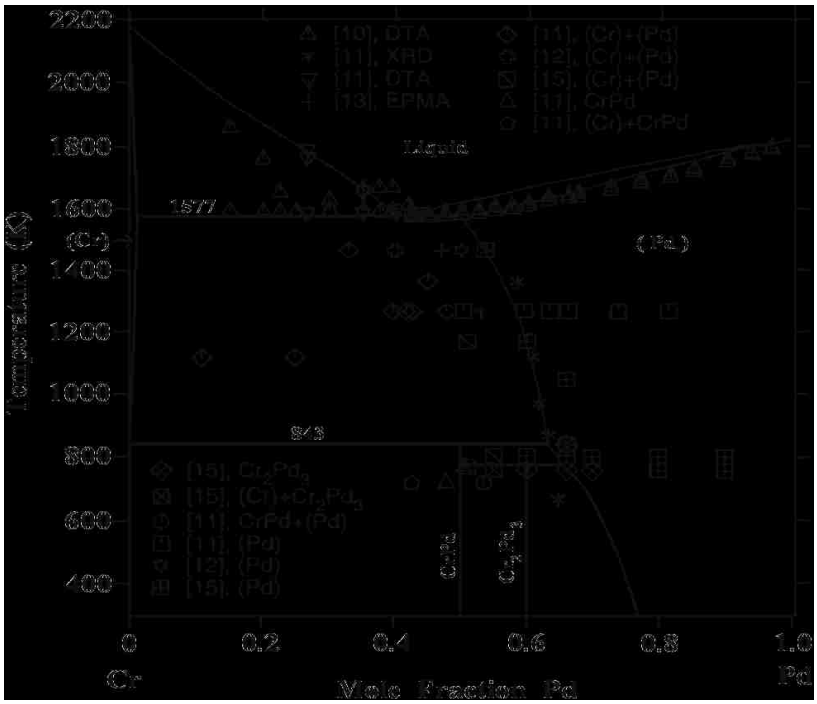

Figure 5.6. The Cr-Pd phase diagram with experimental points (used with kind permission of Springer Science and Business Media [113]).

two ordered intermediate phases of CrPd and Cr_2Pd_3 exist. The phase boundary boundaries involving CrPd and Cr_2Pd_3 are not accurately established due to the presence of very slow ordering reaction kinetics. The homogeneity range for the CrPd phase is quite narrow from 50 to 52 at.% Pd, while the Cr_2Pd_3 phase has a much broader homogeneity range from 55 to 75 at.% Pd. The CrPd phase has a face-centered tetragonal structure isomorphic with AuCu, and Cr_2Pd_3 has a structure isomorphic with Cu_3Au. Ghosh and Olson [113] noted that unlike $FePd_3$, Cr_2Pd_3 was not designated as $CrPd_3$ due to a strong asymmetric homogeneity range exhibited by Cr_2Pd_3, which could not be reproduced using a two-sublattice description of either $(Cr,Pd)_{0.25}(Cr,Pd)_{0.75}$ or $(Cr,Pd)_{0.40}(Cr,Pd)_{0.60}$. Due to this reason, both CrPd and Cr_2Pd_3 were treated as stoichiometric phases. Study of the Pd-Cr solid solutions shows that around 25 atomic % Cr, the Cr_2Pd_3 fcc structure has a lattice parameter of 3.865 Å or 3.874 Å [107]. The CrPd phase has a body-centered tetragonal (bct) unit cell with lattice constants a = 2.74 Å and c = 3.80 Å.

Figure 5.7 shows the bulk phase diagram for the Fe-Ag system. The mutual solubility of Ag and Fe is very low in both the solid and the liquid. The solubility of Fe in Ag is only between 4 and 6 ppm by weight, between 1000 and 1600 °C [112]. In the temperature range 300-900 K (27 – 627 °C), the phase diagram does not exhibit any solubility between Ag and Fe. Thus bulk thermodynamic studies do not predict the formation of any stable or metastable compound phases in the range of temperature and Fe and Ag content of interest.

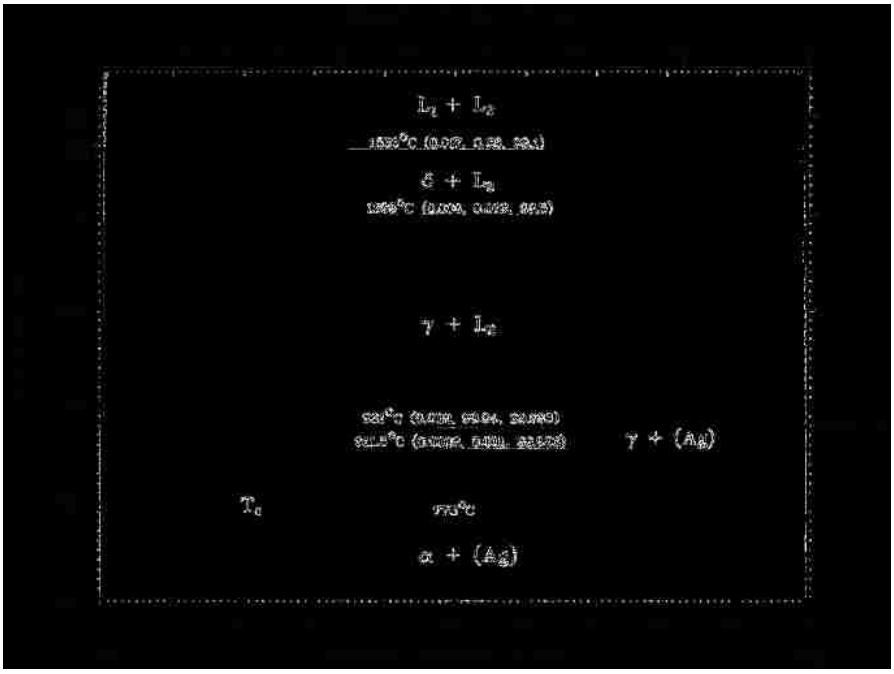

Figure 5.7. The Fe-Ag phase diagram (reprinted with permission of ASM International [112]).

Figure 5.8 shows the phase diagram for the Cr-Ag system [114]. It is characterized by immiscibility of Cr and Ag in the liquid and solid, and by the absence of intermediate phases. Thus, the bulk thermodynamic studies also do not predict any interaction between Cr and Ag.

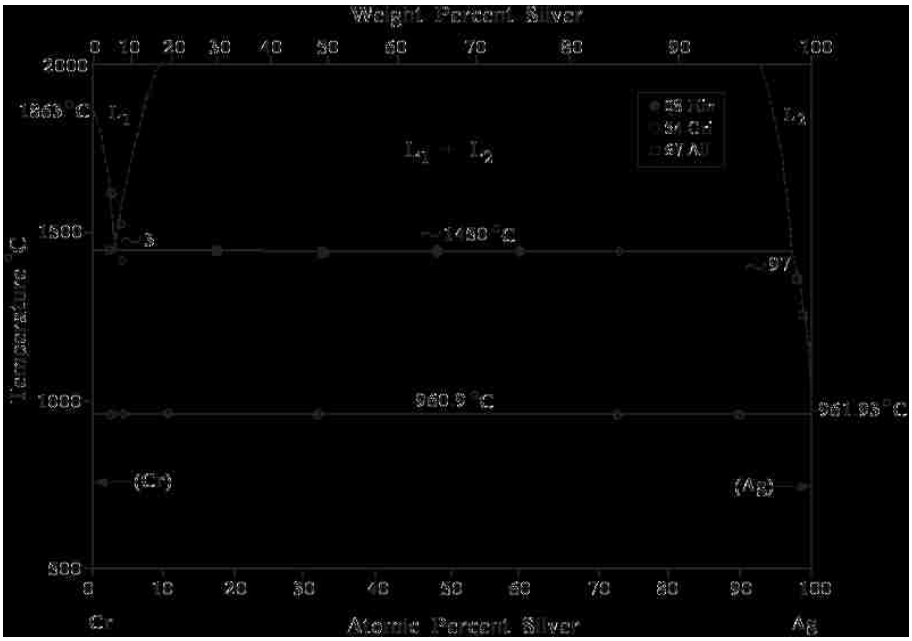

Figure 5.8. The Cr-Ag phase diagram (used with kind permission of Springer Science and Business Media [114]).

5.3.4. Oxidation Kinetics. The oxidation of a metal surface is a complex process that simultaneously involves a number of physical phenomena. In nature, oxides frequently form protective layers that separate the metal from the gaseous oxygen inhibiting further oxide formation. In the laboratory, the growth of dielectric (or semiconducting) oxide films on a metal substrate occurs when the reactive component of the gaseous or solution phase is allowed to interact with the metal crystal. A number of different mechanisms have been hypothesized as being active in initial oxide formation. Knowledge of some of the aspects controlling the various parameters for early-stage oxygen incorporation into metals with subsequent oxide-film growth, such as temperature, oxygen pressure, surface orientation, can provide greater insight into the growth processes of these oxide films.

Growth of ultrathin films deposited on a substrate at low temperatures is often governed by kinetic factors, and metastable phases with unique structural properties may be formed. At high temperatures, phenomena such as admetal cluster formation or diffusion of the adlayer into the bulk of the substrate can occur, leading to the formation

of surface alloys. These surface alloys can exhibit chemical and physical properties very distinct from those of the supported thin film and bulk systems.

Bulk oxide stoichiometries depend strongly on oxygen pressure, as do oxide surface structures and stoichiometries. For oxide materials, the surface termination is determined mainly by the oxygen partial pressure during preparation. For example, for growth of a Fe_2O_3 single crystal at low oxygen pressure, the surface is metal terminated, while growth under high oxygen pressures leads to a complete oxygen termination [115]. Electron redistribution and interlayer relaxations then lead to stabilization of the system. The formation of the oxide depends on the oxygen pressure being greater than the dissociation pressure p of the oxide in equilibrium with the metal, where

$$p = \exp(\Delta G / RT) \tag{5.5}$$

and ΔG is the free energy of formation of the oxide per mole of oxygen consumed. The first stage of the oxidation process is usually chemisorption, in which oxygen is adsorbed on the metal surface and may lead to dissociation and partial ionization of the oxygen. The oxygen may then be incorporated into the metal, leading to formation of ordered surface adsorption structures, with or without significant rearrangements of the surface metal atoms. Specific oxidation conditions, such as those of temperature and pressure, may lead to formation of ordered superlattice domains, or oxide nuclei that grow together to coalesce and form a continuous oxide film. Physical adsorption will only be important for relatively high pressures and low temperatures and primarily as a precursor to chemisorption, while chemisorption is a chemical reaction that involves the rearrangement of valence electrons of the metal and the gas to form a chemical bond. Oxygen, being highly electronegative, has a large affinity for electrons. The chemisorption bond for oxygen is largely ionic, though it may be at least partly covalent when the transition metals having unpaired d electrons are involved.

Surface orientation has a significant effect on the oxidation behavior and relative oxidation rates of single crystal surfaces with different orientations. Similarly, the orientation of the substrate will also affect growth and orientation of the deposited layers. For example, for a substrate, the (100) face is in effect coordinatively less saturated than

the (111) face. As such, for a chemically reactive substrate, the (100) surface will have more electrons available to make bonds with the adsorbate layer than the (111) surface, and as a result the interaction with the overlayer will be more for the (100) surface as compared to the (111) surface.

At the initial stages of oxidation, the processes involved are adsorption of oxygen onto metal, oxygen incorporation into the metal with the formation of some type of metal-oxygen structure, and oxide nucleation and growth. A general overview of these oxidation processes is given below.

5.3.4.1 Oxygen adsorption. The first stage of oxidation is oxygen adsorption. For adsorption to take place, the oxygen molecules must first make contact with the metal surface. The collision rate of molecules with unit area of surface, given by kinetic theory, is given by Equation 5.2. Since the oxygen molecules in the current study are at room temperature, and oxidation is performed at more or less a constant pressure of ~$2x10^{-5}$ Torr, the collision rate can be regarded as a constant of the experiment. While physical adsorption is of primary importance only at relatively high pressures and low temperatures, chemisorption takes place under most conditions of temperature and pressure, and in fact at elevated temperatures it will be the primary chemical reaction. The dissociative adsorption of oxygen may involve surface diffusion prior to chemisorption, and some re-evaporation may occur at higher coverage because of a shortage of suitable binding sites, and so the oxygen sticking coefficient (which can be defined as unity for a monolayer of adsorbed oxygen on the surface in approximately 1 second at room temperature for a gas pressure of 10^{-6} Torr) would vary with both temperature and surface coverage.

In the current experiments, the oxidation process occurred at a specific elevated substrate temperature, and the variation of oxygen adsorption can be expected to vary with film coverage. While physical adsorption is always exothermic and takes place rapidly without any activation energy, chemisorption is generally considered a slower process requiring an activation energy, though there are many cases where chemisorption can also occur in the absence of an activation barrier. It has been observed [116] for Cr that the chemisorbed structure (at 23 °C and $<10^{-2}$ Torr oxygen pressure) of 1-2.5 monolayers is ordered but unstable, and similarly for Fe (at 23 °C and $<10^{-2}$ Torr oxygen

pressure) the chemisorbed structure of < 10 monolayers is also ordered but unstable. Substrate temperature, the particular metal involved, and the oxygen pressure are all important in determining the chemisorbed film stability.

5.3.4.2 Oxygen incorporation into the metal. The second stage is oxygen incorporation into the metal. The oxygen adsorbed onto the metal could remain on the surface as ions, be incorporated into the metal or be converted to oxide. The adsorption can lead to a surface rearrangement of the metal involving oxygen incorporation into the subsurface area, which can produce unstable adsorption layers. This has been attributed to the observation of positive surface potentials after admission of oxygen, since incorporating the oxygen atoms into the metal surface would bring a degree of positive charge to the surface assuming that the metal atoms occupy positions above the oxygen atoms and increase the ionic character of the bond, thus creating polar surfaces.

Generally at low oxygen pressures, somewhat disordered structures are observed prior to the formation of the first ordered structure, and these may be both island and domain structures. The simultaneous presence of two different surface structures or surface phases is manifested in a diffuse or streaked electron diffraction pattern, which may become sharper and more intense with annealing of the surface as a result of enhanced ordering or domain growth. It was observed [116] that for Cr(001), the amorphous adsorption structure obtained at room temperature gave an amorphous three-dimensional oxide on heating. On the other hand, for the Fe(001) surface [116], the oxygen adsorption structure at room temperature was observed to have a c(2x2) diffraction pattern at ½ monolayer, which on annealing at 550 °C resulted in the formation of FeO. During film growth on a substrate, electrons may be transferred from the metal to the substrate in the chemisorption process, and both ordered or disordered structures of oxygen anions on a metal surface can exist during the low coverage stages of chemisorption.

Experimental studies conducted on the exposure of metal surfaces for many metals at low oxygen pressures have reported a reconstruction of the surface during oxygen adsorption at room temperature in which the surface layer consists of both metal ions and oxygen ions. For formation of three-dimensional oxides, reconstruction is a necessary process and may involve more than just one surface layer. While

reconstructions of the room temperature adsorption structures on iron and chromium have not been observed, adsorption at higher temperatures almost always leads to a reconstructed layer. The high temperature reconstruction may involve considerable penetration of oxygen into the metal and thereby a multilayer reconstruction beneath the surface. It may also involve surface faceting of the metal, or the formation of either two- or three-dimensional oxide structures. In fact all of these reconstructions may be simultaneously present on a given metal. The frequent appearance of fuzzy LEED patterns with high background intensity for coverages greater than one monolayer have been attributed to the amorphous adsorption of a second monolayer in the cases of Mo, NI, Cu, Fe, Al. In some cases (Fe, Cu) the fuzzy patterns have also been attributed to the formation of three-dimensional oxide nuclei, which give sharp LEED oxide patterns upon heating.

5.3.4.3 Oxide nucleation and growth. The third stage is oxide nucleation and growth. The structure of the initial monolayer (or submonolayer) or multilayer film formed by the interaction of oxygen with a metal surface could be an oxide, a sub-oxide, a reconstructed adsorption layer, or a surface compound. Sub-oxides, which are intermediate reaction products prior to the formation of stable three-dimensional oxides, are usually the initial products of reconstructions. Nucleation processes for the formation of both sub-oxides and true oxides on the metal surface are complex and depend on the total free energy change ΔG. This, in turn, depends on (1) the volume free energy change, (2) the interfacial free energy change, (3) the strain energy change and (4) energy factors due to compositional changes. The thermodynamics approach to the nucleation process will not be discussed here

For low pressures of oxygen, the activation energy for nucleation is high, and the movement of atoms for the process also requires thermal activation energy which can only be obtained by increasing the temperature. For a given pressure and temperature, the formation of discrete oxide crystallites can be divided into three successive stages: (1) An induction period lasting until the formation of the first oxide nuclei, (2) a lateral growth period of the oxide nuclei until the surface is completely covered by oxide, and (3) a period of uniform growth of the continuous oxide film. The length of the induction period depends on the metal oxidized, crystal face, temperature, and oxygen pressure. Generally,

inductions periods are shorter for high index crystal faces, and the relative order of the length of this period goes as : (100) > (111) > (110) > (311) [116].

For most metals the induction period is marked by the solution of oxygen in the metal, including the formation of an ordered or disordered surface structure of one or two monolayers. Surface oxide formation and its dissolution in the metal are competing processes with solution of the oxide in the metal being predominant at lower pressures and higher temperatures. At a critical value of oxygen concentration at the metal surface (saturation), the formation of oxide nuclei takes over the dissolution of oxygen into the solution. This marks the end of the induction period, and oxide nuclei appear randomly distributed over the metal. The growth of these nuclei takes place rapidly laterally and slowly normal to the surface, with both large and small nuclei, as well as nuclei–free zones about the larger nuclei being present.

The density of oxide nuclei decreases with increasing temperature and decreasing oxygen pressure. At a particular oxygen pressure, after the initial formation of oxide nuclei, no new nuclei appear since the initial precipitation of oxide removes much of the dissolved oxygen. Any additional oxygen adsorbed on the surface is more readily taken up by the existing nuclei, and the critical concentration of oxygen in the bulk necessary to precipitate new oxide particles is not readily obtained. Once the nuclei are formed, further growth of the nuclei is controlled by surface diffusion processes. Defects on the metal surface, like fault terraces, dislocations, kink sites, vacancies, or impurity atoms can also act as sites for nucleation. The laterally growing oxide nuclei will eventually touch one another and form metal oxide islands that grow larger and larger to ultimately coalesce.

5.4. CASE STUDIES

5.4.1. Metal Film Growth on Pd(001) and Ag(001). The growth of Fe and Cr films on Pd(001) and Ag(001) all resulted in bcc film growth, and in each case the LEED results exhibited a consistent p(1x1) pattern.

5.4.1.1 Film growth on Pd(001). The Fe and Cr films were deposited on the Pd(001) substrate at elevated substrate temperature of 300 °C. In the multilayer deposition technique, several layers of the Fe (or Cr) metal film were deposited on the Pd substrate before the oxidation process. In the sequential deposition technique approximately 0.5-0.6 ML of Fe (or Cr) metal film was deposited on Pd prior to the first cycle of oxidation.

Within the experimental parameters of interest in the current study, i.e., the temperature range of room temperature to 400 °C, and at atomic percentages of 90-50 at.% Pd, the bulk thermodynamic phase diagrams for the Fe-Pd and Cr-Pd systems do predict alloy formation for each of the two systems, with these alloys having cubic and tetragonally distorted fcc structures. The lattice parameters observed for the bulk solid solutions of the Fe-Pd and Cr-Pd alloys are a = 3.852 Å and c = 3.706 Å for FePd, a = 3.848 Å for $FePd_3$, a = 3.865 Å or 3.874 Å for Cr_2Pd_3, and a = 2.74 Å and c = 3.80 Å for CrPd. While these bulk phase diagrams cannot be used to directly correlate with what might be happening at the surface in our Fe and Cr films on the Pd(001) since the surface compositions are likely to be different from the predicted bulk phases, they do give an idea of what to expect, namely that interactions between the Fe (or Cr) metal and the Pd substrate may occur at the interface region for the first few monolayers leading to the formation of some ordered alloy with 4-fold symmetry. This view is further supported by surface studies done on the growth of Fe and Cr metal films on Pd(001), in which intermixing of adsorbate and substrate atoms, and alloy formation in the interface region have been reported [59, 64, 83, 102].

As discussed in Section 5.3, after the initial period of thermal accommodation following the deposition of the metal vapor atoms on the clean substrate surface, chemical reaction between the overlayer material and the substrate would lead to the formation of a chemisorbed species that is ordered. The formation of the interface compound for the first few layers is soon followed by saturation of the interface reaction. For deposition of metal film of a few monolayers or submonolayer thickness, the overlayer is an interface compound of the deposit and substrate material, and the thickness at which saturation of the interface reaction takes place would depend on the degree and strength of the interaction. As more and more molecules are deposited, the

nucleation of the first layer of the overlayer metal atoms of Fe or Cr would finally take place. The multilayer metal films deposited would be layers of the metal that have nucleated on the interfacial structure formed from the initial deposition of the vapor atoms on the reactive Pd substrate. The interface compound affects the order and structure of the subsequent metal film formed in the early stages of growth. With increase in thickness of the overlayer, the effect of the interface falls off until, at sufficiently high coverages, the metal film relaxes back to the bulk structure of the deposit material.

A quantitative measure of strain for deposition of Fe (or Cr) on Pd(001) can be calculated from Equation 5.3. For a_0^{Pd} = 2.75 Å, a_0^{Cr} = 2.88 Å, a_0^{Fe} = 2.87 Å, the "f" value for the Cr-Pd system is 0.0473 (4.73%), and the "f" value for the Fe-Pd system is 0.0436 (4.36%). Since $a_{film} > a_{sub}$ for both Fe and Cr, the film will be in compression prior to relaxation in both cases. The strain in either system is not insignificant, however deposition at elevated substrate temperatures results in well ordered and stable 4-fold heterostructures on the substrate as is evident from the p(1x1) LEED patterns (Figures 3.1 and 4.1).

The values of the surface energies at zero temperature obtained from the theoretical calculation of Vitos et al. [117] for bcc Fe(100), bcc Cr(100), and fcc Pd(100) surfaces are 2.222 Jm^{-2}, 3.979 Jm^{-2}, and 2.326 Jm^{-2} respectively. Equation 5.4 would then give the values of the surface energy mismatch Γ_{AB} for the Fe-Pd and the Cr-Pd systems. The surface energy mismatch $\Gamma_{Fe\text{-}Pd}$ = 0.046 is less than $\Gamma^c_{AB} \approx$ ½, and superlattice formation for the Fe-Pd system looks feasible. For the Cr-Pd system the surface energy mismatch $\Gamma_{Cr\text{-}Pd}$ = 0.524 is borderline, and superlattice formation for the Cr-Pd does not look feasible. However, the above mentioned values for surface energies have been obtained at zero temperature, and the situation would be more complicated at room or elevated temperatures. In addition, the interfacial energy γ_i has not been taken into account. The situation would be further complicated by alloying or compound formation at an interface with given misfit, essentially increasing the interfacial bond strength and accordingly the stability against misfit dislocation formation, i.e., enhancing the tendency for layer-by-layer growth. From the surface energy point of view however, the three-dimensional growth of metals with high surface energy on metals with low surface energy is the main factor limiting superlattice growth. It is energetically more favorable

to form three-dimensional crystals with small interface regions than to continue the growth of a highly strained quasi-two-dimensional multilayer film.

5.4.1.2 Film growth on Ag(001). The multilayer Fe and Cr films were deposited on Ag(001) substrate at room temperature before the oxidation process. In the sequential deposition technique, while approximately 0.5 ML of Cr was deposited on Ag(001) at 150 °C prior to the first cycle of oxidation, submonolayer deposition (approximately 0.5 ML) of Fe on Ag(001) was conducted at room temperature prior to the first oxidation

For a_0^{Ag} = 2.89 Å, a_0^{Cr} = 2.88 Å, a_0^{Fe} = 2.87 Å, the "f" value for the Cr-Pd system is 0.0035 (0.35%), and the "f" value for the Fe-Pd system is 0.0069 (0.69%). Since $a_{film} < a_{sub}$ for both Fe and Cr, the film will be in tension prior to relaxation in both cases. However, the lattice misfit is very small, and the strain in the overlayer will be minimal. As such good epitaxial growth of bcc Fe and bcc Cr is obtained on Ag(001) at room temperature [58, 67, 68, 99], and the unit cells of Fe and Cr have near perfect matches with the underlying Ag(001) template. Both Fe and Cr films on Ag(001) yield p(1x1) LEED patterns at all coverages.

The values of the surface energies at zero temperature obtained from the theoretical calculation of Vitos et al. [117] for bcc Fe(100), bcc Cr(100), and fcc Ag(100) surfaces are 2.222 Jm^{-2}, 3.979 Jm^{-2}, and 1.20 Jm^{-2} respectively. The surface energy mismatch for the Fe-Ag and the Cr-Ag systems are $\Gamma_{Fe\text{-}Ag}$ = 0.597 and $\Gamma_{Cr\text{-}Ag}$ = 1.073 respectively. Consequently, superlattice formation for either of these two systems does not look feasible. Studies have been reported on forward-scattering peaks being observed in XPD studies [47] of 1 ML thick Cr films grown on Ag(001), and these peaks result from the 3-D growth of the Cr film on Ag(001). The Stranski-Krastanov growth mode has been reported for growth of Fe on Ag(001) [118].

The bulk phase diagrams for the Fe-Ag and the Cr-Ag systems show that both Fe and Cr are immiscible in Ag. No stable or intermediate phases are formed. As such, strong interactions are not expected to take place between Fe (or Cr) and the Ag substrate when the metal films are deposited. However, recent surface studies have reported not only Fe/Ag(001) and Cr/Ag(001) superlattice formation, but also intermixing of Cr and Ag at elevated temperatures [119-121].

5.4.2. Multilayer Oxide Deposition on Pd(001) and Ag(001). In all the cases, multilayer oxide growth involved oxidation of the Fe(001) and Cr(001) films, and ordered structures were obtained in each case for the growth of Cr_xO_y and Fe_xO_y films on Pd(001) and Ag(001).

5.4.2.1 Multilayer growth of Cr_xO_y and Fe_xO_y on Pd(001). The growth of the multilayer Cr metal films were observed to grow in registry with the substrate lattice with p(1x1) LEED patterns. The LEED pattern observed for the multilayer Cr_xO_y film is also a p(1x1) pattern (Figures 3.4(b), 3.4(c), and 3.4(d)), and the structure proposed is a mixed phase of CrO(001) and Cr_3O_4(001). The Fe films also grow in registry with the substrate resulting in p(1x1) LEED patterns, but the LEED pattern observed for the multilayer Fe_xO_y film is a c(8x2) pattern (Figures 4.4(b) and 4.4(c)), and the structure proposed is FeO(100) with a reconstructed surface. In both cases the symmetry of structures observed is four-fold.

5.4.2.2 Multilayer growth of Cr_xO_y and Fe_xO_y on Ag(001). Both Fe and Cr grow in registry with the Ag(001) yielding p(1x1) LEED patterns. The LEED pattern observed for the multilayer Cr_xO_y film is a c(6x2) pattern (Figure 5.1(b)), and the oxide structure proposed is α-Cr_2O_3(210). The LEED pattern observed for the multilayer Fe_xO_y film is a $(2\sqrt{2}x2\sqrt{2})R45^\circ$ pattern (Figure 5.2(b)), and the structure proposed is Fe_3O_4(100). The symmetry of the structures observed for the growth of chromium- and iron-oxide films on Ag(001) is four-fold.

5.4.2.3 Discussion. Oxidation of the multilayer bcc Fe (or Cr) metal films is equivalent to oxidizing bulk Fe(001) (or Cr(001)) and subsequent oxidation also results in an oxide with 4-fold symmetry. The Fe (or Cr) overlayers would be fixed by the Ag(001) and the Pd (001) lattices which serve as templates for the bcc growth, and oxidizing these multilayer films would be equivalent to oxidizing films that are bulk-like resulting in 4-fold symmetry structures. However, there are differences observed in the LEED patterns, and in the oxide structures obtained. The multilayer chromium-oxide film growth on Pd(001) results in a p(1x1) LEED pattern. On the other hand, the LEED patterns obtained from the multilayer growth of iron-oxide film on Pd(001), and multilayer chromium- and iron-oxide film growth on Ag(001) are not p(1x1), and different oxide structures have been proposed based on the XPD results and MSCD calculations.

The importance of these results is that all the oxide structures have four-fold symmetry. The precise underlying mechanisms responsible for the appearance of CrO or Cr_3O_4 on Pd(001) and Cr_2O_3 on Ag(001), or FeO on Pd(001) and Fe_3O_4 on Ag(001), with different reconstructions, will be impossible to ascertain and explain, and it can only be speculated that these differences arise from the differences in lattice match, metal film-substrate interaction, and oxide growth parameters.

5.4.3. Sequential Oxide Deposition on Pd(001) and Ag(001). The sequential growth of chromium- and iron-oxide films on Ag(001) led to ordered structures, while for chromium-oxide on Pd(001), no well-ordered structures (as observed from LEED results), that could justify XPD measurements, were obtained.

5.4.3.1 Sequential growth of Cr_xO_y and Fe_xO_y on Pd(001). The growth of well ordered iron-oxide films were obtained. The LEED pattern observed is a c(8x2) pattern, and the structure proposed is FeO(001) with a reconstructed surface. This surface has a four-fold symmetry. The metastable Cr_xO_y films obtained also exhibited a four-fold symmetry, as observed from the LEED patterns.

5.4.3.2 Sequential growth of Cr_xO_y and Fe_xO_y on Ag(001). Growth of the chromium-oxide films on Ag(001) led to the formation of a 3-fold symmetry structure, and the oxide proposed is α-Cr_2O_3(111). Growth of iron-oxide films on Ag(001) also led to the formation of a 3-fold symmetry structure, and the oxide proposed is Fe_3O_4(111).

5.4.3.3 Discussion. In the growth of Cr_xO_y on Pd(001), the first submonolayer and the next few monolayers of Cr will probably interact with the substrate to form an interfacial compound (as discussed in Section 5.4.1.1). Deposition at elevated temperatures can also lead to admetal cluster formation. Initial exposure of the first submonolayer of deposited metal to oxygen leads to oxidation of the alloy surface. Subsequent deposition is performed by repeated cycles of submonolayer metal deposition and oxidation. This method of Cr_xO_y deposition on Pd(001) yields very interesting results.

For the very thin Cr_xO_y film on Pd(001) (~2 Å), the LEED pattern (Figure 3.5(b))was observed to be streaked in the (0,1) and (1,0) directions. This would be due to the presence of surface features like irregular steps giving rise to the streaking of spots in the direction of the disorder. For the 4 Å thick film (Figure 3.5(c)) the LEED pattern was

not well ordered, and the streaks broaden and become diffuse, which implies a surface that is less ordered. As discussed in Section 5.3.4.2, low oxygen pressure ($2x10^{-5}$ Torr) in the current experiment gives rise to disordered structures prior to the formation of the first ordered structure, and these structures could have both island and domain structures. The diffuse or streaked LEED pattern becomes sharper and more intense with annealing of the surface as a result of enhanced ordering or domain growth. For the 6 Å films annealed at 420 °C, well-ordered c(4x2) LEED patterns (indicative of the existence of two domains rotated by 90° with respect to one another) were observed immediately after the anneal (Figure 3.5(d)). This pattern, however, proved to be unstable. As the film cooled back to room temperature, the initial c(4x2) LEED pattern reconstructed after approximately an hour to a p(2x2) pattern (indicative of only a single domain) shown in Figure 3.6(b), which then deteriorated further into a p(1x1), as shown in Figure 3.6(e) - again, indicative of a single domain (Figure 3.6(f)). The final LEED pattern obtained was different from the p(1x1), of very poor intensity and not well-ordered, and deterioration continued until no LEED pattern was observed, indicating complete disorder. The order of these films appears to be temperature dependant, and with decrease in substrate temperature, disorder increases until no ordered surface structure remains.

The c(4x2) Cr_xO_y structure on Pd(001) seems to be stabilized only at elevated substrate temperatures, and this superstructure vanishes as the film is cooled. Also, the temperature dependence is reversible, because when the sample is warmed up to 420 °C, the ordered c(4x2) LEED pattern reappears. This is an indication that there is a temperature dependence. A continued reconstruction of the oxide surface with cooling of the substrate implies thermodynamic instability of the system, and of the interfacial region. The poorly ordered LEED pattern (Figure 3.6(f)) observed after approximately 18 hours could due to the adsorption on the surface of trace amounts of ^{-}OH, or CO. Flashing the sample to the temperature at which thermal desorption of the adsorbed species takes place restores the order of the films. Thus direct structural rearrangement of the sample is observed to take place at the surface with temperature, and that the interaction between the adsorbates and the substrate strongly influences the energetics of the structural rearrangement at the surface.

Annealing the Cr_xO_y film on Pd(001) at still higher temperatures (490-500 °C) caused an increased diffuseness of the superstructure (Figures 3.7(b), 3.7(c), 3.7(d)), but completely ordered systems were never obtained at any point. At higher coverages of 11 Å, the diffuse background intensity increases, and the diffuse and streaked diffraction spots increase in number. This would be due to the presence of multiple domains that are not well-ordered. With increase in thickness, there is no enhancement of ordering, and the LEED pattern at ~17 Å resembled that obtained at the previous annealing temperature of 420 ºC.

The sequential growth of Fe_xO_y on Pd(001) is markedly different from that of the chromium-oxide films. Formation of an interfacial compound would result from the initial submonolayer deposition of Fe metal on Pd(001) and interaction of the substrate with overlayer. For the very thin films, exposure of the deposited metal to oxygen leads to oxidation of the interfacial alloy structure. Figure 4.5(b) shows the LEED pattern obtained from a 3.1 Å thick film. The slightly broad diffraction spots would imply the presence of some amount of disorder present at low coverage. However, not only is the interaction of the oxide overlayer with the substrate strong, but the structure is also stable. The good structural quality of the oxidized interfacial region results in the interface proving to be an ordered template for the nucleation and growth of the oxide overlayer, and with increasing coverage, there is enhancement of ordering (Figures 4.5(c), 4.5(d)). There is no structural phase change as the film thickness increases and the LEED patterns remain unchanged up to high coverages, implying thermodynamic stability of the interface region and the c(8x2) superstructure of FeO(001). At low coverages, the XPD results reveal that the oxide structure is strained resulting from the overlayer being forced to adopt the lattice parameters of the Pd substrate. This strain is manifested in the slight broadening of the diffraction spots at low coverages (Figure 4.5(b)). As the thickness of the film increases, ordering is enhanced and at high coverages the influence of the substrate of the film decreases so that the film reverts to a more bulk-like structure. Also, for the rock-salt crystal structure, the surface energy is far lower for the (100) surface than for any other, thus making it energetically the most favorable surface.

The sequential growth of both chromium- and iron-oxide films on Ag(001) (Figures 5.1(c) and 5.2(c)) result in 3-fold symmetry structures on a square substrate

lattice. This could be attributed to the rather weak Fe-Ag and Cr-Ag interaction, so that rearrangement of the overlayer atoms upon oxidation occurs to accommodate the lowest energy oxide surface. This, in general, should only be possible for very thin (submonolayer) films. From the surface energy calculations done by Mishra and Thomas [122] for the low index surfaces of $MgAl_2O_4$, Fe_3O_4, and other spinel ferrites, it was found that the surfaces parallel to the {111} planes are of the lowest energy. For Fe_3O_4, the calculated surface energies for the {111}, {100}, and {110} surfaces are 0.223 J/m^2, 1.451 J/m^2, and 2.164 J/m^2 respectively. Thus, for the sequential growth of Fe_3O_4 on Ag(001), the (111) surface would be the most favorable surface energetically. Lawrence and Parker [123] performed simulation studies to determine the energies of perfect and defective surfaces in Cr_2O_3 at 0 K. For the perfect surfaces of Cr_2O_3, the calculated unrelaxed and relaxed surface energies are given in Table 5.1. The relaxed energies are for the free surfaces of Cr_2O_3 that relax appreciably from the simple bulk terminations with significant reductions in energy. The $(00\bar{0}1)$ and $(10\bar{1}2)$ surfaces are calculated to have the lowest surface energy after relaxation, with the decrease in surface energy for the relaxed $(00\bar{0}1)$ surface being larger than for any other surface considered. The $(00\bar{0}1)$ surface is close packed. Thus the $Cr_2O_3(111)$ structure with a relaxed surface should be an energetically favorable structure on Ag(001).

Table 5.1. Calculated Perfect Surface Energies [123]

Surface	Unrelaxed energy (J/m^2)	Relaxed energy (J/m^2)
$00\bar{0}1$	4.59	1.61
$10\bar{1}0$	5.02	2.10
$11\bar{2}0$	3.42	1.90
$10\bar{1}1$	4.34	2.05
$10\bar{1}2$	2.77	1.70

5.5. SUMMARY AND CONCLUSIONS

Surface energy is an important consideration during the deposition and growth of overlayers on a substrate. It determines to a large extent not only the nucleation and growth morphology of epitaxial overlayers, but also the ordering and stability of the structures formed. Surface energy values of most metals are well documented, and can provide an insight into how the growth of metal films can occur on metal substrates. Prediction of the growth morphology of oxide surfaces is more difficult because surface energies for oxide surfaces are not as well known as for the metal surfaces. In addition, interfacial energies are poorly understood for either the growth of metal or oxide overlayers on substrates. Discussions on the growth of Fe (or Cr) metal on Pd(001) and Ag(001) substrates in Section 5.4. reveal just how complex predictions for the growth of metals on a metal substrate can get. In practice, layer-by-layer growth can be approached only when the surface energies of the film (γ_f) and the substrate (γ_s) match closely or when $\gamma_f < \gamma_s$, and for $\gamma_f > \gamma_s$ growth of three-dimensional islands can be expected to occur.

There are various factors that affect oxidation kinetics, principle among them being temperature, oxygen pressure, and degree of substrate-overlayer interaction. In the present study, the oxide films on Pd(001) were deposited at a constant elevated temperature of 300 ºC and annealed at 400-420 ºC, and at oxygen pressure of 2×10^{-5} Torr. Elevated substrate temperatures would promote domain growth and ordering. The substrate-overlayer interaction (whether strong or weak) would determine the stability and structure of the films, and depending on the degree of interaction, different oxide structures were produced when films were grown on Pd(001) and Ag(001) using the multilayer and the sequential deposition techniques.

Oxide film growth was also seen to depend on the deposition technique. For the chromium- and iron-oxide films grown on Ag(001), the sequential growth technique resulted in the growth of structures with three-fold rotational symmetry on a substrate with four-fold symmetry. In the initial submonolayer regime, due to weak interactions with the Ag substrate, the oxidation of the deposited metal atoms results in rearrangement of the oxide nuclei. This results in the growth of oxides with the more energetically favored surfaces – generally closed packed. With further increase in film thickness, this 3-fold oxide surface becomes the template for the growth of the 3-fold α-Cr_2O_3(111) and

Fe_3O_4(111) structures. The multilayer growth technique resulted in the growth of α-Cr_2O_3(210) and Fe_3O_4(100) structures. For the thicker multilayer metal films deposited, the Ag(001) substrate fixes the symmetry of the metal film prior to oxidation, and oxidation of the metal film is equivalent to oxidizing the bcc(001) surface of the bulk metal. Exposure to oxygen then results in structures with four-fold symmetry since it is energetically unfavorable to rearrange the deposited metal atoms in the multiple layers.

The growth of the iron-oxide films on Pd(001) seems to be relatively independent of the deposition technique. Both types of deposition techniques result in the growth of a FeO(001) structure with a reconstructed surface. While the oxide surface resulting from both the multilayer and sequential deposition techniques yield c(8x2) LEED patterns, there are differences observed between the XPD curves for the low and high coverage films. For the thin oxide films, the substrate-overlayer interaction is strong enough to force the low coverage structure to adopt the lattice parameters of the Pd substrate. In the initial submonolayer regime, oxidation of the interfacial alloy region results in an ordered structure that forms the template for the nucleation and further growth of the oxide. As the film thickness increases, the effect of the substrate decreases and the lattice parameters of the overlayer revert to that of a more bulk-like structure. However, no structural phase change occurs during this transition, implying thermodynamic stability of the c(8x2) structure, and reconstruction of the of the FeO(001) surface results in a surface with finite surface potential that does not diverge with thickness. Oxidation of the multilayer films is equivalent to oxidizing bulk FeO(001), and rearrangement of the metal atoms on oxidation is not energetically favorable. The substrate fixes the symmetry of the oxide structure, and the FeO(001) structure with the reconstructed surface remains the energetically most favorable configuration with a finite surface potential.

The growth of the chromium-oxide films on Pd(001), on the other hand, is found to depend on the deposition technique. The sequential deposition technique does not yield any stable or well-ordered structures. In the initial submonolayer and monolayer regimes, oxidation of the interfacial region leads to a disordered structure at room temperature, which becomes ordered only at elevated temperatures. As such, subsequent metal deposition and oxidation would result in the interaction of the overlayer with the interface, and the change in the stability and order of the structure with temperature

would very much depend on the corresponding stability and order of the interfacial region. Immediately after annealing the film at temperatures of 420 ºC, well-ordered c(4x2) LEED patterns are observed. The LEED pattern however deteriorates as the substrate cools down implying increase in disorder, until the films become completely disordered. Oxidation of the multilayer Cr films whose symmetry is already fixed by the Pd substrate leads to the formation of an ordered oxide with the same 4-fold symmetry as the substrate.

Lattice match (or mismatch), and film(metal)–substrate interaction strength are important factors in the determining the oxide film symmetries resulting from the growth of the films on the substrates. A good lattice match between the film and the substrate can lead to good epitaxial growth of the overlayer with minimal strain, and with increasing lattice mismatch, the build up of strain in the film can lead to misfit dislocation, film buckling, 2D layer-by-layer or 3D island growth, or coincidence lattice formation. In contrast to the weak interaction of the Ag substrate with the overlayer, stronger substrate-film interaction, as in the case for film growth on the Pd substrate, would lead to interface chemistry such as interdiffusion, alloying, and/or oxidation-reduction reactions, and substantially affect the growth and structure of the films.

6. CONCLUSIONS

6.1. CHROMIUM-OXIDE FILM GROWTH ON Pd(001)

This work has shown that well-ordered chromium oxide films may be grown on Pd(001) by oxidation of multilayer Cr films. The multilayer deposition of Cr_xO_y produces a sharp (1x1) LEED pattern for both the low and high coverage oxide films. No structural phase change is observed in going from the thin to the thick films (5–23 Å). The absence of extra LEED spots suggests that the Cr_xO_y overlayer has the same surface mesh as the Pd(001) substrate. Based on the comparison between the XPD results and the MSCD calculations, good agreement is achieved for a CrO(001) structure, as well as for a Cr_3O_4(001) structure with a reconstructed surface. Based on the R-factor calculations, the best agreement between the XPD curves and the MSCD calculations, however, is achieved for a mixed CrO-Cr_3O_4 phase — the CrO(001) structure with the same in-plane lattice structural parameters as that of the Pd substrate ($a_0^{CrO} = a_0^{Pd} = 2.75$ Å), and the reconstructed Cr_3O_4(001) with its bulk lattice parameters ($a_0^{Cr_3O_4} = 2.86$ Å) — with weighted compositions from each individual phase. The CrO phase is not stable in bulk, and so, on the basis of the literature that exists for other studies performed on the growth of CrO on different substrates, the model calculations for this phase were conducted with the CrO(001) structure having the same lattice parameters as that of the Pd substrate. For the Cr_3O_4 structure, the model calculations were performed for a reconstructed B-layer terminated (001) surface (the Cr ions occupy the octahedrally coordinated interstitial sites in the oxygen fcc lattice) that has a mixture of Cr^{3+} and Cr^{2+} ions in the ratio of Cr^{3+}:Cr^{2+} = 5:1. With the exception of the chromium oxidation state, this surface is identical to that of CrO(001) and is in agreement with XPS results indicating the presence of predominantly Cr^{3+} near the surface

For the sequentially grown chromium-oxide films, no well-ordered structures were observed from the LEED results. The sequentially deposited films were subjected to annealing treatments at two different temperature ranges. For the oxide films that were annealed at 400-420 ºC, a well-ordered c(4x2) LEED pattern (from approximately 6 Å onwards) was initially observed immediately after the anneal. However, the structure was

found to be unstable, and from the LEED patterns, several reconstructions of the oxide surface were observed as the substrate cooled down. The final oxide structure at room temperature was not well ordered, and the LEED pattern continued to deteriorate further until there was complete disorder observed. For the films annealed at 490-500 ºC, only partially ordered LEED patterns were observed, and here too, deterioration of the oxide films with time was observed. No well-ordered oxide structures were obtained in this case too. As such, it was decided that further characterization by XPD of the sequentially grown chromium-oxide films was not justified.

6.2. IRON-OXIDE FILM GROWTH ON Pd(001)

Deposition of Fe_xO_y films on Pd(001) by both the multilayer and sequential growth techniques result in the growth of well ordered iron-oxide films that exhibit a c(8x2) LEED pattern. The LEED pattern is consistent with the FeO(001) structure with a reconstructed surface, which consists of 2 domains rotated by 90º with respect to one another. Based on the LEED results, no distinction can be made between the films produced by the two deposition methods. LEED also cannot distinguish between the low and high coverage films, apart from the fact that there is some amount of observable disorder present in the very thin films (~3 Å) produced by the sequential deposition technique, due to which the diffraction spots in the LEED pattern broaden initially (Figure 4.6(b)). However, the high coverage films from both the multilayer and sequential deposition techniques give rise to well ordered c(8x2) LEED patterns.

XPD structural determinations were made for film thicknesses ranging from ~8 Å to 43 Å. Structural investigations for the very thin films (~ 3 Å) were not made because they were too thin for quality XPD studies. From the XPD results, it can be observed that the deposition technique has little effect on the oxide structure growth. However, determination of the variation in lattice structural parameters as we go from the low to high coverage systems is possible. Comparison between the XPD curves and the MSCD calculations reveal that the structure for the thin films (the upper cutoff being at ~13 Å) is a FeO(001) structure with reconstructed surface that adopts the in-plane lattice parameters of the Pd substrate ($a_0^{FeO} = a_0^{Pd} = 2.75$ Å), but, calculations investigating

possible interlayer relaxations at the surface for low coverages proved inconclusive. From model calculations, the best agreement for the high coverage XPD curves is obtained for a FeO(001) structure with bulk-like in-plane lattice parameters (a_0^{FeO} = 3.05 Å), and with a first interlayer separation ~16% less than the bulk value.

6.3. SUBSTRATE-OVERLAYER INTERACTION

The differences observed in the growth of chromium- and iron-oxide films on Pd(001), and Ag(001) [58, 99] using the multilayer and sequential deposition techniques illustrates the importance of growth conditions and substrate/oxide interactions in determining stability and structure of the oxide films.

Oxidation of multilayer Cr (or Fe) films is equivalent to oxidizing bulk-like metal films, whose symmetry is fixed by the substrate lattice. However, the present study is unable to explain the differences observed in the LEED patterns and structures obtained from the multilayer oxidation of the Cr (or Fe) metal films on Pd(001) and Ag(001).

The growth of oxide films using the sequential deposition technique, on the other hand, very much depends on the degree of interaction between the substrate and the film. The initial oxidation of the metal film takes place before multiple layers can form. For the oxide films grown on Ag(001), weak metal film-substrate interaction leads to the Cr (or Fe) rearranging on the surface to accommodate growth of the lowest energy oxide surface. This results in the growth of 3-fold symmetry structures — $Fe_3O_4(111)$ and $Cr_2O_3(111)$ — on a square lattice substrate. For the oxide films grown on Pd(001), initial deposition of metal at the submonolayer and monolayer regime leads to the formation of an interfacial region due to stronger metal film-substrate interaction. The interfacial region, upon oxidation, forms the template for subsequent growth of the oxide films, and the stability and order of the film would depend on the corresponding stability and order of the interface. While ordered c(8x2) oxide structures were observed for iron-oxide growth, no well-ordered stable structures are obtained from chromium-oxide growth on Pd(001).

BIBLIOGRAPHY

[1] S. J. Roosendaal, A.M. Vredenberg, and F.H.P.M. Habraken, Phys. Rev. Lett. **84**, 3366-3369, 2000.

[2] D. P. Woodruff and T. A. Delchar, *Modern Techniques of Surface Science*, 2nd edition, Cambridge University Press, Cambridge, 1994.

[3] F. Gautier and D. Stoeffler, Surf. Sci. **249**, 265-280, 1991.

[4] Ivan V. Markov, *Crystal Growth For Beginners: Fundamentals of Nucleation, Crystal Growth and Epitaxy,* World Scientific Publishing Co. Pte. Ltd., Singapore, 1995.

[5] F. R. de Boer, W. C. M. Mattens, A. R. Miedema, and A. K. Niessen, *Cohesion in Metals*, North-Holland Physics Publishing, Amsterdam, 1989.

[6] H. L Skriver and N. H. Rosengaard, Phys. Rev. B **46**, 7157, 1992.

[7] L. Vitos, A. V. Ruban, and H. L. Skriver, Surf. Sci. **411**, 186-202, 1998.

[8] M. Methfessel, D. Henning, and M Scheffer, Phys. Rev. B **46**, 4816, 1992.

[9] J. Kollar, L. Vitos, and H. L. Skriver, Phys. Rev. B **49**, 11288, 1994.

[10] A. M. Rodrigeuz, G. Bozzolo, and J. Ferrante, Surf. Sci. **289**, 100, 1993.

[11] Gabor A. Somorjai, *Chemistry in Two Dimensions: Surfaces*, Cornell University Press, Ithaca, 1981.

[12] M. D. Pashley, Phys. Rev B **40**, 10481, 1989.

[13] P. W. Tasker, J. Phys. C **12**, 4977, 1979.

[14] C. S. Fadley, Surf. Sci. Rep. **19**, 231, 1993.

[15] C. S. Fadley, Physica Scripta **T17**, 39, 1987.

[16] J. Osterwalder, Arab. J. Sci. Eng. **15**, 273, 1990.

[17] J. Osterwalder, P. Aebi, R. Fasel, D. Naumovic, P. Schwaller, T. Kreutz, L. Schlapbach, T. Abukawa, and S. Kono, Surf. Sci. **331-333**, 1002-1014, 1995.

[18] K. Sigehbahn, U. Gelius, H. Siegbahn, and E. Olson, Phys. Lett. **32A**, 221, 1970.

[19] K. Sigehbahn, U. Gelius, H. Siegbahn, and E. Olson, Physica Scripta **1,** 272, 1970.

[20] C. S. Fadley, *Electron Spectroscopy - Theory, Techniques, and Applications*, Vol. **2**, Academic Press, New York, 1978.

[21] W. E. Spicer, Phys. Rev. **112**, 114, 1958.

[22] Stephen Huffner, *Photoelectron Spectroscopy*, Springer Ser. Solid State Sci., Vol. **82**, Springer-Berlin-Heidelberg, 1996.

[23] C. S. Fadley, Prog. Surf. Sci. **16**, 275, 1984.

[24] M. P. Seah and W. A. Dench, Surface Interface Analysis **1**, 2-11, 1979.

[25] Handbook of X-Ray Photoelectron Spectroscopy: A Reference Book of Standard Spectra for Identification and Interpretation of XPS Data, edited by Jill Chastain, Perkin-Elmer Corporation, 1992.

[26] S. A. Chambers, Adv. Phys. **40**, 357, 1991.

[27] W. F. Egelhoff, Jr., CRC Crit. Rev. Solid State Mat. Sci. **16**, 213, 1990.

[28] S. A. Chambers, Surf. Sci. Rep. **16**, 261, 1992.

[29] C. S. Fadley, S. Thevuthasan, A. P. Kaduwela, C. Westphal, Y. J. Kim, R. Ynzunza, P. Len, E. Tober, F. Zhang, Z. Wang, S. Ruebush, A. Budge, and M. A. Van Hove, J. Electron Spectrosc. Relat. Phenom. **68**, 19, 1994.

[30] C. S. Fadley, M. A. Van Hove, Z. Hussain, and A. P. Kaduwela, J. Electron Spectrosc. Relat. Phenom. **75**, 273, 1995.

[31] J. Osterwalder, Arab. J. Sci. Eng. **15**, 273, 1990.

[32] J. Osterwalder, P. Aebi, R. Fasel, D. Naumovic, P. Schwaller, T. Kreutz, L. Schlapbach, T. Abukawa, and S. Kono, Surf. Sci. **331-333**, 1002, 1995.

[33] Y. Margoninski, Contemp. Phys. **27**, 203, 1986.

[34] H. C. Poon and S. Y. Tong, Phys. Rev. B **30**, 6211, 1984.

[35] David Patrick Moore, *Thin Film Systems: Design of Laboratory Analysis System and Studies of V/ Cu(001) And Cu/ Ag(001) By X-Ray Photoelectron Diffraction and Low Energy Electron Diffraction*, University of Missouri-Rolla (1999).

[36] A. Barbieri and Michael A. Van Hove, http://www.ap.cityu.edu.hk/personal-website/Van-Hove_files/mscd/mscdpack.html.

[37] J. J. Rehr and R. C. Albers, Phys. Rev. B **41**, 8139, 1990.

[38] S. Tanuma, C. J. Powell, and D.R. Penn, Surface and Interface Analysis **17**, 911-926, 1991.

[39] M. Sagurton, E. L. Bullock, and C. S. Fadley, Surf. Sci. **182**, 287, 1987.

[40] C. E. Kuyatt and J. A. Simpson, Rev. Sci. Instrum. **38**, 103, 1967.

[41] E. A. Wood, J. App. Phys. **35**, 1306, 1964.

[42] R. W. G. Wyckoff, *Crystal Structures*, Vols. **2** and **3**, Interscience New York, 1969.

[43] P. Michel and C. Jardin, Surf. Sci. **36**, 478-487, 1973.

[44] S. Ekelund and C. Leygraf, Surf. Sci. **40**, 179-199, 1973.

[45] F. Watari and J. M. Cowley, Surf. Sci. **105**, 240-264, 1981.

[46] H. M. Kennet and A. E. Lee, Surf. Sci. **33**, 377-398, 1972.

[47] H. J. Freund, H. Kuhlenbeck, and V. Staemmler, Rep. Prog. Phys. **59**, 283, 1996.

[48] G. Gewinner, J. C. Peruchetti, A. Jaegle, and A. Kalt, Surf. Sci. **78**, 439, 1978.

[49] A. Stierle, P. Bodeker, and H. Zabel, Surf. Sci. **327**, 9, 1995.

[50] L. Zhang, M. Kuhn, and Ulrike Diebold, J. Vac. Sci. Technol. A **15**, 1576-1580, 1997.

[51] X. S. Du, S. Hak, T. Hibma, O. C. Rogojanu, and B. Struth, J. Crystal Growth **293**, 228-232, 2006.

[52] A. Maetaki, M. Yamamoto, H. Matsumoto, and K. Kishi, Surf. Sci. **445**, 80-88, 2000.

[53] A. Maetaki and K. Kishi, Surf. Sci. **411**, 35-45, 1998.

[54] K. L. Man, Q. Guo, and M. S. Altman, Surf. Sci. **600**, 1060-1070, 2006.

[55] L. Zhang, M. Kuhn, and U. Diebold, Surf. Sci. **375**, 1-12, 1997.

[56] W.A.A. Priyantha and G.D. Waddill, Surf. Sci. **578**, 149-161, 2005.

[57] P. S. Robert, H. Geisler, C. A. Ventrice Jr., J. van Ek, S. Chaturvedi, J. A. Rodriguez, M. Kuhn, and U. Diebold, J. Vac. Sci. Technol. A **16**, 990, 1998.

[58] Osman Ozturk, *Growth And Structure Of Ultra-Thin Epitaxial Chromium And Iron Oxide Films On Ag(001) And Ag(111): A Comprehensive Study Accomplished By X-Ray Photoelectron Diffraction And Low Energy Electron Diffraction*, University of Missouri-Rolla, 2002.

[59] J.C. Cook, M. Dowling, W. Schwarzacher, and E. M. McCash, Surf. Rev. Lett. **4**, 1257-1261, 1997.

[60] P. Steadman, C. Norris, C. L. Nicklin, N. Jones, J. S. G. Taylor, S. A. de Vries, and S. L. Bennet, Phys. Rev. B **64**, 245412, 2001.

[61] J. F. Lawler, R. G. P. van der Kraan, H. van Kemper, and A. J. Quinn, Phys. Rev. B **63**, 11159-11163, 1996.

[62] C. Krembel, M. C. Hanf, J. C. Peruchetti, D. Bolmont, and G. Gewinner, Phys Rev. B **44**, 8407-8410, 1991.

[63] J. Quinn, Y. S. Li, H. Li, D. Tian, F. Jona and P. M. Marcus, Phys. Rev. B **43**, 3959, 1991.

[64] S. –K. Lee, J. –S. Kim, B. Kim, Y. Cha, W. K. Han, H. G. Min, J. Seo and S. C. Hong, Phys. Rev. B **65**, 11423, 2001.

[65] M. Methfessel, D. Henning, and M Scheffer, Phys. Rev. B **46**, 4816, 1992.

[66] S. Tanuma, C. J. Powell, and D. R. Penn, Surf. Sci. **192**, L849-L857, 1987.

[67] C. Xu, M. Hassel, H. Kuhlenbeck, and H. J. Freund, Surf. Sci. **258**, 23, 1991.

[68] A. M. Venezia, C. M. Loxton, and J. A. Horton, Surf. Sci. **225**, 195, 1990.

[69] I. Ikemoto, K. Ishii, S. Kinoshita, H. Kuroda, M. A. Alario-Franco, and J. M. Thomas, J. of Solid State Chem. **17**, 425, 1976.

[70] M. Aronniemi, J Sainio, and J. Lahtinen, Surf. Sci. **578**, 108-123, 2005.

[71] D. Wolf, Phys. Rev. Lett. **68**, 3315, 1992.

[72] O. C. Rogojanu, *Stabilizing CrO By Epitaxial Growth*, University of Groningen, 1973.

[73] M. Schmid, G. Leoardelli, M. Sporn, E. Platzgummer, W. Hebenstreit, M. Pinczolits, and P. Vanga, Phys. Rev. Lett. **82**, 355-358, 1999.

[74] J. B. Pendry, J. Phys. C: Solid State Phys. **13,** 937-944, 1980.

[75] B. Stanka, W. Hebenstreit, U. Diebold, and S. A. Chambers, Surf. Sci. **448**, 49-63, 2000.

[76] E. J. W. Verwey, Nature (London) **144**, 327, 1939.

[77] W. K. Liu and M. B. Santos, *Thin Films: Heteroepitaxial Systems*, World Scientific Publishing Co. Pte. Ltd., 1999.

[78] H. Li, Y. S. Li, J. Quinn, D. Tian, S. Sokolov, F. Jona, and P. M. Marcus, Phys Rev. B **42**, 9195-9198, 1990.

[79] J. Chen, M. Drakaki, and J. E. Erskine, Phys Rev. B **45**, 3636-3643, 1992.

[80] G. C. Smith, H. A. Padmore, and C. Norris, Surf. Sci. **119**, L287, 1982.

[81] Z. Q. Wiu, J Pearson and S. D. Bader, Phys. Rev. Lett **70**, 1006-1009, 1993.

[82] D. E. Burgler, C. M Schmitt, D. M. Sachaller, F. Meisinger, R. Hofer, and H. –J. Guntherodt, Phys. Rev. B **56**, 4149-4158, 1997.

[83] P. Xhonneux and E. Courtens, Phys. Rev. B **46**, 556-559, 1992.

[84] M. Wuttig, B. Feldman, J. Thomassen, F. May, H. Zillgen, A. Brodde, H. Hannemann, and H. Neddermeyer, Surf. Sci **291**, 14-28, 1993.

[85] K. O. Legg, F. Jona, D. W. Jepsen, and P. M. Marcus, Phys. Rev. B **16**, 5271, 1977.

[86] C. Brucker and T. N. Rhodin, Surf. Sci. **57**, 523-539, 1976.

[87] G. W. Simmons and D. J. Dwyer, Surf. Sci. **48**, 373-392, 1975.

[88] C. Leygraf and S. Ekelund, Surf. Sci. **40**, 609-635, 1973.

[89] M. Busch, M. Gruytens, and H. Winter, Surf. Sci. **600**, 2778-2784, 2006.

[90] H. –J. Kim, J. –H. Park, E. Vescono, *Phys Rev B **61***, 15284-15287, 2000.

[91] S. A. Chambers, S. Thevuthasam, and S. A. Joyce, Surf. Sci. **450**, L273-L279, 2000.

[92] Y. Gao and S. A. Chambers, J. Crystal Growth **174**, 446-454, 1997.

[93] G. H. Vurens, V. Maurice, M. Salmeron and G. A. Somorjai, Surf. Sci. **268**, 170-178, 1992.

[94] Y. J. Kim, C. Westphal, R. X. Ynzunza, H. C. Galloway, M. Salmeron, M. A. Van Hove and C. S. Fadley, Phys. Rev. B **55**, R 13448, 1997.

[95] H. C. Galloway, J. J. Benitz and M. Salmeron, J. Vac. Sci. Technol. A **12**, 2302, 1994.

[96] E. L. Lopes, G. J. P. Abreu, R. Paniago, E. A. Soares, V. E. de Carvallo and H. – D. Pfannes, Surf. Sci. **601**, 1239-1245, 2007.

[97] Sh. Shaikhutdinov, M. Ritter, and W. Weiss, Phys. Rev. B **62**, 7535, 2000.

[98] G. D. Waddill and Osman Ozturk, Surf. Sci. **575**, 35-50, 2005.

[99] Weerasinghe Priyantha, *Surface Structure Determination Of Nanoscale Transition Metal Oxide Films Using X-Ray Photoelectron Diffraction And Low Energy Electron Diffraction*, University of Missouri-Rolla, 2005.

[100] C. Liu and S. D. Bader, Phys Rev B **44**, 2205, 1991.

[101] X. F. Jin, J. Barthel, J. Shen, S. S. Manoharan, and J. Kirschner, Phys Rev B **60**, 11809-11812, 1999.

[102] C. Boeglin, H. Bulou, J. Hommet, X. Le Cann, H. Magnan, P. Le. Finre and D. Chandesris, Phys. Rev. B **60**, 4220, 1999.

[103] B. W. Veal and A. P. Paulikas, Phys. Rev. B **31**, 5399, 1985.

[104] J. A. Venables, G. D. T. Spiller, and M. Hanbucken, Rep. Prog. Phys. **47**, 399-459, 1984.

[105] S. A. Chambers, Surf. Sci. Rep. **39**, 105-180, 2000.

[106] E. Bauer and Jan H. van der Merwe, Phys. Rev. B **33**, 3657, 1986.

[107] F. Delbecq, L. Verite, and P. Sautet, Chem. Mater. **9**, 3072-3082, 1997.

[108] St. Lauer, Z. Guan, H. Wolf, H. Natter, M, Schmelzer, R. Hempemann, and Th. Wichert, Nanostructured Materials **12**, 955-958, 1999.

[109] Y. Hsu, J.E. Schmidt, M. Gupta, S. Jan, and L. Berger, J. App. Phys. **54**, 1887-1891, 1983.

[110] S. N. Mishra, Phys. Rev. B **77**, 224402, 2008.

[111] J. E. Van Dam, P. C. M. Gubbens, and G. J. Van der Berg, Physics **70**, 520-564, 1973.

[112] Phase Diagrams of Binary Iron Alloys, Edited by H. Okamoto, ASM International, Materials Park, Ohio 44073-0002, 1993.

[113] G. Ghosh and G.B. Olson, J. Phase Equilibria **21**, 32-39, 2000.

[114] M. Venkatraman and J. P. Neumann, J. Phase Equilibria **11**, 263-265, 1990.

[115] X. –G. Wang, W. Weiss, Sh. K. Shaikhutdinov, M. Ritter, M. Petersen, F. Wagner, R. Schlogl, and M. Scheffler, Phys. Rev. Lett. **81**, 1038-1041, 1998.

[116] K. R. Lawless, Reports On Progress In Physics **37**, 231, 1974.

[117] L. Vitos, A. V. Ruban, and H. L. Skriver, Surf. Sci. **411**, 186-202, 1998.

[118] G. C. Smith, H. A. Padmore, and C. Norris, Surf. Sci. **119**, L287, 1982.

[119] P. Steadman, C. Norris, C. L. Nicklin, N. Jones, J. S. G. Taylor, S. A. de Vries, and S. L. Bennett, Phys. Rev. B **64**, 245412, 2001.

[120] F. Chemam, A. Bouabellou, A. Layadi, and S. Senoussi, Material Science and Engineering: C **19**, Issues 1-2, 125-128, 2002.

[121] Etienne, P. Lequien, S. Nguyen-Van-Dau, F. Cabanel, R. Creuzet, G. Friederich, A. Massies, J. Fert, A. Barthelemy, A. Petroff, and F. Thomson, Journal of Applied Physics **67**, 5400-5402, 1990.

[122] R. K. Mishra and G. D. Thomas, Journal of Applied Physics **48**, 4576-4580, 1977.

[123] P. J. Lawrence and S. C. Parker, J. Am. Ceram. Soc. **71**, issue no. 8, C-389–C-391, 1988.

VITA

Tina Dhekial-Phukan was born in India, in the north-eastern state of Assam. She hails from the city of Guwahati, which is situated on the banks of the mighty Brahmaputra river. She received her primary education in Shillong, Meghalaya, and graduated from Pine Mount High School in 1998. She received a Bachelor of Science degree in Physics from Gauhati University in 2001, and a Master of Science degree in Physics in 2003 from the Indian Institute of Technology Guwahati. In June 2005, she began her PhD in Physics under the guidance of Dr. G. D. Waddill at Missouri University of Science and Technology, Rolla.